Investigative Development of an UWB Radar for UAS-borne Applications

By

Shravan Kaundinya

Submitted to the graduate degree program in Electrical Engineering & Computer Science and the Graduate Faculty of the University of Kansas in partial fulfillment of the requirements for the degree of Master of Science.

Chair: Dr. Carl Leuschen

Dr. Fernando Rodriguez-Morales

Dr. Chris Allen

Dr. Emily Arnold

Date Defended: 14 December, 2021

The thesis committee for Shravan Kaundinya certifies that this is the approved version of the following thesis:

Investigative Development of an UWB Radar for UAS-borne Applications

Chair: Dr. Carl Leuschen

Dr. Fernando Rodriguez-Morales

Date Approved: 14 December, 2021

Abstract

The engineering ethos of the last decade has been miniaturization. Progress in various industries like material design, semiconductor technology, and digital signal processing has resulted in low-profile electrical systems. This has facilitated the means of integration onto platforms. Sensors such as radars are typically large, heavy, and consume a lot of power. Miniaturization of radars can enable important applications like remote sensing the various aspects of the Earth System from Unmanned Aerial Systems (UAS). Information about natural topography like ice sheets, vegetation cover, and ocean currents can improve our understanding of the natural processes and continued measurements offer insight into the changes over time. Soil plays a vital role in the Earth's hydrological cycle. The moisture in soil influences the weather, vegetation, and human endeavors like construction. Models are built using an extensive set of temporal soil moisture data to predict natural disasters like droughts, floods, and landslides. It plays a central role in the areas of agriculture and water resource management and hence can influence policy making and economic decisions.

In this work, an investigative approach to the design, build, and test of a 2 – 18 GHz Frequency Modulated Continuous Wave radar for snow and soil measurements is reported. The radar system is designed to be integrated to the Vapor 55 rotorcraft, which is a Group 1 UAS. The radar can operate as a scatterometer to measure backscatter signatures in all four combinations of vertical and horizontal polarizations; or as a nadir-looking sounder for fine-resolution snow thickness measurements.

One of the primary contributions of this work is the exploration of a single-module that integrates the radar's RF transmitter, RF receiver, receiver's IF section, wideband sweep generator, and the

DC bias circuitry for the active components. The sweep generator is based on a phase-locked loop and frequency multiplication/translation stage. The compact assembly is in the form of two multilayer Printed Circuit Boards (PCB) merged together and it occupies an area of nearly 170 cm2. This thesis describes the design, construction, and testing of the module, along with recommendations for future revisions.

A commercially off-the-shelf module (Arena series by Tomorrow.io, formerly Remote Sensing Solutions) is the digital backend and it consists of an Arbitrary Waveform Generator (AWG) and a data acquisition system capable of sampling up to 250 MSPS. The module is low-profile with dimensions of 7.6 cm x 19.3 cm x 2.3 cm and weighs less than 400 g including the separate aluminum enclosure intended to be integrated with the radar's RF and mixed-signal sections.

A second contribution of this work is the design of a prototype antenna front-end, which consists of four four-element antenna arrays housed in a Delrin plastic fixture and are fed using custom-designed microstrip power dividers. The dimensions of the fixture are 13.7 cm x 5.9 cm x 5.5 cm and the uniform elemental distance is 2.5 cm. The arrays are fastened to a metal sheet and a custom-designed four-layer fiberglass composite fairing protects the arrays. The entire front-end is integrated on the rotorcraft and measured in an anechoic chamber. The measured, fully integrated return loss of each array covers 2 – 18 GHz and the highest value is -7.22 dB at 5.23 GHz. The radiation pattern shows a distinct nadir-pointing main lobe for nearly the entire bandwidth, however the effects of the platform increase the average side-lobe levels to less than 10 dB for 12 – 18 GHz. The measured maximum nadir gain is 15.88 dB at 10 GHz and there is a greater than 6 dB variation in magnitude within the bandwidth. This variation is compensated by processing the backscatter data over distinct sub-bands that have a maximum nadir gain variation of 6 dB.

Lastly, the thesis describes two system tests conducted to evaluate the effectiveness of a prototype radar with soil as the target. These are proof-of-concept measurements to detect differences in backscatter signatures between dry and wet soil. Gravimetric measurements of collected soil samples indicate an average change of 9.5% between the two moisture states. The antenna front-end is exclusively characterized using a Vector Network Analyzer and measurements are recorded for both co- and cross-polarization at three look angles of nadir, 15°, and 30°. The relative measurements are repeated on the same patch of land with a 1U version of the miniaturized radar. There are distinct differences in relative received power and backscatter profile for all four polarizations and at each look angle. It is observed that vertical polarization indicates a change in moisture content by an increase in the relative received power over an extended range beyond the primary backscatter signal. The horizontal polarization results in a greater peak received power for the primary backscatter signal, relative to the vertical polarization. The degradation in backscatter profile for vertical polarization is higher than horizontal polarization as a function of angle and this is observed for both dry and wet soil.

Acknowledgments

Dr. Carlton Leuschen's academic guidance has enabled me to strengthen my fundamentals in applied electromagnetics. His encouragement to enroll in a wide variety of classes has allowed me to grow as a systems engineer. I'd also like to sincerely thank him for the numerous wonderful opportunities at the Center for Remote Sensing of Ice Sheets that has enriched my learning experience.

Dr. Fernando Rodriguez-Morales' experiment and measurement-based teaching is a great method to understand Radio Frequency and Microwaves. His ability to explain concepts in an intelligible way enabled me to appreciate the magic of RF. I truly appreciate his patience, enthusiasm, and benevolence. His eagerness to work alongside students at every project stage is inspiring and admirable.

Dr. Christopher Allen's courses and teaching provided a crucial base throughout my graduate program. His eclectic knowledge of remote sensing made the classes fascinating and it inspired me to pursue this path.

Dr. Emily Arnold's specialization in aerospace and electrical engineering has provided me the opportunity to work on projects from a unique perspective. Her experiment-based teaching has allowed me to develop an intuitive understanding of antennas and airborne structures. She has been vital in educating cross-disciplinary engineering practices. I truly appreciate her patience, mentorship, and compassion.

I'd like to thank Paulette Place, Aaron Paden, Daniel Gomez-Garcia, Jennifer Laverentz, Rachel James, and Jim Rood for their assistance with the project. Each has contributed at various stages of the project and I appreciate their constant support.

I want to express my gratitude to Krishna Teja Karidi, Hara Madhav Talasila, Ankur Patil, and Brad Schroeder for their significant contributions to the project. I also appreciate the time and effort of Brian Macharia, Victor Berger, Sebastian Alvarez, Audrey Evans, Jeffery Redmond, Sri Sai Charan Mathi, William Teeple, and Dillon Fruhwirt.

It would be remiss of me if I do not thank my mentors who have guided me throughout my life: Dinakar S Magadi, Dr. H.S Nagaraj, and Dr. Karthikeya G.S. I am fortunate to be surrounded by great role models who are beacons of light in treacherous waters.

I'd like to sincerely thank my mother whose support I am extremely grateful for. Her resilience, tenacity, and valor has facilitated my success. Lastly, I'd like to dedicate this thesis to my father whose desire is finally fulfilled.

Table of Contents

List of Figures

List of Tables

.

1 Introduction

The thesis discusses the design of an ultra-wideband radar system for integration on an Unmanned Aerial System (UAS). The radar operates over 2 – 18 GHz and the architecture is Frequency Modulated Continuous Wave (FMCW). The radar is intended to function primarily as a scatterometer to record surface backscatter signatures from extended targets like soil and snow. The penetration into the surface is minimum and is on the order of several centimeters. Hence, the system can, in principle, also operate as a nadir-looking sounder for thin snow cover.

The design requirements for an UAS emphasizes the concept of miniaturization. Radars are typically large, heavy, and consume a significant amount of power. Hence, examples of remote sensing radars adapted to low-profile aerial platforms like UAS and CubeSats are not common. The inverse relationship between frequency and wavelength results in challenges for antenna designs in limited space. Ultra-wideband antennas typically have a percentage bandwidth on the order of 100% and such designs require a lot of space and weight, both of which are expensive on an UAS.

The most relevant contributions of this thesis are listed below:

1. Development of a compact RF system that includes all the relevant circuitry (biasing, transmitter, receiver, and intermediate) in a compact two-board design that replaces the old rack-mount system used in previous renditions. It also shows a pathway toward its integration into a small enclosure with digital and power subsystems.

2. Development of an antenna front-end suitable for the Vapor 55. This includes feed networks, isolation structures, and a fairing made of composite material.

3. Proof-of-concept measurements of soil backscatter at discrete frequency sub-bands to assess the feasibility of identifying moisture signatures using a radar mock-up and the antenna front-end.

1.1 Motivation

An overwhelming trend in systems development over the last several years is the reduction of size, weight, and power. Advancement in material design, semiconductor technology, and signal processing techniques have allowed electrical systems to gradually shrink in size and weight. The transistor technology has progressively improved over the decades and GaN-based high-electron mobility transistors (HEMTs) can be operated at a higher frequency, power, and temperature conditions than the silicon versions [1]. Fundamental components of active phased array radars like Transmit/Receive (T/R) modules use GaN HEMTs and operation in X-band with a maximum Radio Frequency (RF) power of 1 kW and moderate efficiencies has been reported [2].

The semiconductor evolution has enabled advanced packaging and miniaturization for a wide variety of applications like Internet of things (IoT) [3] measurement and characterization [4] and remote sensing from CubeSat platforms [5]. In 2019, the National Aeronautics and Space Administration (NASA) and the Jet Propulsion Laboratory (JPL) expressed a strategic intent to emphasize nine areas of technologies for Earth science and inter-planetary exploration [6]. Three of the nine areas are autonomous systems, miniaturized systems, and instruments and sensors. The current challenges for sensor performance can be addressed by focusing on instruments such as direct detectors and optics, coherent detectors and arrays, and active sensor systems.

UAS have exploded in popularity in the last decade. This is due to an increase in accessibility, availability of cost effective materials, and the capability to provide flexible and

controlled flight operation. These assets are highly favorable for remote sensing applications [7]. UAS-based measurements have been performed for archaeology [8], forestry [9], and water resource management [10]. Typically, instruments such as LIDARs, multi-spectral cameras, and infrared cameras are used as payloads due to the limited availability of space and weight.

The advantage of remote sensing over in situ measurements is the repeated and large temporal and spatial coverage [11]. This feature is vital for accurately mapping natural topography like ice sheets, soil, and vegetation. The Earth's ice cover has a significant impact on the global climate by reflecting a large portion of the solar radiation and having an effect on the global sea-levels [12]. Over the years, observations made using remote sensing instruments in the Arctic and Antarctic have indicated that the changes in polar ice are directly connected to the global climate system [13]. It is paramount to continue these polar measurements to better our understanding of climate change and in turn assess the effects on the biosphere.

Soil is one of the key elements in the Earth's hydrological cycle and plays a pivotal role in the ecological processes. The moisture content in the topsoil influences the weather and climate of a region [14]. Extensive temporal soil moisture data from across the planet can assist in predicting natural disasters like droughts, floods, and landslides [15]. Additionally, it is capable of augmenting strategies for agriculture, construction, and water resource management. Therefore, measuring soil moisture with the required resolution and accuracy can influence meteorology, disaster management, policy making, and economic decisions.

Radars are capable of operating under most weather conditions since microwaves can penetrate through clouds and rainfall and do not require an external source of illumination. Electromagnetic (EM) waves of longer wavelength are able to penetrate through targets like ice and vegetation. Hence, shorter wavelengths are typically used to gather information from the surface features like

soil and snow, while the longer wavelengths are used for sub-surface sounding [16]. A significant reason for the use of microwaves, as opposed to other wavelengths of light, is that the information obtained about the target is physically different. Microwave scattering is caused due to a combination of electrical (bulk-dielectric) and geometric (roughness) properties [17]. By customizing the characteristics of a radar, it is possible to infer both properties and derive unique insight into the target. Moreover, the information obtained through radars in the microwave region are complimentary to other instruments operating in the visible and infrared region.

1.2 Thesis Overview

This thesis is organized in six chapters. The introductory chapter first provides some background information regarding the relevancy and motivation.

Chapter 2 provides additional technical background on the type of radar and antenna described in this work. The general theoretical framework is provided as a prelude to the subject matter of this work. A brief summary of the features of the Vapor 55 UAS and its suitability are also discussed in this chapter.

Chapter 3 provides an overview of the radar system. First, the required specifications of the radar for performing scatterometer measurements from a UAS on extended targets is discussed. A link budget is then computed to assess the signal power requirements and the power levels of the expected returns for various types of soil. Backscatter data from literature is used as reference to estimate the values for the radar. Next, the full system design is discussed in detail by dividing into four sub-sections: digital, RF, mixed-signal, and power. The complexity of the RF and mixed-signal sections indicate the difficulty in miniaturizing an UWB system. Lastly, the integrated

system-level test is discussed as a means of experimentally validating the radar's functionality and performance.

Chapter 4 examines the antenna front-end design. The design requirements and challenges include both electrical and physical considerations. The antenna design is progressively discussed starting from a single element, array, feed network, to integrated measurements. The crucial antenna parameters for performing polarimetric scatterometer measurements are discussed at each design stage. It is useful to note the changes in antenna performance as the complexity towards the full setup increases. The final measurement is performed by integrating the entire front-end to the rotorcraft in an anechoic chamber.

Chapter 5 analyzes two full system tests. The performance of the antenna with a distributed target like soil is first tested with a Vector Network Analyzer (VNA). The calibrated cables and VNA allow the tests to show the exclusive performance of the front-end. It provides a reference for the next test, which is testing the antenna front-end with a radar. In this work, a rack-mount version of the miniaturized radar is used to test the same area of soil. These two tests are proof-of-concept measurements to establish a difference between the dry and wet soil backscatter. Sub-band processing is also discussed and how it can assist in discerning wet soil target returns.

Chapter 6 summarizes the work and highlights key results. Future plans for the system and recommendations for improving system are also discussed in this chapter.

2 Background

This section is intended to provide some basic background on the relevant topics discussed in this work. Several salient features are discussed in a theoretical manner. In the first sub-section, the basics of Frequency Modulated Continuous Wave (FMCW) radar are discussed. This is the design architecture of the radar system described in this work. The performance and capability of the radar are directly dependent on these specifications.

In sub-section 2.2, the fundamentals of polarimetric scatterometer are stated. This is a type of mode in which a radar may be operated to discern specific characteristics of the target. Polarimetry is explained mathematically to show how this technique is useful in performing surface backscatter measurements for extended targets like soil.

Sub-section 2.3 details the basics of microstrip antennas. The general operating principle is explained based on a circular microstrip patch antenna and vital performance parameters are discussed. In this thesis, the antenna is a circular microstrip patch antenna and multiple are grouped together to form an antenna array.

Section 2.4 lists the specifications of the Vapor 55 UAS. The radar system is tailored specifically for this vehicle and hence some background is necessary.

2.1 Overview of the FMCW radar architecture

Radars transmit a modulated waveform that scatters in all directions as it impinges on a target. The backscatter from the target is received and digitized after demodulation. The target characteristics like range and velocity are inferred from the received baseband signal. A commonly used architecture is the FMCW scheme. The waveform design is based on the pulse compression concept of achieving signal strength by transmitting a long-duration pulse that has a bandwidth

corresponding to that of a short-duration pulse. One of the primary advantages of this architecture is that it allows for operation over a very wide bandwidth (multiple Gigahertz), while keeping the requirements for data acquisition system (bandwidth and sample and rate) at a moderate level. However, challenges are presented in the form of stretch processing and range side-lobes. Figure 2-1 shows a high-level block diagram of an FMCW radar.

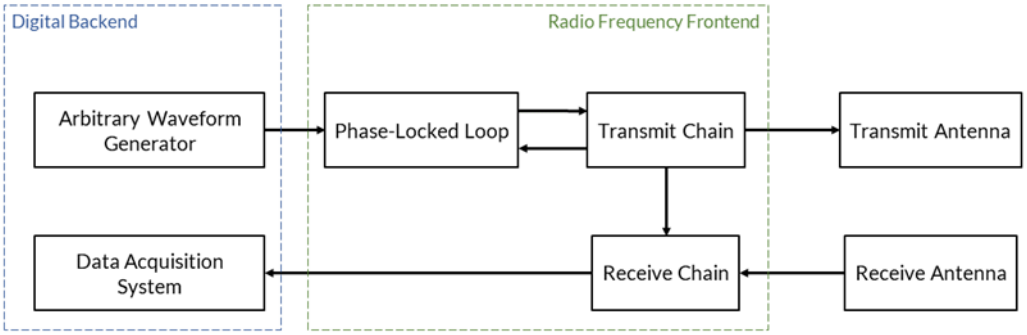

Figure 2-1: High-level block diagram of a Frequency Modulated Continuous Wave (FMCW) radar

An Arbitrary Waveform Generator (AWG) produces a reference signal that is typically three orders of magnitude lower than the carrier frequency of the radar. This reference signal is used in a negative feedback loop to produce the carrier frequency such that the phase is locked to the reference. Therefore, a high quality digital system and Phase-Locked Loop (PLL) are required to ensure the linearity of the frequency modulated or chirp signal. The instability of the chirp signal can result in undesirable frequency sidebands in the demodulated Intermediate Frequency (IF) signal. A linearization method using a PLL and an external compensation signal to reduce the loop tracking error can be used to solve this issue [18]. Other techniques are currently available to produce ultra-wideband chirps, but they tend to be more complex and power hungry [19].

The chirp signal produced at the output of the PLL is filtered and amplified in the RF transmit chain and radiated by the antenna. A copy of the transmit signal is used to mix-down the received chirp signal to produce the IF signal and this process is known as de-chirping. The baseband signal is digitized on the Data Acquisition System (DAQ) and a clock source synchronizes the timing

between the various sub-systems. Figure 2-2 shows a representation of the transmit and receive chirp signals along with an example waveform. The bandwidth of the chirp signal is denoted as B, the pulse length is τ, the beat frequency is fb, and the two-way propagation time is T. In a Continuous Wave (CW) radar, the second transmit signal starts at t2 and correspondingly the second receive signal starts at t2 + T. Therefore, the pulse length is equal to the Pulse Repetition Interval (PRI). The duty cycle, D is given by:

$$D = \tau(PRF) \tag{1.1}$$

The Pulse Repetition Frequency (PRF) is the inverse of the PRI and hence, for a CW radar the duty cycle is 100%. Pulsed Frequency Modulated (FM) radars may have a duty cycle ranging from 1% to 40%. The chirp rate is equal to the slope of the line and is given by:

$$k = \frac{B}{\tau} \tag{1.2}$$

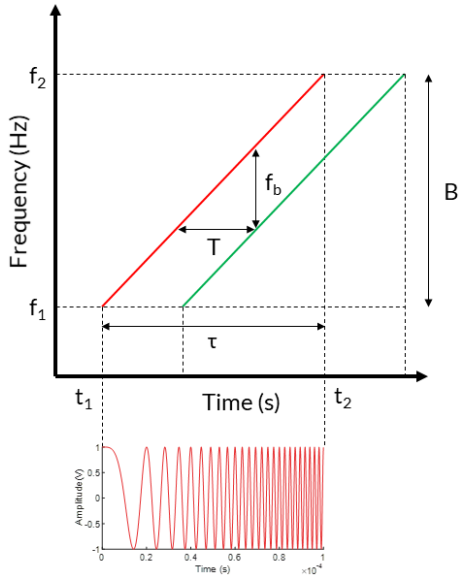

Figure 2-2: Cartesian representation of transmit (red) and receive (green) FMCW signals

The chirp rate of the received signal is equal to the transmit signal and is received after a period, T. For a Pulsed FM radar, B is larger than 1/τ. If the range to the target is R and the speed

of light is c, then the round-trip travel time, T and the corresponding beat frequency, fb are given by:

$$T = \frac{2R}{c} \tag{1.3}$$

$$f_b = kT = \frac{2BR}{c\tau} \tag{1.4}$$

The received signal is passed through a matched filter to maximize the Signal-to-Noise Ratio (SNR) and this results in a compression of the pulse length from τ to τp. This process is often termed as pulse compression and it is quantified by the compression ratio. The frequency resolution of the beat signal is the inverse of the repetition period and therefore the range resolution, ΔR is solely dependent on the bandwidth of the signal. Equation (1.5) shows the relationship below. As the signal bandwidth is increased, the range resolution of the radar gets finer. This is particularly important for extended or distributed targets as the information can be gathered with greater detail. A pulse with a bandwidth of 15 GHz results in one centimeter resolution.

$$\Delta R = \frac{c}{2B} \tag{1.5}$$

The range resolution corresponds to the half-power width of the output of the matched filter. It is defined as the minimum distance between two point targets that can be successfully detected by the radar as distinct targets. The resolution can be degraded by several factors such as windowing of the waveform, longer range delay relative to pulse duration, chirp nonlinearities, etc.

The linear frequency modulated waveform is dependent on the starting frequency f1, chirp rate k, and starting phase φ1. The mathematical expression for the waveform is shown below and an example of the waveform is shown in Figure 2-2.

$$s(t) = A\cos\left(2\pi\left(f_c t + \frac{kt^2}{2}\right) + \varphi_1\right) \quad (1.6)$$
$$for\ 0 \le t \le \tau$$

2.2 **Overview of a polarimetric scatterometer**

Consider a transmitted plane wave with electric field $\boldsymbol{E}^t = \widehat{\boldsymbol{v}_t}E_v^t + \widehat{\boldsymbol{h}_t}E_h^t$ incident on a scattering target. The electric (bulk-dielectric) and geometric (roughness) properties of the target scatter the electric field $\boldsymbol{E}^t$ in both directions $\widehat{\boldsymbol{v}_t}$ and $\widehat{\boldsymbol{h}_t}$. Let the received electric field of the backscattered plane wave be $\boldsymbol{E}^r = \widehat{\boldsymbol{v}_r}E_v^r + \widehat{\boldsymbol{h}_r}E_h^r$. According to the Backscatter Alignment (BSA) Convention, the fields $\boldsymbol{E}^t$ and $\boldsymbol{E}^r$ are related by:

$$\boldsymbol{E^r} = \left(\frac{e^{-jkR_r}}{R_r}\right)\boldsymbol{S}\boldsymbol{E^t} \quad (1.7)$$

$$\text{where, } \boldsymbol{S} = \begin{pmatrix} S_{vv} & S_{vh} \\ S_{hv} & S_{hh} \end{pmatrix}$$

$\boldsymbol{S}$ is the scattering matrix of the target in accordance with the BSA convention and S_{pq} is the scattering amplitude where p, q = v or h. $\left(e^{-jkR_r}/R_r\right)$ is the spherical propagation factor where k is the wave number and R_r is the range to the target.

S_{vv} corresponds to the scattering amplitude of the target when vertically polarized transmit and receive antennas are used. There are a total of four possible combinations for both polarizations and $\boldsymbol{S}$ accounts for the four scattering amplitudes. Each element in the matrix is a complex number and hence has amplitude and phase information. A radar polarimeter typically transmits in one polarization and receives the echoes on both orthogonal polarizations simultaneously. The process is repeated for the other transmit polarization and then alternated to continuously update the scattering matrix.

Each component of $\boldsymbol{S}$ is a function of the incident and scattering angles and for any polarization combination pq,

$$S_{pq} = S_{pq}(\theta_i, \varphi_i; \theta_s, \varphi_s; \theta_j, \varphi_j) \qquad p, q = v \; or \; h \tag{1.8}$$

where, (θ_i, φ_i) are the incident angles, (θ_s, φ_s) are the scattering angles, and (θ_j, φ_j) are the orientation angles of the target. Therefore, for each observation or look angle, four separate data points are obtained. By measuring all four polarization combinations for various look angles, a large sample space of measurements can be collected. However, polarimetry requires additional corrections through calibration for amplitudes and relative phases between the channels. This is a necessary but time-consuming process.

For a distributed target that consists of a large number of resolution cells N_c, the reflectivity $\sigma_{pq}^0$is given by,

$$\sigma_{pq}^0 = \frac{4\pi}{AN_c} \sum_{i=1}^{N_c} \left|S_{pq}^i\right|^2 \tag{1.9}$$

$$= \frac{4\pi}{A} \langle \left|S_{pq}^i\right|^2 \rangle \qquad p, q = v \; or \; h \tag{1.10}$$

where, A is the area of the resolution cell and S_{pq}^i is the polarimetric scattering amplitude for each cell. Each polarization mode carries different information regarding the target and the combination of all four images provides insight on various constituents of the target. Both the amplitudes and the relative phases between each mode carry information about the target. Scatterometers measure the radar cross section of a distributed target by capturing surface or volume backscatter.

The scattering matrix $\boldsymbol{S}$ wholly characterizes the scattering properties of the target. Consequently, the axial ratio in both orthogonal directions may be computed using the four

scattering amplitudes. Therefore, any combination of linear, elliptical, or circular polarization response of the target can be generated from $\boldsymbol{S}$.

2.3 **Overview of microstrip antennas**

Antennas radiate EM waves when the physical length is a specific multiple of the operating wavelength and the input impedance is matched to a transmission line over the specified bandwidth. Microstrip antennas are composed of the primary radiator, feed line, ground plane, and a dielectric substrate. The dielectric constant for the substrates are typically in the range of $2.2 \leq \epsilon_r \leq 12$ and thick substrates with low dielectric constant are favorable for antennas.

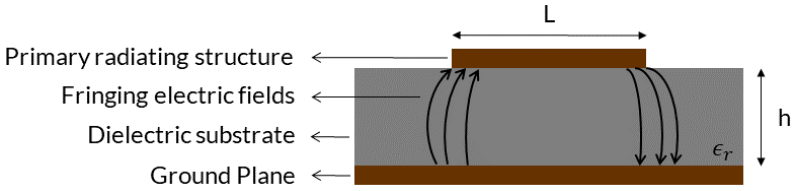

Figure 2-3: Picture of a model showing the mechanism for radiation in a microstrip antenna

The electric fields in a microstrip antenna exist between the primary radiating structure and the ground plane as shown in Figure 2-3. The finite length *L* of the radiating structure causes the electric fields to fringe at the edges. These fringing fields are primarily responsible for antenna radiation. The amount of fringing is a function of the dimensions of the patch and the height of the substrate *h*. Because of the fringing effects, the microstrip antenna looks electrically larger than the physical dimensions. For the dominant TM_{010} mode, the resonant frequency is a function of length is given by,

$$(f_r)_{010} = \frac{c}{2L\sqrt{\epsilon_r}} \tag{1.11}$$

where, *c* is the speed of light in free space. To include the fringing edge effects, the q-factor or fringe factor must be incorporated in the above equation. If the edge effects change the electrical

length by ΔL and the effective permittivity is ϵ_{eff}, then the resonant frequency with fringing effects is given by,

$$(f_{rc})_{010} = \frac{c}{2(L + \Delta L)\sqrt{\epsilon_{eff}}} \tag{1.12}$$

$$q = \frac{(f_{rc})_{010}}{(f_r)_{010}} \tag{1.13}$$

These results are based on a transmission line model for a rectangular patch. If instead the antenna is designed with a circular patch, the resonant frequency is dependent on the radius of the patch a and relative permittivity of the substrate. The following equations use a cavity model and show the relationship for the resonant frequency with and without fringing respectively for the dominant TM_{110} mode,

$$(f_r)_{110} = \frac{(1.8412)c}{2\pi a\sqrt{\epsilon_r}} \tag{1.14}$$

$$(f_{rc})_{110} = \frac{(1.8412)c}{2\pi a_e\sqrt{\epsilon_{eff}}} \tag{1.15}$$

where, a_e is the effective radius and ϵ_{eff} is the effective relative permittivity of the substrate with fringing effects. The value 1.8412 in the numerator arises when solving for the fields within the cavity using the vector potential approach. The constraint equation for the magnetic vector potential A_z is solved using the Bessel function of the first kind for an order m. χ_{mn} represents the zeroes of the derivative of the Bessel function $J_m(x)$ and the first value $\chi_{11} = 1.8412$.

The input impedance of the antenna is the ratio of the voltage to current or the ratio of the appropriate components of the electric to magnetic fields at the input terminal. It is defined as,

$$Z_{in}^A = R_{in}^A + jX_{in}^A \tag{1.16}$$

where, Z_{in}^{A} is the input antenna impedance, R_{in}^{A} is the input antenna resistance, and X_{in}^{A} is the input antenna reactance. The resistive part is the sum of the radiation resistance and the loss resistance of the antenna. The input impedance of the antenna is a crucial parameter as it indicates how much power is delivered to the antenna from the source. For maximum power transfer, the input impedance of an antenna must be a complex conjugate of the source impedance.

If the impedance between two homogenous dielectric media is different, then the EM wave undergoes reflection at the discontinuity. At the input terminal of the antenna, the discontinuity causes the incoming EM wave to reflect back towards the source and the forward propagating wave is radiated. The reflection coefficient is defined as,

$$|\Gamma_{in}| = \frac{Z_{in}^{A} - Z_o}{Z_{in}^{A} + Z_o} \tag{1.17}$$

Typically, the reflection coefficient is analyzed in terms of Return Loss (RL), which is the ratio of the power of the reflected wave to the incident wave at the discontinuity interface. The expression is,

$$RL\ (dB) = -20\log_{10}\left(\frac{P^{-}}{P^{+}}\right) = -20\log_{10}(|\Gamma_{in}|) \tag{1.18}$$

The magnitude of RL is always positive since it is defined relative to the incident wave power, however it is conventionally expressed with a negative sign. This is done to signify the undesirable power that returns to the source and it is termed as loss since it is power that is not delivered to the antenna.

The fields within the circular cavity are calculated using the vector potential approach. From the homogenous wave equation in cylindrical coordinates, it can be shown that for TM^{z} modes, the electric and magnetic fields are related to the vector potential A_z. The fields radiated

by the circular patch can be found using Field Equivalence Principle (Huygens's Principle). The fields in the principal planes are,

E-plane: φ = 0°, 180°; 0°≤ θ ≤90°

$$E_\theta = j\frac{k_0 a_e V_0 e^{-jk_0 r}}{2r}[J'_{02}] \tag{1.19}$$

$$J'_{02} = J_0(k_0 a_e \sin\theta) - J_2(k_0 a_e \sin\theta)$$

$$E_\varphi = 0 \tag{1.20}$$

H-plane: φ = 90°, 270°; 0°≤ θ ≤90°

$$E_\theta = 0 \tag{1.21}$$

$$E_\varphi = j\frac{k_0 a_e V_0 e^{-jk_0 r}}{2r}[\cos\theta\, J_{02}] \tag{1.22}$$

$$J_{02} = J_0(k_0 a_e \sin\theta) + J_2(k_0 a_e \sin\theta)$$

where, k_0 is the wavenumber, a_e is the effective radius, and $V_0 = hE_0 J_1(ka_e)$ at a zero degree azimuthal angle along the perimeter of the patch. The radiated field equations are used to calculate the radiated power P_{rad} and using the conductance G_{rad}, the directivity at θ = 0° can be expressed as,

$$D_0 = \frac{(k_0 a_e)^2}{120 G_{rad}} \tag{1.23}$$

The gain of an antenna relates the directivity D_0 and radiation efficiency ε_R as,

$$G = D_0 \varepsilon_R = \frac{(k_0 a_e)^2}{120 G_{rad}} \tag{1.24}$$

The power accepted by the antenna at the feed point is practically not equal to the power radiated due to conductor and dielectric losses in the antenna material. The radiation efficiency is

a measure of both losses. The total efficiency ε_T combines radiation efficiency and impedance mismatch losses M_L:

$$\varepsilon_T = M_L \varepsilon_R = (1 - |\Gamma_{in}|^2)\varepsilon_R \tag{1.25}$$

The absolute gain or realized gain of an antenna is expressed as:

$$G_R = D_0 \varepsilon_T \tag{1.26}$$

Therefore, the gain of an antenna can be increased by improving the impedance match at the feed, using low-loss materials for higher efficiency, and increasing directivity. Multiple antennas can be grouped together to form an array and the equivalent directivity is larger than the single antenna. The number of elements and the distance between the elements of an array are the important characteristics.

Consider *N* identical antenna elements arranged in a linear array and the distance between each element is d. All elements have uniform, identical magnitude and the phase between each element progressively changes by β. The array factor is given by,

$$AF = \sum_{n=1}^{N} e^{j(n-1)\psi} \tag{1.27}$$

$$\text{where, } \psi = kd\cos\theta + \beta \tag{1.28}$$

The total field of the array can be computed by multiplying the array factor with the field of a single element. This is valid only if the antenna elements are identical.

When *N* radiators are physically placed close to each other at a distance *d*, there is some leakage from one element to the other within the array and this is known as mutual coupling. It is undesirable due to the increase in mismatch losses as the signal is radiated from one element and received on the other. Therefore, the distance between the elements is a compromise between the required radiation shape and the mutual coupling.

2.4 **Overview of the Vapor 55 UAS**

The Vapor 55 rotorcraft is an all-electric UAS by AeroVironment™ (formerly by Pulse Aerospace) and a picture is shown in Figure 2-4 [20]. It uses a high energy density lithium-polymer battery that integrates into a modular payload bay or tray. The vehicle dimensions are 2.56 m x 0.67 m x 0.58 m and the maximum operating altitude is 3,657 m. For a maximum payload weight of 4.5 kg it is capable of 60 minutes of flight time on a single battery charge. The rotorcraft has on-board Global Positioning System (GPS) and three optional data links to downlink the payload data during flight. It is capable of autonomous flight by planning waypoints and the range is 8 km. The UAS has a compact design and this enables it to easily take-off and land on various terrain. The wide stance landing gear ensures stable landings even on rough surfaces. The payload tray is customizable and can accommodate various instruments like hyperspectral sensors and LIDARS. A significant part of the body is made of carbon fiber composite material to withstand the vibrational stresses.

The features of the Vapor 55 rotorcraft are highly suitable for remote sensing applications. The rugged build quality of the UAS makes it suitable for harsh environments and remote locations. It has a ground speed limit of 10 m/s and can withstand gusts of up to 37 km/h. The stable and precision flight enable close-range, high resolution measurements. High-speed data links can downlink the recorded data for external storage without interrupting the science mission.

Figure 2-4: Picture of the Vapor 55 rotorcraft

3 Radar System

3.1 System Specifications

Soil moisture detection using radars has largely been performed at frequencies below the X-band [21] and typically measurements are performed at distinct frequency bands with fractional bandwidths of 30% or less [22 - 26]. For instance, in [22] the fractional bandwidth at the lowest operational frequency is 25%. This can be a limiting factor since different backscatter signatures are presented over a range of different sub-bands. New information about the same target can be interpreted over each sub-band. Hence, a large sample of measurements over unique sub-bands help in discerning the target characteristics accurately.

These crucial points served as the primary motivation for designing an ultra-wideband (UWB) radar system, specifically over the 2-18 GHz frequency range. The large fractional bandwidth of 160% offers a much finer spatial resolution and hence obtain moisture information in greater detail. Additionally, the chosen bandwidth enables the opportunity to explore soil moisture signatures at X- and Ku-bands. Such a system also has application in sounding snow cover, snow layers, and fresh water ice on lakes [27-30].

The system architecture is based on the Snow radar [30]. However, this system is primarily used on manned airborne platforms like the Lockheed P-3 Orion and the Douglas DC-8. In other words, the size of the system electronics is comparable to a single unit in a commercial avionics rack, which is too large to integrate on to a UAS rotorcraft. Hence, one of the primary challenges is incorporating a miniaturized version of the UWB system. Several iterations have been attempted to reduce the SWaP of the Snow Radar at CReSIS [31, 32] and similar systems at other organizations [33 - 36]. However, they are not small enough for a platform such as the Vapor 55.

The limiting factors for the radar design can be viewed through three important parameters: size, weight, and power. The rotorcraft has a cavity below the main body, called the payload tray, which houses the batteries required for flight. The batteries occupy nearly three-quarters of the tray space and the remaining area is the only available space for the radar system. Shrinking the total volume of the Snow radar system into this small space is the most challenging aspect of miniaturization. Further, the UAS is capable of carrying a maximum payload of 5 kg (11 lbs.), which must include the electronics, cables, and the entire RF front-end. Finally, the UAS' batteries will provide the electrical power for the radar. This means that a dedicated power module must be designed to convert the unregulated DC voltage into a regulated supply.

In summary, the system specifications and requirements are as follows:

1. Design a radar system that operates in scatterometer mode for measuring surface soil moisture and alternatively snow thickness
2. Design an UWB system that operates in the 2 to 18 GHz frequency range for wide spectral coverage
3. Miniaturize the Snow radar by focusing on the size, weight, and power requirements of the helicopter
4. Capable of operating at a maximum altitude of 93.75 m (307.58 feet)

3.2 **Link Budget**

One of the fundamental features of a radar transmitter is the power-aperture product. It characterizes the range by considering the average radiated power and the antenna aperture area. This typically sets the upper limit of one operating mode while the lower limit of the receiver is characterized by the sensitivity. This is set by the Minimum Detectable Signal (MDS).

The radar range equation for extended targets is given by:

$$P_r = \frac{P_t G_t G_r \lambda^2 \sigma^o A}{(4\pi^3) R^4} \tag{2.1}$$

where, P_r is the received signal power, P_t is the transmitted signal power, G_t is the gain of the transmitting antenna, G_r is the gain of the receiving antenna, λ is the operating wavelength, σ^o is the backscattering coefficient of the target, A is the surface area of the target illuminated by the antenna, and R is the range of the radar from the target

It must be noted that the above equation does not account for the losses within the system itself since this link budget analysis is only intended to serve as a basic frame of reference. A nominal transmitting power of 0 dBm (1 mW) will be used for computations. This is the intended transmit power for backscatter measurements, however the maximum transmit power is 20 dBm (100 mW). For the sake of simplicity, the gain of a standard wideband horn antenna is used for both the transmitter and receiver [37]. The surface area illuminated by the antenna beam is computed through simple geometry, using the antenna beamwidth and altitude. Finally, the received signal power is computed for two extreme cases, a range of 50 and 307.58 feet. The minimum altitude is limited by the maximum signal power that can be received, which is dictated by the saturation level of the ADC. The maximum altitude is restricted to 400 feet by the Federal Aviation Administration (FAA) under rule 14 CFR Part 107.

The backscattering coefficient describes the surface features of the target. In the case of soil, this factor contains information regarding the surface roughness and moisture content but is dependent on the angle of incidence, surface slope, and polarization of the wave. Additionally, it is also dependent on the type of soil and if any vegetation is present. The inter-dependency between these various factors make it very difficult to absolutely determine the moisture content of the soil.

For the case of the link budget analysis, the scattering coefficient data from [38] will be used to compute the approximate received signal power.

Ulaby et al. report the scattering coefficients for HH polarization, five types of surface roughness, two moisture states, three distinct frequencies, viz., 1.1, 4.25, and 7.25 GHz and across seven angles of incidence. To simplify the data for the purpose of this analysis, only the lowest and highest surface roughness, that is 1.1 cm and 4.1 cm, will be considered with the two moisture states. This results in four distinct soil types. The angle of incidence will also be restricted to only the nadir measurement. Figure 3-1 and Figure 3-2 show the possible received powers for these four soil types at 50 and 307.58 feet respectively.

As the authors state, the backscattering coefficient has a higher dependence on the surface roughness than moisture content, which is also evident from the plots. The difference in received power between smooth and rough surfaces for each moisture state and vice-versa, at an altitude of 50 feet, is tabulated in Table 3-1. It must be noted that the received power difference between the states is the same for both altitudes. Clearly, there is a larger difference for the same moisture content, that is, when the roughness changes from smooth to rough. However, there is also a significant variation among all combinations of differences and this sheds more light on the inter-dependency of multiple factors on the backscattering coefficient. Hence, it is paramount to obtain a large sample space of data for different angles of incidence and polarization, so that an empirical approach can be taken in interpreting the soil moisture content.

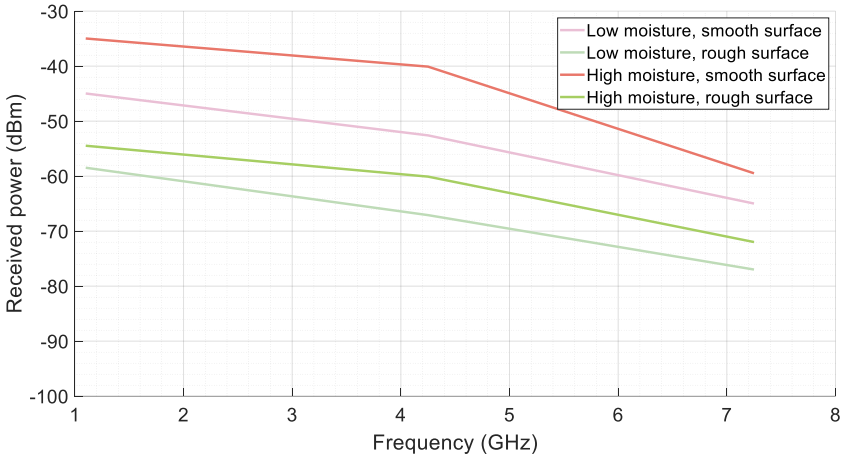

Figure 3-1: Radar link budget at an altitude of 50 feet for four types of soil and antenna pointed at nadir

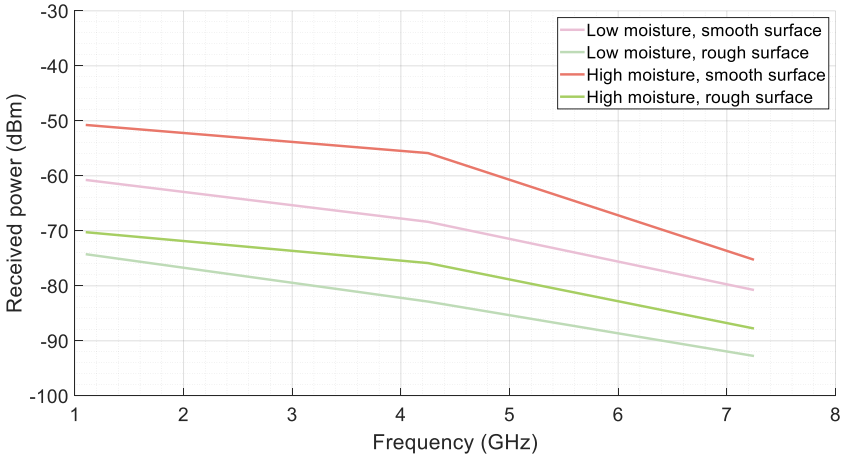

Figure 3-2: Radar link budget at an altitude of 307.58 feet for four types of soil and antenna pointed at nadir

Table 3-1: Differences in received powers between each soil state at distinct frequencies for an altitude of 50 feet

Soil State	**Difference in received power**		
	1.1 GHz	**4.25 GHz**	**7.25 GHz**
Low moisture	13.5 dB	14.5 dB	12 dB
High moisture	19.5 dB	20 dB	12.5 dB
Smooth surface	10 dB	12.5 dB	5.5 dB
Rough surface	4 dB	7 dB	5 dB

The link budget, in terms of the dynamic range of the radar receiver, is characterized only by the highest and lowest expected received signal power. From Figure 3-1 and Figure 3-2, the soil with high moisture content and smooth surface, at 1.1 GHz, results in -34.97 dBm of power at 50 feet and -50.75 dBm at 307.58 feet. On the other hand, low moisture content and rough surface at 7.25 GHz, results in -76.98 dBm at 50 feet and -92.76 dBm at 307.58 feet. For this specific case, the receiver must be able to boost the signal at -92.76 dBm above the noise floor but not allow the -34.97 dBm to saturate the ADC. For instance, if an ADC has a dynamic range from -65 dBm to +10 dBm, a total receiver gain of 37.76 dB would ensure that all signals are successfully sampled at the ADC for all four soil conditions.

The dataset reported in [38] is expansive with several parameters varied independently. This helps in ascertaining the exact requirements for the radar's RF section. However, the only limitation with this dataset is that the maximum operating frequency is 7.25 GHz, while the radar is intended to function over 2 to 18 GHz. In the paper, the backscattering coefficient is shown for moisture levels ranging from 0.03 g/cm^3 (dry) to 0.4 g/cm^3 and rms height of 1.1 cm (smooth) to 4.1 cm (rough). Over incidence angles from 0 to 30 degrees and frequencies 1.1 to 7.25 GHz, the scattering coefficient varies from -30 dB to +22 dB.

Figure 3-3 shows the link budget for 50 and 307.58 feet across the entire 2 to 18 GHz bandwidth, computed without the backscattering coefficient. The lowest received power is at 18 GHz and 307.58 feet altitude and the value is expected to be around -93.73 dBm. If the radar has a MDS of -103 dBm, then the worst backscattering coefficient that can be received is -9.27 dB. From [38], this restricts measurements to less than 10° look angle for frequencies less than 4.25 GHz at the lowest moisture (0.03 to 0.09 g/cm^3) and highest moisture (0.34 to 0.4 g/cm^3). As the frequency increases to 7.25 GHz, the possible incidence angles increases to 25°. Therefore, for

moisture levels between 0.09 and 0.34 g/cm^3, the radar return can be successfully received for angles of incidence up to 30 degrees.

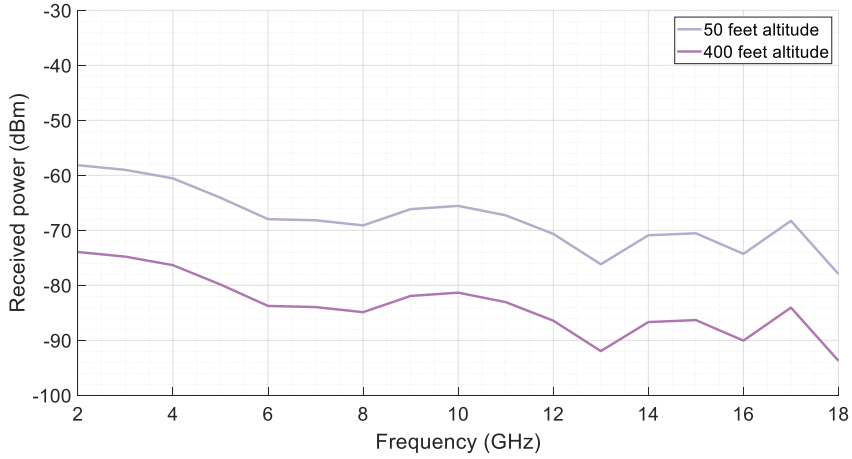

Figure 3-3: Expected received power at an altitude of 50 and 307.58 feet without the backscattering coefficient

In [39], measurements are preformed using waveguide transmission system from 1.4 to 6 GHz and using free-space transmission system from 4 – 18 GHz. Other variables include type of soil, moisture content, sample thickness, and temperature. The results show the variation of real and imaginary part of the dielectric constant of soil across 1.4 to 18 GHz. For low moisture content of less than 0.079 cm^3 cm^{-3}, the dielectric constant is nearly constant for the entire frequency band. For high moisture content of 0.374 cm^3 cm^{-3}, the real part varies by a factor of approximately 10 and the imaginary part by nearly 5. The measured total dielectric constant for two fields of volumetric wetness of 0.079 cm^3 cm^{-3} and 0.36 cm^3 cm^{-3}, changes by factors of 4 and 6 respectively. The maximum change in dielectric constant causes a 12.53% change in reflection coefficient within the band. Therefore, this is proportional to the maximum change in relative received power within the band. Since the backscattering coefficient for specific cases do not change drastically, the typical values used in both papers can be used as reference for 2 – 18 GHz.

Amplifying low received powers can be challenging as in some cases, the total receiver gain may need to boost the signal by 50 or 60 dB. An easy way to deal with this is by distributing

the gain stages over multiple sections and particularly after frequency translation. The lower Intermediate Frequency (IF) band, relative to the carrier band, makes it easier to design high-gain stages. However, it is crucial to find the right balance of amplifiers in the receiver chain to ensure stability.

3.3 **System design**

The high-level block diagram of the radar system is shown in Figure 3-4 and a list of the system parameters is shown in Table 3-2. Since this system is based on the Snow Radar and is miniaturized for a UAS helicopter, this radar system is referred to as the Helo-Snow Radar. It can be divided into four primary sections:

1. Digital section
2. Radio Frequency (RF) section
3. Mixed signal section
4. Power section

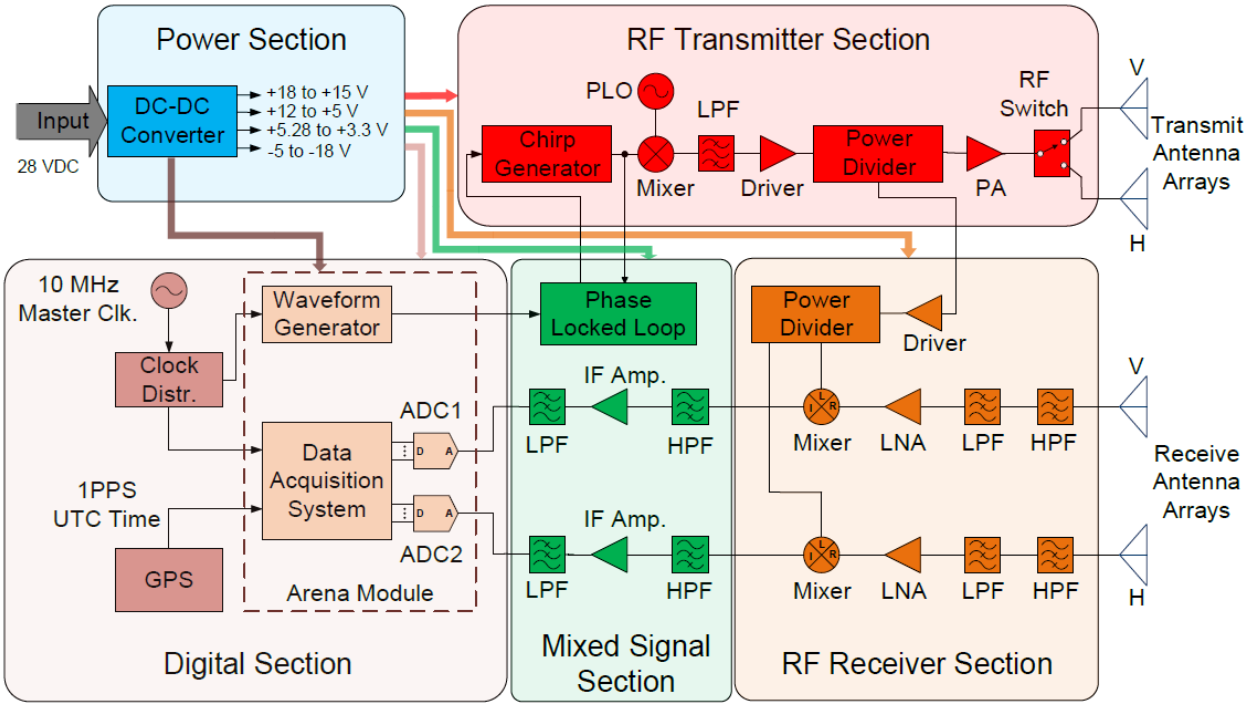

Figure 3-4: High-level block diagram of the radar system

The digital section consists of the Arena module, on-board computer, clock distribution system, and Global Positioning System (GPS) receiver. The Arbitrary Waveform Generator (AWG) in the Arena module generates a nearly ideal reference chirp waveform for the Phase Locked Loop (PLL). The clock distribution system provides a stable and phase coherent clock signal to synchronize the waveform generator and the Data Acquisition System (DAQ). The GPS receiver provides time stamps and geotags for the acquired data. The on-board computer runs the Arena module's software and directs the incoming data onto a storage disk.

The RF section is the central part of the radar and it consists of the chirp generator, transmitter chain, and receiver chain. The chirp generation stage produces the 2-18 GHz chirp, synchronously with the PLL. The transmitter chain conditions the signal using several combinations of gain equalizers and amplifiers. The receiver section amplifies and mixes down the frequency of the received signal. This entire section is designed on a single PCB and will be referred to as the RF Board (RFB)

Table 3-2: Miniaturized Radar Specifications

Radar System Parameters	**Value**
Frequency Range	2 – 18 GHz
Bandwidth	16 GHz
Delay-line Range Resolution (with windowing)	1.45 cm
Peak Transmit Power	1 mW (100 mW max.)
Chirp Duration	200 µs
Pulse Repetition Frequency	2 kHz
Analog-to-Digital Converter Sampling Rate	100 MSPS
Analog-to-Digital Converter Resolution	16 bits
Number of Channels	2 Tx. And 2 Rx.
Flight Altitude	50 – 307.58 feet

The mixed signal section is comprised of the PLL, Intermediate Frequency (IF) section of the receiver, and various biasing circuitry that control components in the RF section. The PLL ensures linearity and stability of the generated RF chirp waveform by comparing it with the ideal digital chirp waveform and correcting for errors. The IF section of the receiver, filters and amplifies the mixed-down received signal. The Analog-to-Digital Converter (ADC) then digitizes the IF signal and stores on the external hard disk. The biasing circuitry provides the correct sequence of DC voltages to switch-on the components in the RF section. This entire section is designed on a single Printed Circuit Board (PCB) and will be referred to as the Low-speed Board (LSB) or Mixed-signal Board (MSB).

The power section provides stable and regulated DC voltages to all components in the radar system. The battery pack of the UAS is the main source of power, which is then converted and regulated into different voltages required for the system.

The system's electronics (all four sections) will be enclosed in an Aluminum chassis with overall dimensions of 23.88 cm x 19.56 cm x 8.64 cm (9.4" x 7.7" x 3.4") installed just aft of the battery carriage. The chassis is vertically divided into two floors. The bottom floor comprises of the power section, Arena module, GPS receiver, and clock distribution system. The top floor contains the mixed signal and RF sections and the disk storage. The on-board computer is integrated external to the enclosure on the topside of the chassis.

3.3.1 Digital Section

The digital section of the radar consists of the following sub-systems: Arena module, Mintbox computer, Clock board, and GPS board. The digital backend is a combination of various levels of execution. The Arena module is wholly designed and manufactured by a company with extensive research and development while the Mintbox is a Commercial off-the-shelf (COTS) component. The Clock Board is a custom in-house design but professionally fabricated and carefully assembled in-house. The GPS board is wholly designed, fabricated, and assembled in-house. Therefore, it is important to ensure signal integrity across these various types of components for accurate operation.

3.3.1.1 Arena Module

The Arena module, designed and manufactured by Remote Sensing Solutions (RSS), is a reconfigurable and modular solution for the digital backend of radars, sonars, and radiometers [40]. It features an arbitrary waveform generator, multi-channel digital receiver, timing and control signal generation and reception, data acquisition and distribution, and supports various signal processing techniques. Most of these hardware components are modular by design, in the form of mezzanine cards. The architecture of the entire module allows synchronous control of the hardware, firmware, and software layers through eXtensible Markup Language (XML) objects.

The small form factor of the module facilitates the miniaturization of the radar system and the plug-and-play solution simplifies integration and operation.

The Series 300 Arena module is used as the digital back-end for the radar. A dual-core Arm Cortex-A9 processor with a 1 GHz CPU clock rate is present at the heart of the module. It provides sustained data rates of more than 20 GB/s. The module requires a 10 MHz reference clock to synchronize the timing. It operates over a wide input voltage range of 7 – 32 VDC and consumes a maximum power of 30 W. In this radar design, the module will operate at 28 VDC. This voltage is provided by the SynQor DC-DC converter after regulating the voltage provided by the UAS battery. The clock signal power limits at all input ports range from -3 dBm to +3 dBm.

The Arbitrary Waveform Generator (AWG) is based on the AD9129 RF Digital-to-Analog Converter (DAC) by Analog Devices. It has a single channel with 14-bit resolution and an output signal frequency range of 1 – 3600 MHz. The clock range is 1400 – 2400 MHz but supports integer multiples of 10 MHz. The clock frequency for this radar system is 2000 MHz. Three Nyquist zones are available while the typical Noise Spectral Density (NSD) is -157 dBm/Hz.

The Complex Digital Receiver is based on the ADS42LB69 Analog-to-Digital Converter (ADC) by Texas Instruments. It has dual channels with 16-bit resolution (ENOB at 170 MHz and 2.5 V_{p-p} full-scale = 12.03 ENOB) and an input signal frequency range of 1 – 250 MHz. The sampling rate ranges from 10 – 250 MSPS and for this radar system the receiver is sampled at 100 MSPS. Two Nyquist zones are available at the maximum sampling rate and the NSD in the first zone is typically -156.5 dBm/Hz.

The module has an SD card that contains preloaded images for an Embedded Linux Kernel and other firmware settings. A computer with a Linux Operating System (OS) is used to access

the module's settings through a Graphical User Interface (GUI) provided by RSS. Figure 3-5 shows a screenshot of the GUI window along with one of the settings window.

The manufacturer delivers the Series 300 Arena module in a 7.62 cm x 19.3 cm x 2.27 cm (3 in x 7.6 in x 0.895 in) Aluminum enclosure weighing 396.89 g. For this radar system, the entire module is integrated directly into the chassis after separating from the manufacturer's enclosure. This is done to ensure easier interconnections with the other parts of the system and to reduce the overall weight of the chassis. Figure 3-6 shows the Arena module in the radar chassis.

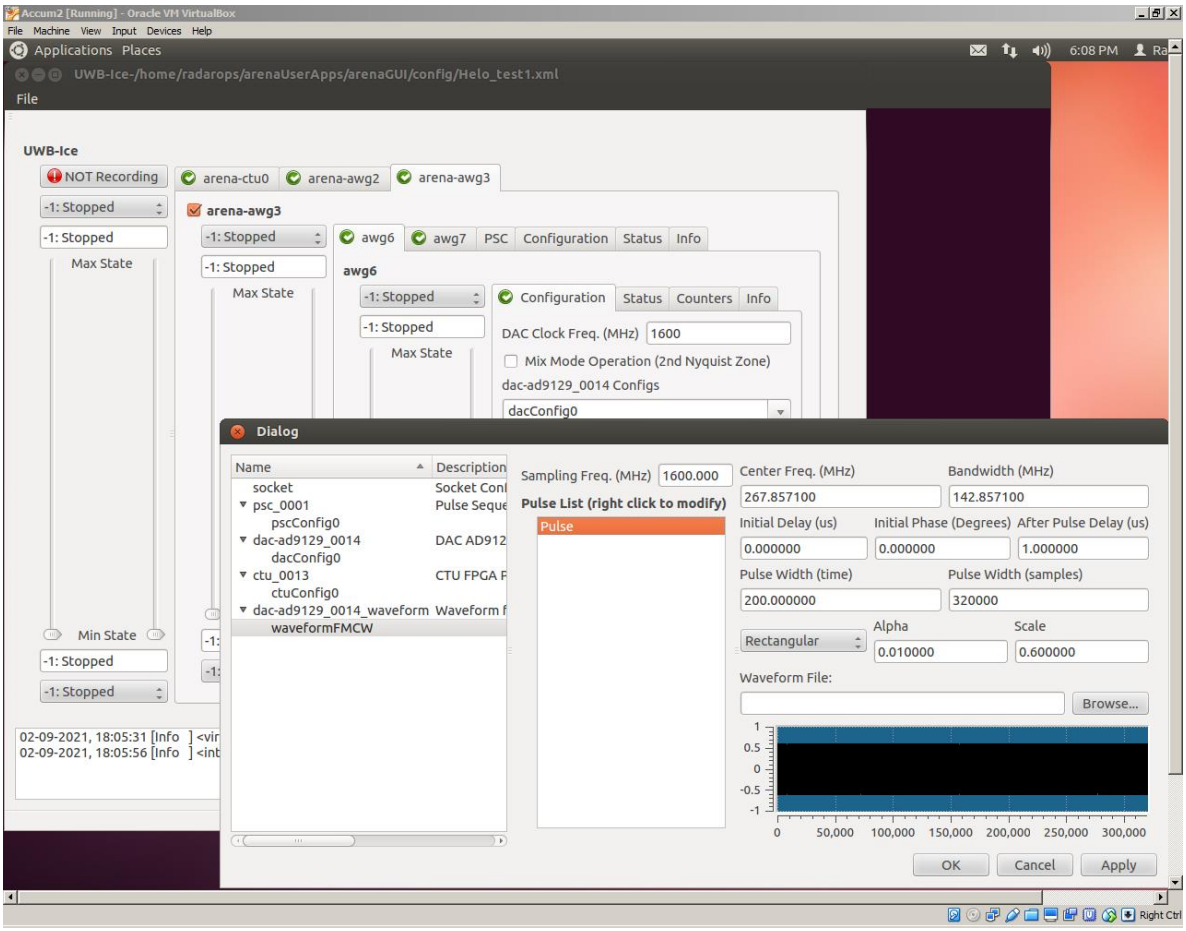

Figure 3-5: Screenshot of the Arena GUI and settings window

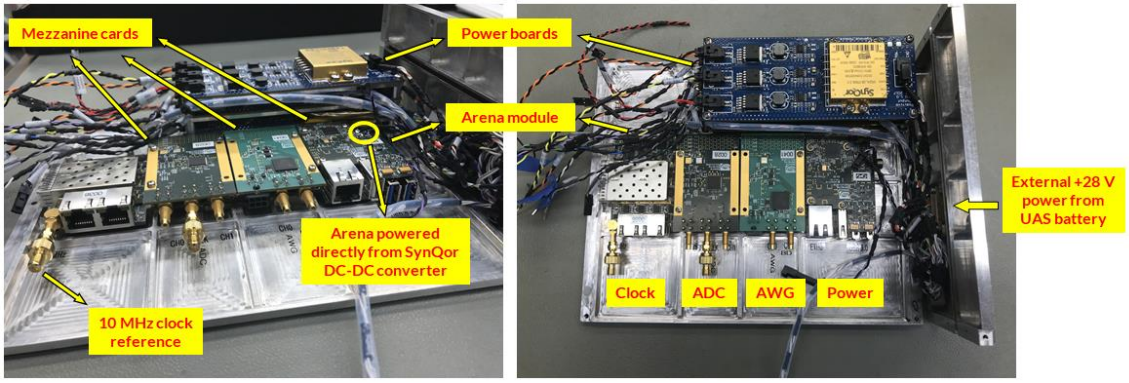

Figure 3-6: Photo of the Arena module integrated into the radar chassis

3.3.1.2 Mintbox Computer

The Mintbox Mini is a miniature computer that is manufactured by Compulab. The central processor is the AMD A4 Micro-6400T System-on-Chip (SoC). It is a 64-bit quad core processor with a clock speed of 1 GHz and can be boosted up to 1.6 GHz. It is pre-built with a 4 GB RAM and a 64 GB SSD. It even supports dual display with an AMD Radeon R3 Graphics GPU and two separate HDMI ports. It has two 3.5 mm audio jacks, a LAN port, WLAN module, two USB 3.0 and three USB 2.0, a serial communication port, and micro-SD slot. The official OS is Linux Mint 18 Cinnamon but also supports Windows 7/8/10. In this radar system, the Mintbox is powered at +12 V and is expected to draw around 800 mA. It has a Thermal Design Power (TDP) of 4.5 W and is cooled using a passive, fanless design. The entire mini-computer measures 10.8 cm by 8.3 cm by 2.4 cm and weighs 250 g.

The compact and lightweight design makes it suitable for operating on a UAS, especially with a low payload limit of 10 lbs. The extensive computing features are sufficient for running the Arena software interface. The Arena itself may be easily configured through its graphical interface by connecting a full set of display monitor, keyboard, and mouse to the mini-computer. The Trimble Studio Software is also installed to configre the GPS module and communicates with it through the serial communication port. The received data is indexed with GPS coordinates and

saved on the on-board SSD. In this manner, the Mintbox ensures that the radar system is running and saving data throughout the mission. Figure 3-7 shows a picture of the Mintbox mounted on top of the radar Aluminum box using Velcro tape. It will also be secured using zip ties running through grommet-lined holes on the box lid.

Figure 3-7: Picture of the Mintbox Mini mounted on the radar box lid

3.3.1.3 Clock Board

In an UWB radar system, coherence is necessary to accurately demodulate the received signal and determine characteristics of the target. This means that the transmit and receive signals must be synchronized and the pulse-to-pulse timing must be accurate. Coherence is observed when the phase relationships between the various signals within the system are preserved. This is achieved with a single primary oscillator or clock source and all other reference and timing signals derived from that single source.

Figure 3-8 shows the clock and signal scheme for the entire radar system. The primary clock source is a 10 MHz oscillator. This is used as input reference for the clock board to generate 2000 MHz clock reference for the AWG. It is also used to generate 100 MHz using the clock synthesizer to set the sampling rate of the ADC. The entire Arena module itself runs on an input clock frequency of 10 MHz. The 100 MHz signal from the clock synthesizer is also used as

reference for the PLO to generate a 20 GHz signal. This is used in the final RF mixing stage to obtain the 2 – 18 GHz chirp signal. While the primary clock source ensures coherence, the PLL is responsible for the stability of the chirp signal.

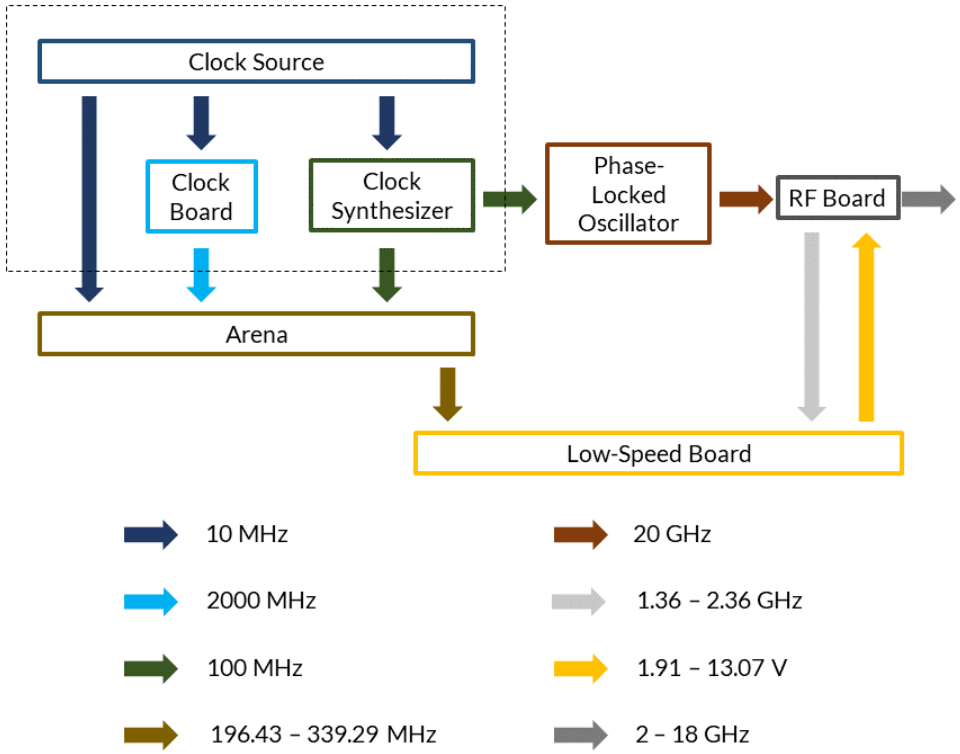

Figure 3-8: Clock and signals frequency scheme for the radar system

The complete clock scheme includes 10 MHz clock source, 100 MHz clock synthesizer, and 2000 MHz clock board. An exclusive design for the former two that integrates into this chassis is yet to be designed. When fabricated in future, the two subsystems will be incorporated on a single PCB that has the same dimensions as that of the clock board. It will be mounted as the third level above the clock and GPS boards. For the final system-level tests described in this work, an oven controlled 10 MHz crystal oscillator by Abracon Corporation and a USB programmable frequency synthesizer by independent RF consultant, Robert Yarbrough, is used. These two external devices are shown in Figure 3-48 as part of the test setup.

The clock board is designed in-house at the Center for Remote Sensing of Ice Sheets (CReSIS) and has been used in other radar systems [41]. It is based on the HMC833 programmable fractional-N PLL with integrated VCO by Analog Devices. Figure 3-9 shows the block diagram for the clock board. The 10 MHz reference from the clock source is AC coupled to the clock buffer. In a clock distribution network or clock tree, a buffer is used to condition the signal. A tighter control of the rise and fall times is established and it reduces signal jitter. The balanced signal is converted into single-ended using a 1:1 transformer and provides reference for the Phase-Locked Loop (PLL). It is programmed using a XC95144XL Complex Programmable Logic Device (CPLD) by Xilinx Inc. The register banks are appropriately set to produce a 2000 MHz signal. It is low-pass filtered to attenuate the harmonics and then amplified to increase the signal amplitude. The output power of the signal from the board is controlled using an RF digital attenuator and its control logic is set using the CPLD. Figure 3-10 shows pictures of the clock board with RF coaxial cables directly soldered to the input and output connector footprints.

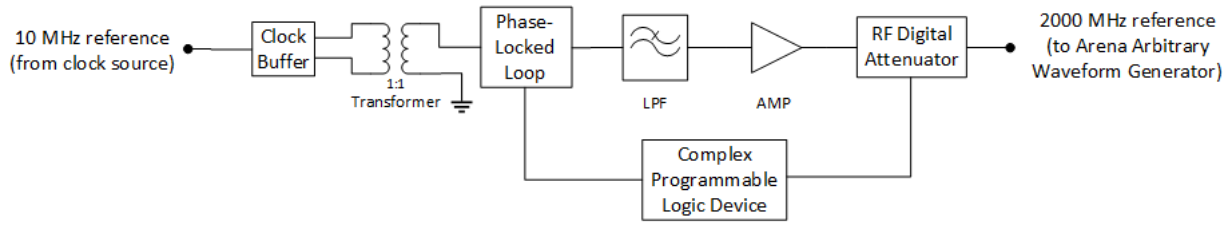

Figure 3-9: Block diagram of the clock board

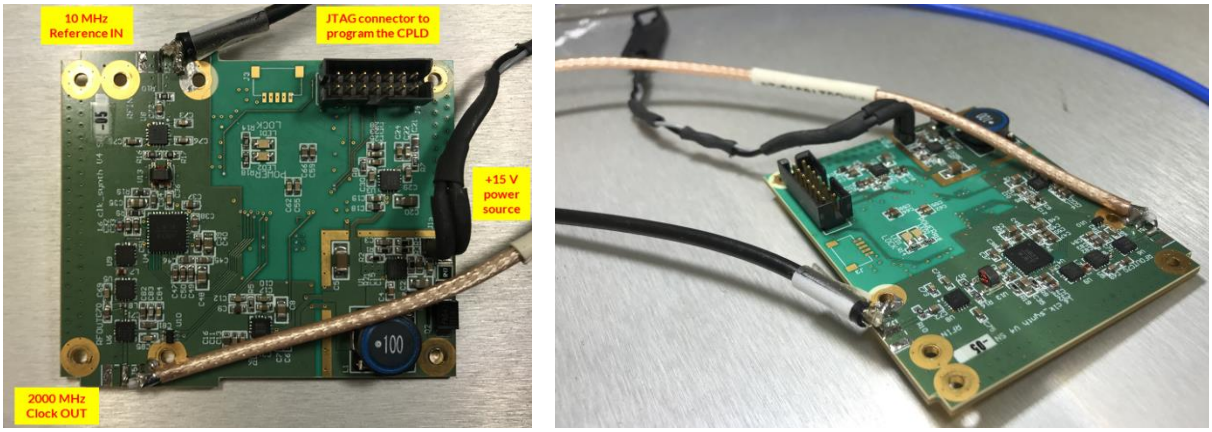

Figure 3-10: Pictures of the programmable clock board

3.3.1.4 GPS Board

The Copernicus II module by SparkFun is used as the GPS receiver. The data is indexed with time stamps and also with respect to global position. Organizing data in this manner provides a method for unique identification and makes it easier for signal processing.

The GPS receiver is a Dual In-Line Package (DIP) mounted on a compact module board. The entire module may be easily incorporated on a printed circuit board, breadboard, or used a standalone component. A PCB mount is favorable to assemble with the other radar components since it is easier to stack vertically. Figure 3-11 shows a picture of the PCB with the Copernicus II module. The module's vertical pins from the DIP are inserted into two rows of vias on the PCB and is soldered in place. The MAX3232 transceiver chip facilitates serial communication between the GPS module and the on-board computer. The module operates with a +3.3 V supply while the transceiver with a +5 V supply, both routed from the power boards.

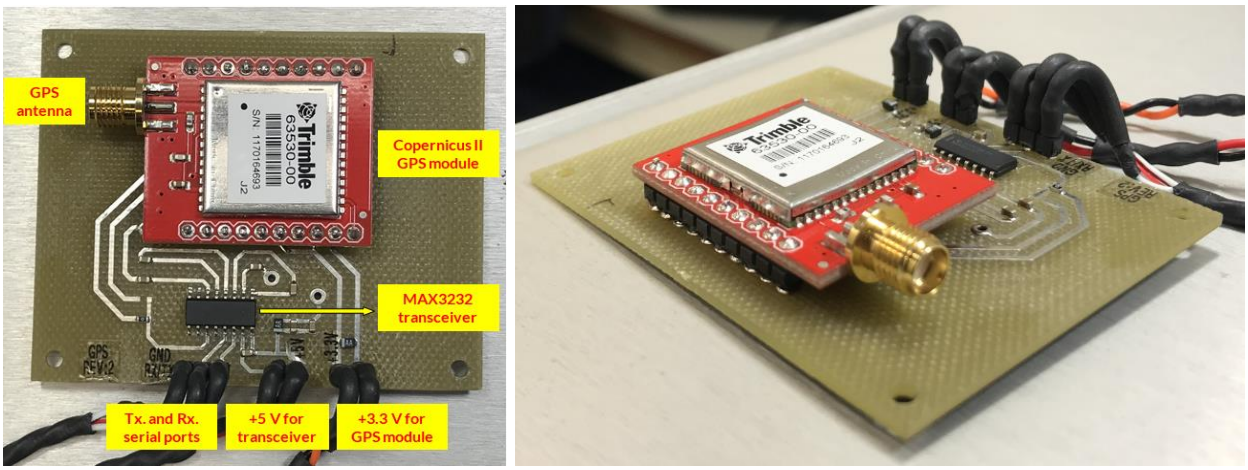

Figure 3-11: Pictures of the GPS board

The GPS antenna is provided along with the UAS and connects directly to the Copernicus II module. The Trimble Studio Software is used to configure the GPS module. The time and position data is configured to be stored in National Marine Electronics Association (NMEA) format. It uses a simple ASCII, serial communication protocol is a widely used data standard. It is compatible with most hardware and software and hence processing the received data is convenient. Figure 3-12 shows a screenshot of a few lines of the received GPS NMEA data.

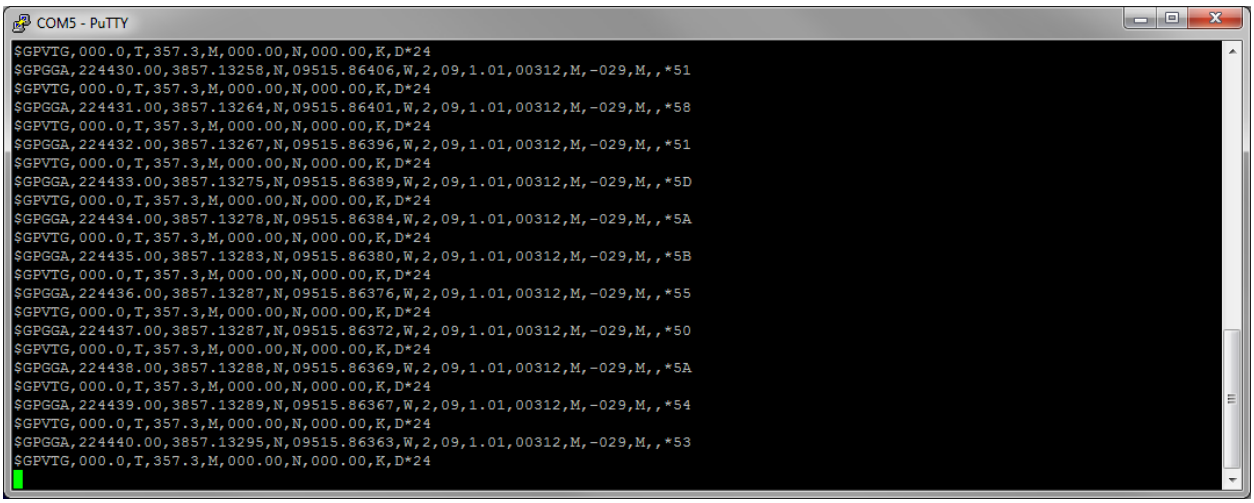

Figure 3-12: Serial port screenshot of received GPS NMEA data

3.3.2 RF Section

The radar system is comprised of numerous subsystems as described in Section 3.3. For an UWB system, it is desirable to have all the RF components and their respective biasing and control circuits on the same PCB. It is much easier to ensure timing and synchronization when the RF components are on the same physical and electrical plane. However, due to limited space available in the chassis, these components must be separated into two separate PCBs.

While the space available can accommodate the two PCBs on two separate levels, it becomes problematic when the volume and weight for inter-board connections are taken into account. In continuing along the same design ethos of miniaturization, the bulky cables are omitted by integrating both PCB's together back-to-back. Via holes are designed at specific locations to allow a 32 gauge wire to pass through from one board to the other. While both boards are held in place using the four mounting holes, electrical connections between components are made by soldering the 32 gauge wire at the via holes on both sides.

The two PCBs are termed as RF Board (RFB) and Low-Speed Board (LSB) or Mixed-Signal Board (MSB), as previously introduced in Section 3.3. The RF section will consist of the following sub-sections: chirp generation, transmitter chain, and receiver chain.

3.3.2.1 Chirp Generation

The Frequency Modulated Continuous Wave (FMCW) signal is generated using a PLL based multiplier. This is an adaption of the scheme developed by [42, 43]. The strategy is to use a wideband Voltage Controlled Oscillator (VCO) to sweep from 11 – 19 GHz, multiply by a factor of two to produce a 22 – 38 GHz signal, and then finally down-convert using a 20 GHz, Phase Locked Oscillator (PLO) to generate the 2 – 18 GHz chirp. The linearity of the chirp is maintained using a PLL. The 11 – 19 GHz swept signal is first divided in frequency by a factor of 56. The

196.42 – 339.29 MHz swept signal is then compared with the reference signal of the same frequency band generated by the Arena's AWG, at the phase-frequency detector. The output is an error voltage proportional to the phase difference between the two chirp signals. A differential loop amplifier converts the differential error voltage to a single-ended voltage signal, which then tunes the VCO to complete the loop.

A well designed and accurately functioning PLL ensures the stability of the chirp signal. The received IF signal is the beat frequency, that is, the difference between transmit and receive chirp signals. Therefore any frequency drift or non-linearity in either of them would result in distortions in the IF waveform and mask information regarding the target. Hence, a rock-solid, stable signal is crucial for measuring the characteristics of targets in an FMCW radar.

Similarly, the stability of the PLO is important since it performs the final frequency translation to produce the 2 – 18 GHz chirp signal. This is ensured by feeding the external reference signal from a common clock source. It is also vital for the PLO to have low-phase noise since this can obscure radar targets and decrease the receiver sensitivity.

A challenging aspect of producing the 2 – 18 GHz chirp signal is the final frequency multiplication and mixing stage. The swept 11 – 19 GHz signal is multiplied to 22 – 38 GHz and then mixed down using 20 GHz to result in 2 – 18 GHz. At these high frequencies, Integrated Circuits (ICs) may usually come in the form of a bare die instead of a package or assembled with connectors. Wire bonding is used to make connections between the bare die and the rest of the Printed Circuit Board (PCB). The tiny, gold strands of wire are prone to breakage and hence the board must be handled very carefully. Furthermore, practical aspects like accessibility to a wire bonding machine and affordability for the cost of operation are causes for concern.

Figure 3-13 shows the circuit diagram of the chirp generation stage. Figure 3-14 and Figure 3-15 show the layout of both boards with the chirp generation stage highlighted. The entire process of generating the 2 – 18 GHz chirp emphasizes the difficulty and importance of this stage. This is further complicated by the method of integration of the boards into the system. To ensure continuity, tests must first be performed when both boards are separated and a picture of this test setup is shown in Figure 3-16. Then, the same tests must be done with the boards integrated together and a picture of this setup is shown in Figure 3-17.

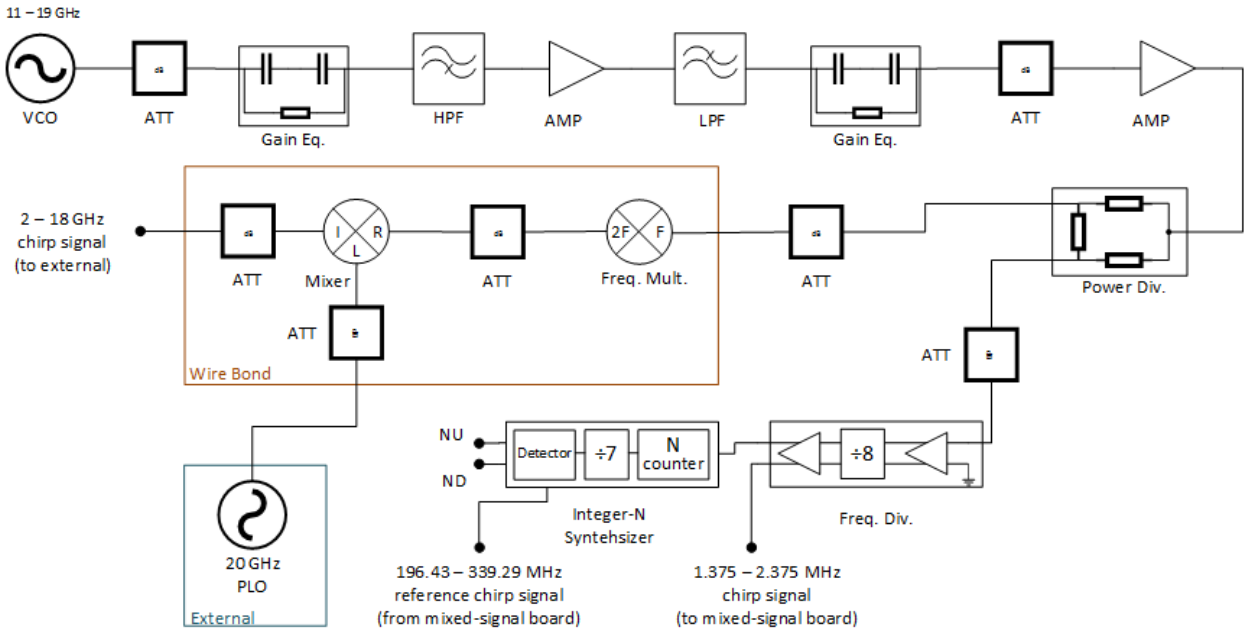

Figure 3-13: Chirp generation stage circuit diagram

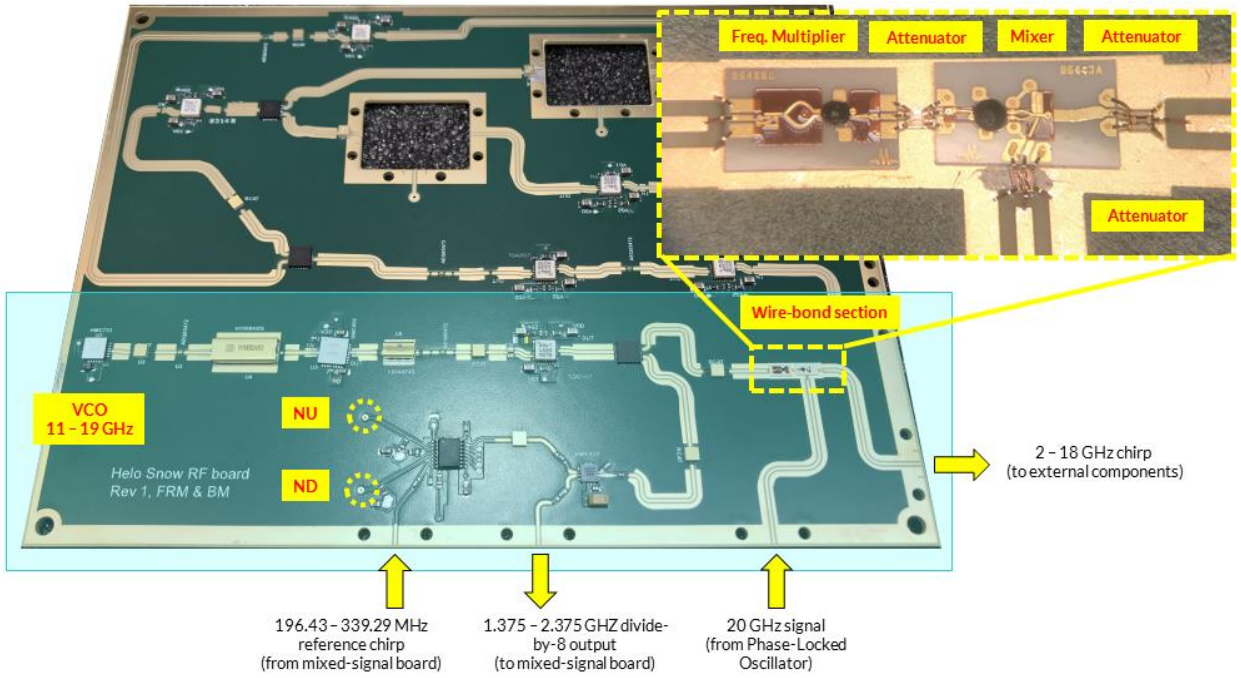

Figure 3-14: Picture of the RF board with the chirp generation stage highlighted

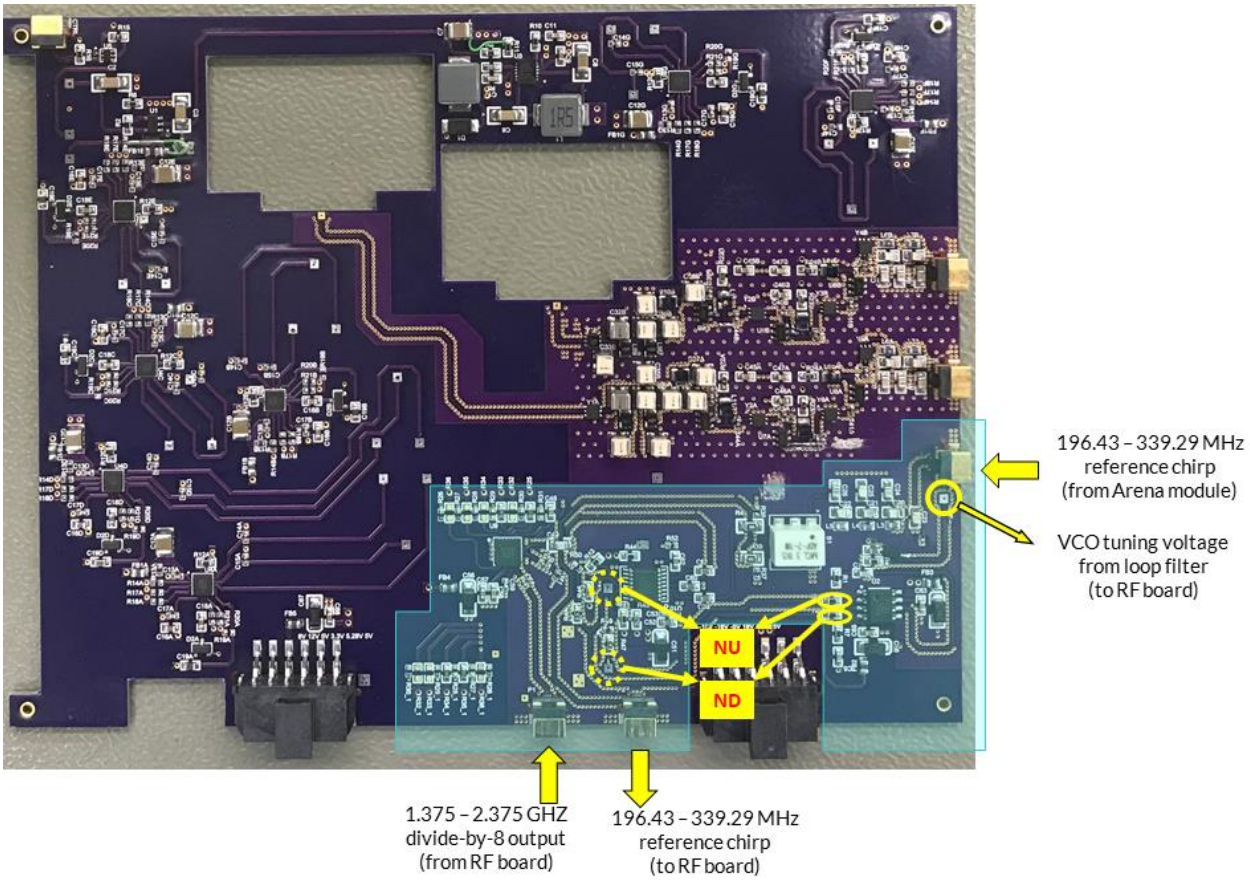

Figure 3-15: Picture of the low-speed board with the chirp generation stage (phase-locked loop) highlighted

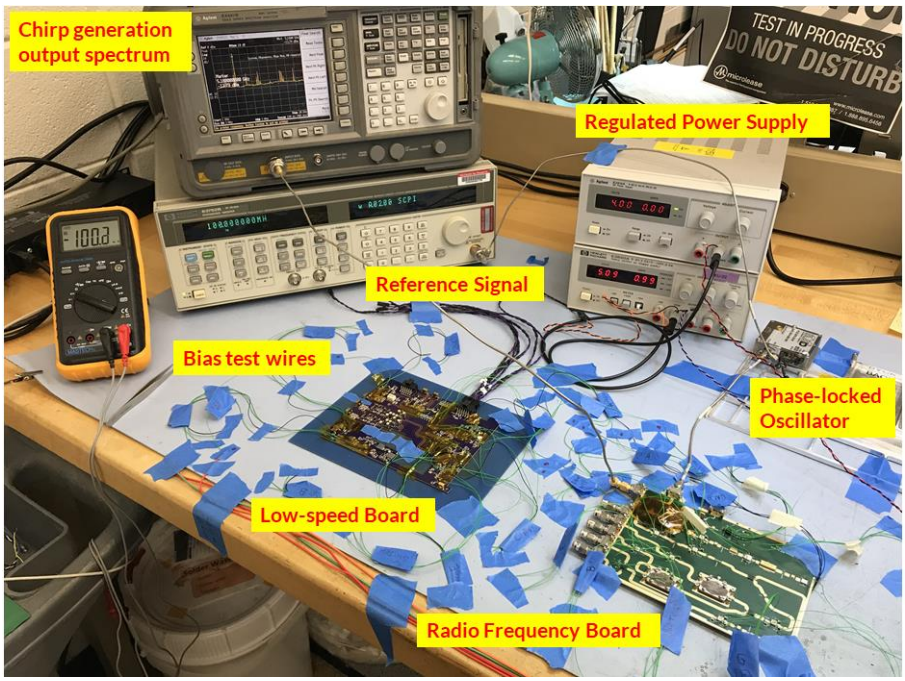

Figure 3-16: Picture of the chirp generation test with separated RF and MS boards

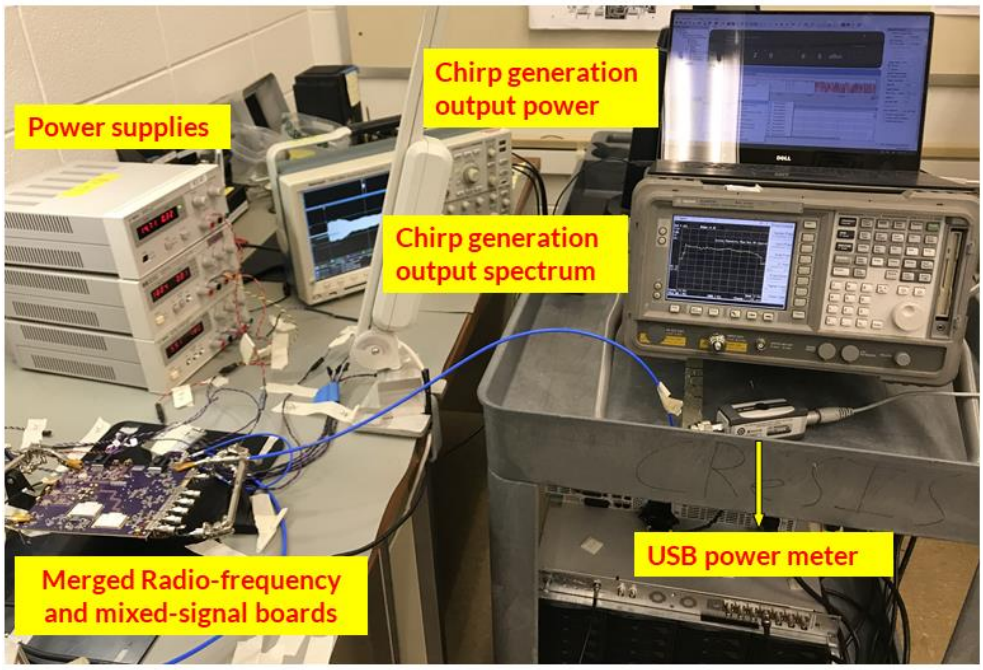

Figure 3-17: Picture of the chirp generation test with merged RF and MS boards

The initial test with both boards separated provides an essential proof-of-concept for the chirp generation stage. Hence, in spite of the long test wires between the boards and manual operation of the VCO through the power supply, the spectral results are still valid and beneficial. The 83752B synthesized sweeper by Hewlett-Packard provides a stable 100 MHz clock reference for the PLO. As the tuning voltage for the VCO is increased on the power supply, the output frequency is gradually increased and this is observed with the spectral peak sliding across the bandwidth on the spectrum analyzer.

The merged tests still involve power supplies and the synthesized sweeper for the PLO reference signal. However, the biggest difference compared with the initial test is that the signal is generated using the entire PLL and is automatically swept using the rack mount Arena module. This configuration is closer to the final expected operation and hence this result serves as a good indication of the true performance. Furthermore, the output is measured using a U2022XA USB wideband power sensor by Keysight Technologies (originally sold by Agilent Technologies). The absolute amplitude accuracy of the power sensor is greater than that of the spectrum analyzer over a wide frequency range.

Figure 3-18 is a screenshot of the power sensor's application window showing the absolute power of the 200 μs long pulse. The peak power of the pulse is -10.35 dBm and the total dynamic range is 14.68 dB with a negative slope. Figure 3-19 shows a similar result but with the addition of a 10 dB gain equalizer at the board output port. In this case, the beginning and ending of the pulse have power levels of -22.53 dBm and -31.01 dBm.

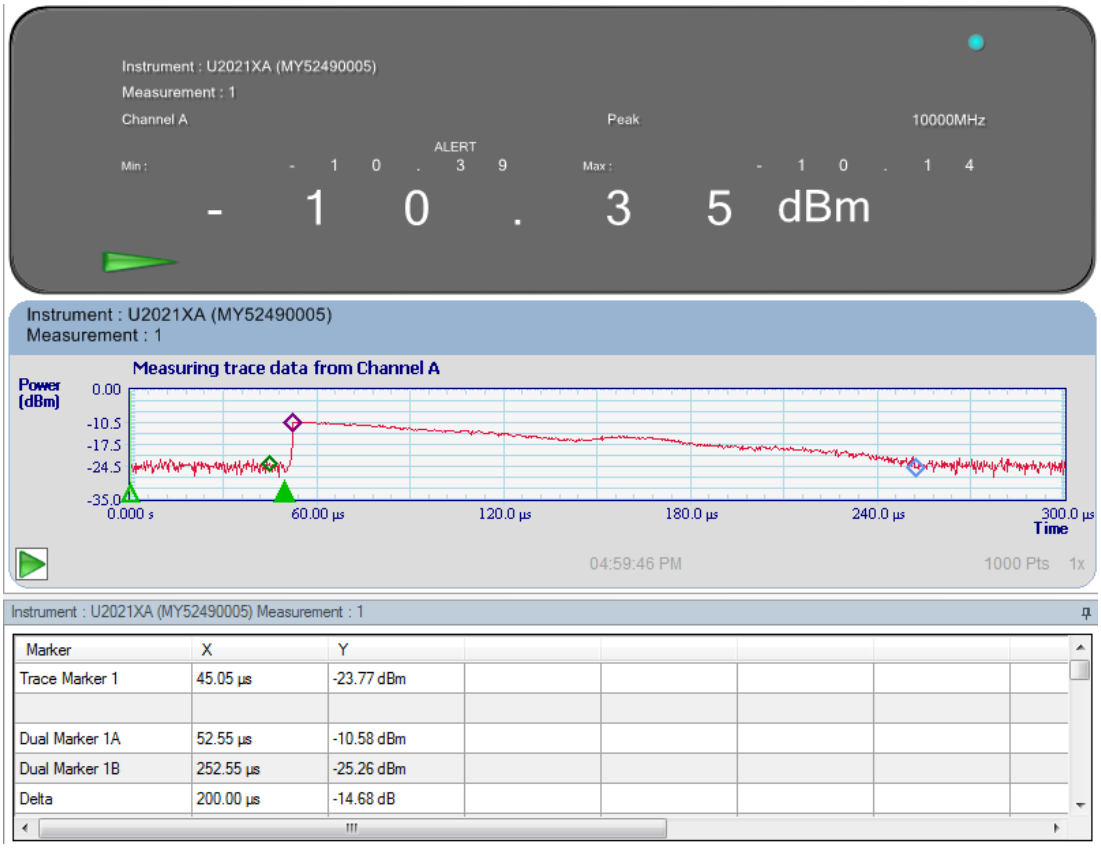

Figure 3-18: Output of merged chirp generation stage measured using power meter

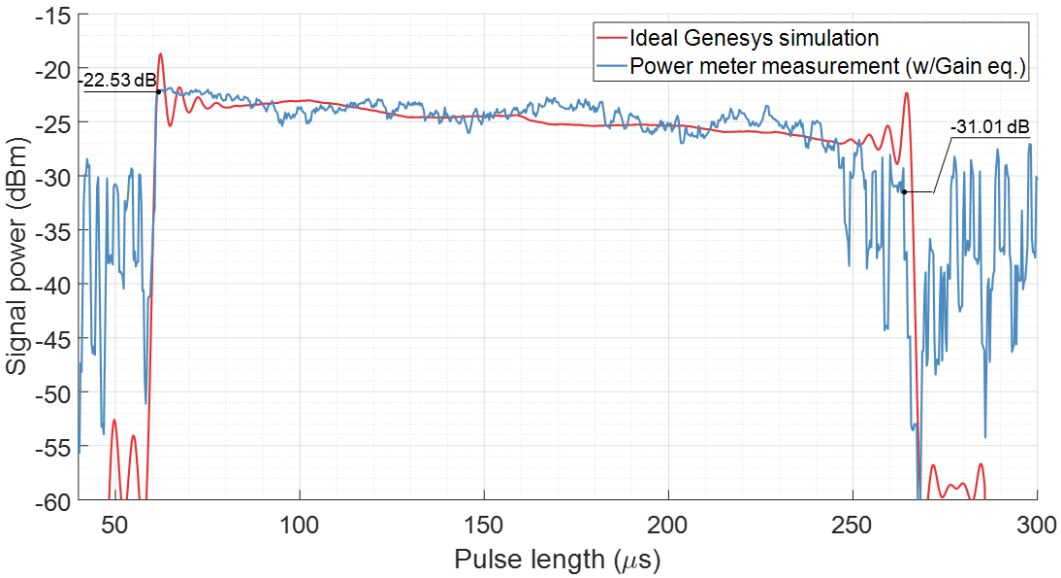

Figure 3-19: Simulated and measured output of the chirp generation stage. The simulation is performed on Genesys while the measurement is done using a power meter on the merged boards, along with a 10 dB external gain equalizer

The simulation in Genesys shows 3.63 dB slope across the bandwidth and the measurement exceeds the expected response by 11.05 dB. Hence, a gain equalizer is used to flatten the slope and this ensures that the signal amplitude over the entire bandwidth is within the LO range of the mixer. This undesirable effect is attributed to the physical imperfections of the wire-bond stage. EM co-simulation of the board and the components can account for the total board effects and this will be investigated in future. Since the PLL spans over both the RF and mixed-signal boards, the interconnections between the boards should be solid and the boards themselves should be flush relative to either ground planes. Misalignment and a gap between the boards can induce noise and attenuate signals. Moreover, due to the wide bandwidth, the effects vary linearly across frequency.

A large dynamic range for the entire pulse is expected due to the UWB frequency range. The higher frequencies in the band, for instance from 14 – 18 GHz, experience much higher transmission line losses than the lower frequencies like 2 – 6 GHz. However, such large variations in power within the pulse can cause instability, particularly with non-linear operators like amplifiers and mixers. Further, the components used in the chain must have a sufficiently wide dynamic range to accommodate the entire pulse. This was discovered to be a problem and necessitated additional external components, which is discussed in the next section.

3.3.2.2 Transmit Section

The chirp generation stage defines two of the three important characteristics of the desired signal: frequency and phase. The PLL-based multiplier produces a stable 2 – 18 GHz chirp signal. The transmit section defines the third important characteristic, amplitude. In an FMCW radar system, there are two amplitude considerations: Output transmit power at the antenna and transmit power at the Local Oscillator (LO) port of the mixer.

An FMCW radar system uses a copy of the transmitted chirp signal to down-convert the received chirp signal. The resulting Intermediate Frequency (IF) or beat signal contains information about the target. This copy of the transmitted chirp signal is fed to the LO port of the mixer. It is relatively easy to amplify the generated chirp signal to the desired output power level at the antenna. However, the challenge in an UWB system is to amplify the entire pulse to fit within the dynamic range of the mixer's LO port.

This radar system uses two 2 – 18 GHz double-balanced mixers by Miteq (DB0218LW2). The LO power range for this mixer is +7 to +13 dBm. As stated in the previous section, the total dynamic range of the generated chirp signal is 14.68 dB. Therefore, the full UWB signal must be appropriately conditioned so that the entire pulse falls within the 6 dB dynamic range of the mixer's LO port. This is one of the biggest challenges of this radar system.

The signal conditioning is achieved by using a carefully selected set of external components. This is highlighted in the circuit diagram shown in Figure 3-20. A specific combination of amplification, attenuation, and gain equalization is used to over-correct the slope of the chirp signal. This over-correction allows the signal to have a nearly flat slope at the LO port of the mixer, as the signal experiences further losses due to the other on-board components.

The setup to correct the dynamic range of the pulse is similar to the merged chirp generation test. The chirp output from the board is connected to the external components chain and its output is directly measured using the power sensor. The selection of components was tricky due to the availability of only two gain equalizers that have a 10 dB and 15 dB slope. After attempting various combinations with the available components, the conditioned chirp pulse is shown in Figure 3-21.

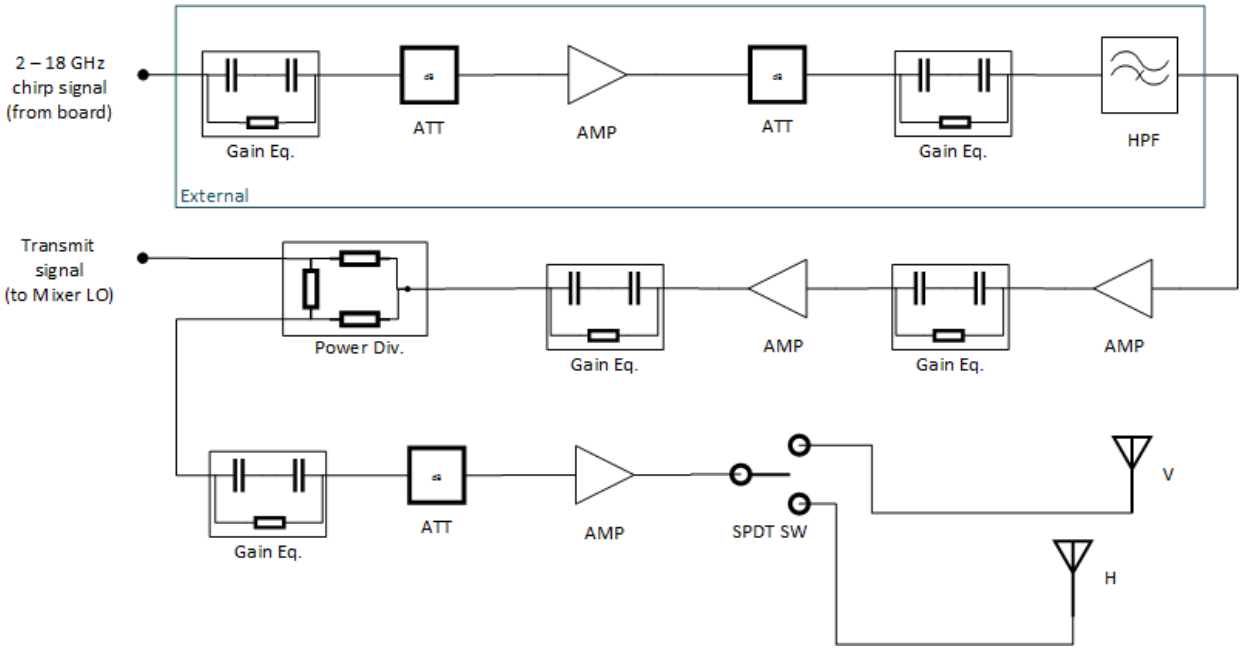

Figure 3-20: Transmit section circuit diagram

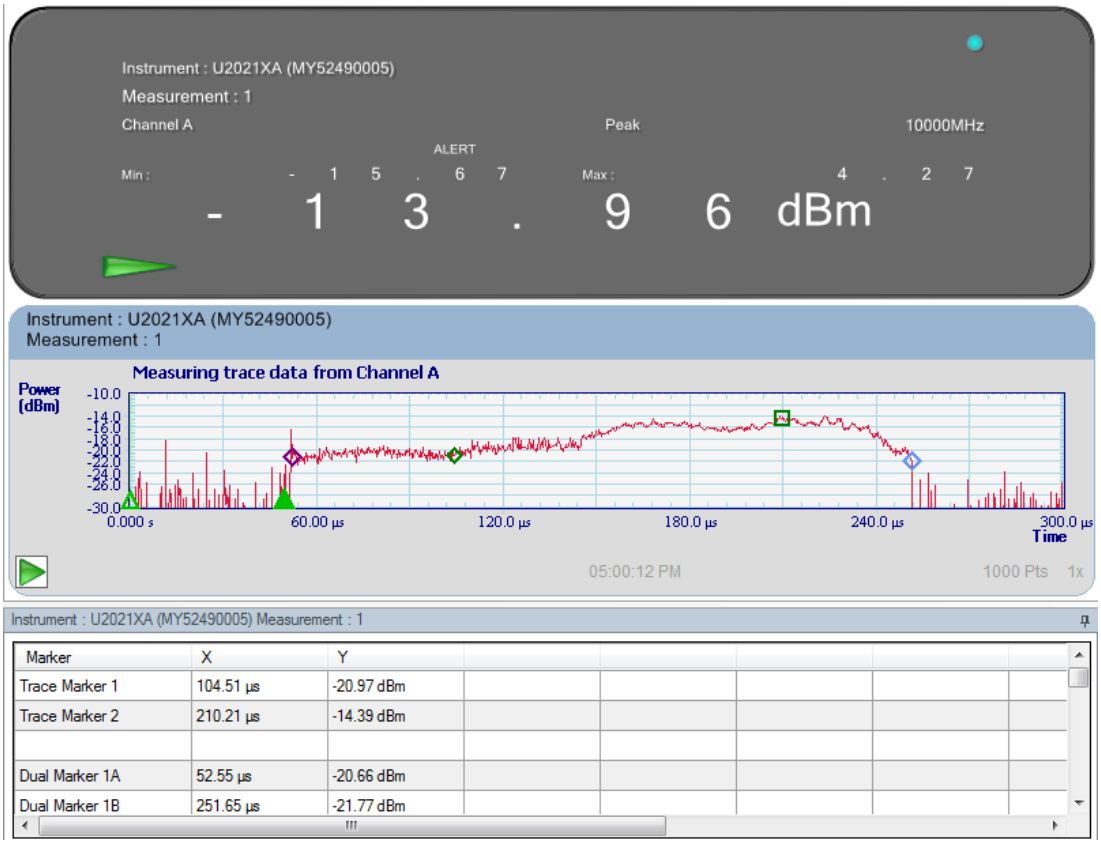

Figure 3-21: Output of the external components chain measured using power meter

The beginning of the pulse is attenuated from -10.58 dBm to -20.66 dBm while the other end is amplified from -25.26 dBm to -21.77 dBm. The peak power of the pulse is measured to be -13.96 dBm. The magnitude of the second half of the pulse is approximately 6.58 dB larger than the first half and the positive slope indicates over-correction. The total dynamic range of the pulse is reduced from 14.68 dB to 7.38 dB. The typical negative slope of the transmission line losses flattens the pulse and also further reduces the dynamic range to less than 6 dB.

The rest of the transmit section on the RF board provides sufficient amplification to achieve the desired output transmit power at the antenna. A SPDT RF switch alternates between the two channels to transmit from both antenna polarizations. Figure 3-22 shows the highlighted transmit section on the board and the external components chain.

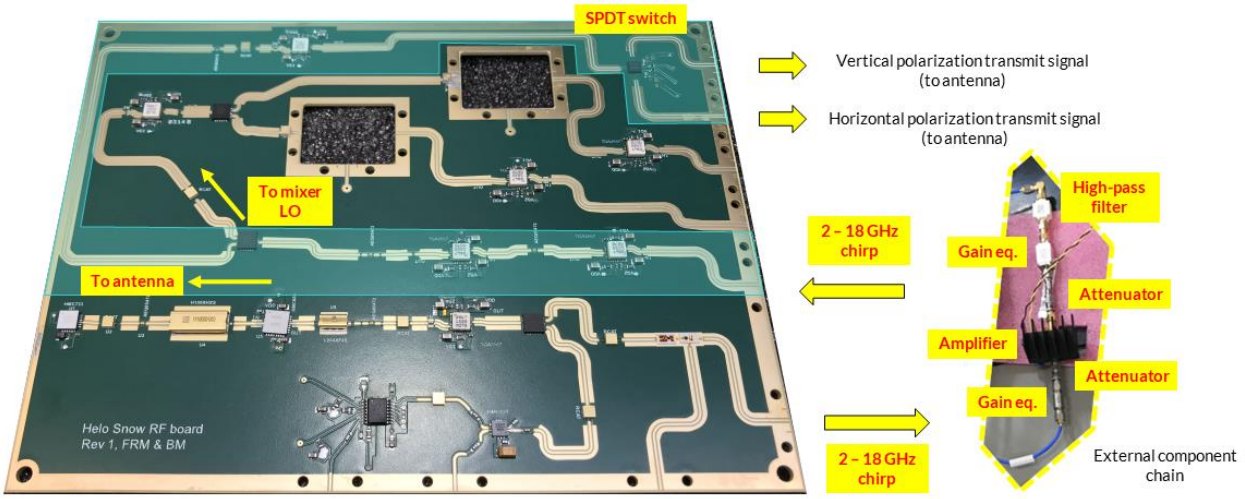

Figure 3-22: Picture of the RF board layout and external components with the entire transmit section highlighted

Figure 3-23 shows the transmission gain of the on-board transmission section for both polarizations. An S21 measurement is performed using the Vector Network Analyzer (VNA) between the port where the chirp is fed back into the board from the external components and either of the output ports to the antenna. The total dynamic range for horizontal polarization is 12.09 dB and for vertical is 11.45 dB. The respective peak gain are 35.34 dB and 35.2 dB. The

signal path to the LO port is similar to that of the antenna ports, therefore the transmission gain may also be approximately equal. If the slopes of the chirp pulse and the transmission gain are combined, the signal dynamic range at the LO port may be estimated. The signal power range at the upper and lower mixer LO ports are approximately 5.51 dB and 4.87 dB. Hence, it is likely that the LO ports are driven correctly for the entire pulse as the range is less than 6 dB.

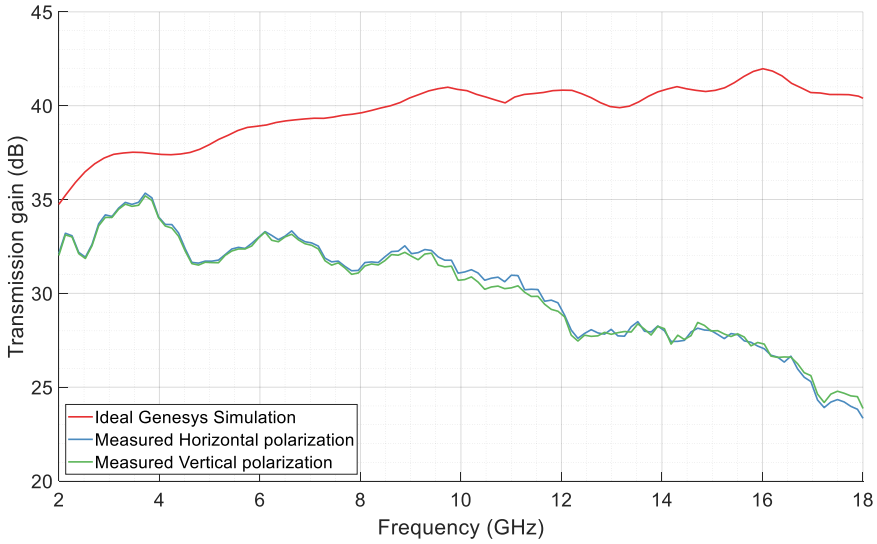

Figure 3-23: Simulated and measured gain of the transmit section excluding external components

3.3.2.3 Receive Section

In an UWB radar system, setting an appropriate Noise Figure (NF) is paramount. The total losses over the entire bandwidth can have a large slope, as observed in the previous two stages. Hence, careful consideration must be given for the first component in the receiver stage. The TGA2567 low-noise amplifier (LNA) is chosen as the first component since it provides an average NF of 2 dB over the entire band. An external low-pass or band-pass filter may be included before the LNA to prevent interference from other noise sources. However, due to the significance of the NF, the filtering aspect may instead be relied on the antenna's return loss to reject out-of-band frequencies.

Figure 3-24 shows the receive section circuit diagram. While the LNA sets the NF and provides crucial amplification of the low-power received signal, the second component is prudently selected to be the mixer. It is desirable to down-convert to IF as quickly as possible to minimize further losses of the UWB pulse. As previously discussed, the signal at the LO port of the mixer is a copy of the transmit chirp after conditioning the power using a chain of external components. The RF and LO components of the receiver are present on the RF board as shown in Figure 3-25. The down-converted IF signal is transferred to the mixed-signal board through the direct board-to-board connection and this section is shown in Figure 3-26.

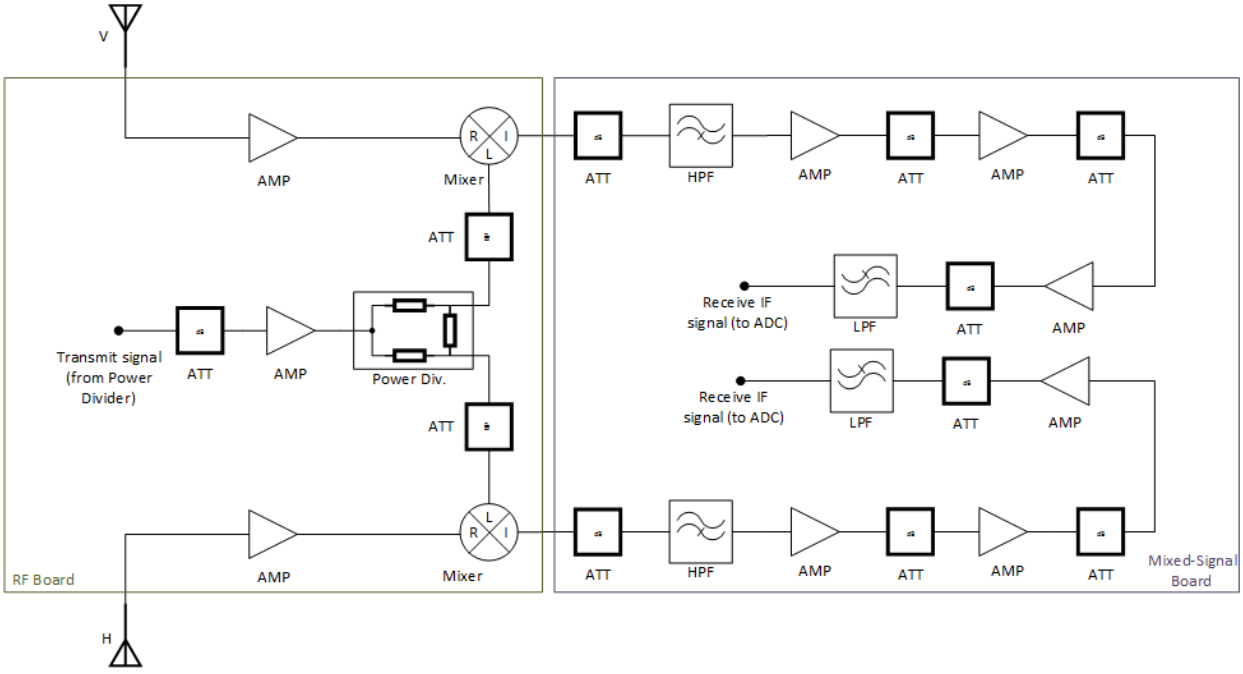

Figure 3-24: Receive section circuit diagram

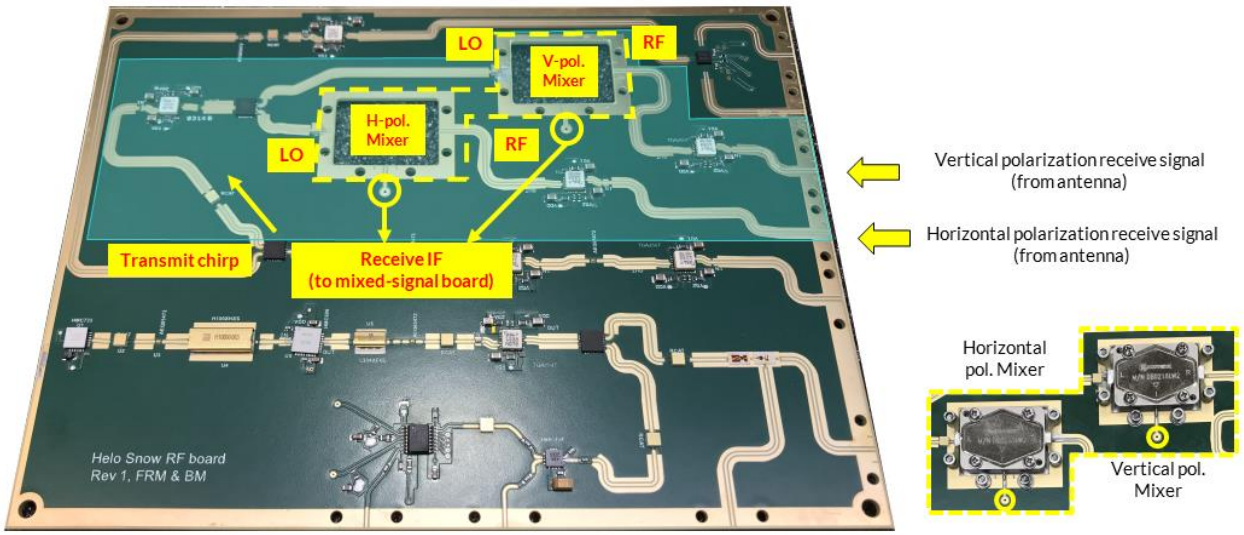

Figure 3-25: Picture of the RF board layout with the receive section highlighted

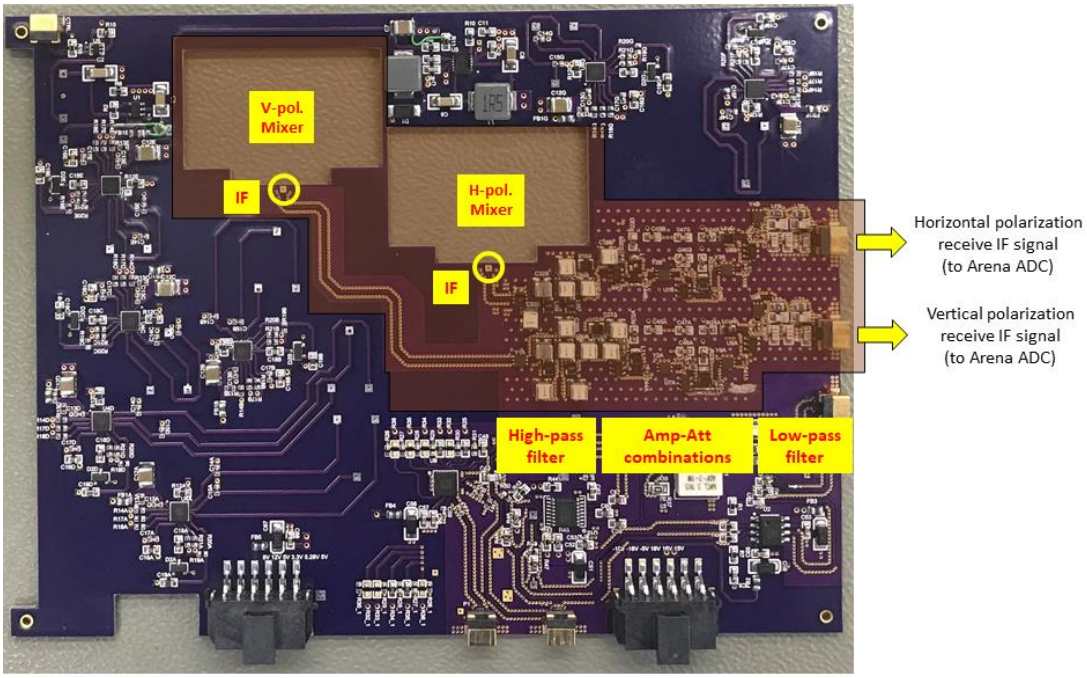

Figure 3-26: Picture of the mixed-signal board layout with the receive (intermediate) section highlighted

The IF section of the receiver on the mixed-signal board is bookended by two filters. The cut-off frequency for the high-pass filter is 3 MHz and for the low-pass filter is 50 MHz. The frequency of the beat signal is proportional to the time difference between the transmit and receive chirp. The time difference is in turn related to the altitude of the UAS. Hence, the frequency range of the Nyquist zone sets the cut-off frequencies for the IF section. The relatively low-power,

received IF signal is further amplified in three stages. Attenuators are used between each stage to sufficiently dampen the signal to prevent instability and saturation. The IF signal is then finally digitized in the Analog-to-Digital Converter (ADC) in the Arena module. It is sampled at 100 MSPS to satisfy the Nyquist sampling requirement.

Figure 3-27 and Figure 3-28 shows the frequency response for the horizontal and vertical polarizations. An S21 measurement is performed using the VNA between the IF port and the output port that connects to the ADC. The IF port on the MS board is a direct solder connection from the RF board. Hence, for the S21 measurement a stripped coaxial cable is probed on the test point. To complete the circuit, an Exacto knife is used to short the outer braided conductor of the cable to a ground via right beside the test point. Since this is an unconventional method of measurement, it would likely account for some losses. So, the magnitude of the insertion loss measured is likely to be slightly lower, relative to a measurement with connectors.

The cut-off frequencies of the frequency response clearly correspond to that of the high-pass and low-pass filters. Although the magnitude shown exactly at 3 MHz is a lot lower than 3 dB from the mid-passband point, the passband does begin within the next few data points due to the sharp roll-off. Therefore, the cut-off may be approximated to 3 MHz. The higher cut-off occurs exactly at the end of the first Nyquist zone. However, there is a nearly 2.5 dB difference at the cut-offs and 1.5 dB difference at the mid-passband point between the two channels. Since both channels use the same components and a very similar build quality is probable, the difference could be caused due to the longer transmission line from the IF point for the vertical polarization.

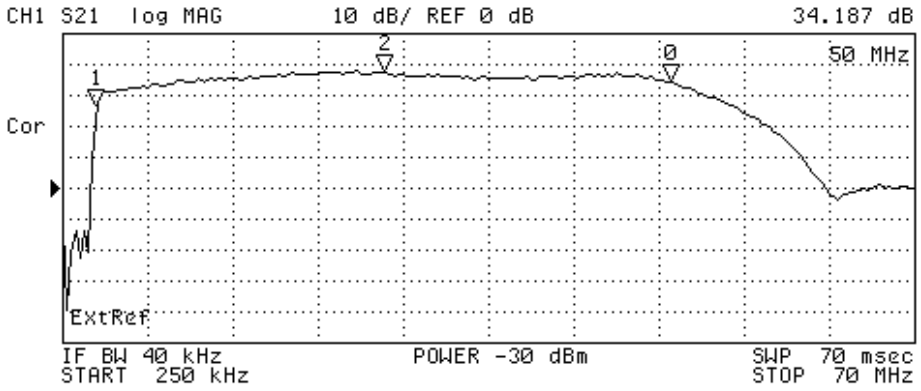

N	SWP PARAM	VAL
0	50 MHz	34.187 dB
1	3 MHz	25.985 dB
2	26.5 MHz	37.408 dB

Figure 3-27: Frequency response of the IF section for horizontal polarization

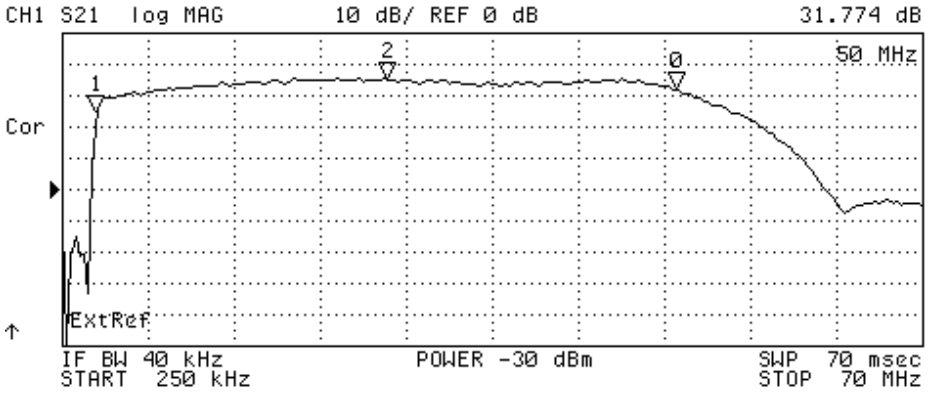

N	SWP PARAM	VAL
0	50 MHz	31.774 dB
1	3 MHz	24.468 dB
2	26.5 MHz	35.075 dB

Figure 3-28: Frequency response of the IF section for vertical polarization

For Figure 3-29 to Figure 3-32, the test setup involved performing a mixer-mode measurement. In the default mode of measurement, the frequency ranges of multiple ports are fixed. However, a mixer performs frequency translation. So, the three ports of measurement must be tuned to the respective RF, LO, and IF frequency ranges. The RF port is connected to one of

the receive signal connectors, the LO port is connected to the input transmit section connector, and the IF port is connected to the corresponding output IF section connector.

In Figure 3-29 and Figure 3-30, the input RF frequency is set to 1 to 19 GHz, input LO frequency to 0.98 to 18.98 GHz, and the output IF frequency is fixed at 20 MHz. The input power at the RF and LO ports are calculated in accordance with the link budget of the respective chains. The input RF power is fixed at -40 dBm while the LO power is set at five different levels, as shown in the figures. This test shows the power required at the input of the transmit section on the board to successfully drive the LO port of the mixer. For the horizontal polarization mixer, the drive power is around – 17 dBm while for the vertical polarization mixer it is slightly above -17 dBm. The difference indicates that the vertical channel appears to be lossier than the horizontal channel. It is also evident from the roll-off at the higher frequencies when the mixer is under-driven.

In Figure 3-31 and Figure 3-32, the LO power is now held constant, while the conversion loss is recorded at different IF frequencies. At a constant RF frequency range of 1 to 19 GHz and power of -60 dBm, the LO frequency range is appropriately changed to obtain the list of IF frequencies shown in the Figures. The LO port of the horizontal polarization mixer is driven at -18 dBm and due to the extra losses observed, the vertical mixer is driven at -16 dBm.

This test shows the change in conversion loss across the full signal bandwidth, as the IF signal is moved across the first Nyquist zone. The various conversion loss levels correspond to the insertion loss of the frequency response. This test essentially characterizes the effect on the entire UWB signal as the UAS altitude is increased.

There is a severe degradation in gain between 2 and 3.5 GHz at all frequencies within the IF band. This is caused due to the roll-off of the high-pass filter at the beginning of the IF section. The roll-off at the IF cut-off of 3 MHz must be sharp so that it filters out-of-band response but

does not encroach within the passband. This undesirable effect causes a loss in gain at the lower frequency band, between 2 and 3.5 GHz. This must be corrected in future designs as it can mask target returns.

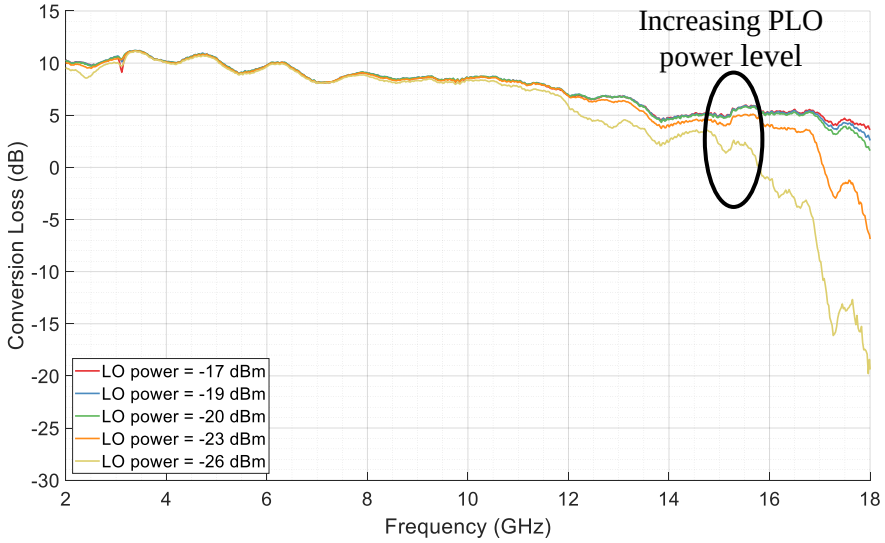

Figure 3-29: Conversion loss at an input RF power of -40 dBm, an output IF frequency of 20 MHz, and at various LO power levels for the horizontal polarization mixer

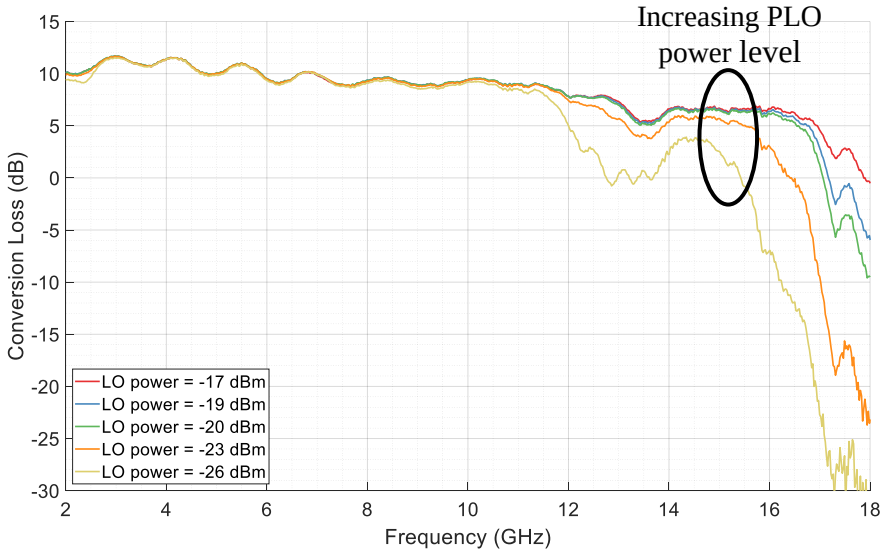

Figure 3-30: Conversion loss at an input RF power of -40 dBm, an output IF frequency of 20 MHz, and at various LO power levels for the vertical polarization mixer

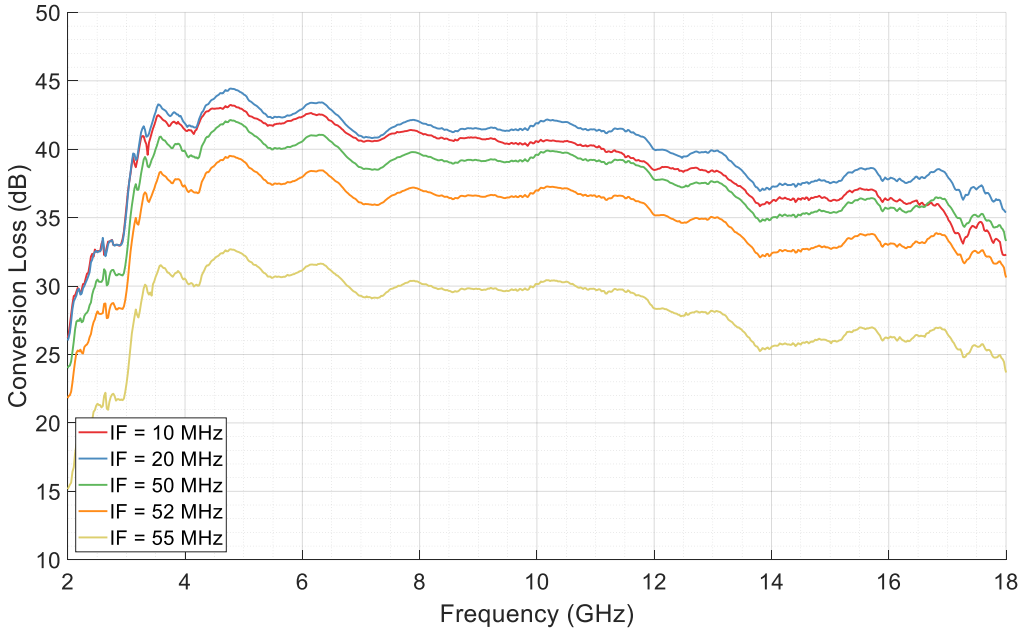

Figure 3-31: Conversion loss at an input RF power of -60 dBm, an input LO power of -18 dBm, and at various output IF frequencies for the horizontal polarization mixer

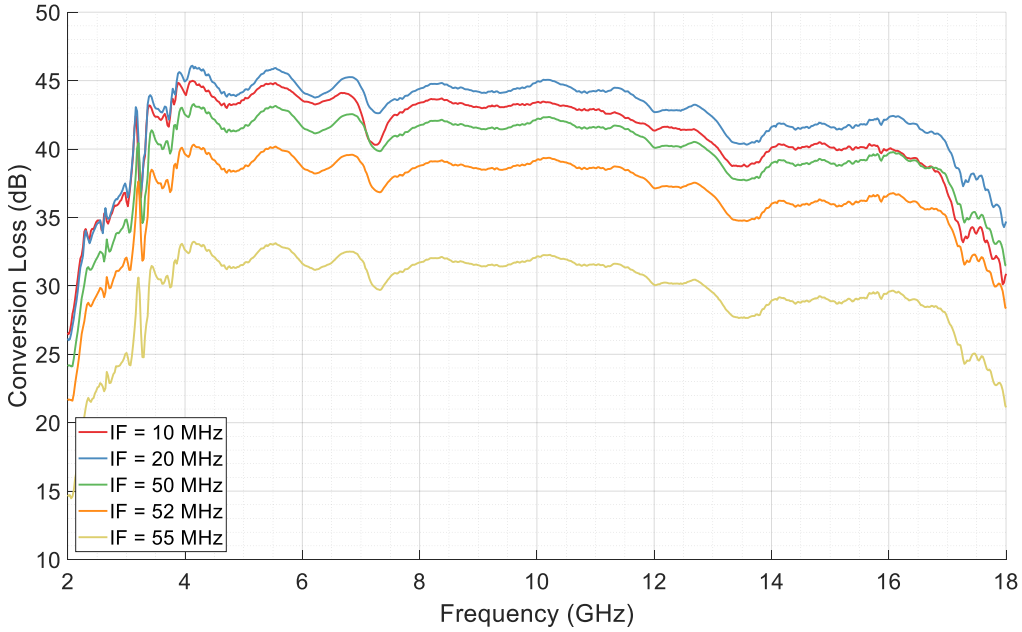

Figure 3-32: Conversion loss at an input RF power of -60 dBm, an input LO power of -16 dBm, and at various output IF frequencies for the vertical polarization mixer

3.3.3 Mixed-signal Section (Low-speed Board)

As previously discussed in the introduction of Section 3.3.2, the strategy of integrating both boards back-to-back is preferable considering the space issue. However, this increases the complexity and level of difficulty in terms of execution. Both boards must be designed in such a way that interconnect via holes exactly align and must be milled by manufacturers with tight tolerances. It is important that the interconnecting 32 gauge wires pass straight through the via holes and are not angled or bent.

While the boards were designed and manufactured correctly, a slight misalignment resulted due to obstruction from the mixer cradles. These Aluminum pieces act as a base to the two mixers soldered on the RFB. The pieces are fastened to the board itself to provide support, so that the entire mixer is not just held by its soldered pins. The outline of one of the cradles does not match the cutout on the MSB and hence causes a slight lateral misalignment. The result of this is that the interconnecting wires are slightly angled.

The bottom layer of the RFB, that is the ground plane, is completely exposed. Even though the interconnect vias are separated from the ground plane, the angled wires increase the chances of shorting. To address this problem, the area around the interconnect vias are covered with pieces of Kapton tape. This is done on both boards and can be seen in Figure 3-33. Holes are punched through the tape to make it easier for the interconnecting wires to pass through.

On the other hand, the bottom layer of the MSB, that is the ground plane, is completely covered. While shorting with the wires is an issue, there must be sufficient electrical contact between the ground planes of both boards. If both ground planes are not at the same potential, then it would introduce severe noise into the system and prevent accurate functioning. In fact, during the chirp generation stage test, shown in Figure 3-16, a similar noise was observed due to ground

loops caused by the long test wires. The parasitic inductance of the wires cause the ground potential to be inconsistent.

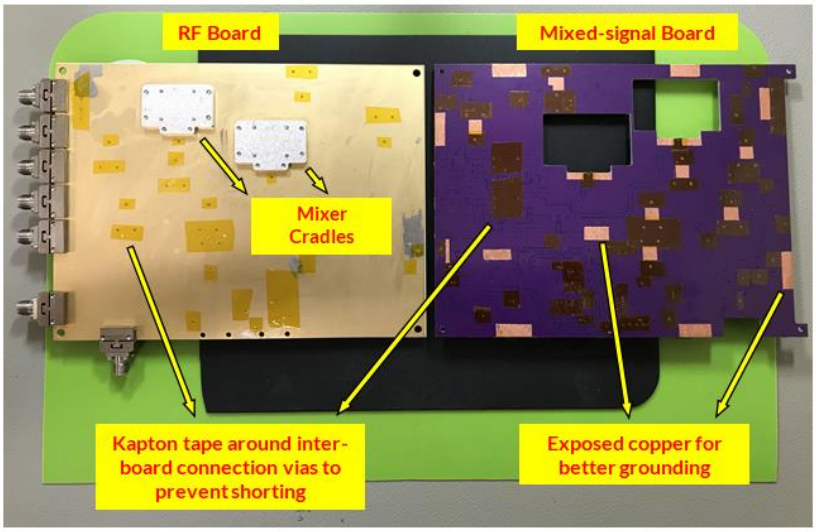

Figure 3-33: Picture of the back side of both RF and Mixed-signal boards showing Kapton tape and solder-mask scraped areas

To ensure sufficient ground contact, specific areas of solder mask are scraped off the MSB. It is advisable to scrape out the area directly underneath the chip for maximum effect. Furthermore, pieces of Indium are applied on the same spot, as shown in Figure 3-34. The sandwiched Indium between the exposed copper areas fills in any possible gap between the boards and further ensures electrical contact.

It is extremely important to prevent any sources of noise from within the system. In addition to maintaining uniform ground potential, another example is having a separated section with its own power plane for the IF section on the MSB. In Figure 3-26, as the highlighted part of the MSB shows the IF section of the receiver chain, this entire part has a separate power plane and the perimeter is lined with a row of vias. This is to prevent interference from the other biasing circuits into the relatively high-speed received IF signal. The Mixed-signal section will consist of the following sub-sections: TGA2567 biasing circuit, ADRF5020 biasing and control circuits, and Phase-locked loop.

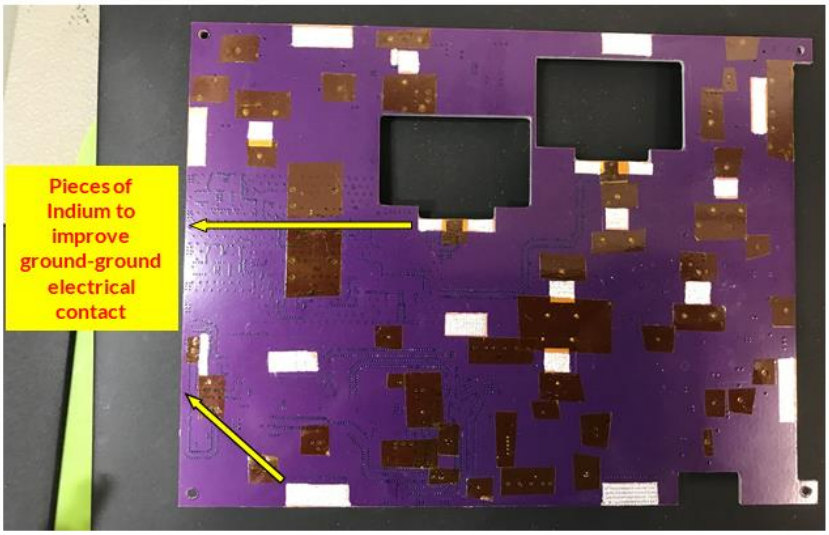

Figure 3-34: Picture of the back side of the Mixed-signal board showing Indium applied to the exposed copper

3.3.3.1 TGA2567 Biasing Circuit

The TGA2567-SM by Qorvo is a LNA gain block that is essentially an enhancement mode, Class-A amplifier. In a p-channel enhancement mode amplifier, a negative gate-source voltage is applied to the terminal. This allows the channel to conduct and the drain current flows through the channel. In the case of the TGA2567, a secondary gate voltage controls the gain of the amplifier.

Metal Oxide Semiconductor Field Effect Transistors (MOSFETs) are used in common-source configuration to function as amplifiers. Under certain conditions, that is, when a voltage is applied across the terminals, MOSFETs naturally exhibit a switching nature. To successfully operate in a particular region, the voltages must be applied in a specific sequence. This is commonly termed as power sequencing. A table showing the bias-up and bias-down procedure for the TGA2567 is in the Appendix.

While it is easy and convenient to follow this procedure manually using bench-top power supplies, a specific power sequencer circuit must be used to automate this process on the board-level. The HMC981LP3E by Analog Devices is an Active Bias Controller that is designed to perform this exact process. It is capable of biasing an enhancement or depletion-type Class-A

amplifier and achieving a constant bias current. Using appropriate resistor networks, the desired voltages can be set and the stability of the bias current is ensured using a feedback network. The typical application circuit reported in the datasheet is used for both components.

The TGA2567 sections on the RF board with designators are shown in Figure 3-35 and the respective HMC981 sections on the MS board are shown in Figure 3-36. Each amplifier has three bias points that are marked with yellow circles within each highlighted section. V_D sets the drain-to-source voltage, V_{G1} sets the gate voltage for the channel to conduct, and V_{G2} sets the gain of the amplifier. The typical operating conditions for the TGA2567 are V_D = +5 V, V_{G1} = -0.7 V, and V_{G2} = +1.3 V for a drain current of 100 mA.

A typical application circuit like that on an evaluation board may require a gate voltage of -0.7 V for a drain current of 100 mA. However, this is likely to be different for customized application circuits. Therefore, the specific gate voltage for the drain current requirement must be ascertained by testing the application circuit. The first step is measuring the open-circuit voltages of the TGA2567 using benchtop power supplies and the results are shown in Table 3-3. The required gate voltages for a 100 mA drain current varies between -0.52 V and -0.54 V for all seven amplifiers.

The resistor network for the HMC981 circuit is appropriately chosen to target the measured gate voltages. The second step is measuring the open-circuit voltages of the HMC981 using benchtop power supplies and the results are shown in Table 3-4. The open-circuit gate voltage for a target closed-circuit voltage of -0.53 V is approximately +2.2 V. Although the voltages vary around the expected value, they are all within an acceptable coarse range.

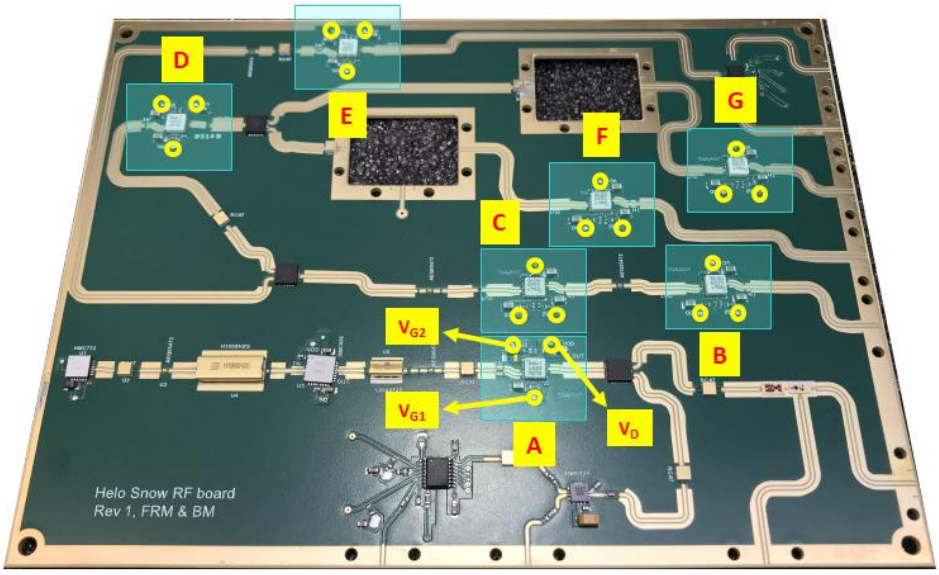

Figure 3-35: Picture of the RF board layout with the seven TGA2567 sections highlighted

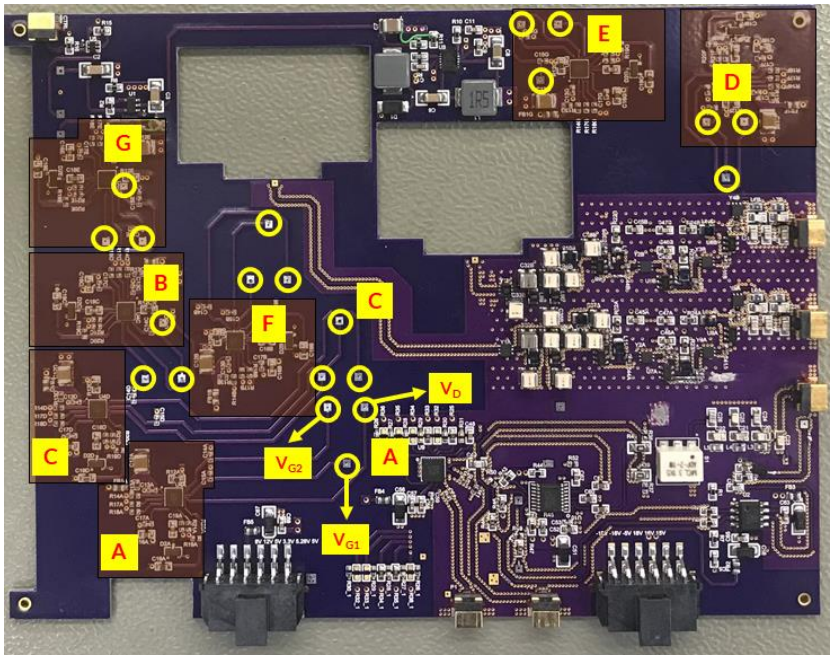

Figure 3-36: Picture of the mixed-signal board layout with the seven HMC981 sections highlighted

Table 3-3: Benchtop, measured open-circuit voltages of the TGA2567 amplifiers for a constant drain current requirement of 100 mA

Designator	Circuit placement	Drain Voltage (V_D)	Gate Voltage (V_{G1})	Gate Voltage (V_{G2})
TGA2567-A	Chirp generation	+5 V	-0.53 V	+1.3 V
TGA2567-B	First transmit	+5 V	-0.54 V	+1.3 V
TGA2567-C	Second transmit	+5 V	-0.54 V	+1.3 V
TGA2567-D	Mixer Local Oscillator	+5 V	-0.54 V	+1.3 V
TGA2567-E	Final transmit driver	+5 V	-0.52 V	+1.3 V
TGA2567-F	Lower receive	+5 V	-0.54 V	+1.3 V
TGA2567-G	Upper receive	+5 V	-0.52 V	+1.3 V

Table 3-4: Benchtop, measured open-circuit voltages of the HMC981 active-bias controllers for a drain voltage of +5 V, drain current of 100 mA, and second gate voltage of +1.3 V

Designator	Circuit placement	Drain Voltage (V_D)	Gate Voltage (V_{G1})	Gate Voltage (V_{G2})
HMC981-A	Chirp generation	+4.961 V	+2.259 V	+1.296 V
HMC981-B	First transmit	+4.96 V	+2.218 V	+1.29 V
HMC981-C	Second transmit	+4.96 V	+2.283 V	+1.29 V
HMC981-D	Mixer Local Oscillator	+4.96 V	+2.37 V	+1.288 V
HMC981-E	Final transmit driver	+4.96 V	+2.195 V	+1.287 V
HMC981-F	Lower receive	+4.958 V	+2.161 V	+1.293 V
HMC981-G	Upper receive	+4.959 V	+2.397 V	+1.298 V

The third and final step is to measure the closed-circuit voltages after the boards are merged and the results are shown in Table 3-5. The gate voltages are all close to the required ones shown in Table 3-3. This ensures that the TGA2567 amplifiers would all receive the correct bias voltages for optimum performance. However, the drain voltages drop to around +4.4 V due to the increased resistance after merging. This is still within the operating range of the amplifiers but it slightly changes the gain near 18 GHz. In fact, the effect of this is beneficial since it slightly flattens the

gain response and in turn reduces the signal power variation within the pulse. But the drain voltage may be increased if the current requirement is not matched.

One of the challenges for the MS board design is arranging the various sections in accordance with the position of the bias points relative to the RF board. Figure 3-36 shows the bias points marked with yellow circles and the designators indicate the respective positions. The traces are carefully considered to prevent voltage drops and utilize the board space appropriately.

Table 3-5: Integrated, measured closed-circuit voltages of TGA2567 and HMC981 after merging the boards

Designator	Circuit placement	Drain Voltage (V_D)	Gate Voltage (V_{G1})	Gate Voltage (V_{G2})
A	Chirp generation	+4.374 V	-0.536 V	+1.297 V
B	First transmit	+4.406 V	-0.531 V	+1.281 V
C	Second transmit	+4.401 V	-0.534 V	+1.288 V
D	Mixer Local Oscillator	+4.408 V	-0.535 V	+1.278 V
E	Final transmit driver	+4.413 V	-0.513 V	+1.286 V
F	Lower receive	+4.414 V	-0.539 V	+1.284 V
G	Upper receive	+4.405 V	-0.513 V	+1.28 V

3.3.3.2 RF Switch Bias and Control

The ADRF5020 by Analog Devices is a single-pole, double-throw switch that is capable of operating over an UWB frequency range. It is a general purpose switch with excellent isolation of 60 dB and operates from 10 0MHz to 30 GHz. It requires dual supply voltages of +5 V and -2.5 V and consumes very low current. A notable feature is that the design is non-reflective or absorptive. This means that the ports are terminated in 50 Ω and hence provide excellent return loss and isolation. This is particularly important for an UWB system to prevent unintended noise. While the power boards provide the commonly used + 5 V supply, additional circuitry is required for the -2.5 V supply. The LT8364 voltage inverter by Analog Devices is used to convert +5 V to

-5 V and the MAX1735 linear regulator by Maxim is used to step-down from -5 V to -2.5 V. Additionally, the 74LVC1T45 translating transceiver is used to control the switching from the Arena module. The typical application circuit suggested in the datasheets are used to ensure optimum performance. The three individual sections and the respective connection points with yellow markers are highlighted on the MS board layout in Figure 3-37.

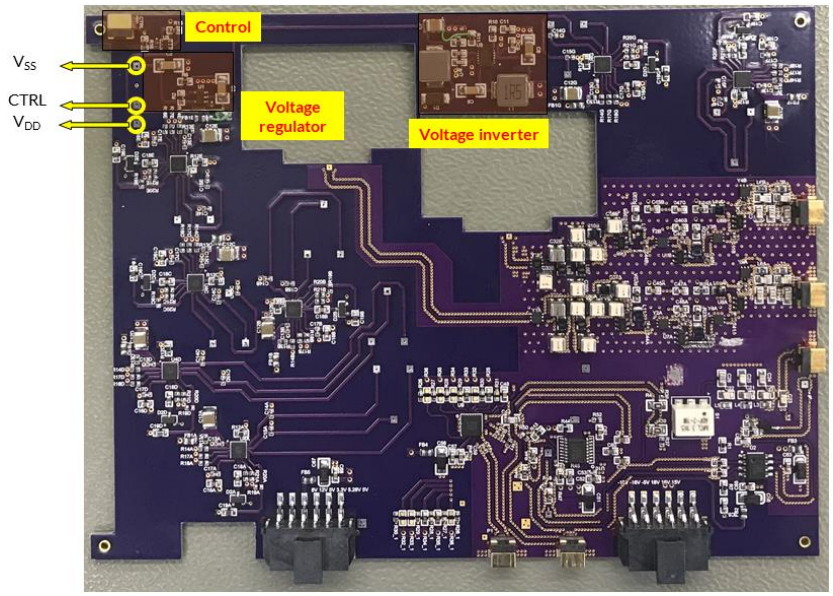

Figure 3-37: Picture of the mixed-signal board layout with the ADRF5020 biasing and control sections highlighted

The tricky method of integrating both boards together caused problems when soldering the biasing points. The negative power supply pin of the RF switch was accidentally shorted to ground during the integration process. However, after consulting Analog Devices, it was learned that the rugged design of the ADRF5020 is able to function with a single positive power supply. This affects the performance by reducing the 1 dB power compression by an average of 10 dB and the third order intercept by an average of 12.5 dB, across the whole frequency band. It also increases the switch's settling time by 15 ns at 10 GHz for an input power of 0 dBm. These changes are acceptable since the radar is intended to be operated with a 0 dBm transmit power and does not require fast switching characteristics.

Figure 3-38 shows the gain and loss of the transmit section for both polarization channels, as the control port of the switch is toggled. This test measures both the insertion loss and isolation of both channels. Thereby, the frequency response of the switch's truth table is characterized. RF1 corresponds with horizontal polarization, while RF2 with vertical. The isolation for the respective channels at the lowest frequency is 62.07 dB and 60.83 dB, while at highest frequency it is 47.88 dB and 45.53 dB. The decrease in isolation at the higher frequency range could be attributed to the effects of the short and operation with a single positive power supply.

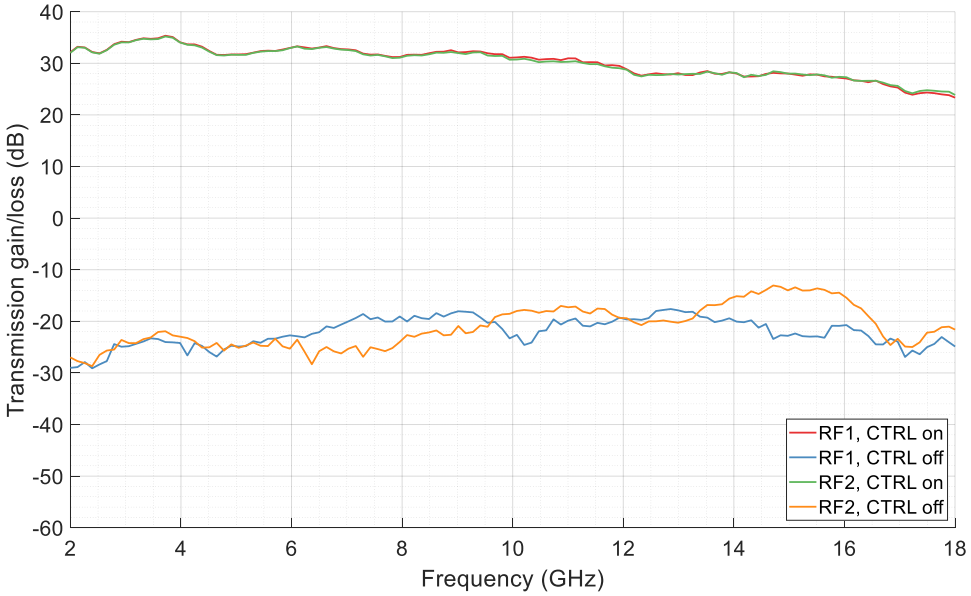

Figure 3-38: Transmission gain/loss through both transmit sections (excluding external components) for each control port state of the RF switch

3.3.3.3 Phase-locked Loop

A Phase-Locked Loop (PLL) primarily consists of three components: VCO, phase detector, and loop filter. The VCO produces oscillations at the intended frequency while the phase detector compares the phase of this signal with a reference signal. The resulting phase difference between the signals is converted into an error voltage by the loop filter and is fed back into the VCO. Depending on the error signal, the VCO is tuned to increase or decrease the frequency to exactly

match the reference frequency. The VCO output signal is continuously compared with the reference signal through the feedback mechanism and hence resulting in a stable frequency output.

The PLL design features two options to translate the chirp signal in frequency and compare the phase with the reference signal. Figure 3-39 shows the circuit diagram of the entire setup along with both the options. The first option divides the 11 – 19 GHz signal by a factor of 8 using the HMC494 to obtain a 1.375 – 2.375 GHZ signal. The HMC440 contains a programmable divider and a phase-frequency detector. The signal is further divided by a factor of 7 and the phase is compared with the reference signal from the mixed-signal board. The reference signal is provided by the Arena module which is then filtered and then divided in power between the two PLL options.

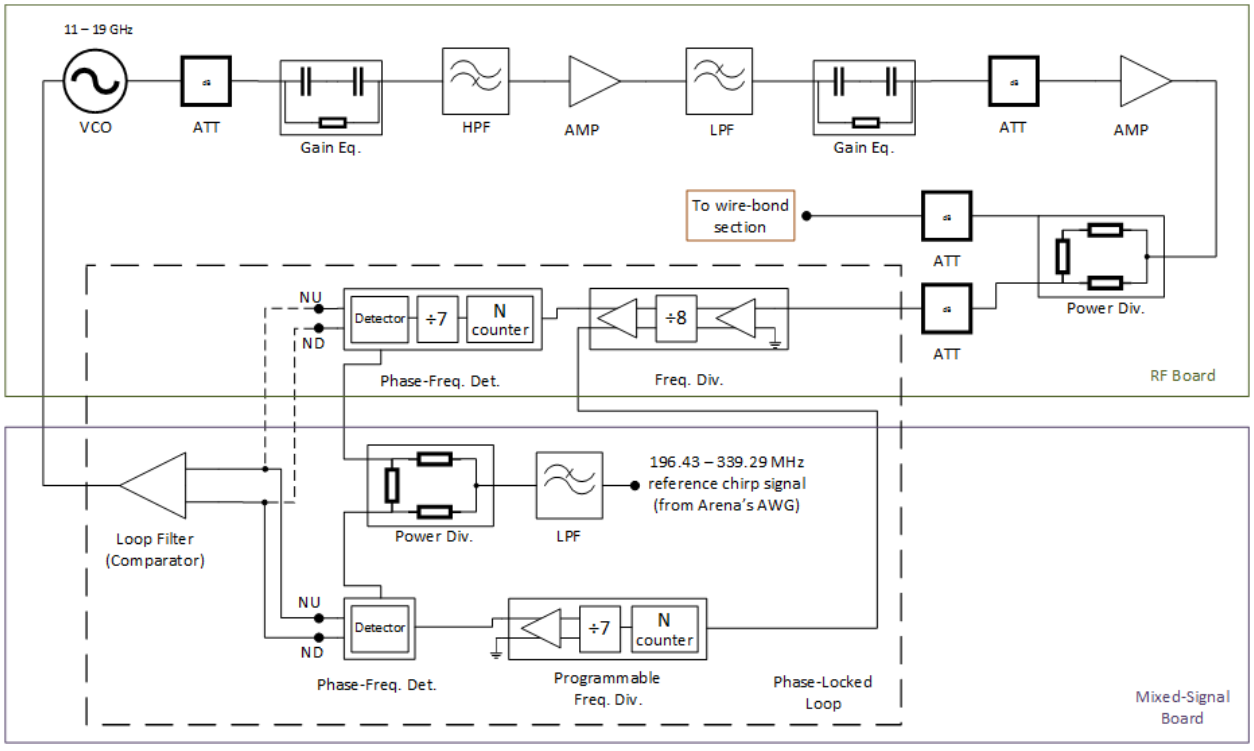

Figure 3-39: Phase-locked loop circuit diagram

The second option offers the same process but in three separate stages. After the signal is divided by a factor of 8, it is separately divided by a factor of 7 using the programmable HMC705,

and then the phase is compared using the HMC439. This option provides flexibility, redundancy, and eases the process of troubleshooting. Moreover, the design's separated stages provides convenience when testing since the entire loop must be closed to successfully test the working of the PLL. However, the challenge in separating the two design options is ensuring integrity as different signals are passed between the boards.

Figure 3-40 shows the performance of the VCO for three separate trials. This test is performed to determine the stability, repeatability, and precision of the VCO. Since the error signal tunes the VCO to adjust the frequency, the response must be precise to ensure a stable output. For this test, the VCO is individually biased and manually tuned using power supplies to determine distinct data points for output frequency and power. Although there is variation in output power, the change is indistinguishable in the insertion loss for the entire chain. More importantly, there is minimal variation in output frequency and this result qualifies this particular VCO for the design.

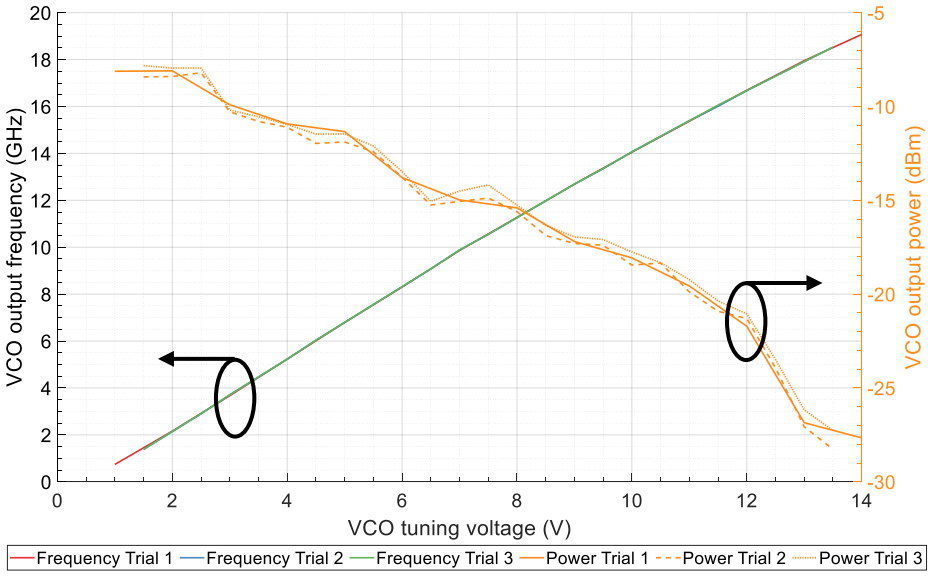

Figure 3-40: Performance of the VCO for three separate trails to determine precision

Figure 3-41 shows the output spectrum of the PLL from a test setup similar to the one in Figure 3-17. A rack mounted Arena module is used to sweep through the full pulse and a spectrum analyzer is used to measure the output spectrum. The measurement is captured on a laptop using a LabView application that communicates with the spectrum analyzer through a GPIB connection. The response is similar to the one shown in the chirp generation section, except with additional attenuation and the same gain equalizer.

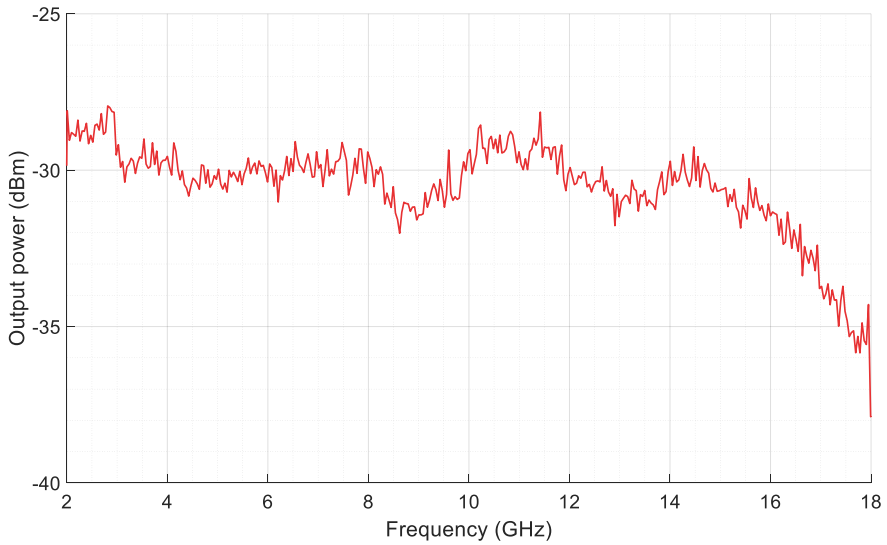

Figure 3-41: Output of the Phase-locked Loop measured with an additional 10 dB attenuation and gain equalizer as the reference chirp is swept across the full frequency band

3.3.4 Power Section

The main source of power for the radar system is the UAS's battery. It supplies +28 V but is unregulated and unfiltered. A DC-DC converter is required to regulate and filter this voltage and a linear regulator is required to step-down to the numerous required voltages. Four power boards with each one providing three distinct voltages cover the power requirements for the entire radar system. Table 3-6 lists all components that require a power source and the required voltages.

Table 3-6: List of voltage and current requirements for the radar system

Board/Placement	**Components**	**Required Voltage**	**Expected current draw**	**Power**
Radio frequency board	Voltage Controlled Oscillator, Distributed Amplifier, Divide-by-8, Synthesizer	+5 V	487 mA	2.435 W
Mixed-signal board	Active bias controllers, RF switch bias and control circuits, IF section amplifiers, Phase-locked loop components	+5 V	1086.3 mA	5.4315 W
Mixed-signal board	Loop filter/comparator	+18 V, -18 V	6.5 mA	0.234 W
Stand-alone	Phase-Locked Oscillator	+15 V	220 mA	3.3 W
Global Positioning System board	GPS module and serial transceiver	+3.3 V, +5 V	44 mA, 0.3 mA	0.147 W
Clock board	Programmable PLL and others	+15 V	290 mA	4.35 W
Stand-alone	Arena module	+28 V	600 mA	16.8 W
External	Mintbox computer	+12 V	600 mA	7.2 W
Total power consumption expected for the entire radar system				39.9 W

The MQHL-28-28S and MQHL-28-7R5S DC-DC converters by SynQor are used for both the positive and negative power boards. It is a high-reliability, high-efficiency synchronous rectifier technology designed and built for military standards. It operates at a fixed frequency and the design contains no opto-isolators. The power conversion is performed in two-stages: first, a buck-converter that retains constant output voltage; second, a transformer that provides isolation and voltage transformation. The SynQor block filters and regulates the +28 V source from the UAS battery and maintains it over any changes in current, load, or temperature. Thermal

dissipation is achieved using thermal paste underneath the component and the Aluminum frame structure.

The positive power board uses a switching buck converter and then a low-dropout (LDO) regulator, as shown in Figure 3-42. A switching converter is first used to step-down the voltage since they generally have a higher conversion efficiency and better thermal performance than a linear regulator. However, since the energy is stored in the inductor's magnetic field, it tends to be noisy. A LDO is then used in the next stage since it is able to regulate the output when the voltage difference between supply and output is very small. More importantly, the signal is cleaner since the LDO provides a steady, low-noise output without any switching. However, the excess energy is dissipated as heat and hence proper thermal management is vital. In addition to thermal paste and metal frame, the temperature of the LDOs must be monitored due to the closely spaced channels and compact board placement.

For both the switching converter and the LDO, a resistor divider network at the output sets the required voltage. An extra parallel resistor is also included for fine voltage tuning. It is important to choose the correct value of input and output capacitors, ensure high physical quality, and sufficient voltage and temperature rating. The input decoupling capacitors filter high-frequency noise and provide some damping to the voltage spike due to the lead inductance of the trace. The output capacitors "affect the steady state output voltage ripple, loop stability and the voltage over/undershoot during load current transients".

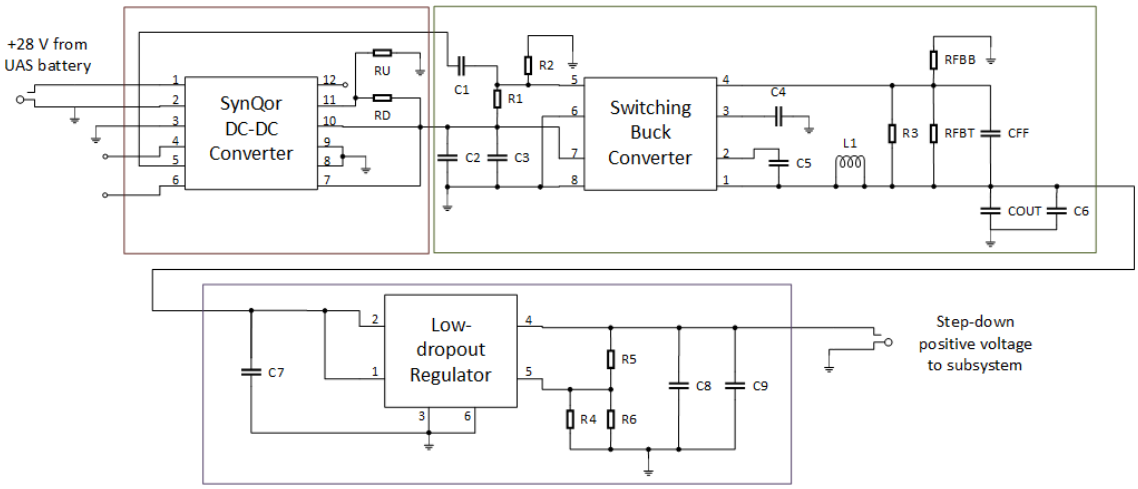

Figure 3-42: Circuit diagram of the positive voltage power board

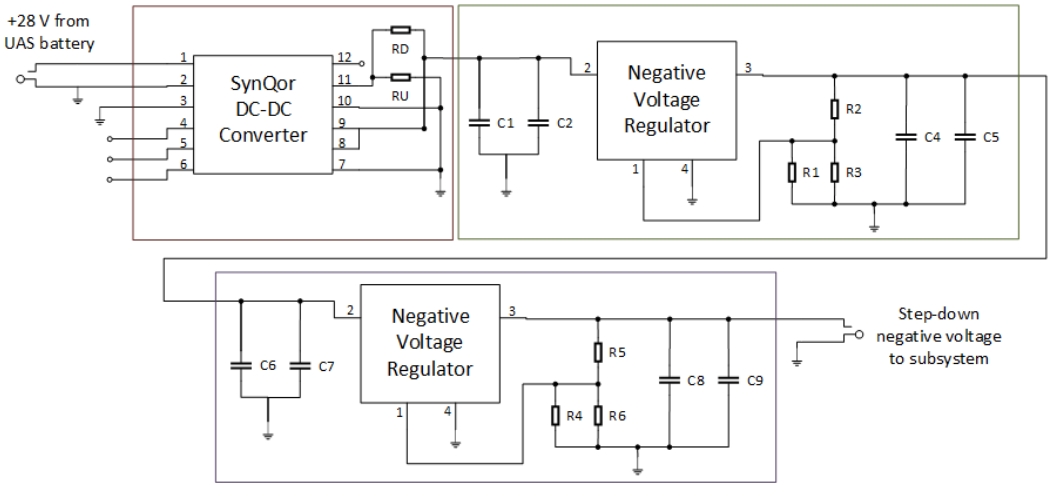

Figure 3-43: Circuit diagram of the negative voltage power board

The negative power board is designed by stepping-down the voltage in two stages using two linear regulators, as shown in Figure 3-43. This is possible since the load current requirements of the negative voltages are low and hence a switcher is not necessary. To keep the efficiency and thermal performance high, the voltage is transformed in two stages through an intermediate stage. This is done to reduce the voltage difference between the input and output, which is directly tied to the performance of the regulator. Appropriate resistor divider networks are chosen for the output of each stage to set the required voltage. Decoupling and output capacitors keep the signal clean and stable.

Figure 3-44 and Figure 3-45 shows the layouts for both boards and the individual stages highlighted. In the right subset of Figure 3-6, under the Arena module section, the picture shows the position of the connector on the chassis wall that provides +28 V from the UAS battery. Twisted-pair cables are routed from this connector on the chassis wall to the Molex input connectors on the board seen in Figure 3-46: Picture of all four power boards stacked inside the radar chassis. It also shows the three positive power boards (A, B, and C) and the negative power board vertically stacked in the radar chassis.

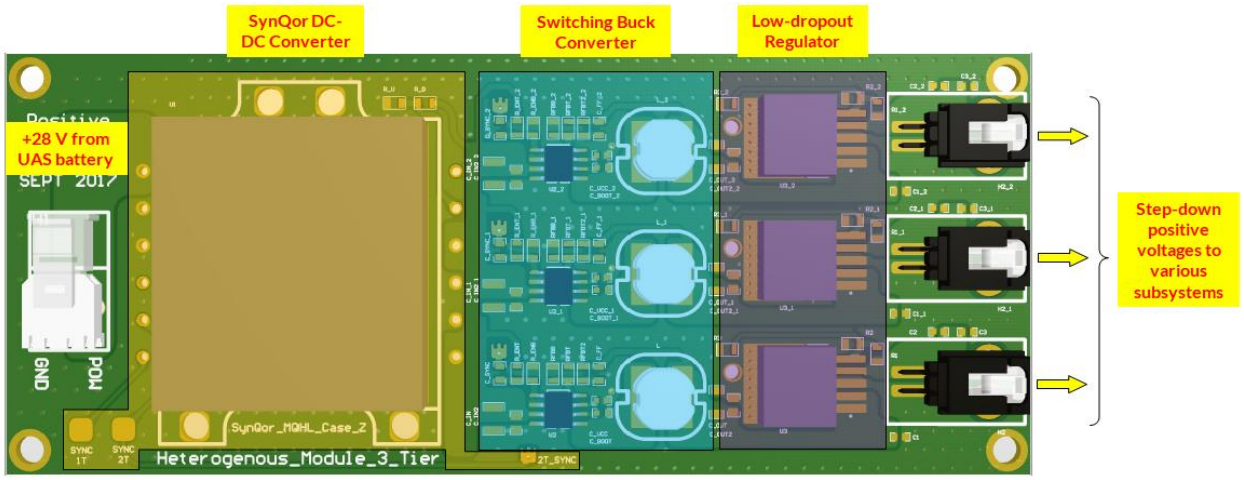

Figure 3-44: Positive board layout with individual sections highlighted

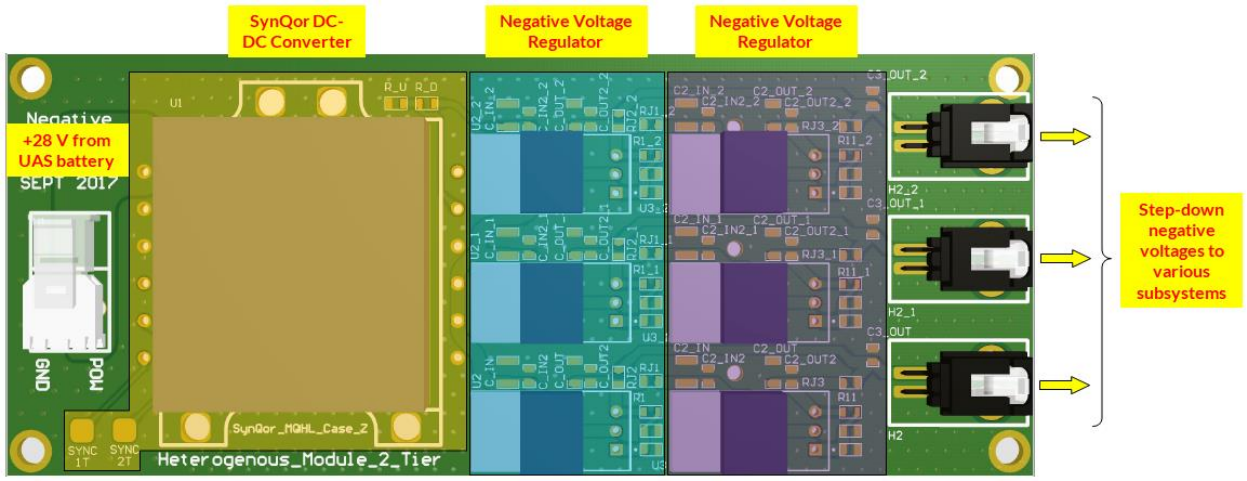

Figure 3-45: Negative board layout with individual sections highlighted

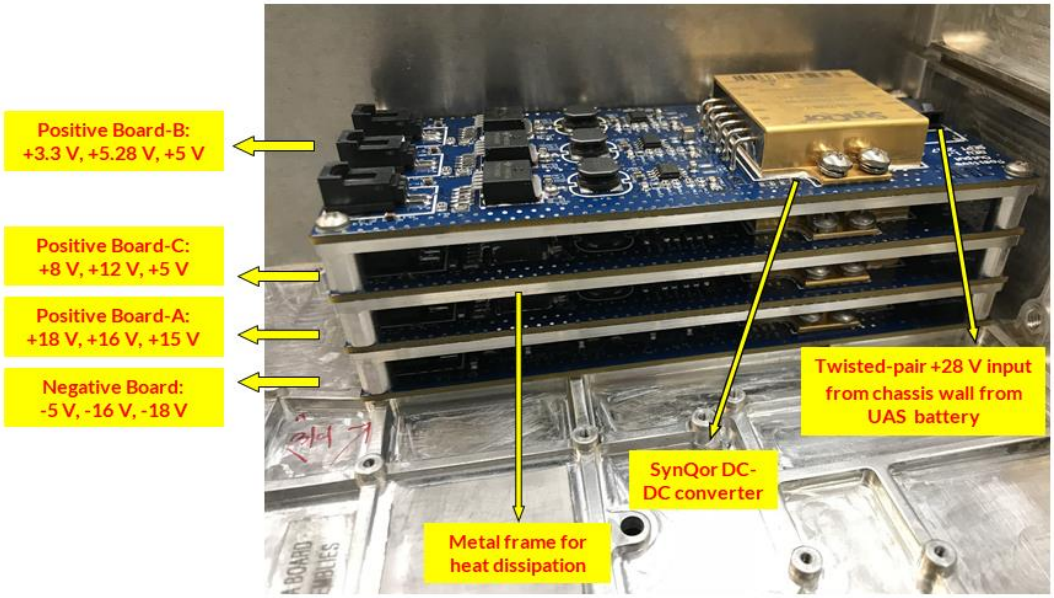

Figure 3-46: Picture of all four power boards stacked inside the radar chassis

Table 3-7: List of voltages for each power board and their performance parameters shows a list of all the voltages for each power board. It also lists the measured voltage, current, and temperature when the power boards are operational with no load and a full load. In spite of the thermal paste and aluminum frame, the total heat generated by the regulators over a long-period of time is high. In one experiment, the temperature of the regulators on one power board reached 70° C after 30 minutes with a full load. When assembled in the radar chassis together, due to the compact profile a fan would be required to assist in heat transfer. This could be a necessity since the UAS can fly for 45 – 60 minutes on a single charge and the regulators should ideally measure below 70° C for the entire duration.

Table 3-7: List of voltages for each power board and their performance parameters

			No load			Full load		
Power boards	**Req. output voltage (V)**	**Typ. load current (mA)**	**Meas. output voltage (V)**	**Temp. of switcher (°C)**	**Current drawn from supply (A)**	**Meas. output voltage (V)**	**Temp. of switcher after 5 min. (°C)**	**Current drawn from supply (A)**
Negative T2	-5	100	-5.12	34	0.13	-5.11	62	0.23
	-16	300	-15.99	35	0.13	-15.95	60	0.44
	-18	130	-18.25	36	0.13	-18.23	50	0.26
Positive T3-A	+18	130	+17.67	48	0.17	+17.64	56	0.26
	+16	570	+15.81	52	0.17	+15.75	65	0.55
	+15	510	+14.82	45	0.17	+14.75	58	0.49
Positive T3-B	+3.3	35	+3.42	33	0.08	+3.4	36	0.08
	+5.28	1200	+5.67	35	0.08	+5.35	46	0.36
	+5	805	+5.3	38	0.08	+5.04	42	0.25
Positive T3-C	+8	675	+8.28	45	0.16	+8.06	62	0.39
	+12	600	+12.19	50	0.16	+11.97	61	0.46
	+5	810	+5.26	49	0.16	+5	63	0.35

3.4 **Loop-back test**

The functioning of the entire radar system is verified through a delay line or loop-back test. The output signal from the antenna transmit connectors are fed back into the respective antenna receive connectors after passing through an optical-delay line system. This setup simulates a single point target by introducing propagation delay and looping back the same signal into the system. The RF signal is converted into the optical domain so that large propagation distances may be

simulated within a limited form factor. A custom designed fiber-optic delay transceiver is used that introduces a 1.725 µs delay and an attenuation of 26 dB.

Figure 3-47 shows the entire setup for the loop-back test. A single power supply that provides +28 V acts as the UAS battery. This is connected to all four power boards through the connector on the chassis wall. The boards in turn supply power to the merged RF and MS boards, PLO, and 10 MHz clock source. For the sake of convenience, the amplifier in the external components chain is powered using a separate power supply. The 100 MHz frequency synthesizer is powered through the USB port from a computer.

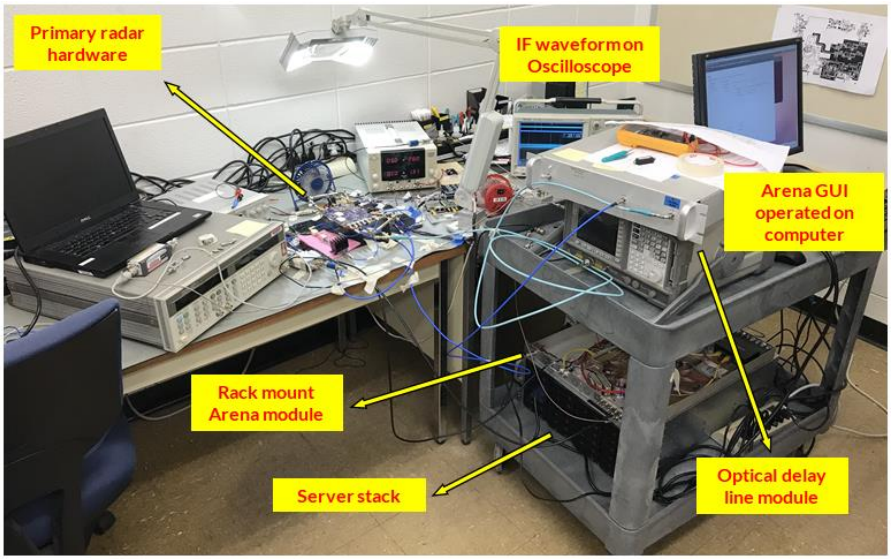

Figure 3-47: Picture of the overall delay-line test setup

This primary purpose of this test is to measure the functionality of the core part of the radar that is the merged RF and MS boards. Although most of the components belong to the actual miniaturized system, some are borrowed from other radar systems. This is done in part out of convenience but also to reduce the number of unknowns in the entire setup. Hence, a separate rack mounted Arena module is used for this test, even though the module for the miniaturized radar is already integrated into the chassis, as seen in Figure 3-48. The design and capability of both Arena modules are similar, so the performance is practically unchanged.

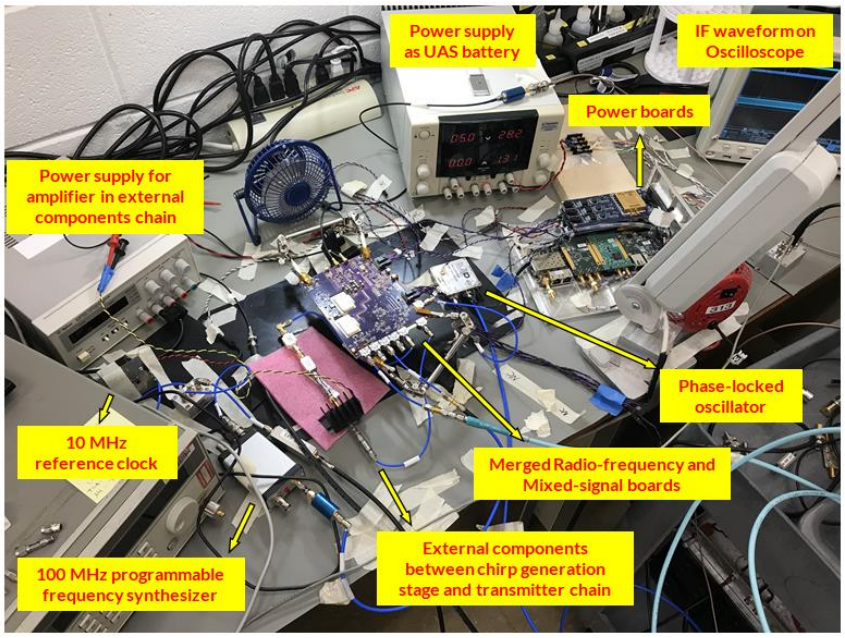

Figure 3-48: Picture of the delay-line test setup with a close-up of the individual hardware components

The IF signal is received and sampled on the MSO 4054 Mixed-Signal Oscilloscope by Tektronix. It has a maximum receive frequency of 500 MHz and samples at 2.5 GSPS. Figure 3-49 shows the transmit AWG and receive IF waveforms on the oscilloscope. The attenuation effect of the delay-line is clearly seen in the amplitude variations of the received waveform. The characteristics of a target are manifested as a change in waveform shape and the information is contained within the entire pulse. The timing of the measurement is synchronized with the AWG by triggering the oscilloscope with the Extended Pulse Repetition Interval (EPRI) signal. A square pulse is generated by the Arena module at the beginning of each transmit pulse in accordance with the PRF. The timed transmit and receive pulses are seen at the top of the oscilloscope screen in Figure 3-49.

The Fourier transform of the received IF waveform with a Hanning window applied is shown in Figure 3-50. This is the delay-line or loop-back response of the radar system. It characterizes the performance of the radar as it simulates the scattering from an ideal single target. The response of a close-to ideal radar for such a target is a narrow peak with very low side-lobe

levels. For this system, the leading-edge sidelobe level is at a relative magnitude of 14 dB. This is caused due to imperfections in the waveform and non-linearity of the chirp signal. The first trailing-edge sidelobe level is at a relative magnitude of 16.85 dB. This is caused due to internal reflections within the system. This level appears to be high for a single target response, and it may be attributed to noise from within the system and interference from other external sources. The nearly 30 dB drop between the peak and the first trailing-edge null highlights the primary requirement of a distinct, narrow peak. These parameters qualify the performance of the radar system.

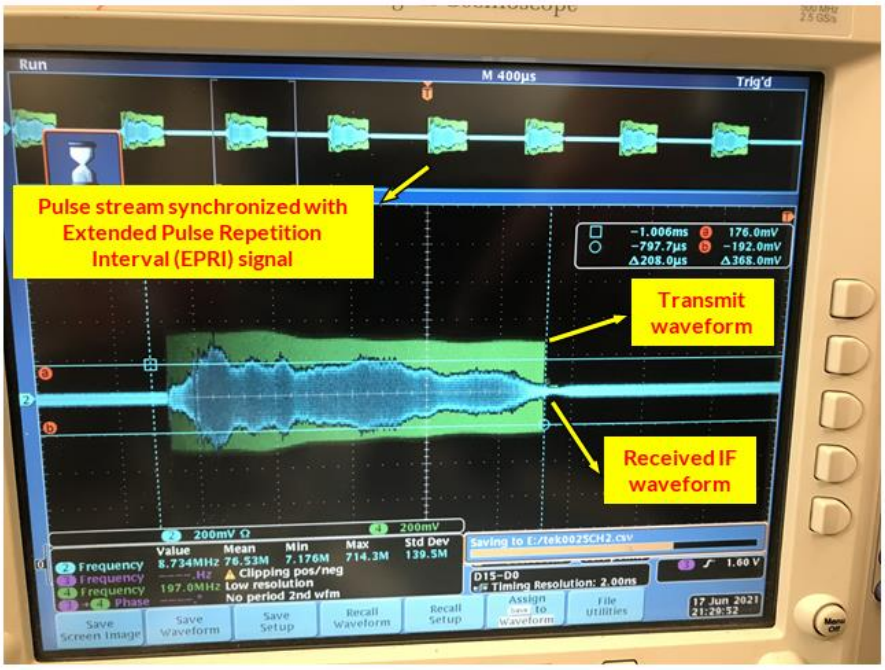

Figure 3-49: Picture of the transmit (PLL reference) and received IF waveforms on the oscilloscope

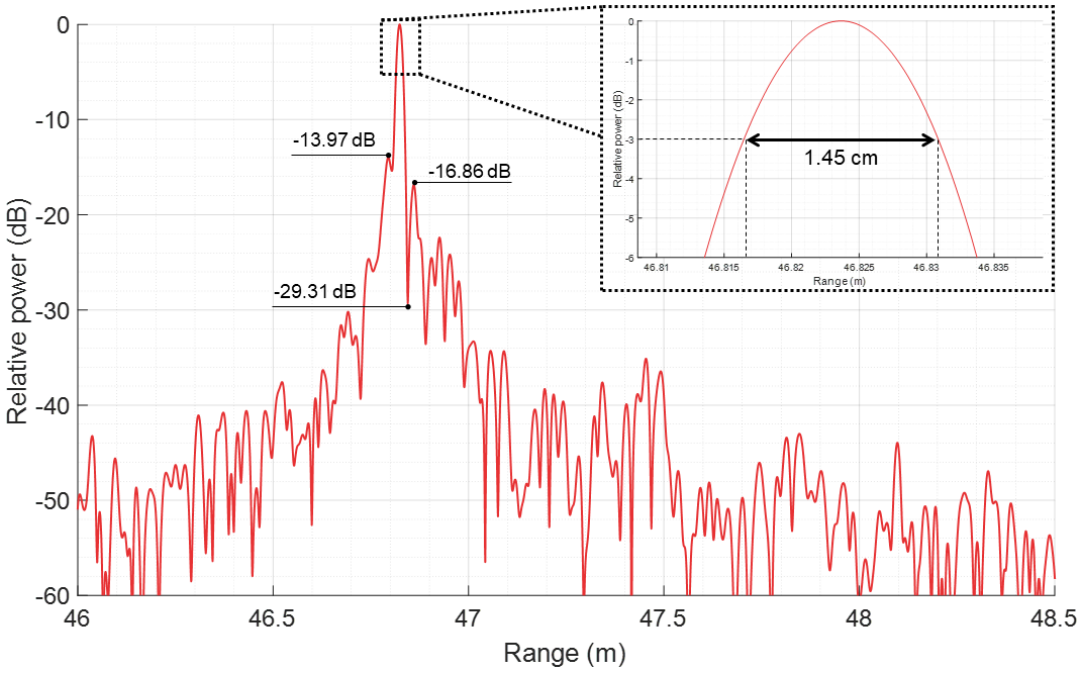

Figure 3-50: Delay-line response of the radar with inset picture showing a close-up of the main peak

The range resolution of the radar is measured at the 3 dB level of the main peak. With a Hanning window applied, the resolution is 1.45 cm. This characterizes the radar's ability to discern between two targets. When combined with the integrated bandwidth of the antenna, the resolution is further reduced due to the gain variations. Figure 3-51 shows the spectrogram of the IF pulse in linear domain. The high side-lobe levels and noise in the system may also be attributed to the Intermodulation Products (IMP) shown in in the figure.

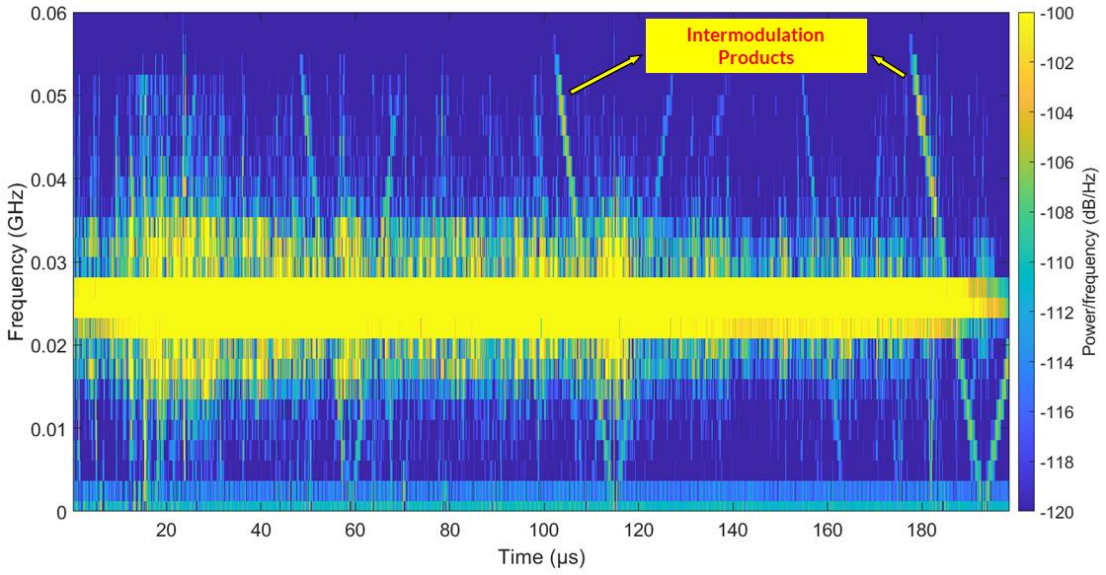

Figure 3-51: Spectrogram of the received IF pulse

4 Antenna and Feed Network

4.1 Design requirements and challenges

The design strategy for the antenna is based on two types of requirements: electrical and physical. The features of the radar system set the electrical requirements of the antenna. The antenna's bandwidth must be 2 – 18 GHz and preferably have gain with a maximum variation of 6 dB across the bandwidth. A distinct nadir-pointing main-lobe is necessary and low side-lobe levels help prevent radar clutter. A linearly polarized antenna is designed to obtain all co- and cross-polarized radar returns. Consequently, this results in four antennas for both transmit and receive. Isolation between the pair of antennas is essential in FMCW systems to ensure high receiver sensitivity [17].

The dimensions of the UAS set the physical requirements of the antenna. The radar chassis is designed to be integrated behind the battery pack in the payload tray. The two realistic options for integrating the antenna are underneath the payload tray or above the radar chassis on either side of the rotorcraft. The antenna is designed to mount underneath the tray since detailed

consideration must be given to vehicle stability when mounted on either side, closer to the main rotor.

However, this mounting mechanism defines two additional restrictions: planar and height. The surface area underneath the payload tray is physically and electrically limited to accommodate four UWB antennas. The vertical distance between the payload tray and landing surface is small due to the wide angle of the landing legs. Further, a fairing must be designed to prevent physical damage to the antennas since the carbon-fiber legs flex vertically when the vehicle lands on a hard, flat surface. Hence, the available space on the rotorcraft for a payload is the primary limitation for designing an UWB antenna.

Furthermore, due to the 4.54 kg (10 lb) payload limit of the UAS, the antenna and fairing system must be lightweight. Dielectric materials such as fiberglass and Delrin plastic are typically used for aerodynamic structures. However, the challenge is ensuring satisfactory electrical performance of the antenna with the lossy dielectrics and the (partially or fully) conducting surfaces of the platform.

4.2 **Single Element Design**

Microstrip antennas typically have a low-profile and are convenient for structural integration. The dielectric materials are lightweight and hence are suitable for UAS applications. However, they tend to have a narrow bandwidth, low gain, and significant ohmic losses. The required performance is achieved by using design strategies such as different radiating geometries, feed mechanisms, parasitic elements, matching networks, and arrays [44].

Planar microstrip monopole over a metal plate, metamaterial antennas, and dielectric resonator antennas have been explored for wideband and UWB performance [45]. Printed

monopole antennas are described specifically for low-profile integration and the performance of several geometries are discussed.

A simple circular disc is reported in [46] and the bandwidth is 2.78 to 9.78 GHz. The radiation pattern is nearly omni-directional at 3 GHz and the maximum directivity changes direction at 6.5 and 9 GHz. This is also shown in the simulated gain plot for 30°, 90°, and 150°. The bandwidth may be increased by adding notches but largely retaining the circular feature as shown in [47]. It operates from 3 to 11.4 GHz and the radiation patterns have a distinct main lobe for the frequencies shown. The gain profile may be divided into sub-bands and the trend is typical for UWB printed monopole antennas.

Other simple geometries like a planar triangular monopole [48] and a rectangular patch with a slotted ground plane [49] have reported bandwidths of 3 to 12 GHz and 2.95 to 13.95 GHz respectively. In [50], a Teflon-based substrate with dimensions 30 mm x 8 mm x 0.8 mm is reported with a bandwidth of 2.75 to 16.2 GHz. The monopole geometry is a rectangular patch but the feed line is a trident-shaped strip and a tapered impedance transformer results in the wideband resonance.

Complex geometries like fractals tend to have multiple distinct resonances with narrow bandwidth [44]. However, a combination of fractals at a high iteration number can result in a 1.9 to 16 GHz band [51]. The numerous sequential electrical lengths of every iteration resonate together at a wide range of frequencies. However, the radiation pattern of fractal antennas often shifts and the direction of directivity changes across the bandwidth.

Radiating geometries with non-linear curves like tapered exponentials and high degree polynomials typically resonate across a wide range of frequencies [44, 45]. Surfaces with monotonically increasing curved edges may be viewed as a composite of parts with incremental

electrical lengths. As the current moves across the surface, multiple successive resonators radiate together over a range of wavelengths. Radiation is caused at the curve edge from the fields generated by the surface current. A typical wideband design that utilizes non-linear curve geometry is the Vivaldi antenna.

The so-called Newton's Egg is another non-linear curve that has been explored for wideband designs [52]. The design in the paper has a bandwidth of 2.9 to 11 GHz. A rotation of the main radiation lobe is observed as the frequency increases and only the peak gain is reported. The shape is a closed geometry derived from Newton's diverging parabolas, which is the third class of equations in the classification of cubics []. The general form of this type of equation is:

$$y^2 = ax^3 + bx^2 + cx + d \tag{4.1}$$

A reduced form of this equation may be used to form the egg shape []:

$$y^2 = c(x^2 - 1)(x - b)\ , -1 \leq x \leq 1 \tag{4.2}$$

The geometry of the antenna in this work is based on the Newton's Egg shape. As discussed in [52], the Egg's curvature directly affects the bandwidth of the antenna. The optimal curvature is parametrically chosen to cover 16 GHz of bandwidth, while the whole shape is scaled-up in size to shift the starting frequency point down to 2 GHz.

The antenna is designed on a Rogers RT/duroid 5870 substrate of thickness 1.575 mm. It has a relative permittivity of 2.33 and a dielectric loss tangent factor of 0.0012. The design along with relevant dimensions are shown in Figure 4-1. Photographs of the front and backside of the fabricated antenna are shown in Figure 4-2. This antenna design will be referred to as 'bulb' in this work.

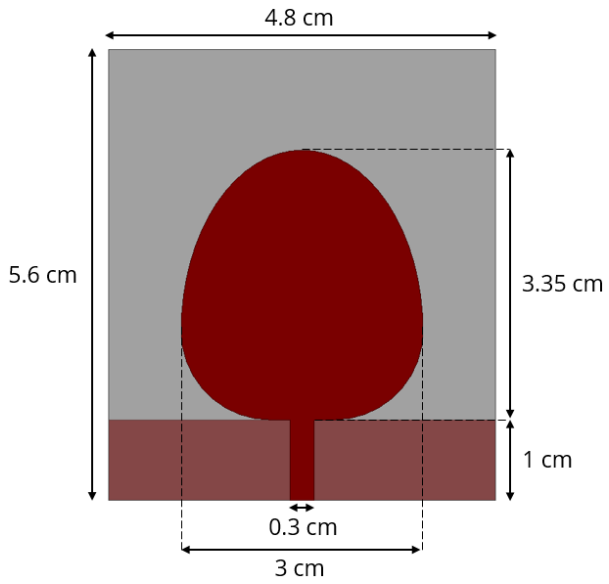

Figure 4-1: Design of the 2 - 18 GHz bulb antenna

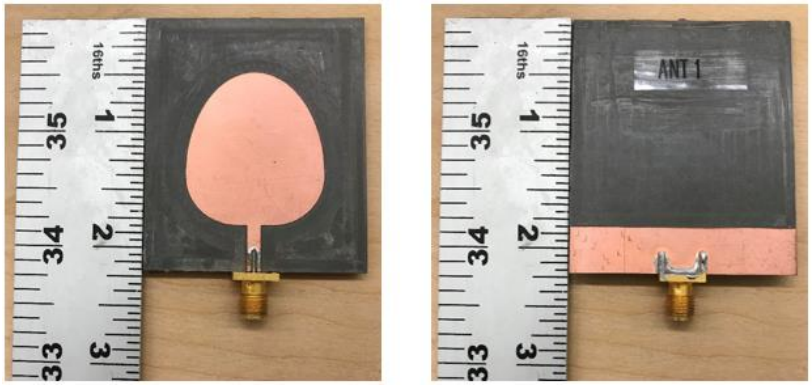

Figure 4-2: Front and backside of the fabricated bulb antenna

The length of the ground plane for the bulb antenna is equal to the feed line. This is in contrast to [52], where there is a small gap of 0.15 mm between the edge of the ground plane and the base of the Newton's egg geometry. It is stated that this resulted in optimal bandwidth since the equivalent capacitance of the gap balances the inductance of the feed line. However, the change in curvature for the bulb resulted in an optimal bandwidth with no gap

The bulb is designed using a combination of simple shapes as shown in Figure 4-3. This design method provides a unique set of degrees of freedom which results in a novel shape.

Furthermore, this method is found to be convenient when performing parametric analysis on Ansys' High Frequency Structure Simulator (HFSS) for non-linear, closed 3D surfaces.

Curve fitting is done on the bulb to analytically compare with the cubic equation derived for Newton's Egg. A ninth degree polynomial, with robust linear least squares fitting and bisquare weights, is found to have the lowest root mean squared error. The polynomial equation is shown in equation 4.3 and its goodness-of-fit statistics are shown in Table 4-1. Figure 4-4 shows a comparison of the full-scale dimensions of the Newton's Egg and the bulb curves.

$$y = ax^9 + bx^8 + cx^7 + dx^6 + ex^5 + fx^4 + gx^3 + hx^2 + kx^1 + l \quad (4.3)$$

where, $a = 0.1872, b = -0.8119, c = -0.2849, d = 1.211, e = 0.1381,$

$f = -0.8793, g = 0.0415, h = -0.1428, k = -0.1889, l = 0.8587$

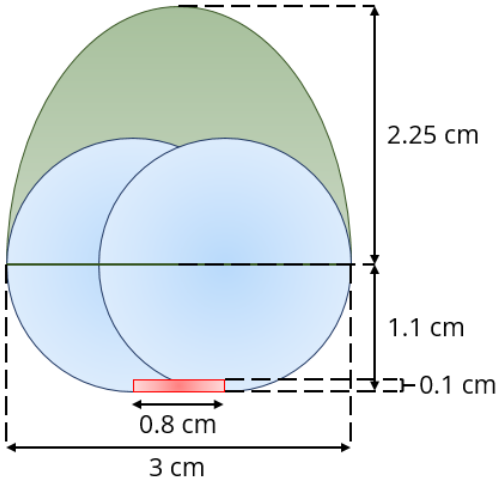

Figure 4-3: Construction of the bulb shape in Ansys HFSS for parametric analyses

Table 4-1: Goodness-of-fit statistics comparing bulb curve with the fitted ninth degree polynomial

Sum of squares due to error	0.0231
R-squared (coefficient of determination)	0.9969
Degrees of freedom in the error	191
Degree-of-freedom adjusted (coefficient of determination)	0.9968
Root mean squared error	0.011

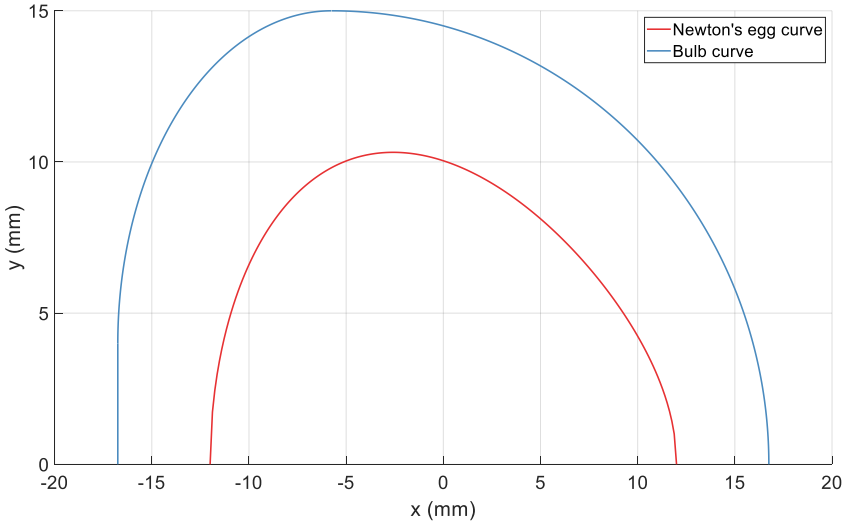

Figure 4-4: Comparison of the full-scale dimensions of the Newton's egg and bulb curves

The microstrip antenna is fabricated in-house on a LPKF Laser & Electronics PCB milling machine. Both impedance and far-field measurements are done in an anechoic chamber for the entire bandwidth. Figure 4-5 shows the return loss simulation and measurement of the bulb antenna. The simulation model has a bandwidth of 15.68 GHz and the starting frequency is 2.32 GHz. The measurement of the fabricated antenna shows a similar bandwidth but with an increase in return loss magnitude in the 2 – 8 GHz frequency range. The average difference in return loss magnitude between simulation and measurement is approximately 3.5 dB. The reduction in impedance matching at the lower frequencies is caused due to the electrically small size of the antenna. The increased reflections at 4.33 and 6.67 GHz is acceptable since the operational transmit power of 1 mW is sufficiently low.

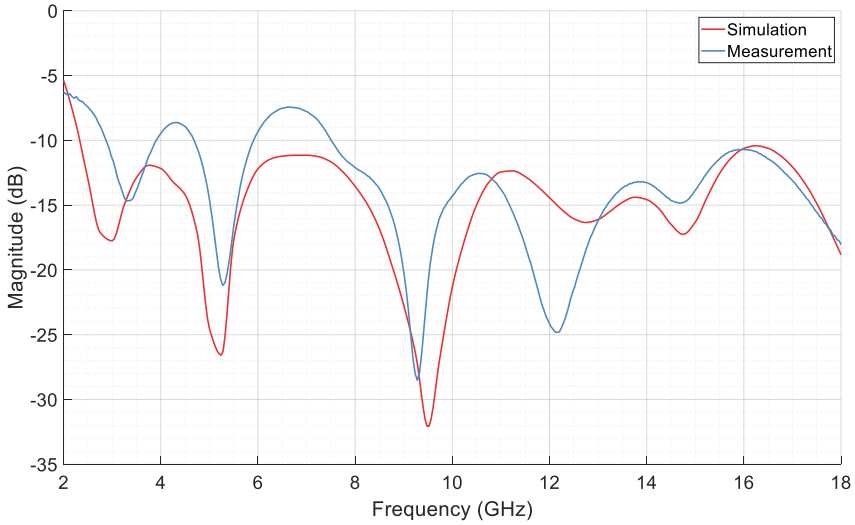

Figure 4-5: Return loss of single element 'bulb' antenna

The radiation pattern of the bulb antenna is measured using the ETS Lindgren Double-Ridged Waveguide Horn Model 3117 as the reference antenna. Figure 4-6 shows the orientation of the antenna in both the Cartesian and Spherical coordinate systems. Theta is elevation and Phi is azimuth for all far-field parameters in this document. Figure 4-7 (a) to (e) show the normalized radiation patterns for simulation and measurement at 2, 6, 10, 14, and 18 GHz respectively. The patterns show the change in magnitude of the phi component of the electric field vector for elevation angles of 0° to 360° and an azimuth of 90°.

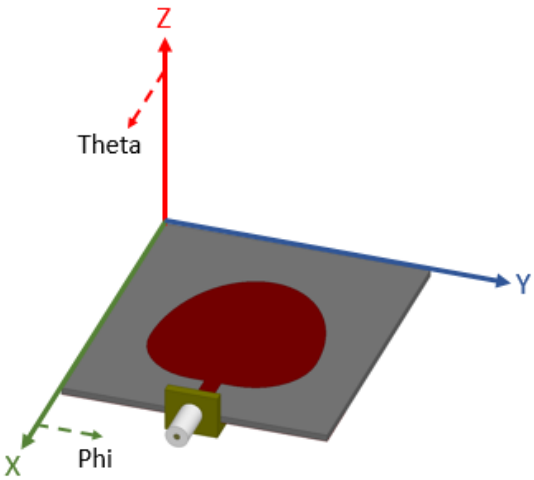

Figure 4-6: Orientation of the antenna in the spherical coordinate system

The plots in Figure 4-7 show an increase in directivity at theta = 90° and 270° in the entire frequency band. The radiation lobes are along the Y-axis and at an X-axis level close to mid-point. Therefore, to point the main beam at the target, the antenna must be integrated vertically such that the Y-axis is pointing towards nadir. This mounting mechanism reduces the ground clearance significantly and hence a fairing is required to protect the antennas. The fairing must be light due to the payload limit but strong enough to withstand vibrational loads and physical damage from the elements.

The gain at theta = 90° and phi = 90° is shown in Figure 4-8 and the surface current distribution is shown in Figure 4-9 (a) to (e). There is an increase in the gain trend across the frequency band, as indicated by an increase in directivity in the pattern plots. However, there are nulls at three distinct frequency points. The magnitude at 5, 10, and 15.75 GHz for simulation is -17.24, -10.34, and -0.61 dB. The magnitude at 5, 10, and 15 GHz for measurement is -12.78, -6.12, and -7.12 dB. The half-wavelength values at the respective frequencies are approximately 29.98, 14.99, and 9.99 mm and the length of the perimeter of the bulb shape is 99.05 mm. Therefore, the perimeter is 3.3, 6.6, and 9.9 times the respective half-wavelengths.

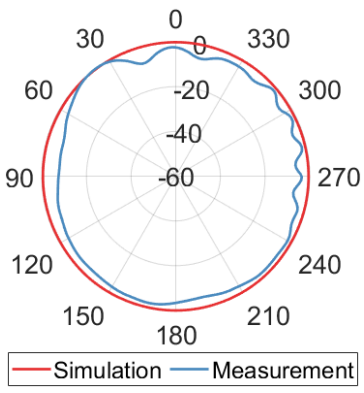

(a)

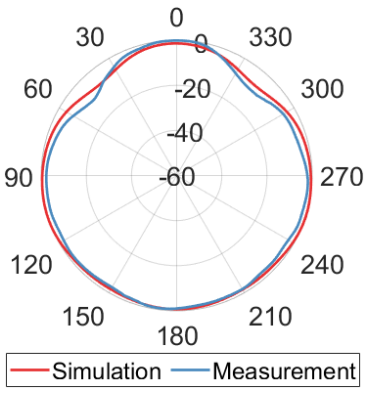

(b)

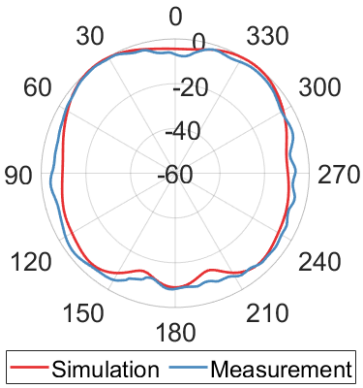

(c)

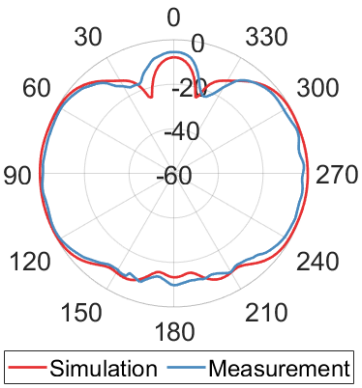

(d)

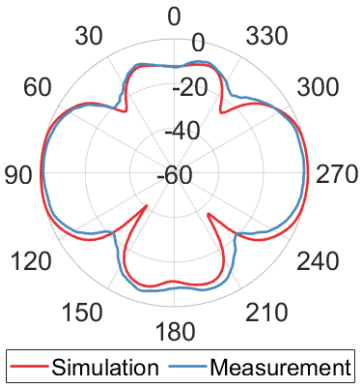

(e)

Figure 4-7: Radiation pattern of bulb antenna at (a) 2 GHz, (b) 6 GHz, (c) 10 GHz, (d) 14 GHz, and (e) 18 GHz

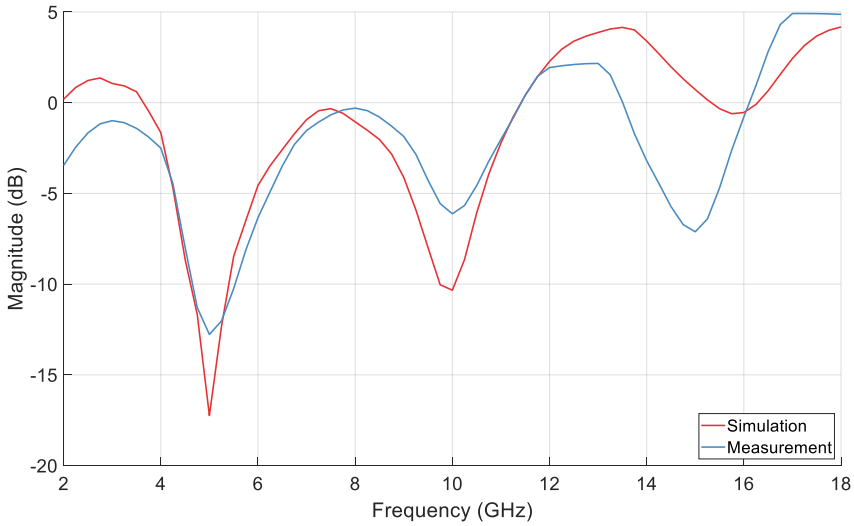

Figure 4-8: Gain of bulb antenna at phi = 90° and theta = 90°

Radiation arises at the edge of the bulb shape due to the surface currents, as seen in Figure 4-9 (a) to (e). The electrical shape may be interpreted as a loop, starting from one point of the feed-line to the other. Therefore, the radiator is a half-wavelength loop or folded-dipole at 99.05 mm. The number of peaks and nulls for the current distribution depends on the value of the multiple of the operating wavelength. This is indicated by the change in number of current hotspots along the edge of the bulb in Figure 4-9 (a) to (e).

Typically, odd multiples of half-wavelength loop and folded-dipole antennas result in a null at the mid-point of the antenna. Due to the asymmetry of the bulb curve, the null is at the widest point of the bulb and is along the nadir axis when the antenna is oriented vertically. Thus, there is a decrease in gain at the frequency multiples along the nadir direction.

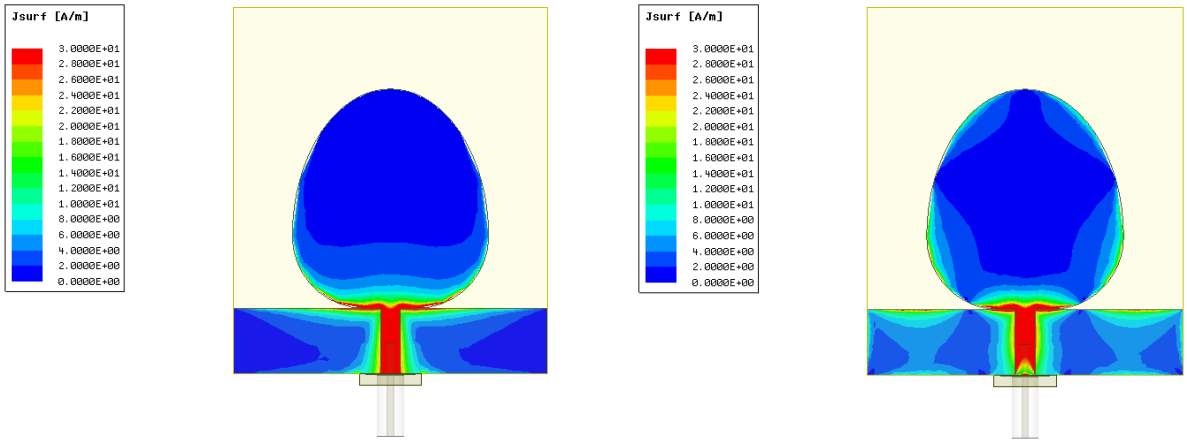

(a) (b)

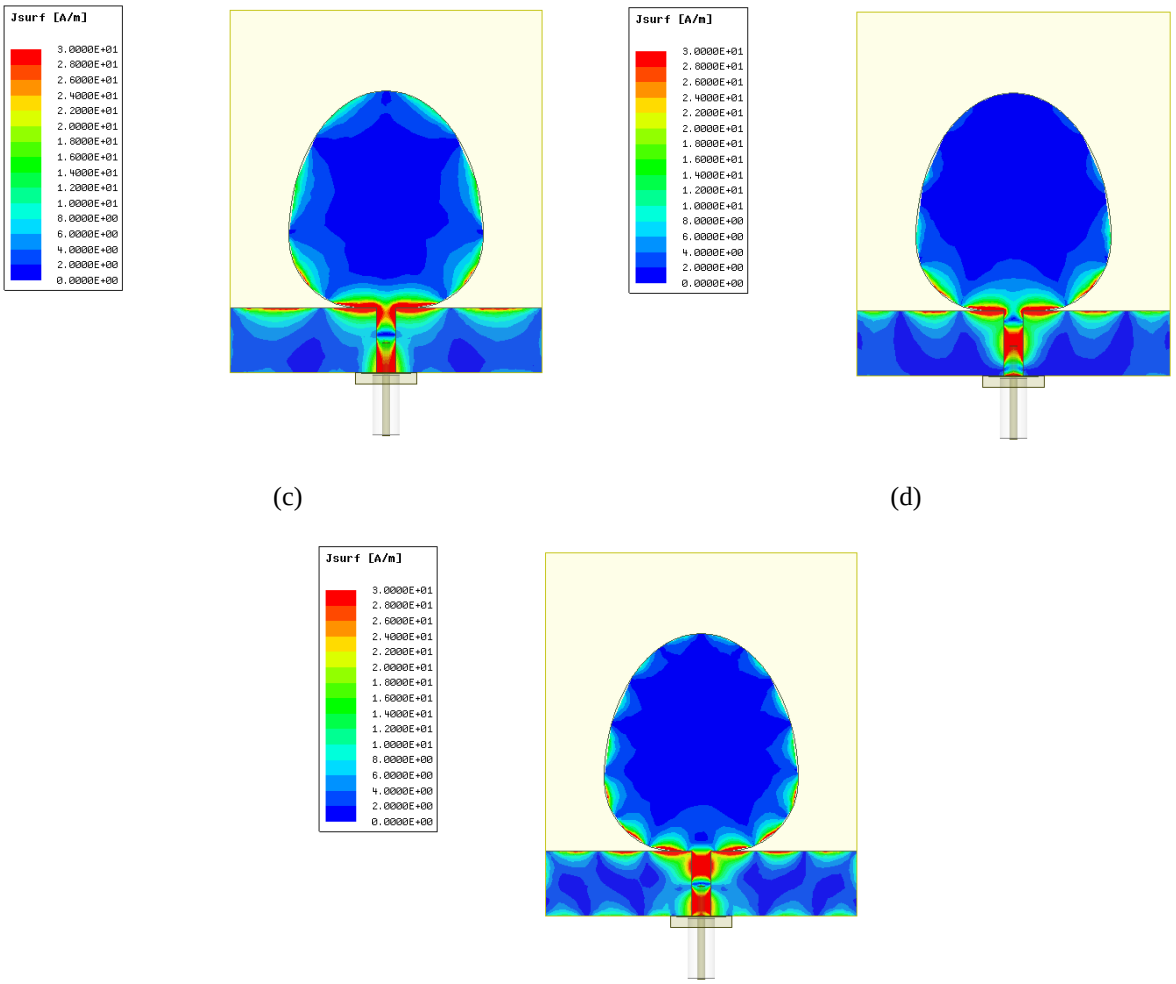

Figure 4-9: Surface current distribution of bulb antenna at (a) 2 GHz, (b) 6 GHz, (c) 10 GHz, (d) 14 GHz, and (e) 18 GHz

The nulls at specific frequencies is unavoidable since a single monopole radiator is responsible for the ultra-wideband resonance. The wavelength across the bandwidth changes from 150 mm to 16.66 mm. This wide range inevitably results in distinct odd-multiples of the bulb perimeter. To improve the gain at these frequency points, the antenna is grouped to form an array and this is discussed in the next section. The performance of the array relative to the radar system is assessed based on the average nadir gain across the entire frequency band. The average gain of the single element simulation is -1.37 dB and the measurement is -2.17 dB.

The oscillating change in gain across the frequency band translates to variations in signal power within the pulse. This can cause problems in the frequency down-conversion process as discussed in the previous chapter. It can also hinder in interpreting target information during post-processing. To overcome these problems, sub-band processing is used where the radar returns are analyzed over discrete bands within the overall bandwidth [53 - 56]. This is discussed further in Chapter 5.

Antenna designs for UWB applications often report the variation of peak gain across the bandwidth [46 - 52]. This parameter indicates the maximum total gain at a single frequency point across all elevation and azimuth angles. The spherical coordinates are not defined for peak gain since the angle of maximum directivity may be different for each frequency point. Figure 4-10 shows the simulated total peak gain for the bulb antenna. However, this parameter is not useful in determining the performance of the antenna for radar applications. Since the main beam is required to point towards the target for the entire bandwidth, the gain at a single direction indicates the true performance. Hence, Figure 4-8 shows the antenna's capability for radar applications and Figure 4-10 for general purpose UWB applications.

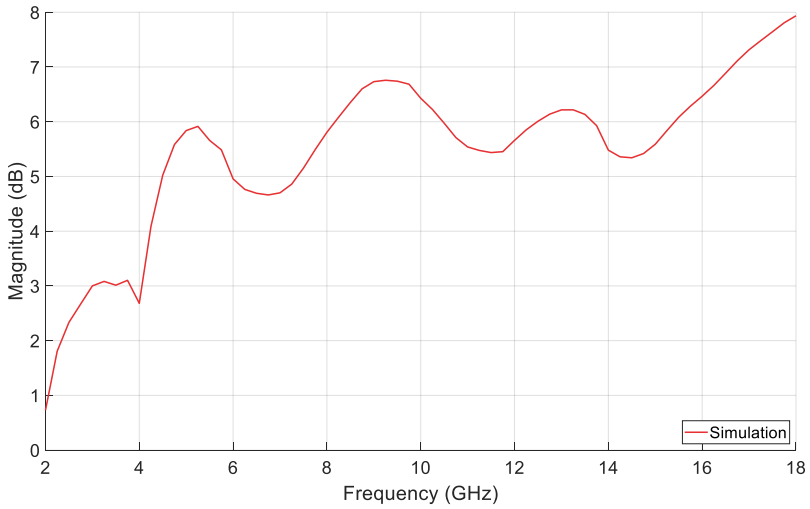

Figure 4-10: Total peak gain of bulb antenna

The axial ratio across the bandwidth at theta = 90° and phi = 90° is shown in Figure 4-11. The ratio of the x- and y-components of the electric field indicate the polarization of the radiated wave. The polarization is circular when the components are equal. The theoretical axial ratio is 0 dB, while the practical reference is typically considered at 3 dB. A large axial ratio magnitude indicates linear polarization and practically the reference is typically considered at 10 dB. Therefore, the polarization of the antenna at nadir is linear except between 9.4 – 10.1 GHz and 15.8 – 17.5 GHz. Consequently, the polarization loss increases as the axial ratio decreases between those frequency points and it degrades the backscatter power from the target. However, the effects are minimized if the gain value at that frequency point is sufficiently high.

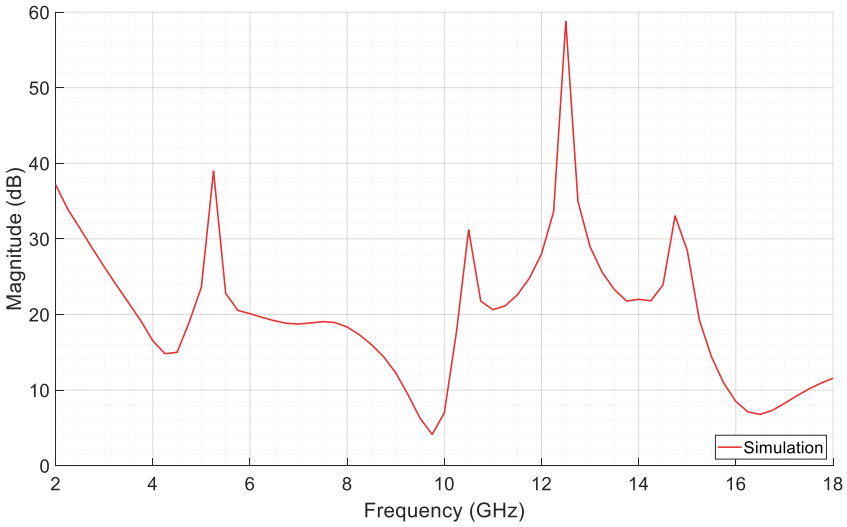

Figure 4-11: Axial ratio of bulb antenna at phi=90° and theta=90°

4.3 **Array Design**

The chief deficiency of the bulb antenna is the low magnitude of gain at phi = 90° and theta = 90°. The measured value is less than 0 dB for 2 to 11.5 GHz and 13.5 to 16 GHz. While the effect of the variation in magnitude can be diminished, the absolute value is insufficient to satisfy the system link budget. In section 3.2, the gain of a standard wideband horn antenna is used to compute the link budget. The horn antenna has a gain varying from 5 to 12 dB and an average gain

of 10.31 dB. Therefore, the value of the average gain for the bulb antenna is targeted to within 3 dB deviation of the horn antenna.

A total link budget deviation of 6 dB from both transmit and receive antennas is acceptable. Based on the link budget analysis, an approximate receiver gain of 35 dB is sufficient to detect typical soil states. From the previous chapter, the measured average receiver gain for both channels is approximately 43 dB. Therefore, the targeted average antenna gain deviation is within the 8 dB margin.

To increase the gain, multiple bulb antennas are oriented vertically and arranged in groups with uniform spacing between them. The salient factors of an antenna array are the number of elements and the distance between the elements. The design strategy is guided by a compromise between the electrical performance and ease of integration. The optimal array design, after several parametric analyses, is four elements with a spacing of 25 mm. The ratio of the wavelength to the elemental distance is 1/6 at 2 GHz, 5/6 at 10 GHz, and 3/2 at 18 GHz. Figure 4-12 shows an array of four bulb antennas with both the Cartesian and Spherical coordinate systems.

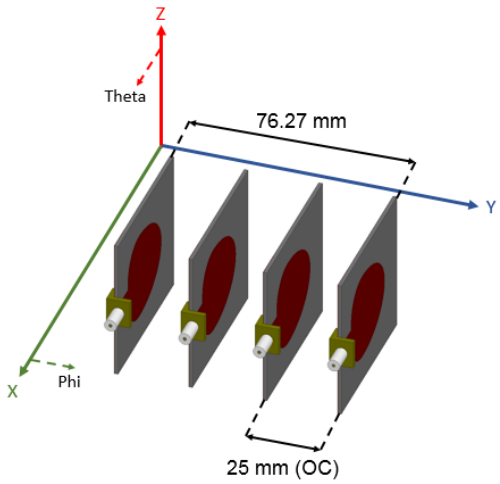

Figure 4-12: Four-element bulb array

The antenna array is grouped and mounted together using a cage-like structure made of a dielectric material. Delrin acetal resin, a crystalline plastic, is used due to its favorable electrical

and mechanical properties. It has a dielectric constant of 3.7, dissipation factor of 0.005, and material density of 1.42 g/cm^3. The plastic is suitable for UAS applications due to its high tensile strength and high fatigue endurance.

Figure 4-13 shows the antenna array and the Delrin mounting structure. The structure is designed based on antenna performance and the structural loads. The electrical performance is affected by the dielectric material and hence minimal material usage is preferable. On the other hand, sufficient material is required to ensure that the mounting structure can handle the vibrational loads of the UAS.

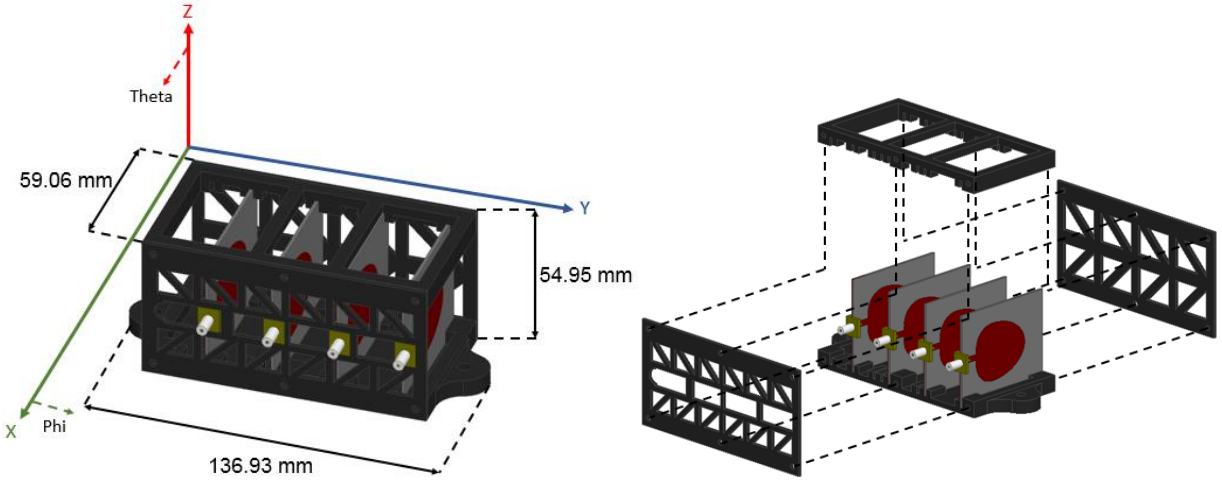

Figure 4-13: Four-element bulb array with Delrin fixture (left) and an exploded view of the array with the fixture (right)

A balance between the two requirements is achieved by removing the dielectric material at specific areas. The lid has large gaps to accommodate the main radiation lobe since the top face would be pointing at nadir when integrated on the UAS. The thick vertical strips of dielectric are designed to handle the loads of the UAS. Similarly, the material on the walls are removed in a pattern to provide support to the structure. The lid and the base have slots for the four bulb antennas to slide in. The whole structure is boxed and held together using screws. The base also has two

semi-circular extensions on either side that are used for platform integration. The fabricated antennas within the Delrin fixture is shown in Figure 4-14.

Figure 4-14: A picture of the fabricated four element array within the Delrin fixture

The mounting structure affects the impedance matching of the array through dielectric loading. The dielectric material around the bulb antennas have a capacitive effect, increasing the Q-factor. Hence, the return loss trend shifts down in frequency. Figure 4-15 shows the differences in simulated active return loss with and without the Delrin fixture. Active return loss indicates the magnitude of the reflected wave at an element, subtracted by the mutual coupling with every other element.

The dielectric loading also affects the radiation characteristics of the antenna. Figure 4-16 (a) to (e) show the simulated radiation patterns at 2, 6, 10, 14, and 18 GHz for the four-element array with and without the Delrin fixture. The dielectric losses in the reactive near-field of the antenna array increase the side-lobe levels. This interference is not a cause of concern since the increased side-lobes are present at a large angle away from the main lobe.

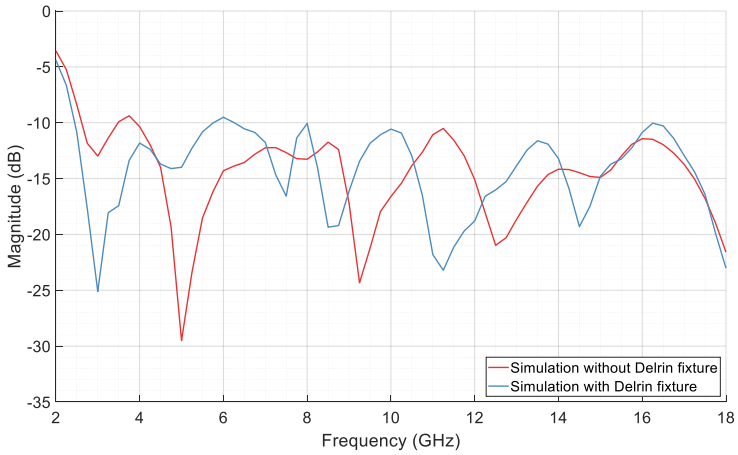

Figure 4-15: Active return loss of the four-element array

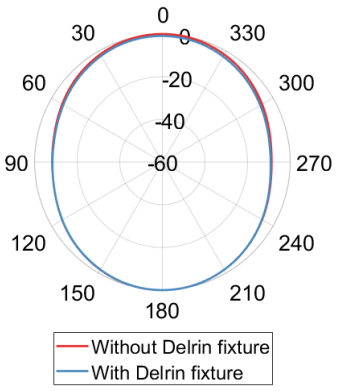

(a)

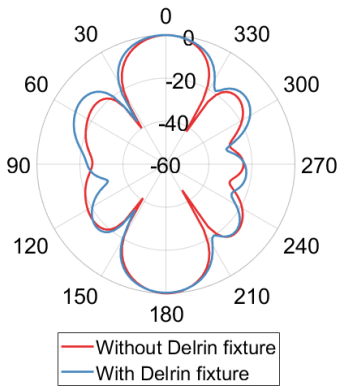

(b)

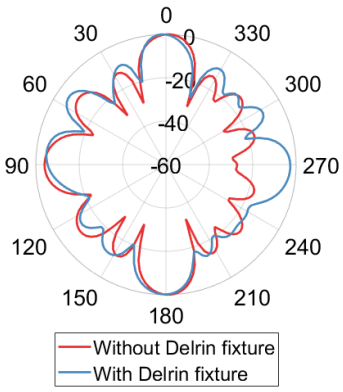

(c)

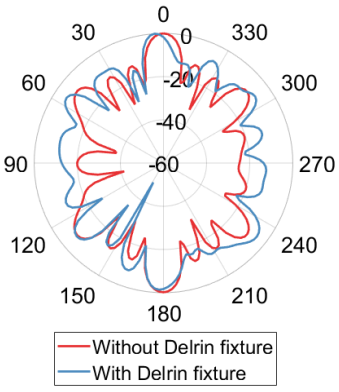

(d)

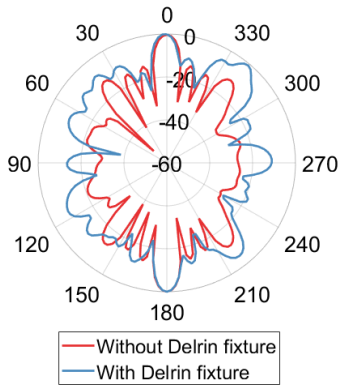

(e)

Figure 4-16: Radiation pattern of four element array at (a) 2 GHz, (b) 6 GHz, (c) 10 GHz, (d) 14 GHz, and (e) 18 GHz

A four-element array is constructed from a single element by doubling the antenna size twice. Consequently the gain of the antenna is theoretically increased by 6 dB. However, since the physical distance between the elements is fixed and the electrical distance varies over a wide range, the change in gain is not uniform across the bandwidth. Figure 4-17 shows the gain of the four element array at phi = 90° and theta = 0°.

A vital change from the single element is an increase in gain at the frequency nulls. The magnitude at 5, 10, and 15 GHz for without the fixture is -2.66, 1.35, 7.72 dB and with the fixture is -0.61, 5.34, and 10.16 dB respectively. The frequency of the three nulls appear to have shifted slightly but this is only apparent due to the coarse sampling of the data points. The four element array (without the fixture) does produce another null at 11.5 GHz. When the data is sampled at a finer rate, the null is likely closer to 12 GHz since the wavelength is almost equal to the distance between the elements. The array factor results in grating lobes for this element separation and decreases the magnitude of the main lobe.

The effect of the dielectric material shifts-down the frequency of the nulls that are present from 8 to 18 GHz and also significantly changes the absolute value. However, there is minimal change in gain from 2 to 6 GHz, except the magnitude of the null at 5 GHz. The dielectric losses

affect the radiation efficiency when the wavelength is less than the height of the fixture. The wavelength for 6 to 18 GHz ranges from 49.97 to 16.66 mm, while the height of the fixture is 54.95 mm.

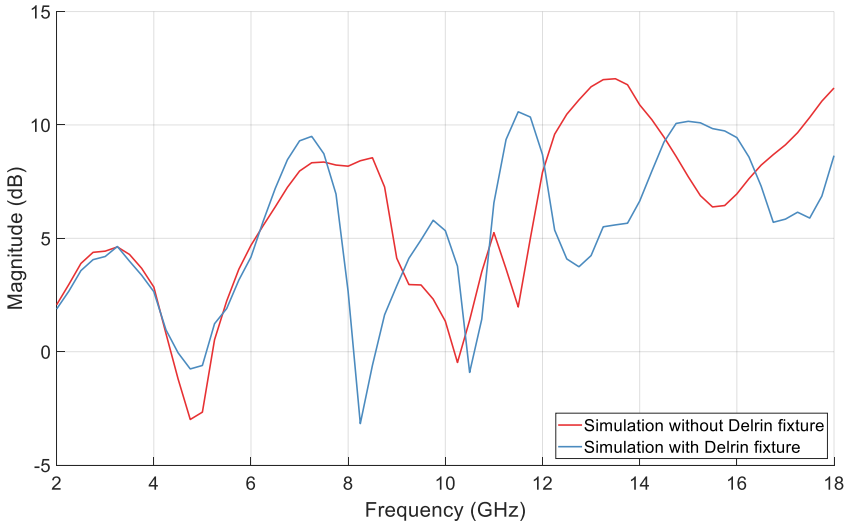

Figure 4-17: Gain of the four element array at phi = 90° and theta = 0°

The average gain of the simulated array without the Delrin fixture is 5.27 dB and with the fixture is 6.05 dB. The value of the latter is less than the targeted minimum average gain of 7.31 dB, which is the 3 dB deviation from the average gain of the horn antenna. However, the requirement of further tuning is determined after accounting for the effects of the platform and the mounting mechanism and this is discussed in Section 4.5. Figure 4-18 shows the peak gain of the array and Figure 4-19 shows the axial ratio at phi = 90° and theta = 0°.

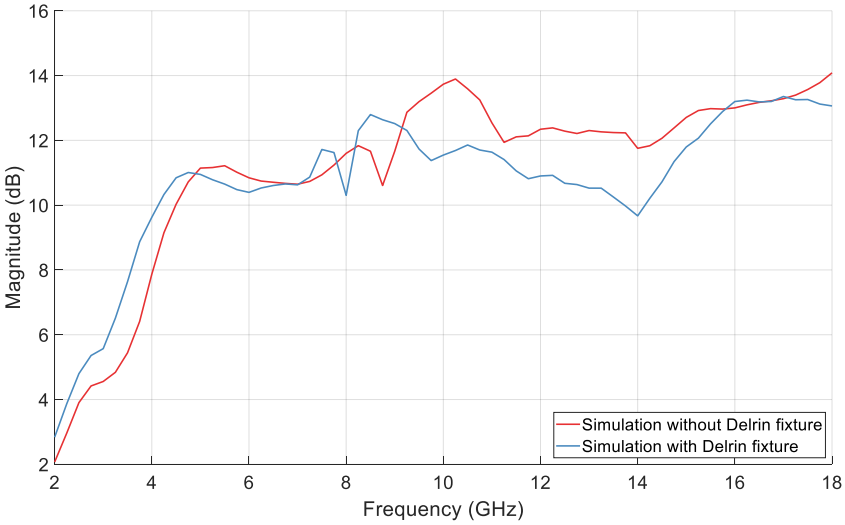

Figure 4-18: Peak gain of the four element array

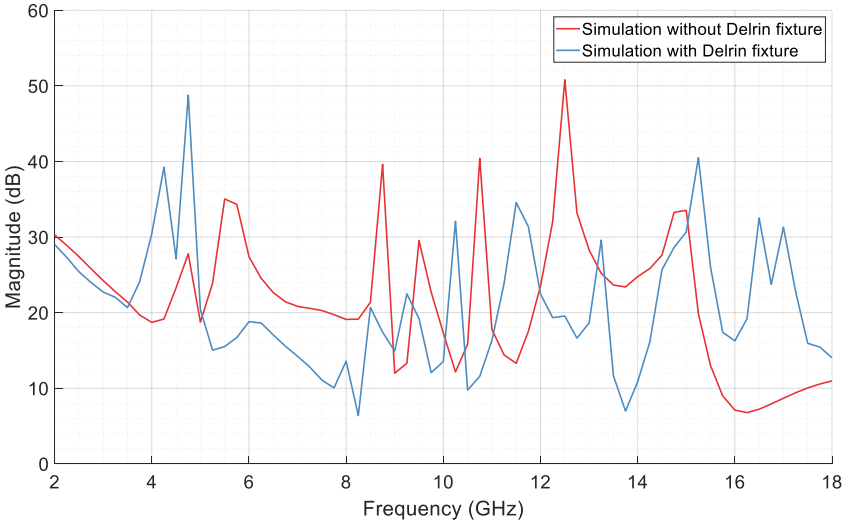

Figure 4-19: Axial ratio of the four element array at phi = 90° and theta = 0°

4.4 **Feed Network**

Two radar channels on transmit and receive connect to the four antennas and each channel is fed to a four-element array. A feed-network or power divider is required to feed all four elements of the array. Two crucial characteristics of a power divider are the magnitude of power division

and the phase shift across each branch. Each antenna element must be fed with equal power and the signals must arrive in-phase to achieve the required radiation pattern. A difference in input power causes a change in the pattern shape and side-lobe levels. A phase difference causes a change in the angular position of the lobes.

The power divider is custom designed and manufactured in-house due to the size and weight constraints of the UAS. Most commercial power dividers that cover the 2 to 18 GHz range are either too heavy or too expensive. Moreover, the general purpose enclosures are not suitable for mounting on the UAS and custom adapters would have to be designed.

The feed-network is based on a Wilkinson power divider. The methodology was developed by Seymour Cohn as a three-port TEM-mode hybrid and the derivation of the model is described in [57]. The design of the divider has been reported in [58] along with the important design parameters and simulations. This section primarily describes the final 1:4 implemented design and means of integration.

The circuit diagram of the three-port hybrid is shown in Figure 4-20. The input and output resistors with value ‘Zo’ denote the characteristic impedance and is equal to 50 ohm. The values of the resistors for the 2 to 18 GHz hybrid are listed in Table 4-2. The 1:2 hybrid shown is cascaded with two other sections at each output port to form the 1:4 power divider.

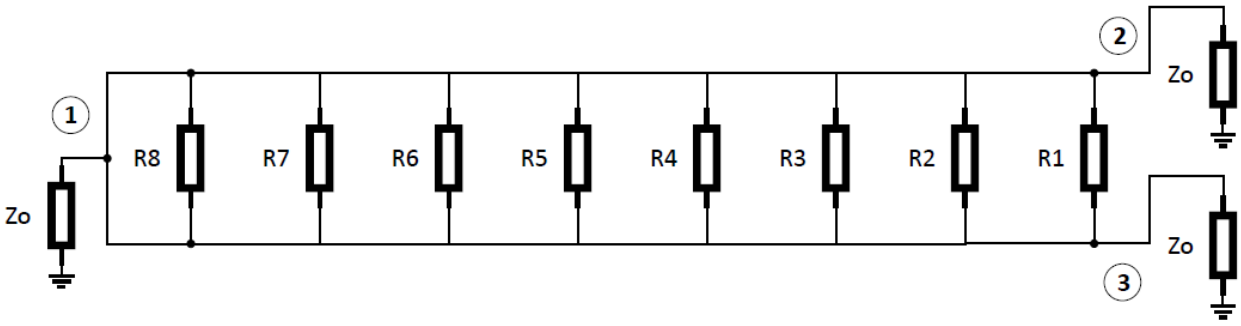

Figure 4-20: Circuit diagram of the three-port hybrid with eight resistor sections

Table 4-2: List of resistor values for the 2-18 GHz three-port hybrid

Label	Resistor value (ohms)
R1	680
R2	360
R3	500
R4	360
R5	240
R6	160
R7	750
R8	300

A layout of the microstrip five-port hybrid or 1:4 power divider design is shown in Figure 4-21. The substrate is Rogers RT/Duroid 5880 with a thickness of 0.508 mm. It has a dielectric constant of 2.2 and a loss tangent of 0.0009. The surface mount, thick film resistors in each 1:2 hybrid section are connected to each other via semi-circular traces. The length of each trace between a pair of resistors is approximately equal to quarter-wavelength at 10 GHz. The mid-frequency point is chosen to balance the insertion loss across the band.

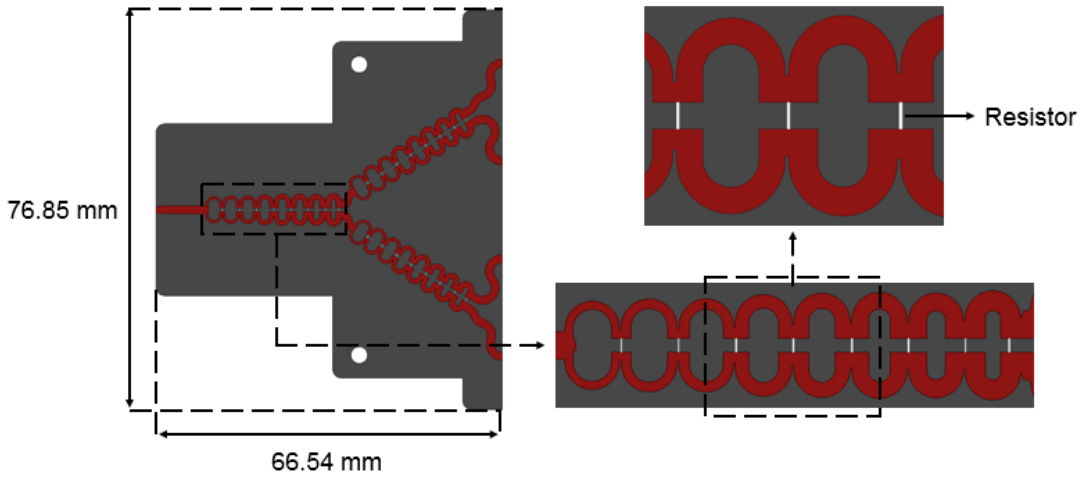

Figure 4-21: Layout of the microstrip five-port hybrid/1:4 power divider

The power divider is placed inside a custom designed Aluminum enclosure and the dimensions are shown in Figure 4-22. The ground plane of the power divider is coated with a thin layer of silver epoxy [59] to ensure electrical continuity. The substrate is screwed down into the enclosure to prevent warping due to the small thickness. Figure 4-23 shows pictures of the fabricated and assembled power divider. The two holes on the walls of the enclosure near the mid-point of the power divider are used for platform integration.

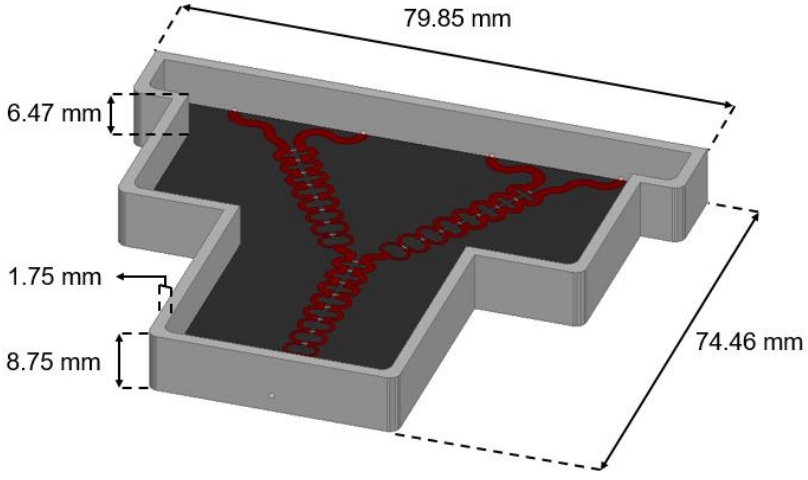

Figure 4-22: Isometric view of the power divider and Aluminum enclosure model

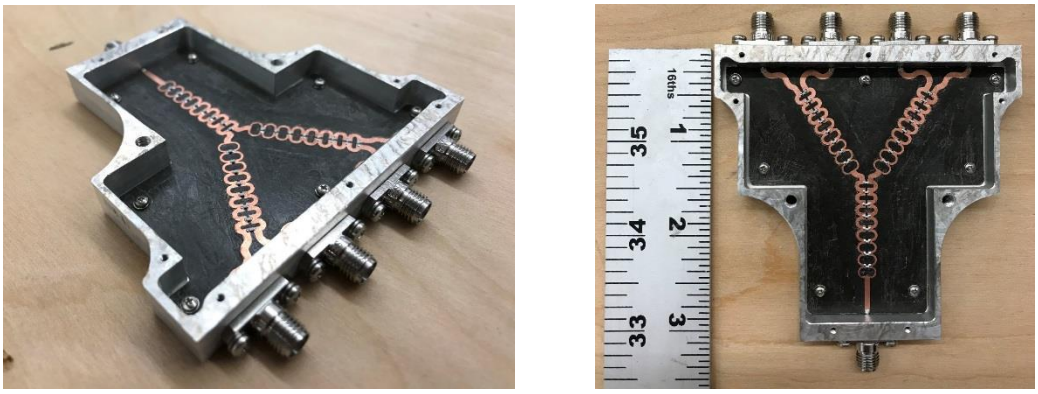

Figure 4-23: Pictures of the fabricated 1:4 power divider

The primary factors for the Aluminum enclosure design is the size and weight. Four antenna arrays require four feed networks, therefore a low-profile is necessary. Furthermore, the components must be positioned appropriately to ensure proper balance for stable flight. It is also crucial to account for the size and weight of the coaxial cables between the arrays and feed networks.

The height of the enclosure is determined based on the margin required to accommodate the connectors. This results in a total height of 8.75 mm and the height between the substrate the lid is 6.47 mm. While the dimensions of the enclosure are catered to the physical requirements, the internal gap between the substrate and the lid has an effect on the electrical performance. When the lid is closed and the enclosure is completely sealed with fastened screws, it results in a noisy response of the transmission parameters. This is due to multiple internal reflections from the fringing fields caused at the edge of the microstrip traces. After performing multiple tests using the VNA, it was determined that the top must not be completely sealed and a small gap is necessary for ideal performance.

The simulated and measured s-parameters are shown in Figure 4-24 and Figure 4-25 respectively. Port 1 refers to the single, input connector that connects to the radar channels. Ports 2 to 5 refer to the four, output connectors that connect to the antenna array elements. The simulated

transmission parameters are at the 6 dB level since the signal power is equally divided twice (3 dB for each division). The measurement largely follows this level from 2 to 10 GHz but the insertion loss gradually increases from 10 to 18 GHz and the maximum value is approximately -7.5 dB. The measured return loss is satisfactory across the full bandwidth except for a slight mismatch at 10.86 and 17.02 GHz. The mismatch is not a cause for concern since the increase in return loss is approximately 1.5 dB and only covers a few KHz of frequency points.

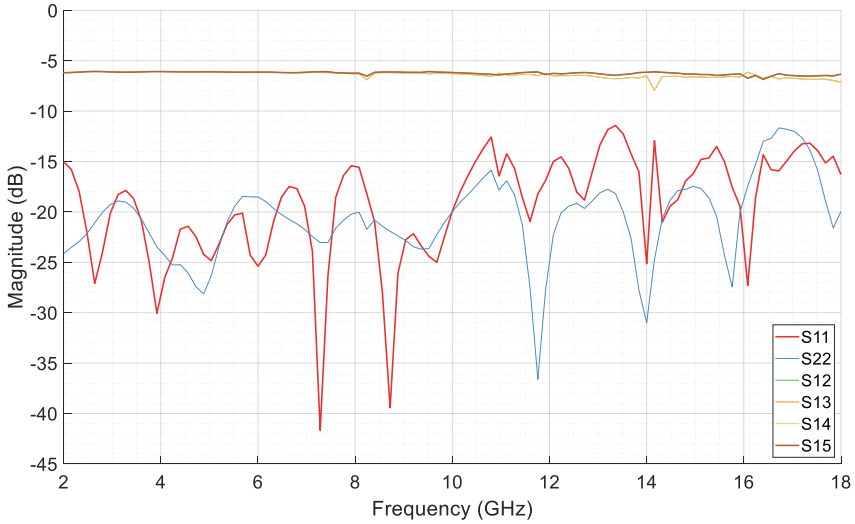

Figure 4-24: Simulated s-parameters of the 1:4 power divider

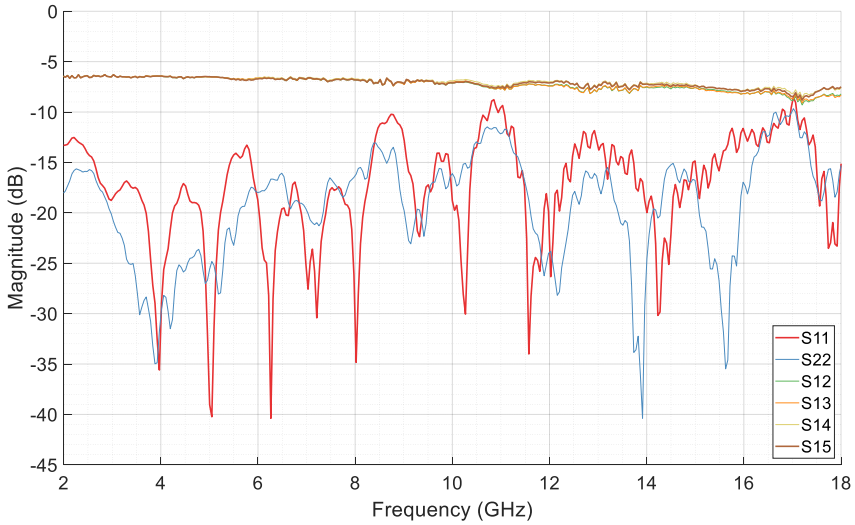

Figure 4-25: Measured s-parameters of the 1:4 power divider

The measured phase imbalance between each channel is shown in Figure 4-26. The channel connecting ports one and two is considered as reference and the phase of the other channels are subtracted from the reference. This indicates the phase difference between each channel and the plot shows the deviation across the bandwidth. The maximum imbalance occurs at 17.52 GHz and results in an angular change of 0.079°. The extremely low value of measured phase difference shows that the signals arrive at the antenna elements in-phase.

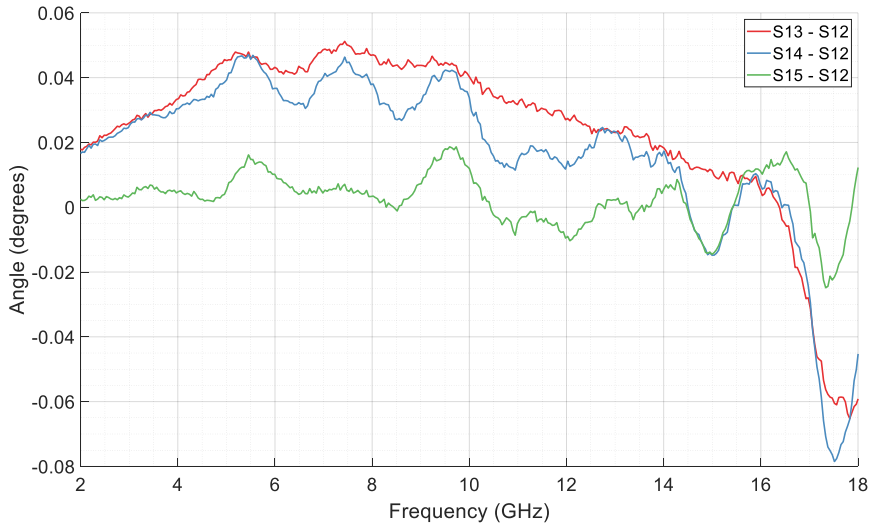

Figure 4-26: Measured channel-to-channel phase imbalance

4.5 Platform Integration

The payload tray is uniquely designed to hold the battery pack of the rotorcraft. Figure 4-27 shows the side and bottom views of the payload tray and the locations of the battery and radar electronics are highlighted. The underside of the tray has a rib-like structure and is made of carbon fiber composite material. The Aluminum lined edges on the payload tray have hard points to integrate external structures. The radar box is held in place by two Aluminum straps attached to the hard points right above the blue box in Figure 4-27. However, the positions of these hard points are inconvenient for the designed array. In spite of the fastener points incorporated on the Delrin

fixture, the orientation of the antenna makes it difficult to integrate to the hard points on the bottom edge. In addition to the arrays, four power dividers and the coaxial cable connections must also be installed. Therefore, an additional structure with a different mounting mechanism is required to integrate the entire front-end.

A rectangular Aluminum sheet of dimensions 59.69 cm by 21.9 cm by 0.13 cm is fastened to the underside of the payload tray as shown in Figure 4-28. In the forward direction relative to the rotorcraft, the sheet is fastened at the two hard points on the starboard and port side of the bottom edges on the payload tray. In the aft direction, the sheet and the radar box are fastened together at four points, two forward and two aft of the radar box. The Aluminum straps on either side of the radar box connect the metal sheet to the two hard points as shown in Figure 4-28 . The sheet covers the entire area occupied by the battery and the radar box.

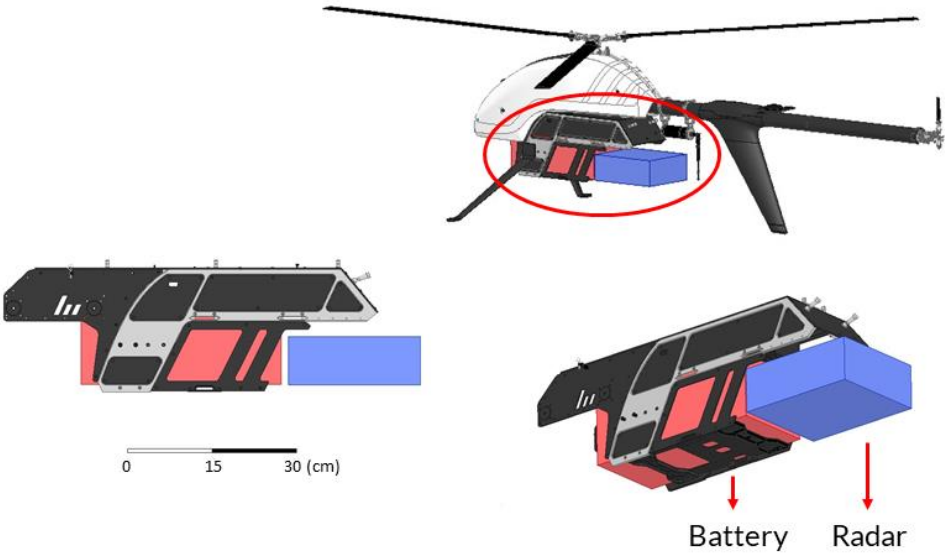

Figure 4-27: Side and bottom views of the payload tray with the locations of the battery and radar highlighted

The Aluminum sheet has two functional roles: provide a mechanical solution for array integration and provide electrical isolation between the arrays and the rest of the vehicle. Holes are drilled at specific locations on the sheet to fasten the four Delrin fixtures by the two semi-circular tabs on either side. The arrays are fastened on the underside and the power dividers on the

topside of the sheet. Two holes of diameter 19.05 mm (0.75 inch) are drilled near the forward and aft side of the sheet to allow coaxial cables to pass through.

Electrically, the sheet acts as a flat, uniform ground plane and the effects of the platform on the antenna arrays are excluded. The radar enclosure is an Aluminum box, the battery is packed in Plastic material, and most of the rotorcraft is made of carbon fiber composite material. These surfaces scatter the incident electromagnetic (EM) wave and interfere with the nadir pointing radiation lobes. This can increase the side-lobe levels, distort the main lobe, or rotate the pattern. Therefore, the metal sheet separates the arrays and the platform and it provides a uniform reference for the antenna radiation.

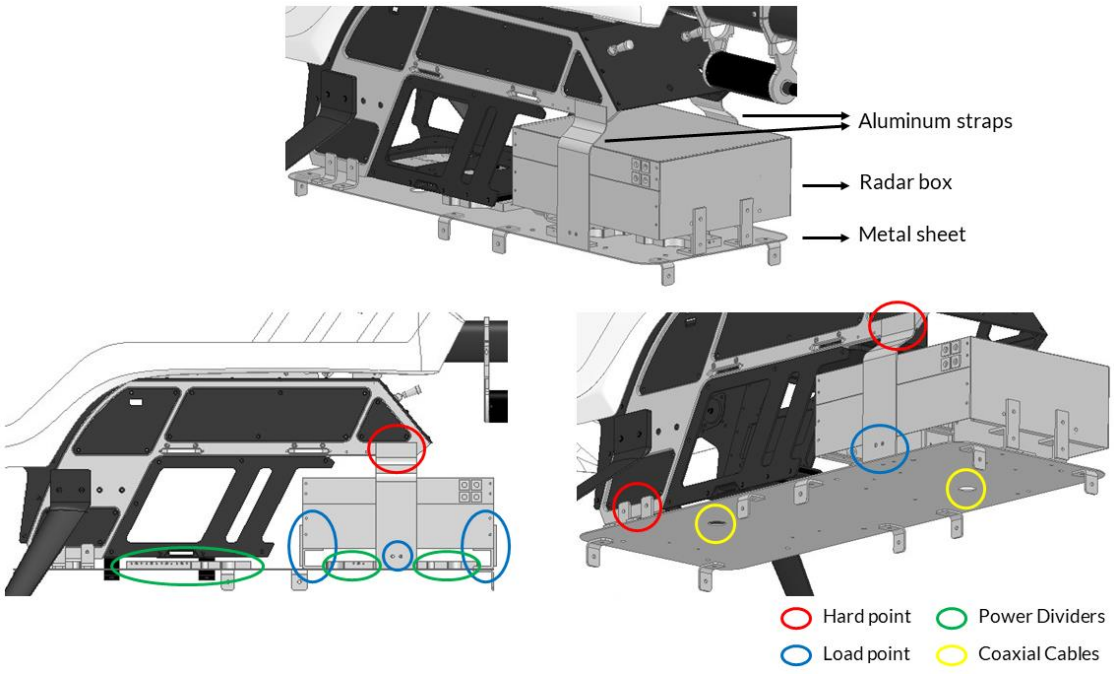

Figure 4-28: Isometric, side, and bottom views of the metal sheet, radar box, and aluminum straps integrated with the rotorcraft

4.5.1 Array on metal sheet

The bottom surface area of the Aluminum sheet is 1,307.21 cm^2 and the bottom surface area of the Delrin fixture (that fastens to the sheet) is 80.83 cm^2. The total area of four fixtures is 24.73% of the metal sheet. Therefore, nearly a quarter of the metal sheet is occupied by the antenna

arrays. This quantifies the low availability of space and the difficulty in integrating four arrays to the Vapor 55 rotorcraft. Moreover, this also implies low electrical isolation due to limited physical space between the arrays.

The arrangement of the antenna arrays is based on the polarization requirements of the radar. Figure 4-29 shows the orientation of the flight, antenna, and radar parameters relative to each other. The linear polarization for the system is defined by the direction of the Electric Field vector relative to the direction of flight and the ground surface. For vertical polarization, the bulb antenna elements are vertically oriented along the direction of flight, such that the long dimension of the Delrin fixture is perpendicular to the direction of flight. For horizontal polarization, the fixture is rotated by ninety degrees such that the long dimension is along the direction of flight. The corresponding along-track and cross-track radar parameters are also shown in Figure 4-29.

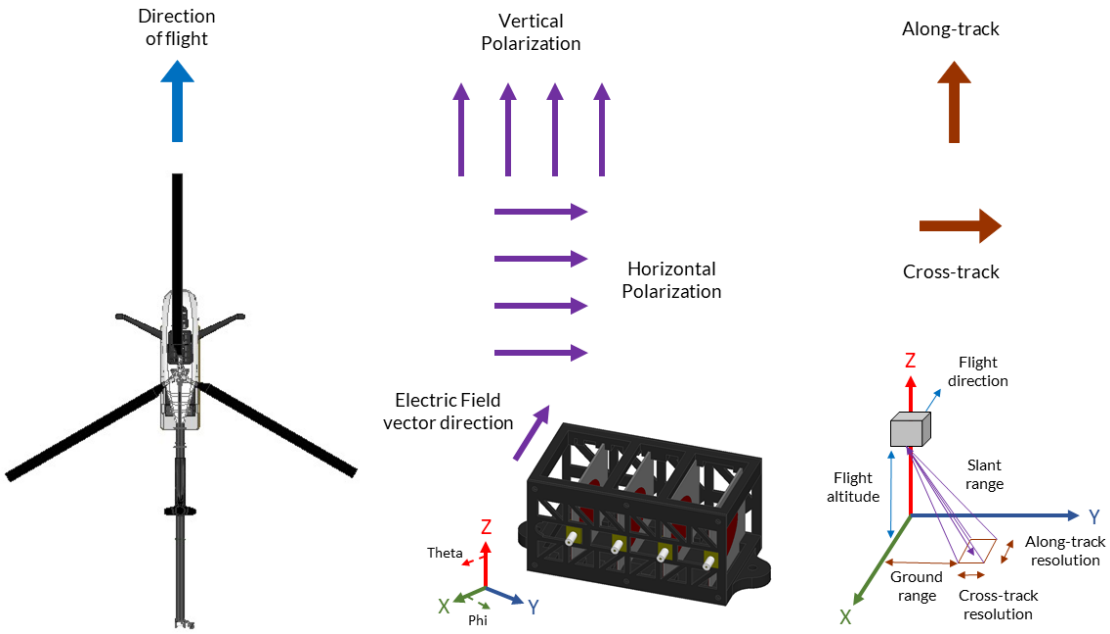

Figure 4-29: Orientation of flight, antenna, and radar parameters relative to each other

The positions of all four arrays on the metal sheet are shown in Figure 4-30. The transmit arrays are placed on the front-half of the sheet, while the receive arrays are on the back-half. The vertically polarized antennas are placed along the short edges and the 13.7 cm long Delrin fixture

occupies most of the width of the Aluminum sheet. The horizontal arrays are placed along the long edges but on opposite sides. This ensures maximum separation between the transmit and receive horizontal arrays. However, it also results in a small physical distance of 1.1 cm vertical gap between the transmit arrays and a 3.6 cm vertical gap between the receive arrays.

The isolation wall is a rectangular piece of Aluminum with two rounded corners on the same side and the radius of curvature of the corners is 2.44 cm (0.96 in.) It is placed perpendicular to the metal sheet at the mid-point, such that the rounded corners are on the bottom side. The two bottom corners are rounded to accommodate a favorable aerodynamic shape at the edges of the fairing. The metal wall electrically isolates the transmit and receive arrays and this reduces the magnitude of signal power feedthrough from the transmitter to the receiver.

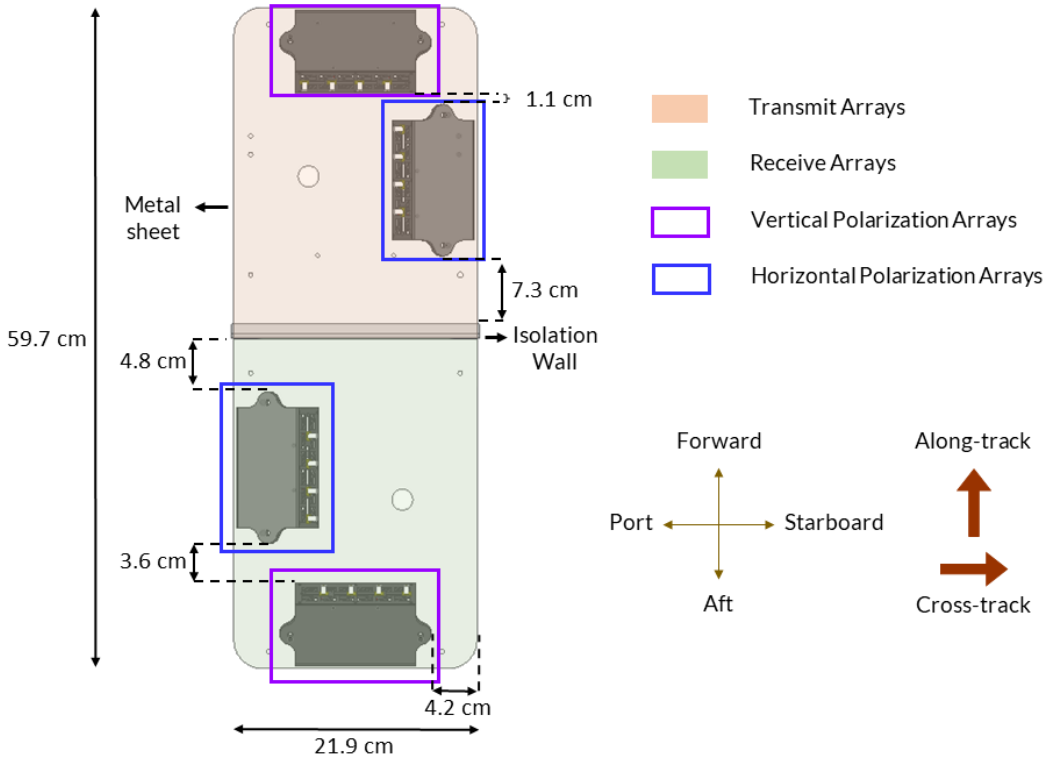

Figure 4-30: Top view of the metal sheet showing the positions of the antenna arrays and the corresponding flight and radar directional references

The performance of an antenna is highly dependent on the position over a finite ground plane and the dimensions of the ground plane relative to the operating wavelength. In theory, an infinite ground plane is typically considered for computations. However in practice, the characteristics of the antenna may be significantly altered due to diffraction of EM waves at the edges of conductors. The property of diffraction is explained using Huygen's principle. When an EM wave is incident on a corner or wedge, it diffracts around the obstacle as each point on the primary wave-front may be considered as a source for a secondary cylindrical wave [60].

In [61], the effect of ground plane edge diffraction on the performance of phased array antennas is discussed. The total field of an antenna placed near the edge of a finite ground plane is a superposition of the direct reflection due to Geometric Optics (GO) and the diffracted field. It is shown that the edge effects can cause distortion and rotation of the radiation lobes. Another example is seen in [62], where the radiation of four monopole antennas in the upper UHF band is affected by the ground plane edges.

The ground plane edge effects on the Delrin arrays causes a decrease in nadir gain, specifically at the frequency nulls, and this is due to a rotation of the main beam away from the ground plane in the forward direction. For the vertically polarized arrays, the rotation is in the along-track direction and for the horizontally polarized arrays, it is in the cross-track direction. Therefore, the main beams of all four arrays are spread outward from the nadir target, similar to a monopulse tracking radar [63].

It is vital to amend the rotation of the radiation lobe since all four arrays must point at the same target area. Wedge-shaped pieces of Delrin are used to rotate the entire Delrin fixture from the surface of the metal sheet. The optimal angle of rotation is experimentally determined to be 20° through radiation pattern measurements in the anechoic chamber. The wedges are trapezoidal

in shape such that one surface lies flat on the metal sheet and the other surface is at 20° relative to the sheet. A pair of similar wedges are fastened together on either side of the metal sheet through the drilled holes and the semi-circular tabs on the Delrin fixture. Therefore, four similar pieces of wedges are required to fasten one antenna array to the metal sheet at the optimal angle. Figure 4-31 shows isometric and side views of the four rotated arrays integrated to the metal sheet.

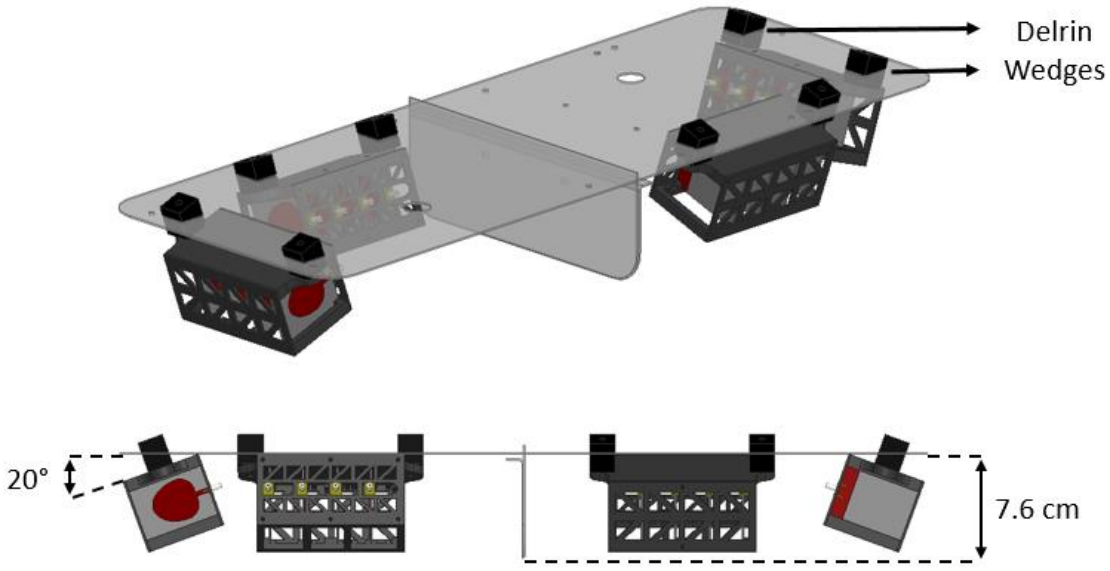

Figure 4-31: Isometric and side views of the four rotated arrays integrated to the metal sheet

The effect of array rotation is characterized through simulation and measurement. Figure 4-32 shows a HFSS simulation model of one vertically polarized array, isolation wall, and one-half of the metal sheet. The model is simulated for two cases: array flush against the metal sheet (0°) and array rotated at an angle of 20°. Since the wall electrically isolates both halves, one-half of the metal sheet is sufficient to simulate the EM effects. The reduced model also enhances the computation time of the simulation. On the other hand, the setup for the measurement involved the usage of foam pieces and duct tape to maintain the array at the two required positions. The metal sheet is aligned vertically so that the array is pointed directly at the reference antenna on the wall of the anechoic chamber.

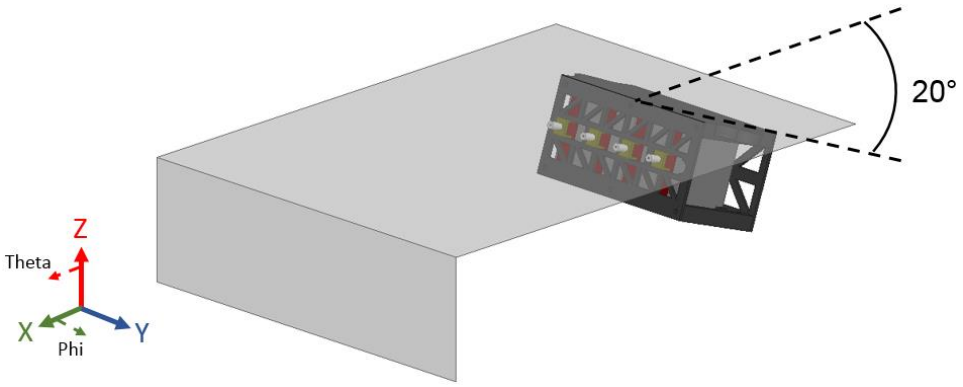

Figure 4-32: Simulation model of one vertically polarized array rotated by 20° with the isolation wall and one-half of the metal sheet

The active return loss of the array is shown in Figure 4-33. The effect of rotation does not have a significant effect on the return loss and the highest return loss of -7.21 dB is acceptable for the RF section of the radar. The measurement is distinctly different from the simulation between 2 and 14 GHz, however the magnitude is within acceptable (usable) range.

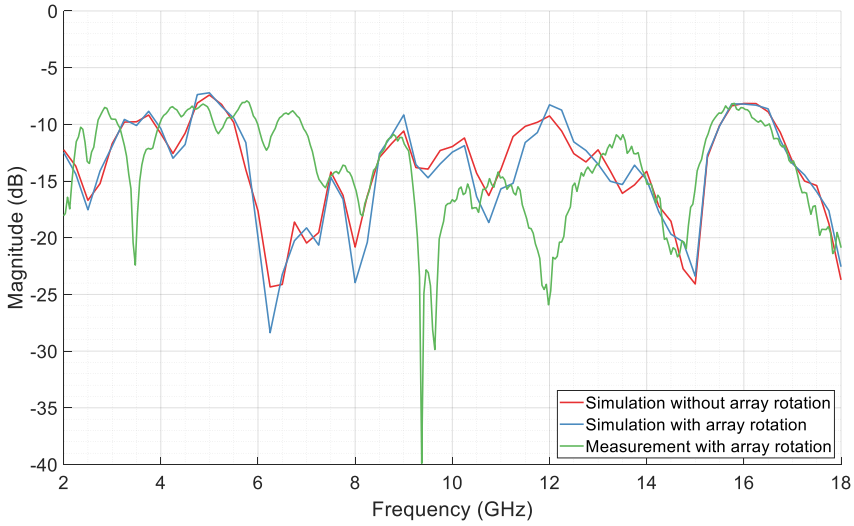

Figure 4-33: Active return loss of the array mounted under the metal sheet with isolation wall

The cross-track radiation patterns for 2, 6, 10, 14, and 18 GHz are shown in Figures 34 (a) to (e). The plots show the normalized values of the magnitude of the electric field vector at phi = 90° and theta varied from 0° to 360°. The effect of rotation is minimal since the radiation lobe and array are rotated in the along-track direction for the vertically polarized arrays. The changes in

side-lobe levels are caused due to the non-uniform distance between the array and the ground plane (metal sheet). The consequence of array rotation is seen in the nadir gain plot shown in Figure 4-35. The criteria for experimentally determining the optimal rotation angle is the magnitude of the nadir gain of the array.

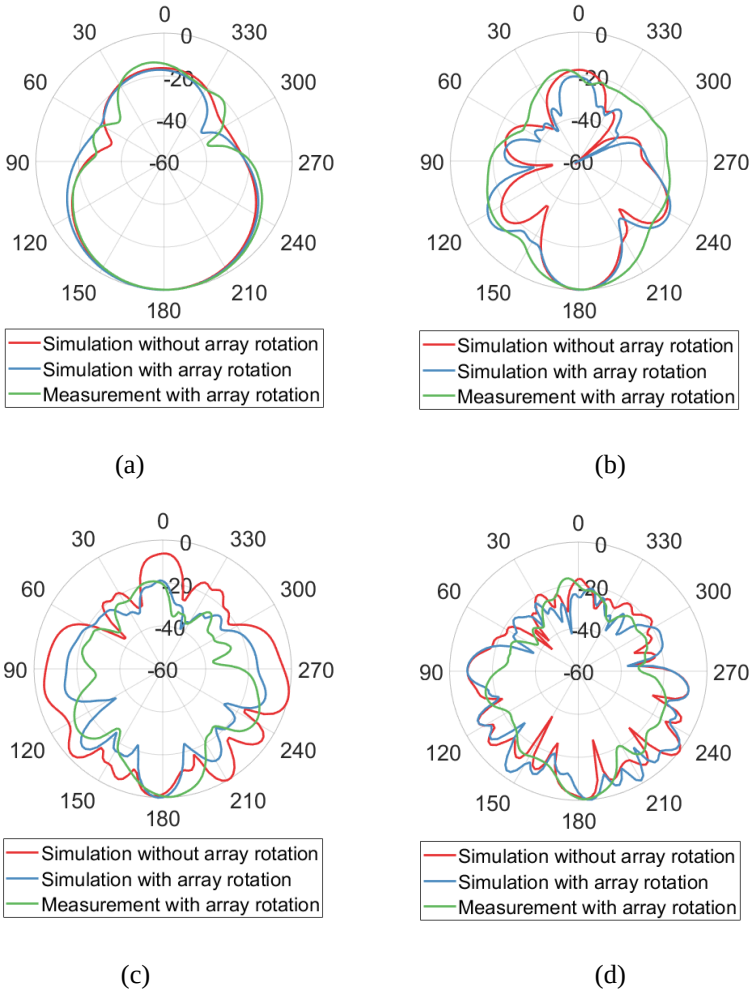

(a) (b)

(c) (d)

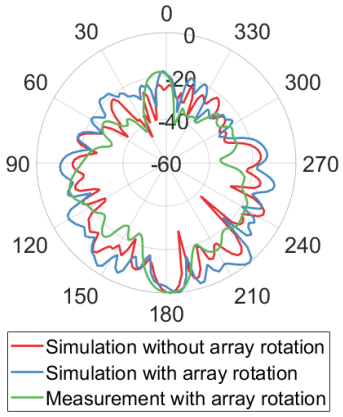

(e)

Figure 4-34: Radiation pattern of four element array with metal sheet at (a) 2 GHz, (b) 6 GHz, (c) 10 GHz, (d) 14 GHz, and (e) 18 GHz

In Figure 4-35, the simulated nadir gain without array rotation shows two deep nulls at 4.5 and 15.5 GHz and a low magnitude of -2.45 dB is seen at 11.5 GHz. These three data points are close to the previously discussed frequency nulls at 5, 10, and 15 GHz. The array is rotated in steps of 10° and multiple far-field measurements are performed in the anechoic chamber to improve the magnitude of the nulls. The optimal angle relative to all the nulls and magnitude of average gain is experimentally found to be 20°.

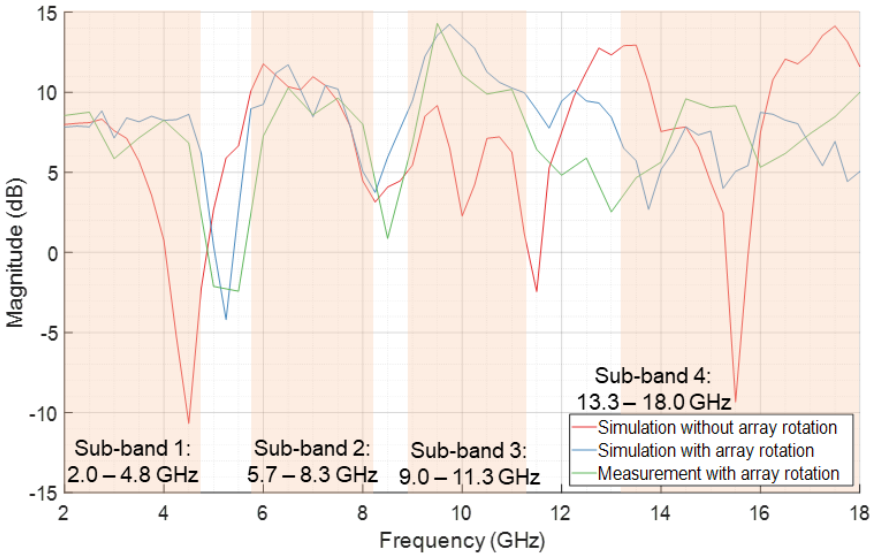

Figure 4-35: Nadir gain of the array mounted under the metal sheet with isolation wall (phi=90°, theta=180°)

The increase in gain is evident from the simulation and measurement nadir gain traces with array rotation. From Figure 4-36, the magnitude of the first null for the measurement is -4.19 dB at 5.25 GHz. Instead of the second null typically seen at 10 GHz, there is a decrease in magnitude of 0.87 dB at 8.5 GHz and 2.53 dB at 13 GHz. The third null at 15.5 GHz is completely eliminated and the value at the 16 GHz dip is 5.32 dB. In terms of the magnitude of the gain for the link budget within the bandwidth of the pulse, only one null with a low value exists at 5.25 GHz.

The value of the average nadir gain for the measurement with array rotation is 7.06 dB. The scattering from the metal sheet has resulted in an increase of 1.01 dB in average nadir gain, relative to the standalone array with Delrin fixture. A low value of increase in gain is attributed to the closely spaced, non-uniform ground plane (metal sheet) distance. For a target average gain of 7.31 dB, the difference with this setup is 0.25 dB.

In Section 4.2, under the single element design, it was alluded that the variations in gain within the pulse may hinder the interpretation of target information. To overcome this problem, the entire frequency band is divided into sub-bands that contain a maximum gain variation of 6 dB. This is a typical maximum value over which the processing gain may be uniformly applied, however this is adaptive based on the total dynamic range of the received waveform. In Figure 4-35 and Figure 4-36, four sub-bands are highlighted: 2 – 4.8 GHz, 5.7 – 8.3 GHz, 9 – 11.3 GHz, and 13.3 – 18 GHz. The backscatter response is divided into each sub-band and individually processed. The final transform of each sub-band is stitched together to obtain an equivalent response of nearly the entire band.

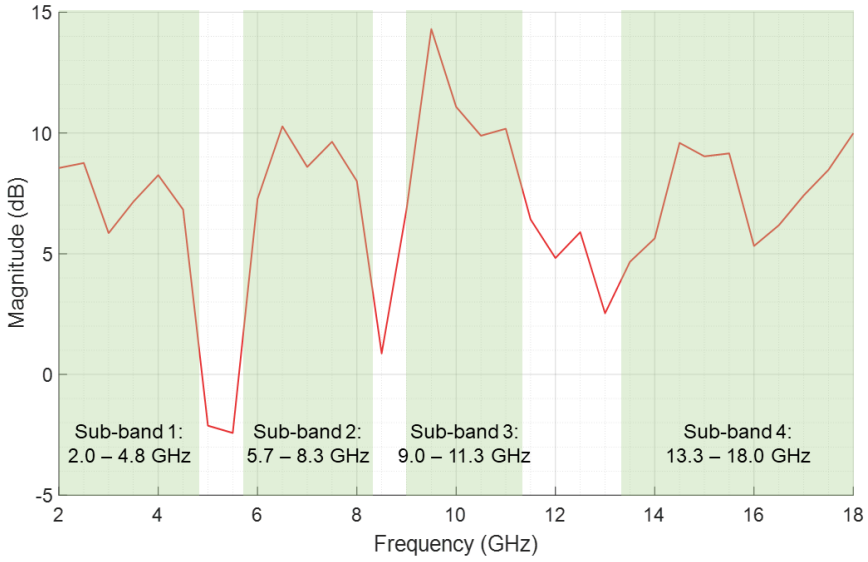

Figure 4-36: Measured nadir gain of the rotated array, mounted under the metal sheet with isolation wall. The highlighted sections denote sub-bands with 6 dB variation in gain

4.5.2 Electrical isolation between arrays

In FMCW radar systems, the electrical isolation between the transmit and receive front-ends is particularly important. The signal from the transmit array is fed through directly to the receive array and this fixed propagation time typically sets the minimum detectable range for the radar. The leakage signal raises the noise floor and it decreases the sensitivity of the receiver [Skolnik]. The physical constraints of the platform typically set the ceiling limit of the isolation. However, in many cases, additional isolation is achieved by integrating external components like an isolation wall.

Primarily, the required isolation is dependent on the saturation level of the receiver. This is typically the value of the 1 dB compression of the LNA or the mixer. The performance of the receiver can be improved by targeting a higher isolation based on the maximum rejectable SNR and the minimum detectable SNR [64]. The best isolation is achieved by considering the minimum detectable signal based on the dynamic range of the ADC.

Due to the limited physical space available for the antenna arrays, a pragmatic target is set for the electrical isolation. The range is based on the expected received power for the various types of soil. The absolute minimum level is still dictated by the compression point. However, the expected minimum isolation is for the maximum received power for high moisture and smooth soil. The receiver is expected to be isolated for at least the best target return. The preferred isolation level is the minimum received power for low moisture and rough soil. This ensures that the receiver is isolated from the transmitter for all expected types of target. The absolute maximum level or best possible is the minimum detectable signal, which isolates the full dynamic range.

The upper limit of the receiver is based on the lowest value of the 1 dB compression point in the receiver chain. Typically, this is either the mixer or the ADC. In this case, the mixer has the lowest compression point of +5 dBm. The LNA is the only preceding component in the receiver chain and with a gain of 17 dB, the maximum input power into the receiver is -12 dBm. The full voltage scale of the ADC is 2.5 $V_{p\text{-}p}$ and this is equivalent to an upper limit of +12 dBm. The ENOB of the ADC is 12 bits and this implies a dynamic range of 72 dB. Therefore, the lower limit of the ADC is -60 dBm. For an average receiver gain of 43 dB, the Minimum Detectable Signal (MDS) for the receiver is -103 dBm. These values and their significance are shown in Figure 4-37 in a rotary format.

As previously discussed in Section 3.2, under the Link Budget section, the largest received power expected for the most favorable soil condition, in terms of backscatter properties, and at the lowest range of 50 feet is -34.97 dBm. Therefore, the realistic minimum isolation between the arrays is set to be 35 dB. Similarly, the smallest received power expected for the least favorable soil condition and at the highest range of 400 feet is -95.04 dBm. Therefore, the realistic maximum isolation between the arrays is set to be 95 dB. These values are also shown in Figure 4-37.

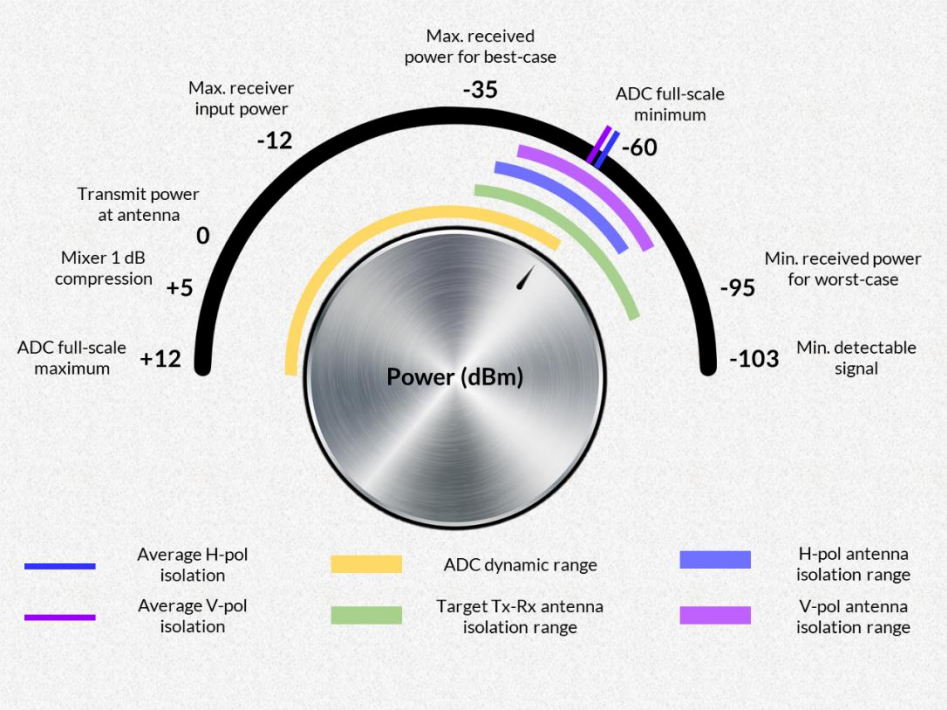

Figure 4-37: Rotary representation of the isolation range between antenna arrays and other salient power parameters of the RF sub-system

In the case of [64], for an S-band system with 1 GHz bandwidth and a maximum rejectable SNR of -30 dB, an isolation of 81 dB is required. This isolation requirement appears to be high but their system features higher transmit power, higher maximum power into receiver, and higher noise figure. On the other hand, in [63] it is discussed that when restricted by the nature of the application, large isolation may not be possible. It is reported that, on space restricted platforms such as missiles, typical isolations might be about 20 dB at L-band , 50 dB at X-band, and 70-dB at K-band. Therefore, in this work, for a transmit-receive array isolation range of 35 dB to 95 dB, an average isolation of 65 dB across the bandwidth is targeted.

A picture of the four arrays on the metal sheet is shown in Figure 4-38. The setup has the isolation wall and fairing brackets installed on the sheet. Semi-rigid coaxial cables are used to achieve optimal routing and repeatable insertion loss performance. In another setup, two RF absorber foams of dimensions 21.9 cm by 4.8 cm by 7.6 cm are taped in place on either side of the isolation wall. The absorbers provide further attenuation and thereby increase isolation.

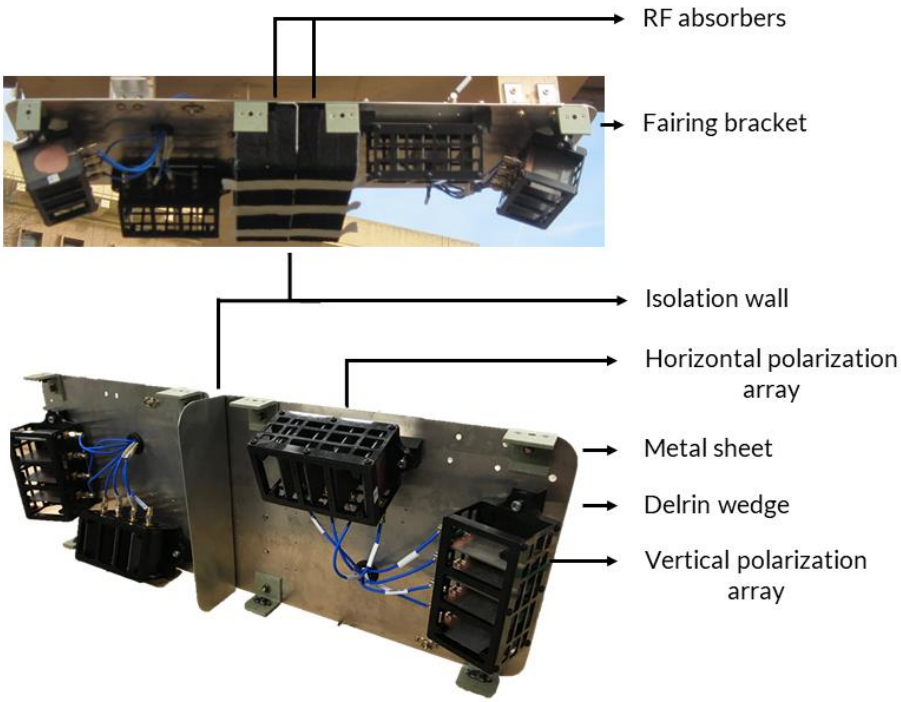

Figure 4-38: Photographs of the four arrays on the metal sheet with the isolation wall and RF absorbers

Transmission parameters or S_{21} measurements are performed on a VNA between each polarization array. When a set of arrays are under test, the other two arrays and power dividers are terminated. S_{21} measurements are done between both sets of arrays, with and without RF absorbers and the results are shown in Figure 4-39 and Figure 4-40.

The isolation between 2 – 3 GHz is relatively low due to the shorter electrical distance between the arrays. As the wavelength decreases, the isolation gradually increases. The minimum isolation with absorbers is -40.27 dB at 2.44 GHz for vertical polarization and -36.79 dB at 2 GHz for horizontal polarization. The difference with and without absorbers for vertical polarization at 2.44 GHz is 3.21 dB. However, for horizontal polarization, due to a difference in orientation and distance, a significant amount of attenuation is observed between 3 – 8 GHz. The maximum isolation with absorbers is -75.67 dB at 16.93 GHz for vertical polarization and -73.02 dB at 17.29 GHz for horizontal polarization. The average isolation with absorbers is -58.72 dB for vertical polarization and -59.26 dB for horizontal polarization. The respective isolation for the arrays are

off by 6.28 dB and 5.74 dB from a target of -65 dB. Nonetheless, an average isolation of close to 60 dB is sufficient to detect most soil types.

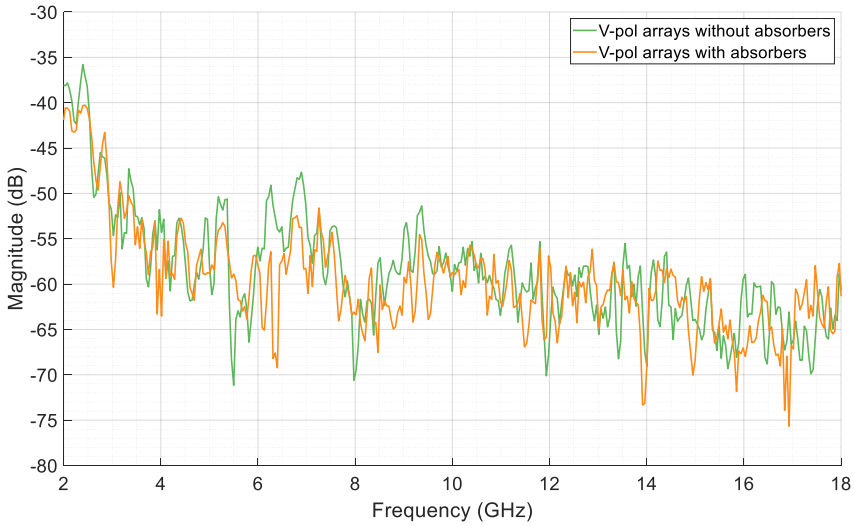

Figure 4-39: Measured transmission s-parameters between the vertically polarized arrays with and without RF absorbers

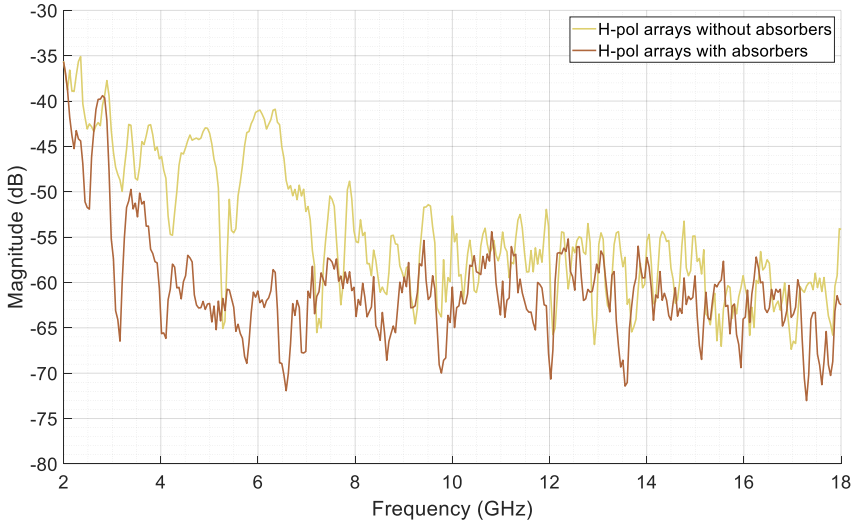

Figure 4-40: Measured transmission s-parameters between the horizontally polarized arrays with and without RF absorbers

4.5.3 Array with feed network and fairing

In Section 4.4, the power divider issue of a noisy transmission response when the top opening is completely covered was discussed. The experimentally determined solution is to leave a small gap between the walls of the enclosure and the top covering. This reduces the effect of the internal reflections on the signal.

The lid is designed to protect the power divider from the weather and the elements during flight. To work around the electrical performance problem, the feed network is flipped, such that the top is face-down, and then fastened to the metal sheet. Multiple washers are used on the fasteners to maintain a small gap between the enclosure and the metal sheet. The metal sheet effectively functions as a lid and protects the power divider. The positions of the power dividers on the metal sheet are shown in Figure 4-41 and a picture of the top side is shown in Figure 4-42.

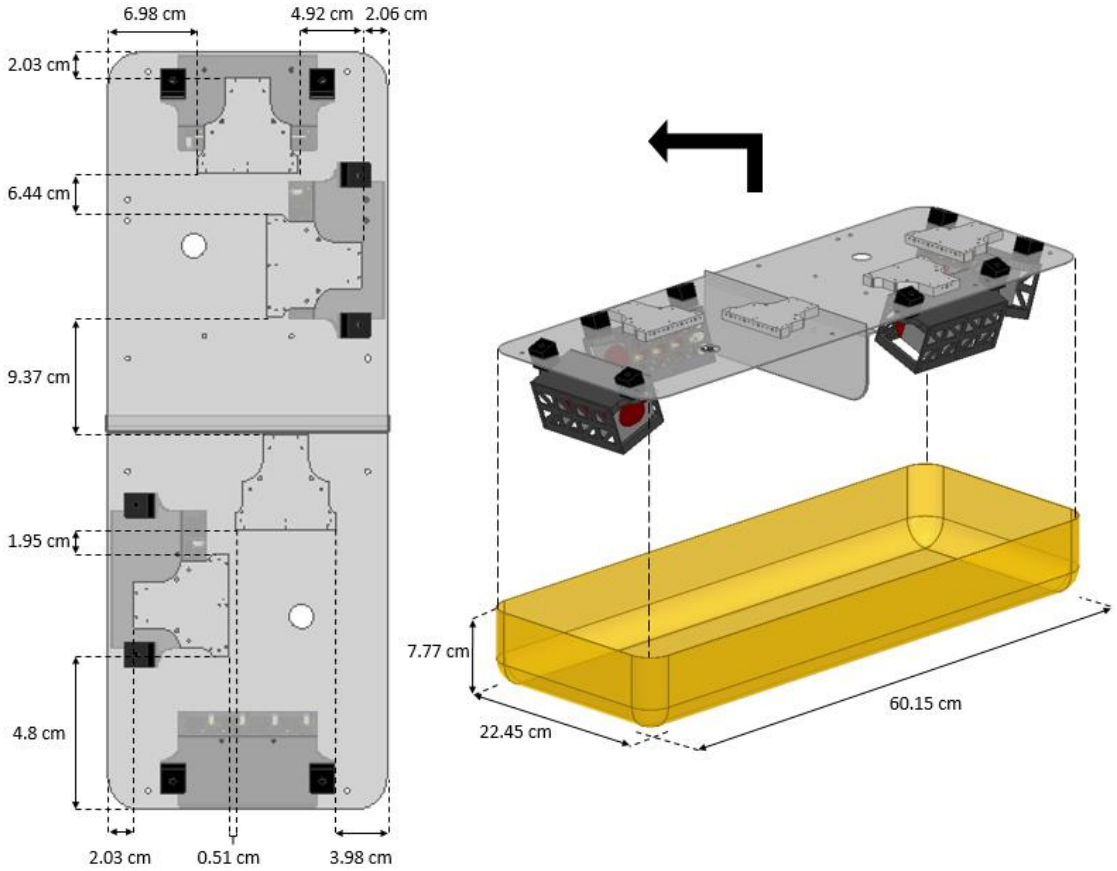

Figure 4-41: Top and isometric views of the power dividers integrated to the metal sheet along with the fairing

A cuboid shaped fiberglass is designed and the dimensions are shown in Figure 4-41. The corners and edges are curved to make the shape aerodynamic and the radius of curvature is 2.54 cm. The fairing is a monolithic panel of four layers of S2 fiberglass/epoxy prepreg material. The walls of the fairing are bolstered with ten layers of fiberglass and the extra layers are along the entire fairing at a height of 5.33 cm. The thickness of the side walls are increased since they are fastened to the brackets on the metal sheet and it ensures that the fairing can withstand the vibrational loads. The extra layers of the fiberglass can be seen as a dark yellow band on the fairing in Figure 4-42.

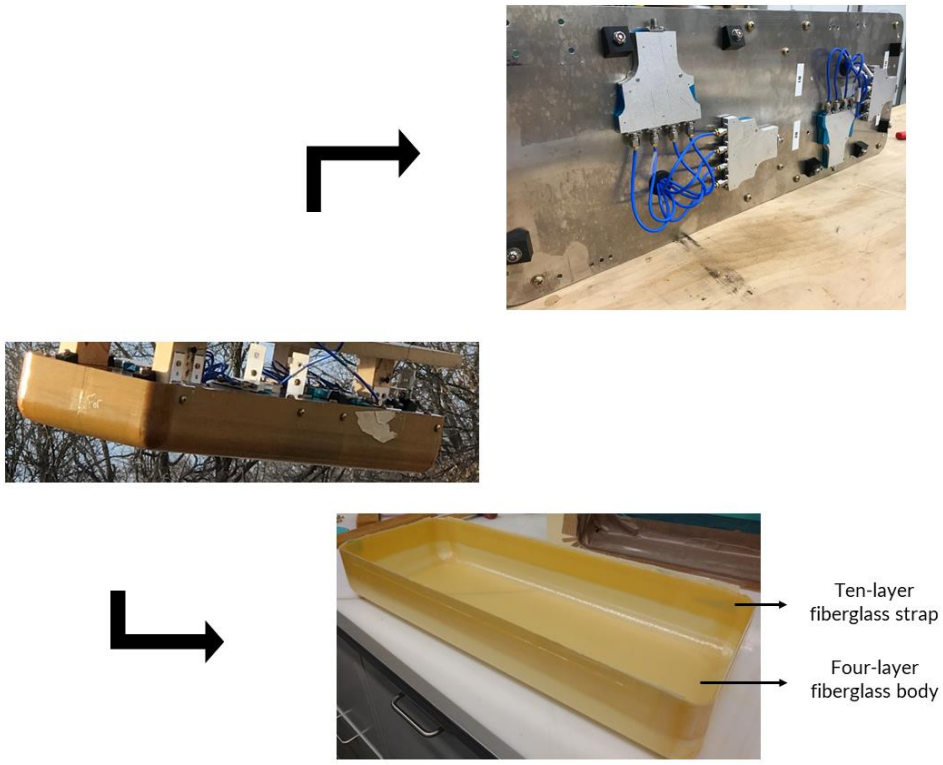

Figure 4-42: Pictures of the integrated and separated metal sheet and fiberglass fairing

The results showing the effects of the power divider and the fairing are shown Figure 4-43 and Figure 4-44. The active return loss of the antenna array is not shown since the measurement is performed at the input of the power dividers. Therefore, the signal reflections are observed at

the input of the power divider when the output impedance is referenced to the antenna's input impedance. Hence, the far-field measurements are used to compare the changes in performance.

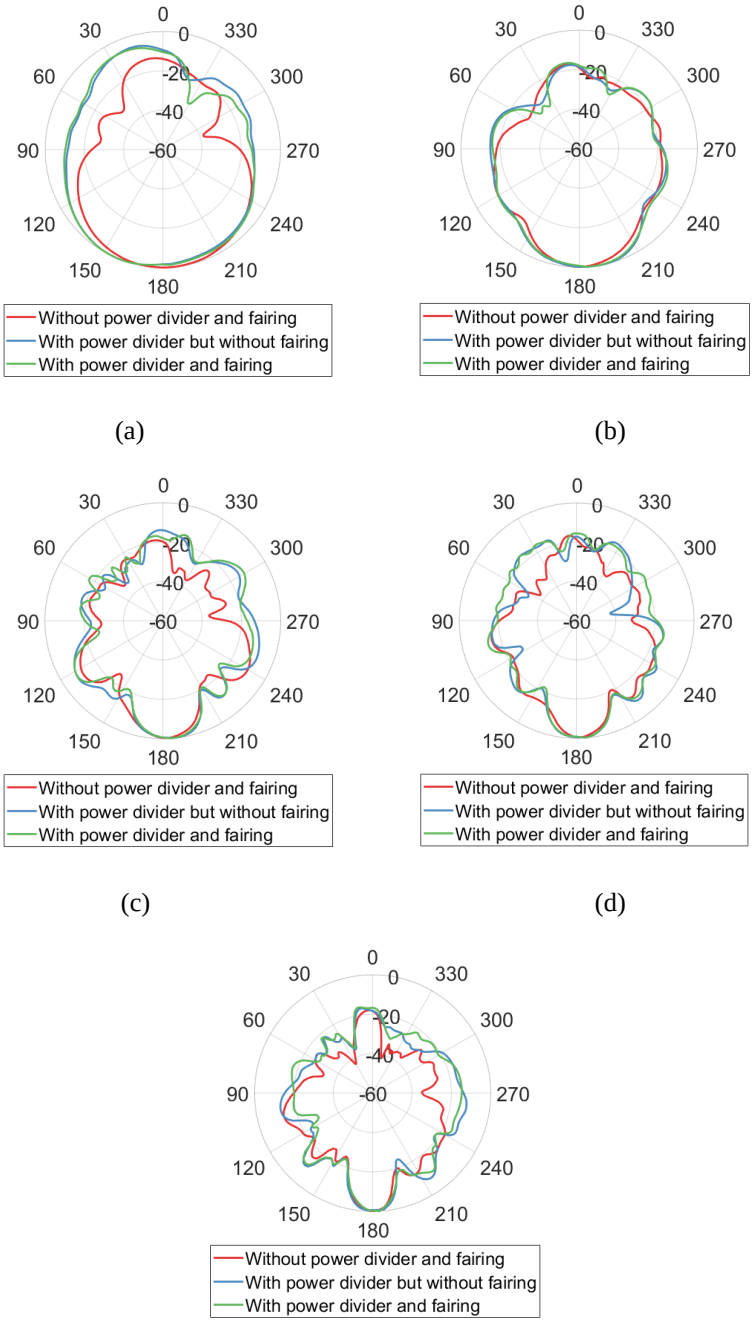

Figure 4-43: Radiation pattern of four element array with and without power divider and fairing at (a) 2 GHz, (b) 6 GHz, (c) 10 GHz, (d) 14 GHz, and (e) 18 GHz

The radiation patterns at 2, 6, and 10 GHz show an increase in side-lobe levels, as seen in Figure 4-43 (a) to (e). The power dividers change the input impedance of the antenna and the fairings are in close physical proximity to the antennas. This changes the surface current density on the metal sheet and it increases the side-lobes. The change in reflections from the metal sheet are also seen in the nadir gain plot in Figure 4-44. There is an increase in gain in the first three sub-bands with power divider and fairing. The nadir gain values at 3, 8, 10, and 12 GHz are 12.41, 12.25, 10.1, and 10.79 dB. There are nulls of magnitude -0.68 dB at 5 GHz, -0.22 dB at 13 GHz, and -0.99 dB at 17.5 GHz, however the values are large enough to be sufficient for the link budget. From the plot, it is evident that the power divider has a larger effect on the antenna performance than the fairing. The average gain without either part is 7.06 dB, with power divider is 7.88 dB, and with both the divider and the fairing is 7.97 dB. Therefore, this satisfies the goal of reaching within the 3 dB deviation of the average gain of the horn antenna.

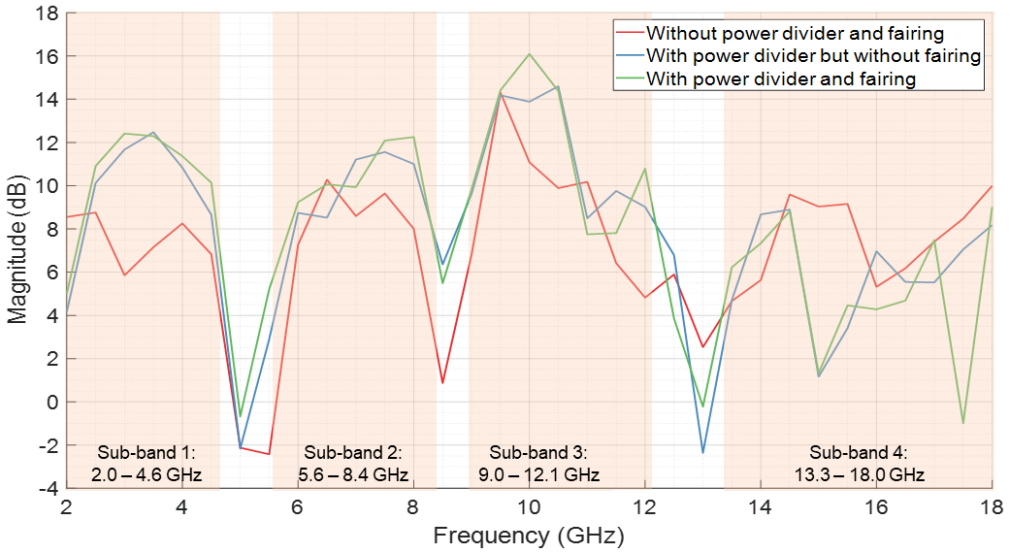

Figure 4-44: Measured nadir gain of the integrated array with power divider and fiberglass fairing

4.5.4 Final setup with rotorcraft

The front-end design for the Helo-Snow radar comprises of numerous components and an isometric view of the full setup is shown in Figure 4-45. The basic element is a bulb shape

microstrip monopole antenna and each array has four elements. The arrays are enclosed in a Delrin fixture and fastened at an angle of 20° to the metal sheet. Four 1:4 microstrip power dividers connect the radar channels to the antenna arrays. The transmit and receive arrays are separated by an isolation wall sandwiched between two pieces of RF absorbers. A four- and ten-layer fiberglass composite fairing protects the arrays. The previous sections detail the design and results of each component progressively added to the setup. The final step is analysis with the platform itself.

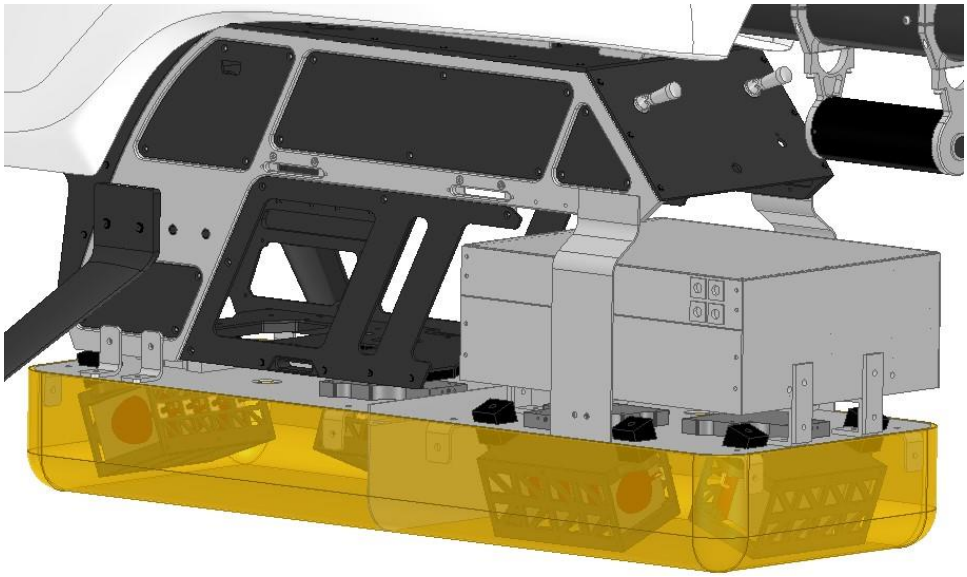

Figure 4-45: Isometric view of the assembled metal sheet, antenna arrays, isolation wall, power dividers, fairing, and radar box on the rotorcraft

The final tests with the rotorcraft are of two types: Structural and Electrical. All parts except the connectors, cables, brackets, and fasteners of the front-end are custom made in-house. The numerous parts must correctly stay fastened together during the entire flight to ensure stability and proper operation. Therefore, it is vital to assess if the custom structures are capable of tolerating the vibrational loads of the rotorcraft.

All components of the front-end are assembled on the rotorcraft and a picture of the full setup is shown in Figure 4-46. The vehicle is flown at the Remote Control (RC) field in Lawrence, Kansas and a picture from one of the flight tests is also shown in Figure 4-46. A series of basic

maneuvers like roll, pitch, and yaw are performed and then inspected for any changes. The tests are done multiple times and the longest duration of continuous flight was approximately 30 minutes. However, the intended flight time for data collection is 45 – 60 minutes. Nonetheless, all components passed quality checks and the front-end is certified for flight.

Figure 4-46: Photographs taken during a flight test to assess the vibrational stresses on the custom built structures

The electrical test involved the rotorcraft inside the anechoic chamber. The far-field measurements are performed on the entire setup and this required constructing a test fixture to hold

the rotorcraft. In Figure 4-47, the picture on the left shows the entire test setup in the chamber. A custom test fixture made of balsa wood is built to hold the rotorcraft vertically, such that the aft direction is pointed down. This is required to measure the nadir point and the arrays must point directly at the chamber wall antenna. The rotorcraft and the balsa wood fixture are placed on a pink foam stand, such that the tail passes through a hole in the stand. This provides a base and also sets the correct height between the arrays and the chamber wall antenna. In Figure 4-47, the picture on the right shows a close-up of the test setup taken during far-field measurements.

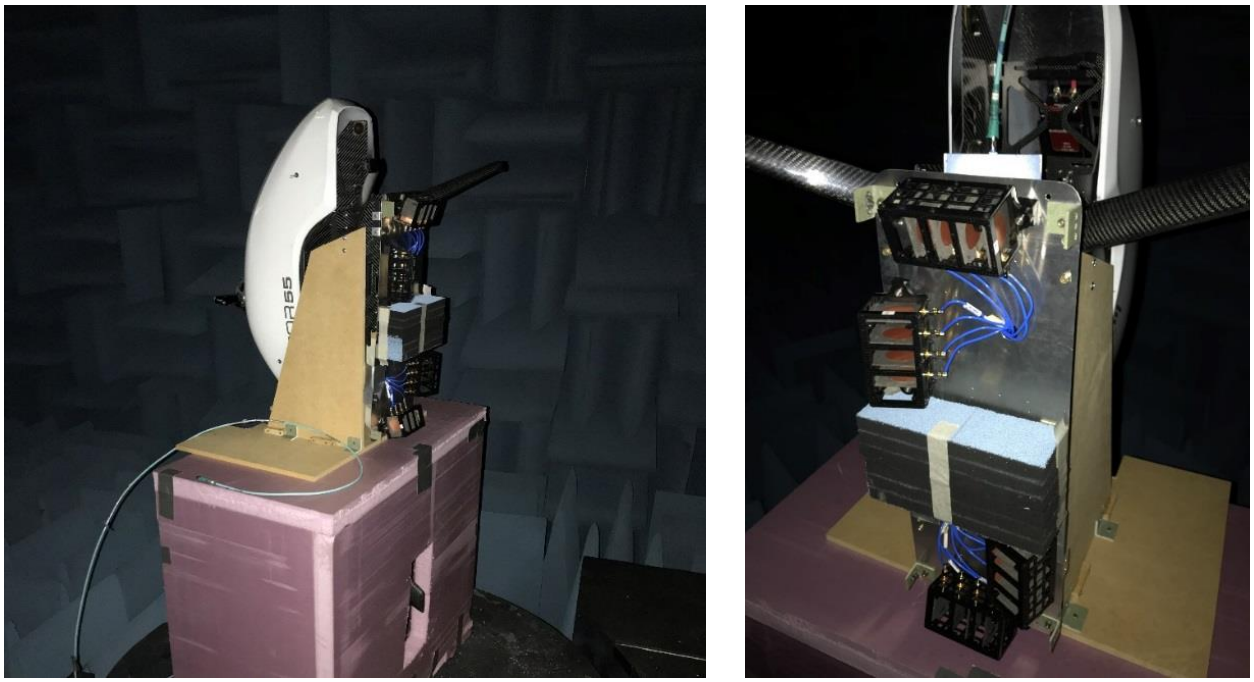

Figure 4-47: Photographs of the radar front-end (with fairing removed) on the rotorcraft taken inside the anechoic chamber during the far-field measurements

The result for the final setup in shown in Figure 4-48. This is compared with the previous return loss result in Figure 4-33, which showed the measured active return loss of the array mounted under the metal sheet with the isolation wall. The similarity between the two results indicate that the rotorcraft has minimal effect on the impedance measurement of the antenna. The

metal sheet provides high isolation such that the port reflections under the sheet are mostly unaffected by the various conductors on the platform. This is also evident in the similarity between the radiation pattern traces in Figure 4-49 (a) to (e).

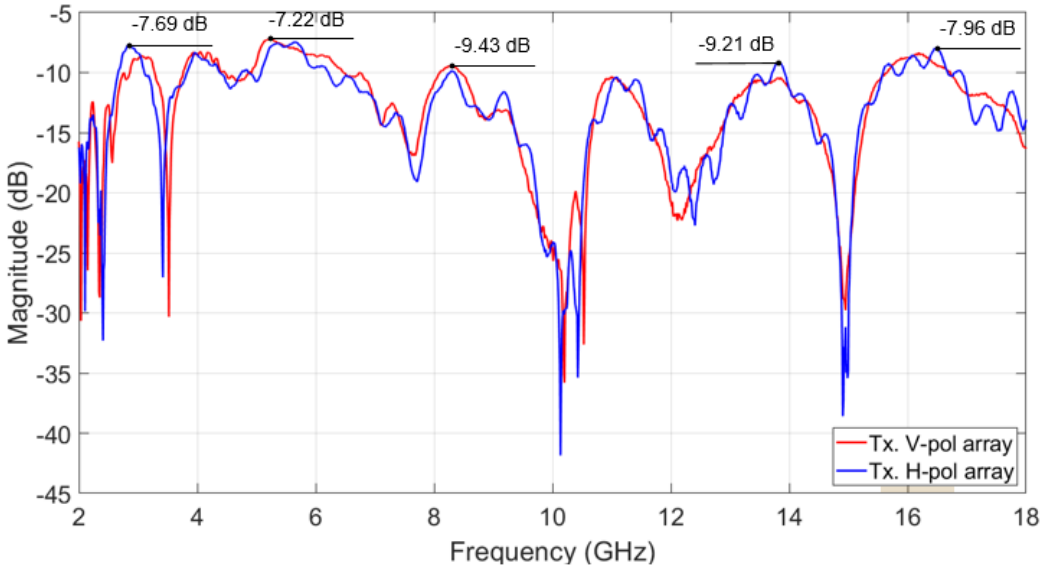

Figure 4-48: Measured active return loss of the transmit arrays with the rotorcraft and fairing (no power divider)

The highest return loss value is -7.22 dB at 5.23 GHz and the other points of impedance mismatch are -7.69 dB at 2.83 GHz, -9.43 dB at 8.27 GHz, -9.2 dB at 13.83 GHz, and -7.96 dB at 16.49 GHz. As previously discussed, these points of increased reflections are caused due to the interaction with the metal sheet. Further, the reflected power is within the reverse isolation range of the RF switch and the LNAs. The effect of the variation in signal power within the band may be pre-emptively fixed by amplitude shaping the digital waveform. There is a good match between the return loss of the transmit arrays. The horizontally polarized array's response is noisier relative to the vertical array and this could be caused due to connector and cable issues or mismatch with the power divider.

The radiation patterns at 2, 6, 10, 14, and 18 GHz are shown in Figure 4-49 (a) to (e). In spite of the isolation from the metal sheet, the position of the arrays at the edge of the sheet cause

the platform to have an effect on the side- and back-lobes. At 18 GHz, there is a rotation in the main lobe by approximately 10° and an average increase in side-lobe levels. The platform has a greater effect at the higher frequencies due to increased backscatter and free-space loss. Since soil is an extended radar target, the downsides of the antenna characteristics are minimized. However, further improvement is required to improve the sensitivity of the radar.

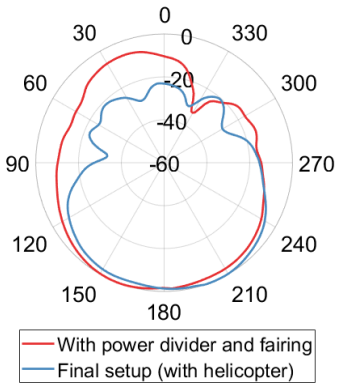

(a)

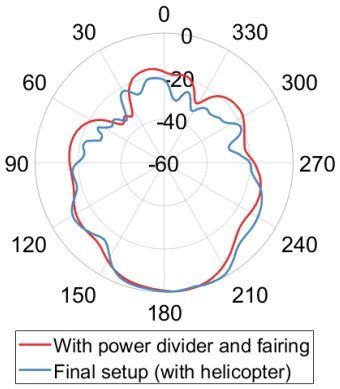

(b)

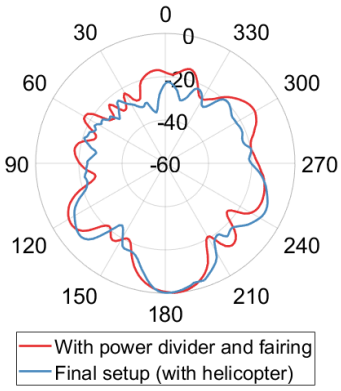

(c)

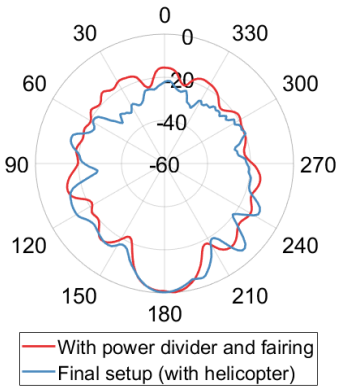

(d)

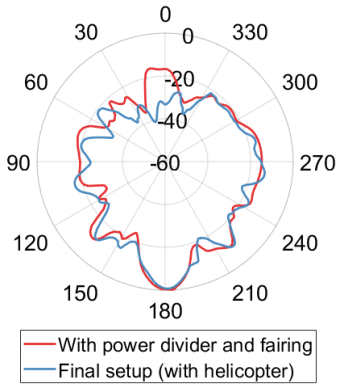

(e)

Figure 4-49: Radiation pattern of four element array on the full setup with rotorcraft at (a) 2 GHz, (b) 6 GHz, (c) 10 GHz, (d) 14 GHz, and (e) 18 GHz

The measured nadir gain of the transmit vertically polarized array on the full setup is shown in Figure 4-50. The platform effect is non-uniform due to the asymmetrical physical shape of the rotorcraft. The peak nadir gain is 15.88 dB at 10 GHz and the lowest is -5.63 dB at 13 GHz. There are effectively three nulls as the null at 1.23 dB in sub-band 4 has a large enough magnitude so that the three highlighted bands may be merged into a single one. The magnitude of the other two nulls is 2.49 dB at 5.5 GHz and 4.24 dB at 8.5 GHz. As previously discussed, each sub-band highlights a maximum of 6 dB variation in nadir gain and each band is processed individually. The equivalent backscatter response of the full pulse is stitched together from each sub-band.

The average nadir gain with power divider and fairing is 7.97 dB and with the final setup is 8.34 dB. The goal of having the nadir gain of the bulb antenna array within the 3 dB deviation of the average gain of the standard horn antenna is achieved. This satisfies the link budget requirements of the radar system. In addition to the signal processing techniques and digital

waveform shaping, the front-end is suitable to measure surface backscatter of extended targets like soil and snow.

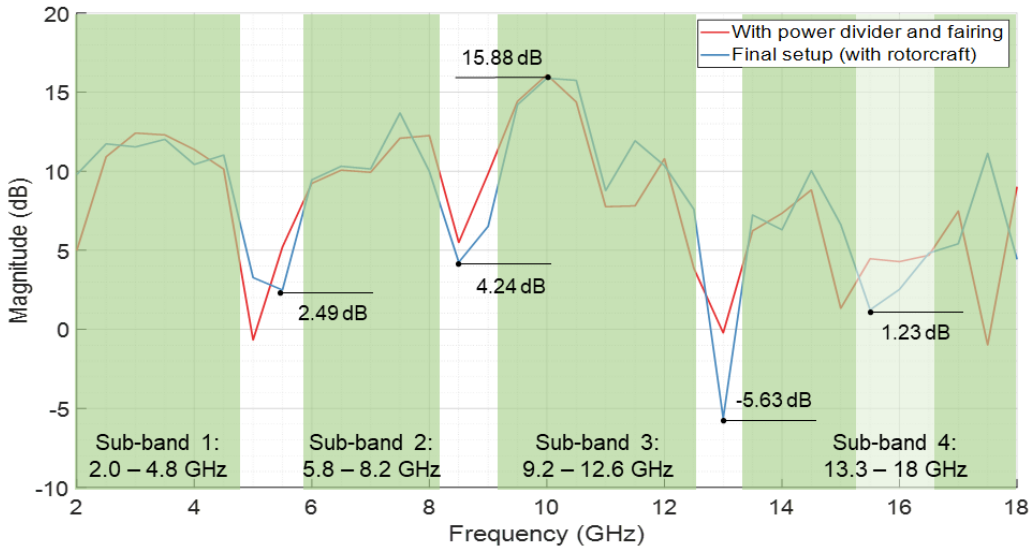

Figure 4-50: Measured nadir gain of the transmit vertically polarized array on rotorcraft with fairing and power dividers

5 Field Experiment

The full system tests are performed behind Nichols Hall at the University of Kansas campus. The test area is a patch of land with approximately two to three inches of mowed grass. A large metal sheet with dimensions approximately 1.83 m by 1.83 m (6 feet by 6 feet) is used for calibration.

The tests described in this section are initial proof-of-concept measurements. They are divided into two sub-sections: VNA measurements and 1U radar measurements. The antenna front-end system is separately characterized with metal and soil targets using a four-port VNA. A VNA is a transceiver primarily used for impedance measurements but can be setup to function as a radar. The crucial feature of this test setup is that the VNA and the cables can be calibrated such that the measurement is normalized and only the effect of the front-end on the target is recorded.

Further, the effects of the front-end may be corrected in the radar data to accurately discern target returns.

A large, 1U version of the RF section described in Section 3 is used for the radar measurements [42]. This design was the basis of the miniaturized system. The 1U system uses the same architecture of the miniaturized version. The test setup included the same Arena module to be used in the miniaturized rendition as the digital backend. The detection of soil moisture through these tests paved the way for assembling the miniaturized version on the Vapor 55.

In Section 3, the radar system is validated through the delay-line measurement. It characterizes the ability of the radar to detect a single point target but without the front-end. The effects of the antenna characteristics on the radar signal is discussed in Section 4. The impact of the front-end at distinct frequency points indicates the performance within a single pulse. However, when the full system is integrated together, the front-end also affects the signal in fast time. Figure 5-1 shows a simplified picture of signal transmission relative to the front-end and the respective radar response measurement.

In Section 4.2, the current distribution of the single element shows that the surface current flows symmetrically along the perimeter of the bulb. When placed under the metal sheet, the radiation arises at nadir towards the soil and at zenith towards the metal sheet. In Section 4.5.1, the antenna is integrated such that the reflected wave from the metal sheet is intended to be the primary signal. Hence, the array is rotated so that the main radiation lobe is pointing at nadir and maximum gain is achieved. The consequence of achieving this favorable characteristic results in two transmit signals.

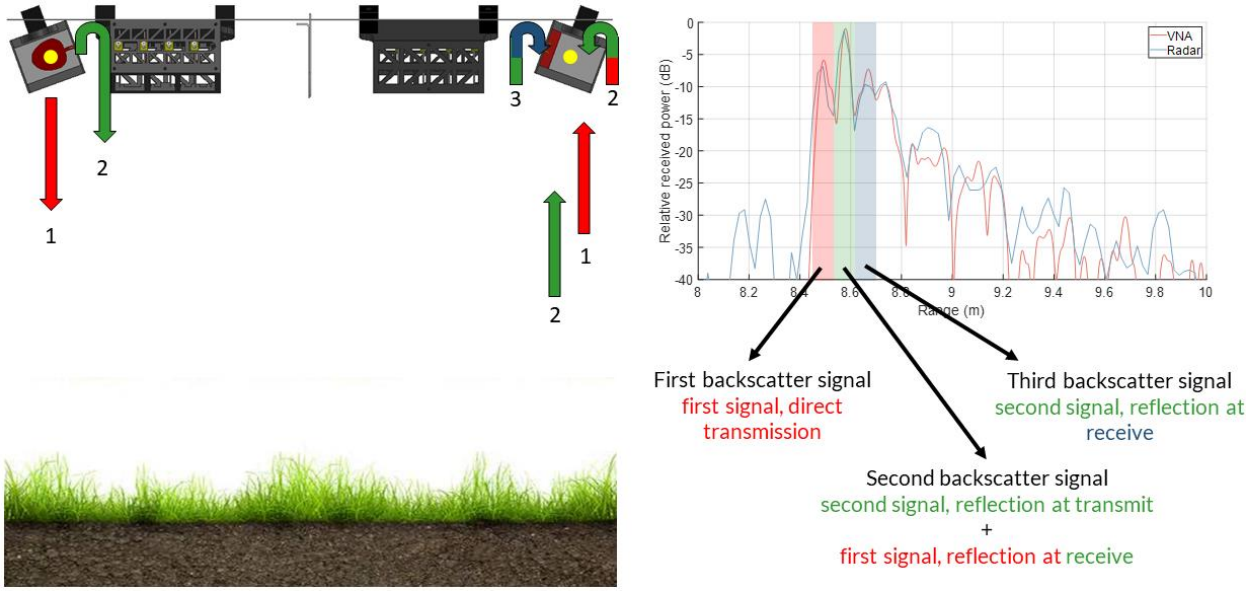

Figure 5-1: Effect of the front-end assembly observed in the frequency-domain response of the VNA and radar measurement

The first signal, shown as the red arrow in Figure 5-1, is the direct transmission from the antenna. The second signal is reflected off the metal sheet and is shown as the green arrow. The yellow circle on the antenna array denotes the phase center. The distance from the phase-center to the metal sheet along the 20° line towards nadir is 3.82 cm and the shortest distance between the phase-center and metal sheet is 3.44 cm. Therefore, as the second signal gets reflected from the metal sheet, the first signal is 7.64 cm away in the nadir direction.

The frequency domain response of the received signal relative to fast time is shown on the right side in Figure 5-1. The first received backscatter signal is the first signal from the direct transmission. As the second signal arrives at the receive antenna, a portion of the first signal that is not received proceeds past the phase center towards the metal sheet. The first signal reflects off the metal sheet and arrives at the phase center at the same time as the second signal. Hence, the second backscatter signal is a combination of the second signal reflected at transmit and the first signal reflected at receive. Similarly, the third backscatter signal is the second signal reflected at receive.

The position of the three backscattered signals relative to each other for VNA and Radar measurements is shown in Table 5-1. The values are from the calibration measurements performed with the large metal sheet. The difference between the co-polarized measurements and the distance from the phase-center to the metal sheet ranges from 0.6 cm to 1.7 cm. Similar difference in the relative received power are also observed for both co-polarization measurements. On the other hand, the relative positions for cross-polarization are significantly different and more tests must be performed to determine the reason for deviation.

The criteria for the proof-of-concept is to detect differences in backscatter between dry and wet soil. Multiple polarization measurements are recorded for three distinct look angles. The entire front-end is rotated about the longer dimension such that the antenna beam is rotated in the cross-track direction. The moisture state of the soil at the beginning of the test is considered as dry and after recording the measurements, a watering can is used to uniformly dampen the test area.

Table 5-1: Difference in range and relative power between the three backscatter signals for VNA and Radar tests with large metal sheet calibration

Measurement Type	VNA				Radar			
	Difference in Range (cm)		Difference in Relative Power (dB)		Difference in Range (cm)		Difference in Relative Power (dB)	
	1st and 2nd signal	2nd and 3rd signal	1st and 2nd signal	2nd and 3rd signal	1st and 2nd signal	2nd and 3rd signal	1st and 2nd signal	2nd and 3rd signal
Co-pol. Vertical	8.6	8.93	4.89	6.31	8.24	9.94	5.61	8.38
Co-pol. Horizontal	8.82	9.93	6.25	7.79	10.31 (8.4)	8.62	6.04	6.22
Cross-pol. Vertical	6.62	4.96	9.19	3.85	18.55	12.37	7	3.1
Cross-pol. Horizontal	5.41	6.51	10.03	7.05	-	-	-	-

The precise amount of water is not recorded as the goal of this test is to only discern between dry and wet state. The correlation between the backscatter changes and the exact change in moisture is out of scope for this work. To accurately determine the relative backscattering coefficient for each soil state a large sample space of soil measurements is required. Meaning, data must be recorded over a large piece of land instead of a single, static test area. Hence, for the initial tests, only the relative received power for each soil state is compared. The backscatter signatures that are indicative of soil moisture content will be used as reference for future tests with the miniaturized system on the UAS.

5.1 Vector Network Analyzer and front-end

The antenna front-end is suspended at a height of approximately two meters from the ground using a wooden fixture as shown in Figure 5-2. A wood panel is fastened to the payload tray brackets on the metal sheet. This assembly is attached to the triangular mount on the central rail of the wooden fixture. A close-up of the integrated assembly is shown in the inset of Figure 5-2.

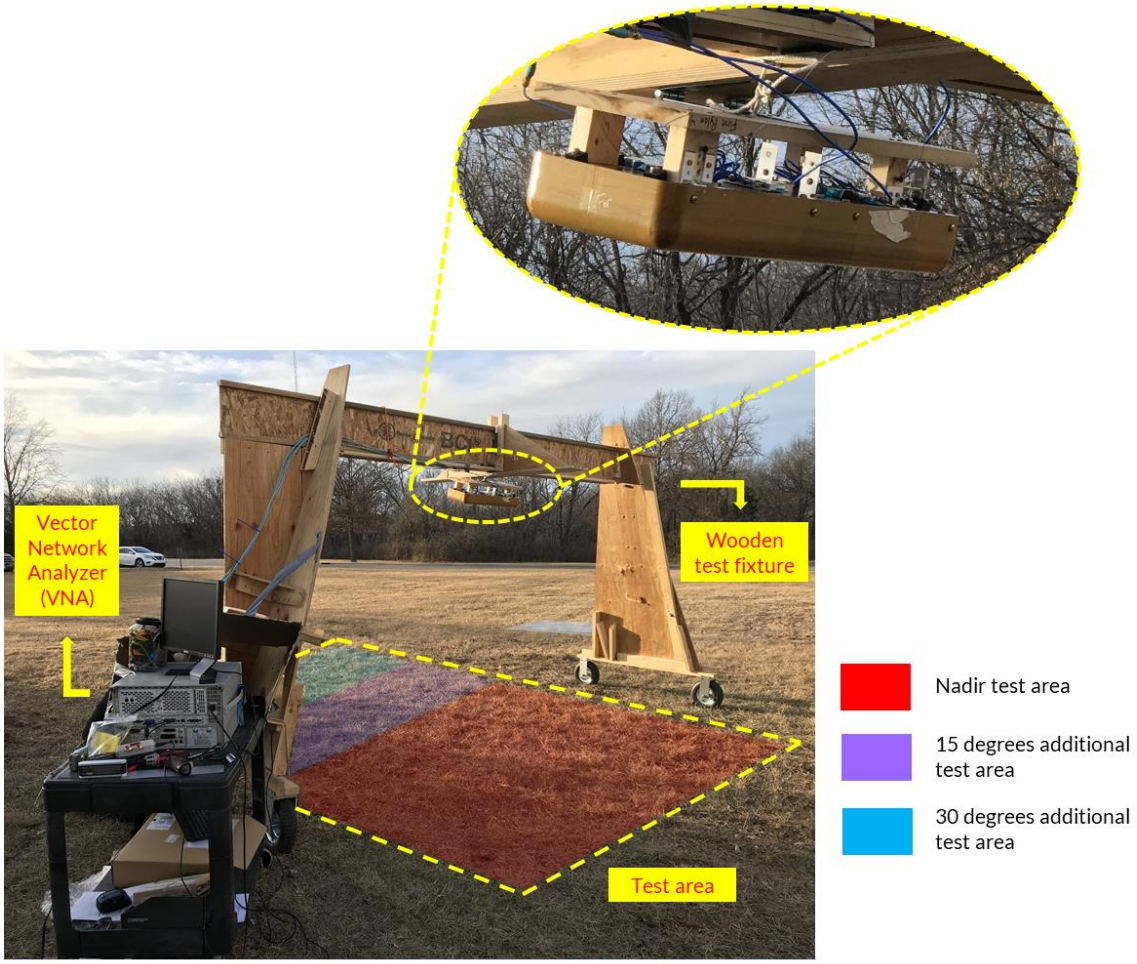

Figure 5-2: Picture showing the test setup for the VNA measurements

The four-port N5230C PNA-L Vector Network Analyzer and N4433A Electronic Calibration Module (ECal) by Keysight are used for the tests. All four polarization measurements are performed at three look angles and for two soil states. The data products discussed in this chapter are a combination of these variables and they are shown in Table 5-2.

Table 5-2: List of variables for the data products

Soil State	Look Angle	Polarization
Dry	0 degree	Co-polarization Vertical
Wet	15 degrees	Co-polarization Horizontal
	30 degrees	Cross-polarization Vertical
		Cross-polarization Horizontal

In addition to electromagnetic measurements, in-situ soil samples are collected to perform gravimetric measurements. Figure 5-3 shows the locations of the soil samples collected relative to the test fixture. The samples are weighed and then baked in a convection oven for 24 hours. Table X shows the values of the weights and the respective gravimetric moisture content. The measurements clearly indicate a change in moisture content between the dry and soil states. The average water content for dry soil is 36.97%, for wet soil is 46.44%, and hence there is an average change of 9.5% between the two moisture states.

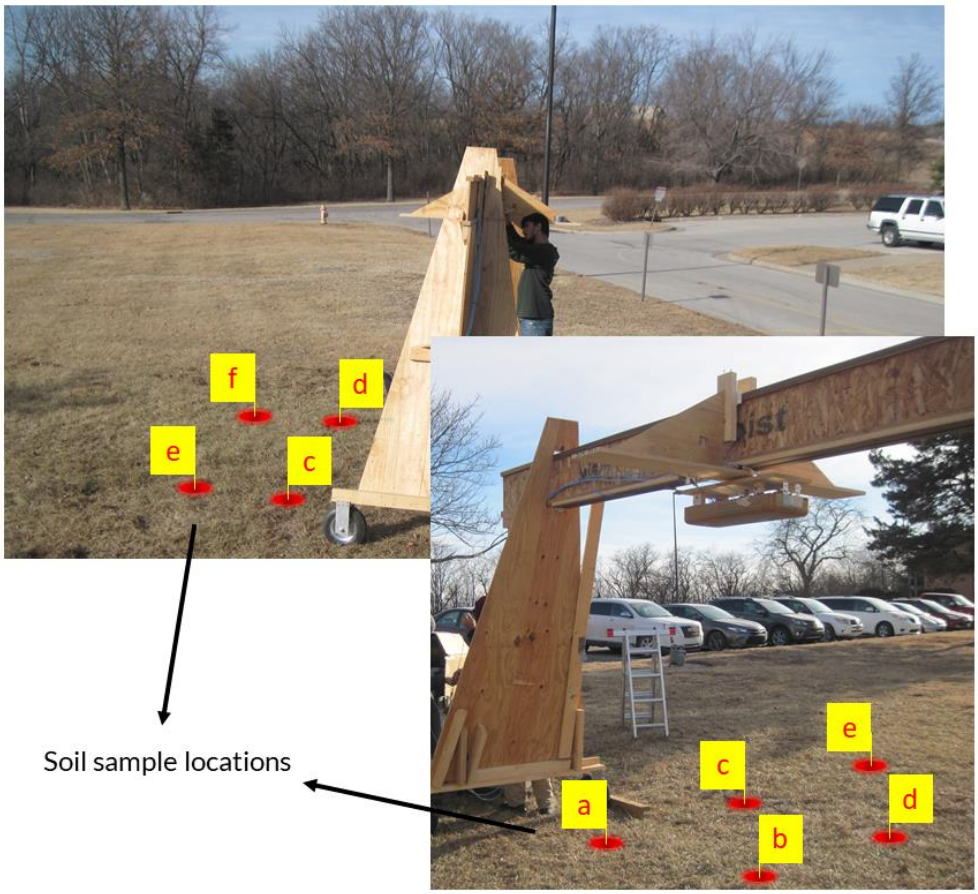

Figure 5-3: Pictures showing the locations of soil samples collected for determining gravimetric water content

The backscattering coefficient is dependent on the moisture content and surface roughness. To minimize the change in surface roughness, the samples for dry soil measurements are collected from locations ‘a’, ’c’, and ’e’. These are intentionally collected away from the nadir point of the

antenna footprint. To maximize the detection in moisture, the samples for wet soil measurements are also collected from locations ‘b’, ’d’, and ‘f’. It is assumed that the soil moisture in the ground is similar over a distance of two meters.

Table 5-3: List of recorded weight of soil samples and the evaluated gravimetric water content

Sample	Measurement	Location	Weight of jar (g)	Weight of original sample and jar (g)	Weight of dried sample and jar (g)	Gravimetric water content
A	Nadir Dry	a	144.65	209.96	193.64	33.31%
B	15 degrees Dry	c	145.23	233.64	208.84	38.99%
C	30 degrees Dry	e	144.94	217.71	197.44	38.61%
D	Nadir Wet	a	144.8	201.02	183.89	43.82%
E	Nadir Wet	b	144.73	233.9	202	55.7%
F	15 degrees Wet	c	144.18	208.5	186.86	50.7%
G	15 degrees Wet	d	144.39	207.49	189.89	38.68%
H	30 degrees Wet	e	144.39	224.52	199.18	46.25%
I	30 degrees Wet	f	144.89	220.3	197.45	43.47%

The gravimetric measurements provide a true reference for the change in moisture states when comparing the backscatter responses. On the other hand, the reference for time of arrival and backscatter profile is provided by the large metal sheet. The radar system and the soil responses are calibrated against the response to the large metal sheet. Figure 5-4 shows the frequency domain response of the VNA for the large metal sheet and Table 5-4 shows the values for the data points labeled in the figure.

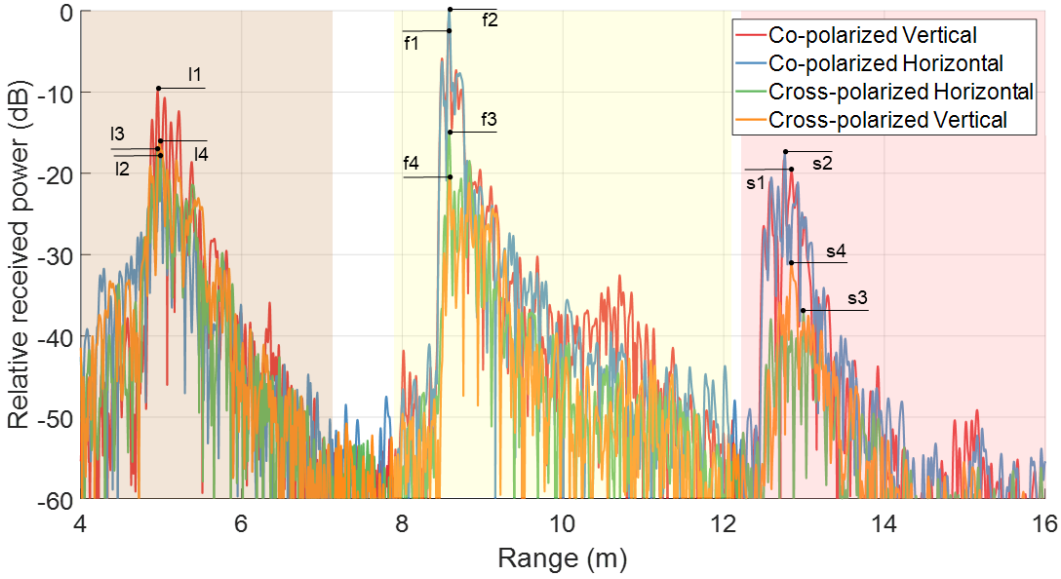

Figure 5-4: Frequency domain response of the VNA for large metal sheet calibration

Table 5-4: Range and relative power values for the data points marked in Figure 5-4

Signal Type	Label	Range (m)	Relative Received Power (dB)
Transmit leakage	l1	4.9544	-9.81
	l2	4.9809	-17.6
	l3	4.9544	-17.13
	l4	4.9754	-16.23
First backscatter	f1	8.5798	-0.99
	f2	8.582	0
	f3	8.5831	-15.18
	f4	8.5875	-20.63
Second reflected backscatter	s1	12.75	-18.36
	s2	12.7599	-17.57
	s3	12.9926	-37.15
	s4	12.8426	-31.13

The first band of signals received is the leakage from the transmitter (highlighted in tan color). This is easily removed with further signal processing as the leakage is fixed and constant in fast time. The second band of signals is the return from the large metal sheet (highlighted in light yellow color) and the third is the double-reflection as the signals are re-transmitted from the antenna front-end metal sheet towards the calibration target (highlighted in rose color).

In the first backscatter, the magnitude of the peak of the cross-polarized components are 19.64 and 15.18 dB below the respective vertical and horizontal co-polarization components. The two sharp peaks for the vertical and horizontal polarizations indicate the primary return from the calibration target. The difference between the maximum value of the peaks in the first and second backscatter indicates the two-way range between the antenna front-end and calibration target. The difference between the peaks is 4.1779 m and therefore the VNA detects the calibration target at 2.089 m below the antenna front-end. The range vector in the frequency-domain plots is relative and does not indicate the absolute value of the target range. The signal fast time includes the propagation delay through the coaxial cables and hence further correction is necessary.

The frequency-domain response for dry soil at nadir, 15°, and 30° look angles is shown in Figure 5-5 (a) to (c). There is sufficient backscatter at nadir for the relatively dry soil to result in a second reflected backscatter similar to the large metal sheet calibration. The difference between the first and second backscatter for the metal sheet is 17.37 dB for vertical and 17.57 dB for horizontal co-polarization. Similarly, for dry soil at nadir, the difference is 26.54 dB and 26.44 dB respectively. Therefore, the dry soil causes extra attenuation of 9.17 dB and 8.87 dB respectively relative to the large metal sheet.

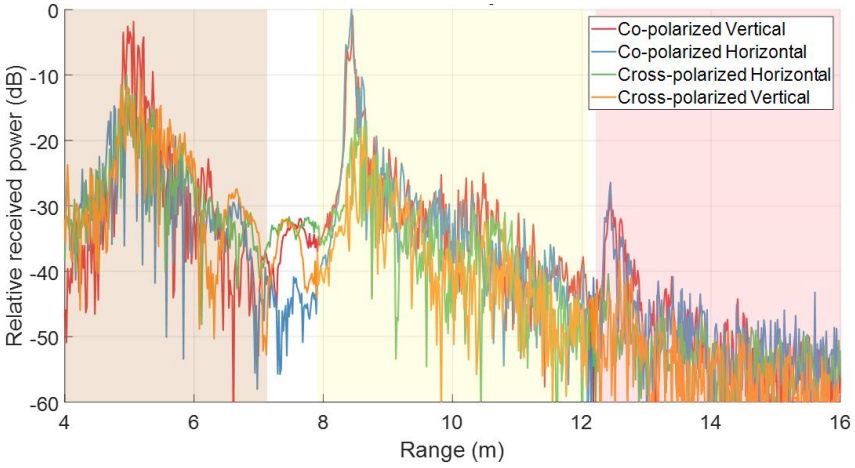

(a)

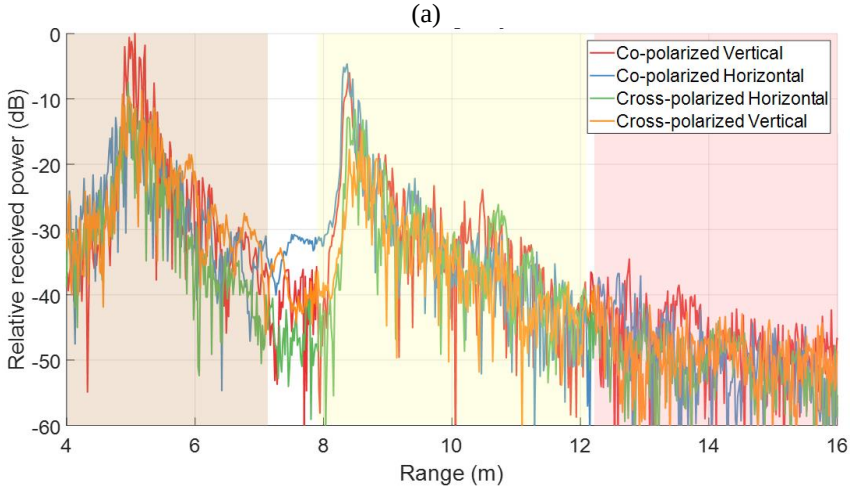

(b)

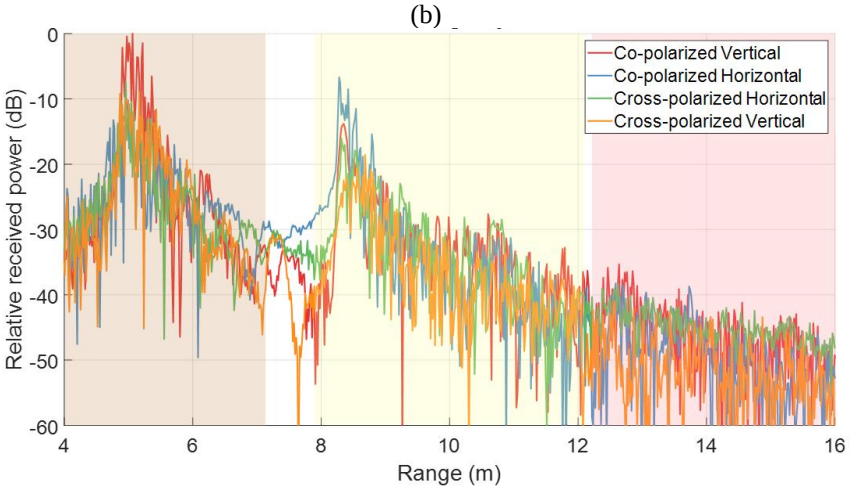

(c)

Figure 5-5: Frequency domain response of the VNA for dry soil at (a) Nadir, (b) 15 degrees, and (c) 30 degrees look angles

Figure 5-5 (a) to (c) show the change in the trend of the first backscattered signal as the look angle is changed. The magnitude of the peak for vertical co-polarization changes from -0.95 dB at nadir to -5.9 dB at 15°, and to -14.01 dB at 30°. Similarly, for horizontal co-polarization it changes from 0 dB at nadir to -4.64 dB at 15°, and to -6.68 dB at 30°. Therefore, based on the trend, horizontal polarization provides a stronger backscatter than the vertical component for dry soil at different look angles in the cross-track direction. This is also observed for cross-polarization in the same figures.

The response for wet soil at nadir, 15°, and 30° look angles is shown in Figure 5-6 (a) to (c). Similar to dry soil in Figure 5-5 (a), there is a second reflected backscatter for wet soil as shown in Figure 5-6 (a). However, there is a decrease in magnitude by an average value of 4.68 dB. The difference between the first and second backscatter is 29.49 dB for vertical and 28.76 dB for horizontal co-polarization. Therefore, the wet soil causes extra attenuation of 12.12 dB and 11.19 dB respectively relative to the large metal sheet. The increase in moisture relative to dry soil decreases the difference between the first and second backscatter by 2.95 dB and 2.32 dB respectively.

The peak magnitude of the first and second backscatter decreases, however there is an increase in relative received power over successive range bins. The maximum power received from the nadir point decreases as the average power over the entire antenna footprint area increases. The effect over a wider range is seen in the close-up of the soil returns for vertical and horizontal co-polarization in Figure 5-7 (a) and (b). The tables beside the figures show the values of the data points labeled in the figures.

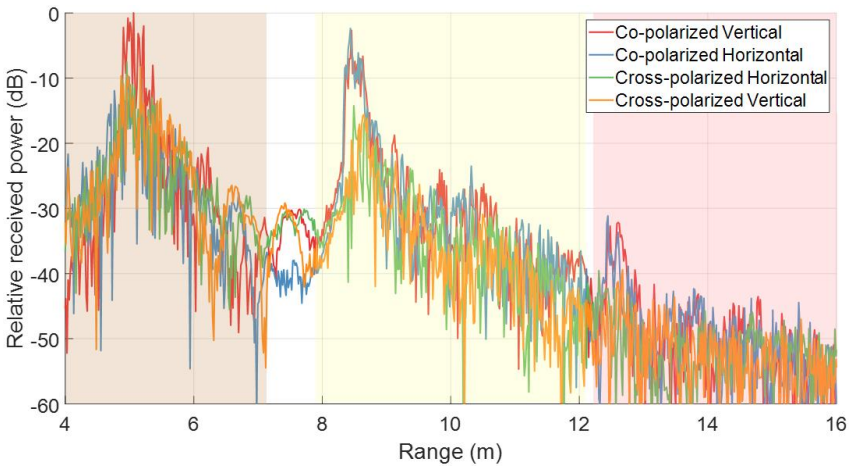

(a)

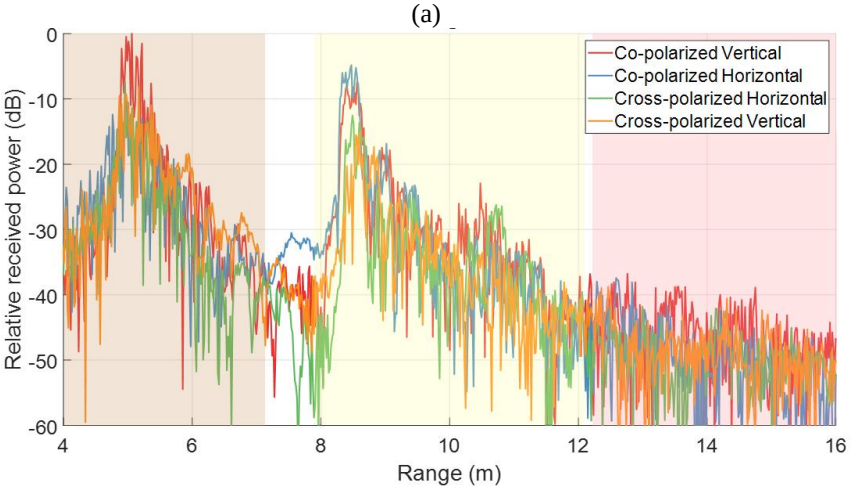

(b)

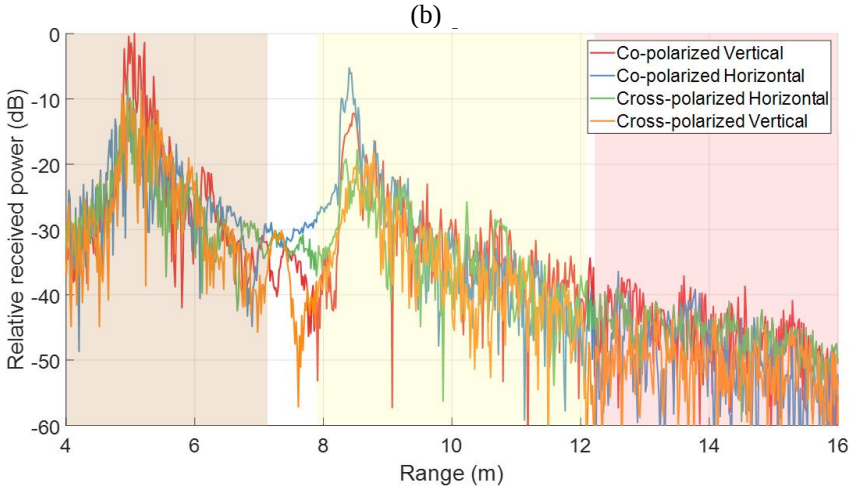

(c)

Figure 5-6: Frequency domain response of the VNA for wet soil at (a) Nadir, (b) 15 degrees, and (c) 30 degrees look angles

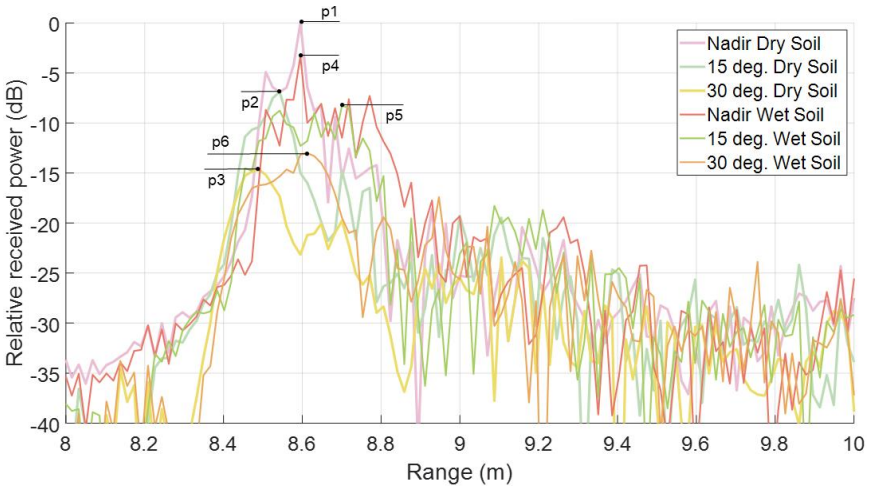

(a)

Label	Range (m)	Relative Received Power (dB)
p1	8.5951	0
p2	8.5423	-6.87
p3	8.4896	-14.65
p4	8.5951	-3.33
p5	8.7006	-8.24
p6	8.6127	-13

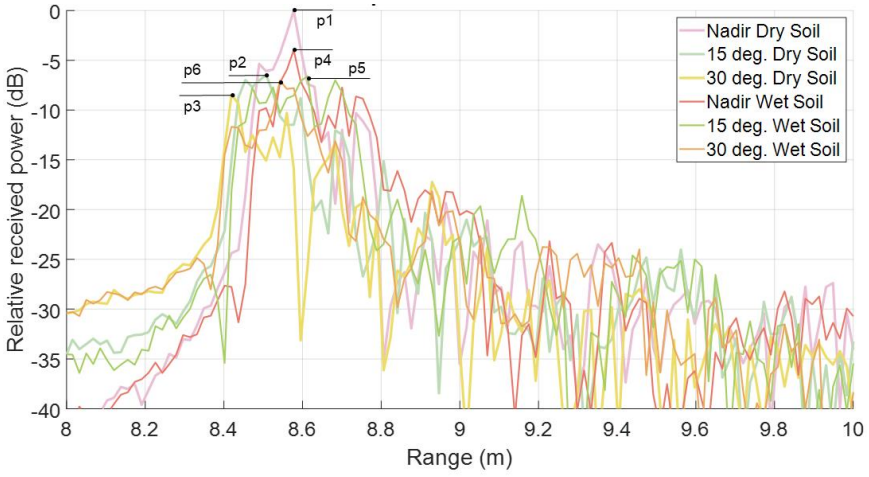

(b)

Label	Range (m)	Relative Received Power (dB)
p1	8.5775	-0
p2	8.5072	-6.47
p3	8.4193	-8.47
p4	8.5775	-3.99
p5	8.6127	-6.6
p6	8.5423	-7.03

Figure 5-7: Close-up of the VNA soil return for (a) Vertical and (b) Horizontal co-polarization

To analyze the widening of the backscatter response, a point of 10 dB from the peak is chosen as the cut-off to include approximately 90% of the average received power. The difference in range from the peak to this cut-off is compared for each look angle and soil state. In Figure 5-7 (a), the cut-off for dry soil at nadir is 0.0879 m away from the peak and for wet soil it is 0.1934 m. Therefore, the relative received power at nadir for wet soil has increased at more than twice the range for dry soil.

Similarly at 15°, the cut-off for dry soil is 0.0703 m from the peak and 0.0879 m for wet soil. However, the peak power does not occur at the same range bin for both soil states. The relative received power for wet soil at the same range bin of the dry soil is lower by 0.52 dB from the peak power of the wet soil. If the cut-off is considered from the same range bin, the value for wet soil is 0.2461 m. Therefore, the power at 15° for wet soil has increased at more than thrice the range for dry soil.

At 30°, the cut-off for dry soil is 0.1055 m from the peak and 0.123 m for wet soil. Similar to the 15° case, the peak power does not occur in the same range bin as the dry soil. The power at the same bin for wet soil is 3.23 dB lower from the peak and the cut-off from this point is 0.2461 m. Therefore, the relative received power at 30° for wet soil has increased by more than twice the range for dry soil.

On the other hand, for horizontal polarization in Figure 5-7 (b), the relative received power for wet soil increases nearly twice the range for nadir and 15° and close to one-half times at 30°. The moisture content increases the power received from a section of the footprint area but is distinctly less than vertical polarization. However, as mentioned previously, the peak power of the backscatter for horizontal polarization is larger. In particular, the relative received power increases by 6.18 dB for dry soil at 30°, 1.64 dB for wet soil at 15°, and 5.97 dB for wet soil at 30°.

In addition to calculating the deviation in range at the 10 dB cut-off, the curves are normalized and the trapezoidal area under the curve is computed. Figure 5-8 shows the normalized plots and a table shows the area under the normalized curve for each look angle and soil moisture state. There is a clear distinction in the width of the curves between the dry and wet soil states except for horizontal polarization at 30°. The exception is due to an increase in peak power of 1.44

dB and a decrease in average power over an area due to dominant forward scattering at 30° for high moisture.

The increase in received power over a wider range can be easily discerned by the highlighted sections (not at 10 dB cut-off) in Figure 5-9 (a) to (c). Figure 5-9 (a) also includes the results from the metal sheet calibration for comparison. The cross-polarization measurements do not indicate any clear patterns like the co-polarization counterparts and more tests are required to determine the reason.

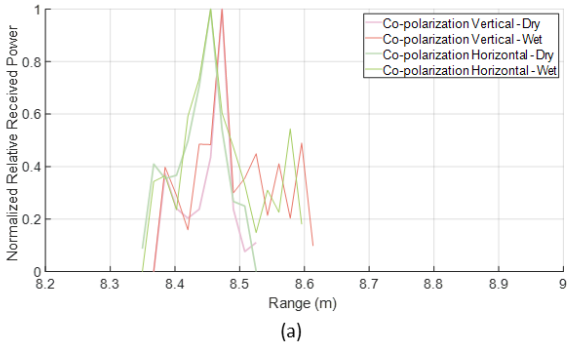

(a)

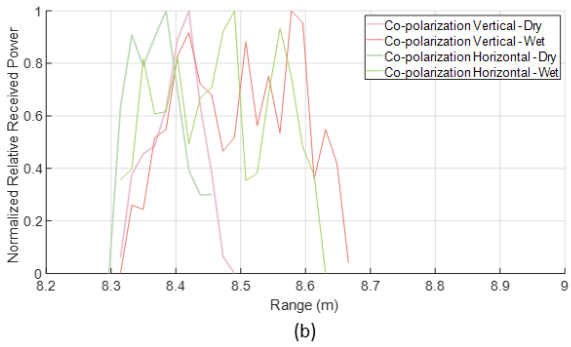

(b)

Look angle	Soil moisture state	Area under normalized curve (cut-off at 10 dB from peak)	
		Vertical	Horizontal
Nadir	Dry	2.86 sq. units	4.44 sq. units
Nadir	Wet	5.29 sq. units	5.99 sq. units
15 degrees	Dry	4.95 sq. units	5.77 sq. units
15 degrees	Wet	11.73 sq. units	11.18 sq. units
30 degrees	Dry	8.84 sq. units	9.2 sq. units
30 degrees	Wet	9.55 sq. units	6.47 sq. units

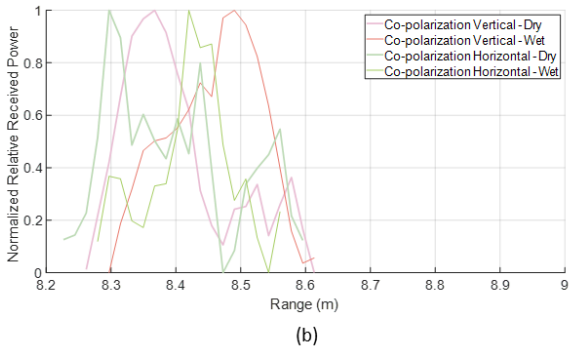

(b)

Figure 5-8: Normalized plots of the soil returns at the 10 dB cut-off for (a) Nadir, (b) 15°, (c) 30°, and a table showing the area under the normalized curve for each look angle and soil moisture state

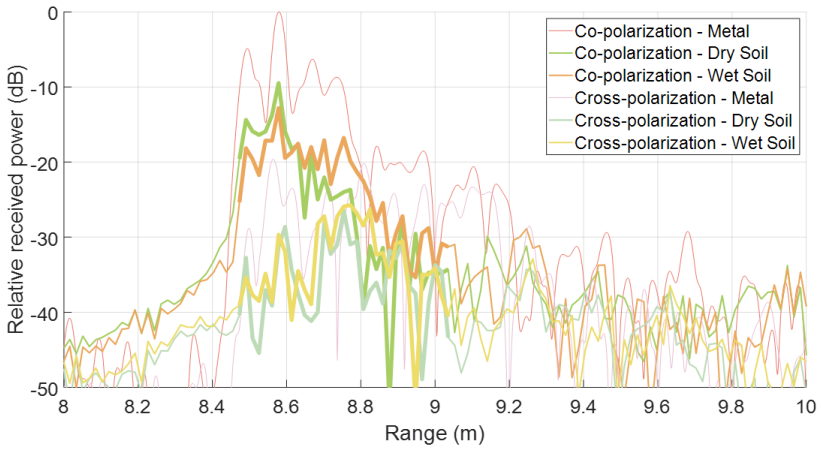

(a)

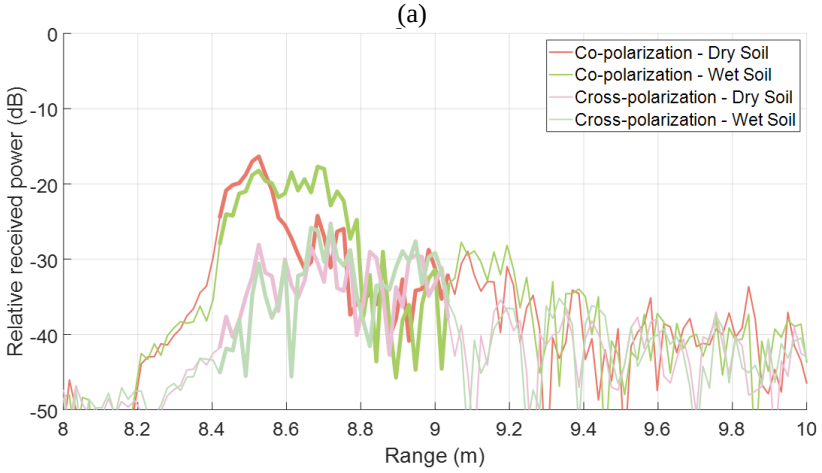

(b)

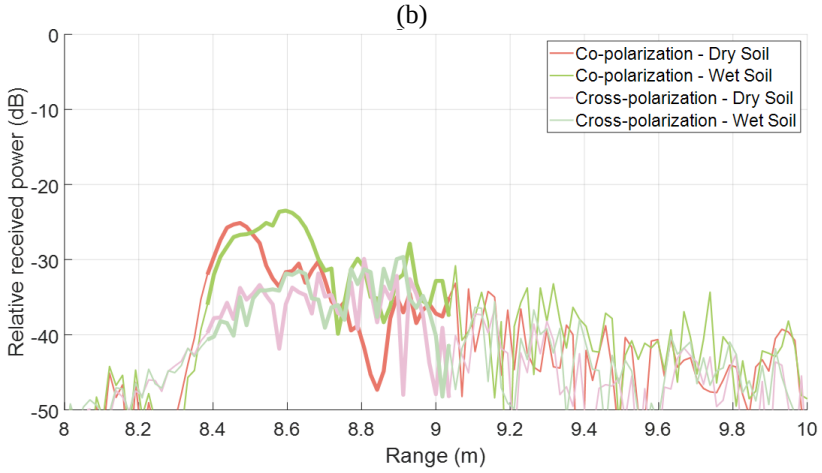

(c)

Figure 5-9: Close-up of the VNA soil return for vertical polarization at (a) Nadir, (b) 15 degrees, and (c) 30 degrees and the highlighted sections indicate the difference between dry and wet soil

The inference from these tests is that vertical polarization indicates the moisture content by increasing the received power over a wider range. The horizontal polarization results in a larger

peak power and the backscatter is less affected at smaller rotation angles in cross-track direction. The VNA and antenna front-end are capable of detecting changes in soil moisture and the effects of the front-end relative to soil as an extended target is documented.

5.2 Prototype radar and front-end

The radar measurements are performed at the same location a month apart from the VNA measurements. The absolute moisture level of the soil is likely to have changed between tests. However, the change in absolute value does not affect the measurements since the relative change in moisture during the duration of the test is measured.

The exact same coaxial cables and connectors used for the VNA tests are re-used to maintain consistency between the measurements. Figure 5-10 shows a picture of the 1U radar and delay line on a cart beside the wooden fixture. The performance of the 1U radar is verified through a delay-line measurement before the soil test and the result is shown in Figure 5-11. The response is detected at 60 dB above the noise floor and the 3 dB resolution is 1.56 cm.

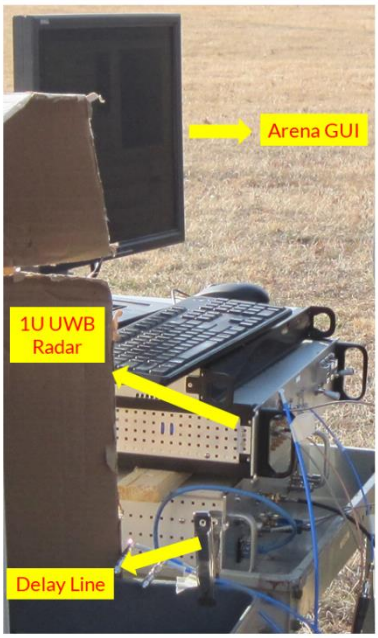

Figure 5-10: Picture showing the 1U Radar and delay line on a cart

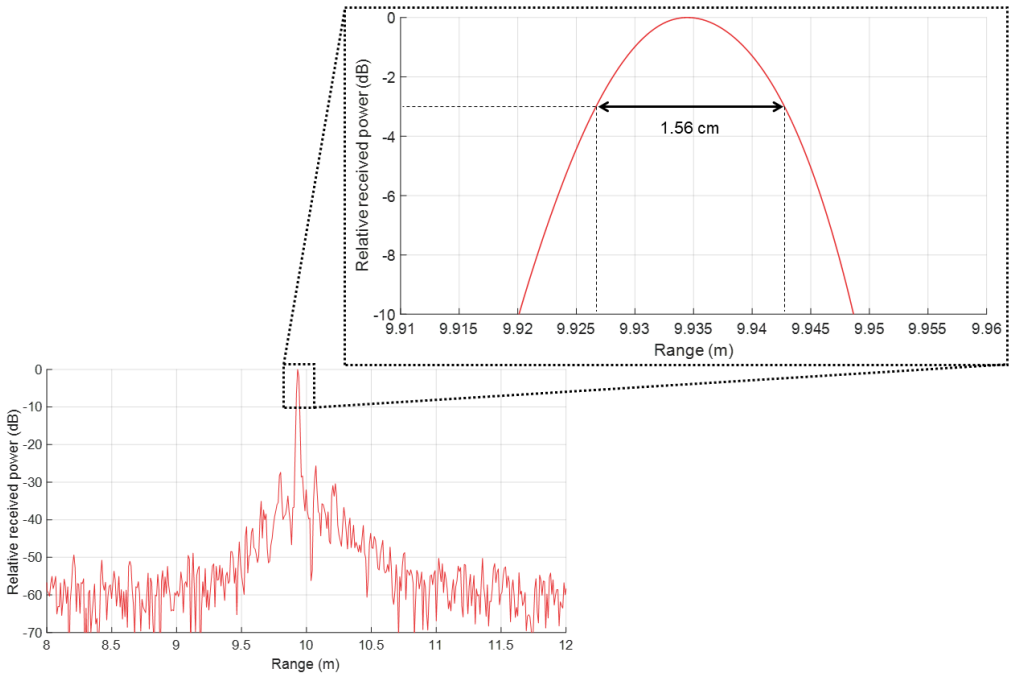

Figure 5-11: Delay-line response of the 1U radar and a close-up of the peak indicating the resolution

Figure 5-12 shows a picture of the entire setup during the radar measurements. The large metal sheet used for calibration is shown along with the highlighted test area. Clutter from the metal rim of the wheels on the wooden fixture may be excluded by measuring the shortest path distance between the antennas and the wheels and excluding the measurement from that range bin.

The frequency-domain response of the 1U radar for the large metal sheet calibration is shown in Figure 5-13 and the values of the labeled data points are shown in Table 5-5. The leakage from the transmitter is present at the same range bins as the VNA measurement and the magnitude of the peaks in the leakage band is between 10.1 dB and 20.7 dB relative to the first backscatter maximum. The overall shape of the backscatter profile and the magnitude of the first and second backscatter are similar to the VNA measurement. The second backscatter is 20.58 dB and 22 dB below the respective peaks for vertical and horizontal co-polarization. The two-way range between the first and second backscatter is 4.1434 m and hence the radar detects the calibration target at 2.0717 m below the front-end.

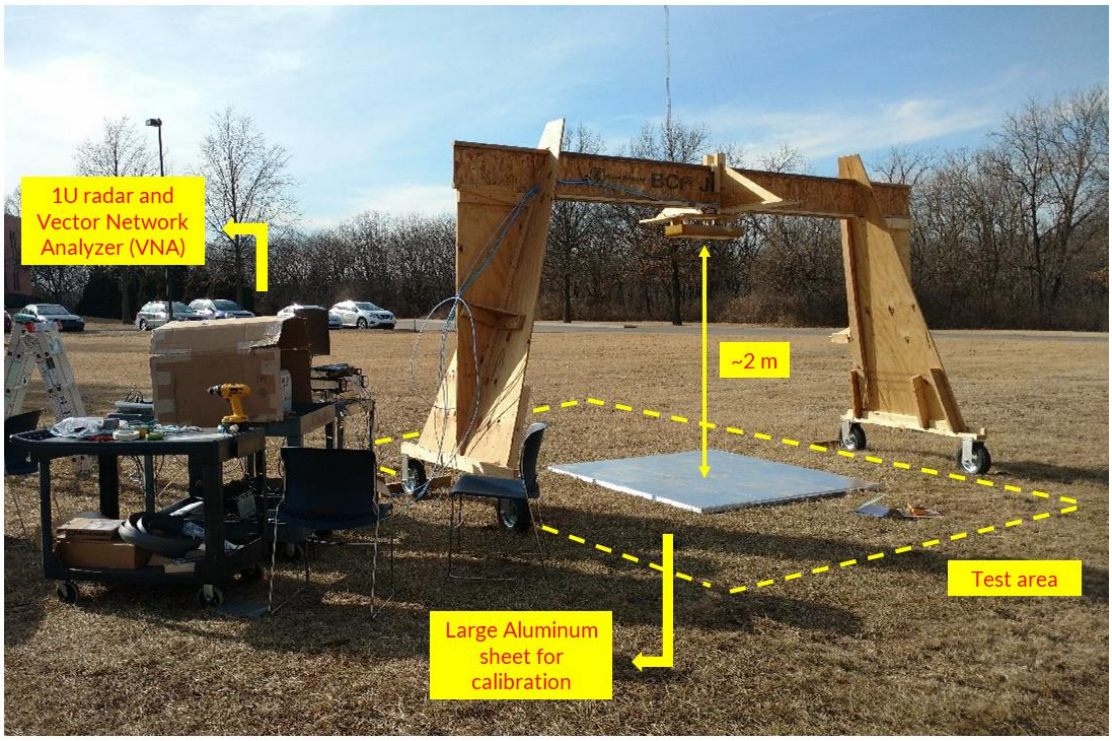

Figure 5-12: Picture showing the test setup for Radar measurements

The radar measurements are recorded only for three polarization combinations as the 1U radar only has two channels. Therefore, the measurements are repeated by swapping the cables for each antenna array. For these initial tests, the horizontal cross-polarization is excluded for convenience but will be explored in future.

The response for dry soil at nadir, 15°, and 30° look angles is shown in Figure 5-14 (a) to (c). Unlike the VNA measurements, the second backscatter signal is not detected for dry soil at nadir for radar measurements. This is attributed to a reduction in transmit power of 10 dB from the VNA measurements and a likely change in soil moisture and roughness.

The magnitude of the peak for the vertical co-polarization at nadir is -5.85 dB, at 15° is -18.7 dB, and at 30° is -21.35 dB. For horizontal co-polarization, the magnitude changes from -4.17 dB at nadir, to -10.3 dB at 15°, and -8.26 dB at 30°. Therefore, similar to the VNA measurements, the horizontal polarization has a stronger backscatter power than the vertical counterpart. This is also observed for the wet soil measurements shown in Figure 5-15 (a) to (c).

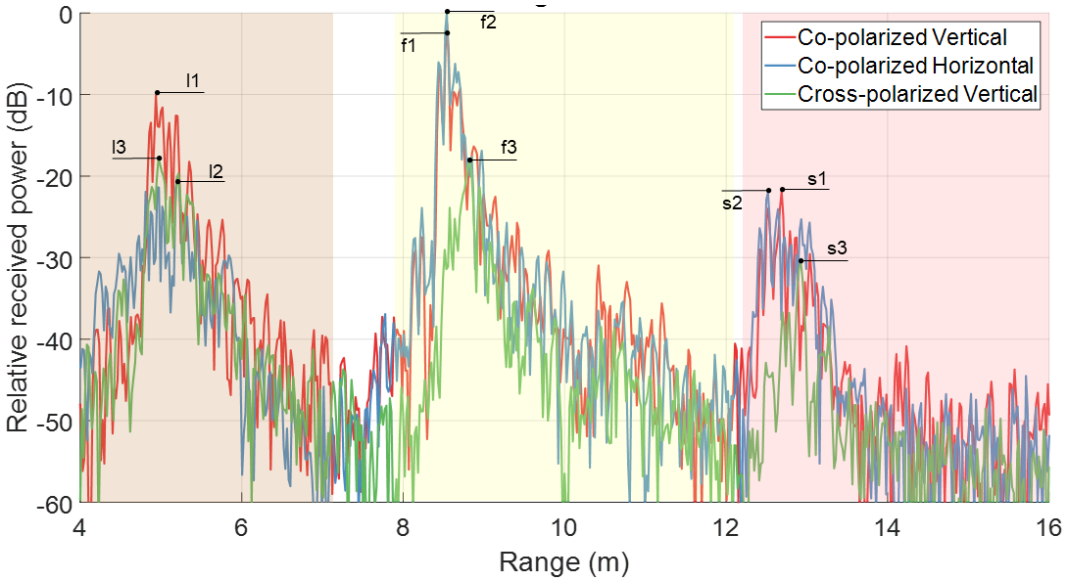

Figure 5-13: Frequency domain response of the radar for large metal sheet calibration

Table 5-5: Range and relative power values for the data points marked in Figure X

Signal Type	Label	Range (m)	Relative Received Power (dB)
Transmit leakage	l1	4.9662	-10.1
	l2	5.2304	-20.07
	l3	4.9982	-17.86
First backscatter	f1	8.5737	-1.29
	f2	8.5699	0
	f3	8.8531	-18.28
Second reflected backscatter	s1	12.7171	-21.87
	s2	12.5485	-22
	s3	12.9553	-30.63

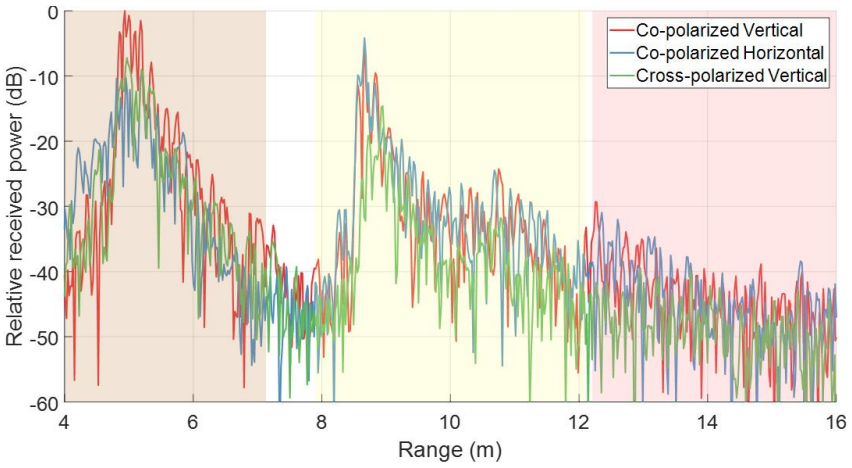

(a)

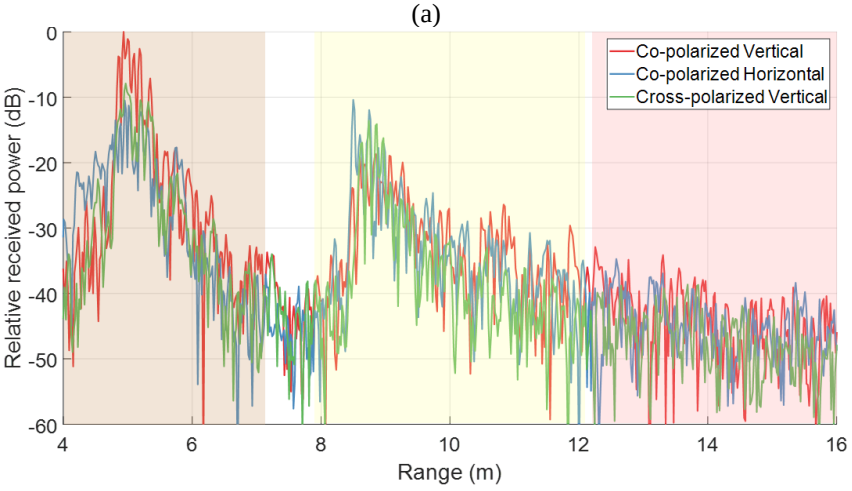

(b)

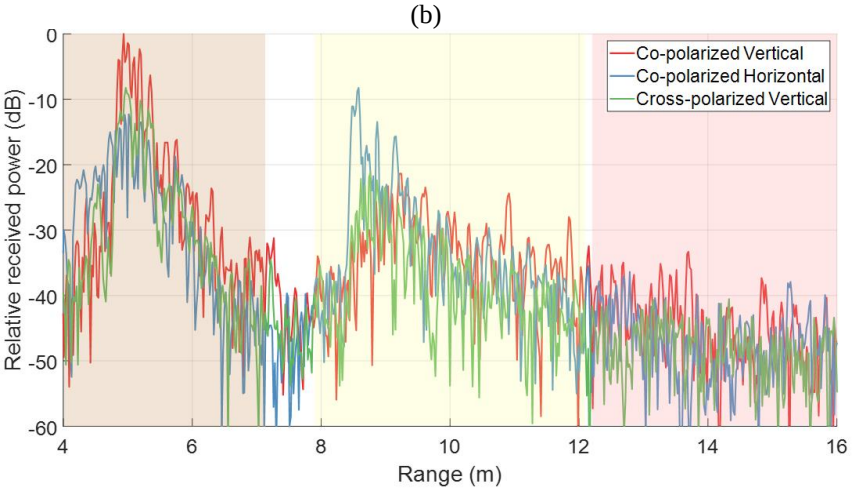

(c)

Figure 5-14: Frequency domain response of the Radar for dry soil at (a) Nadir, (b) 15 degrees, and (c) 30 degrees look angles

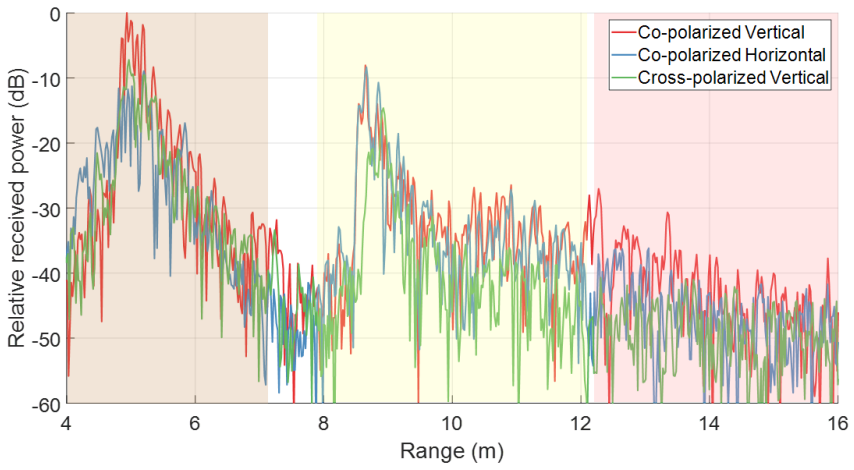

(a)

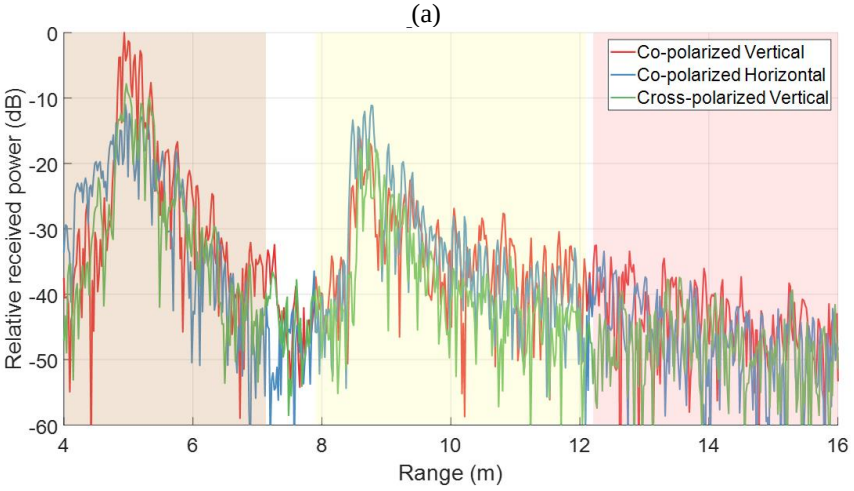

(b)

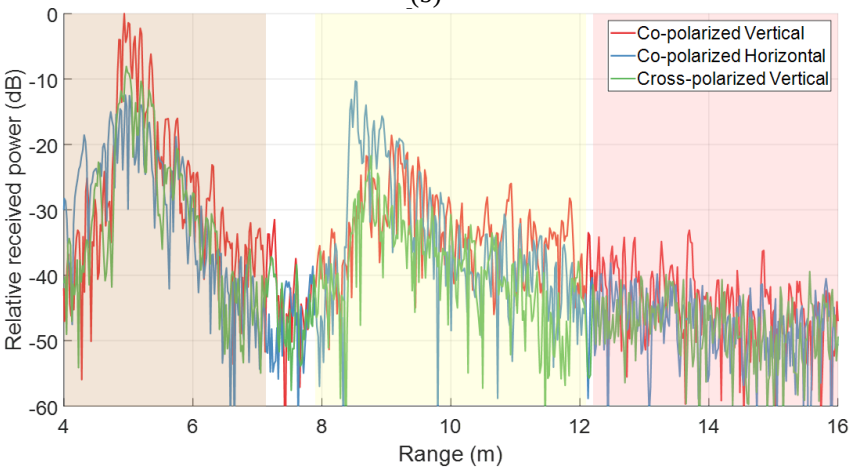

(c)

Figure 5-15: Frequency domain response of the Radar for wet soil at (a) Nadir, (b) 15 degrees, and (c) 30 degrees look angles

In Figure 5-15 (a), three distinct peaks are observed in the second backscatter region for the wet soil measurement at nadir. The magnitude of the peaks are -28.03 dB, -27.04 dB, and -30.66 dB and relative to the dry soil measurement, the moisture content increases the second backscatter by approximately 4 – 5 dB at nadir. Further, the magnitude of the peak in the first backscatter region diminishes in magnitude, as also seen in the VNA measurement. For vertical co-polarization, the relative received power at nadir is -8.05 dB, at 15° is -15.68 dB, and at 30° is -18.61 dB. For horizontal co-polarization, the power of the maximum peak at nadir is -8.35 dB, at 15° is -11.13 dB, and at 30° is -10.3 dB. Clearly, a larger soil return is observed for horizontal polarization at all three look angles for wet soil.

A close-up of the soil return for both vertical and horizontal co-polarizations and for each look angle is shown in Figure 5-16 and Figure 5-17. The respective tables show the values of the data points labeled in the figures. The radar measurements show a difference between dry and wet soil but the distinction is not as apparent as the VNA measurements. A significant widening of the received power over successive range bins is not clearly observed.

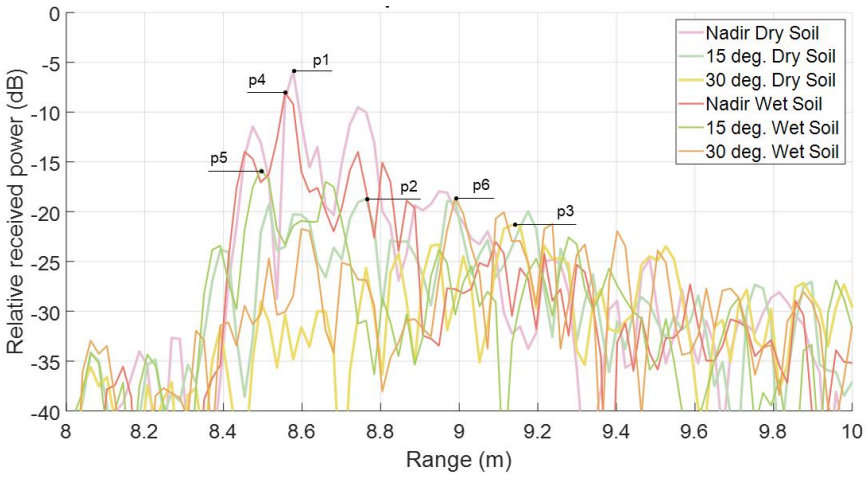

Label	Range (m)	Relative Received Power (dB)
p1	8.5774	-5.85
p2	8.7629	-18.7
p3	9.1339	-21.35
p4	8.5567	-8.05
p5	8.4949	-15.69
p6	8.9896	-18.61

Figure 5-16: Close-up of the Radar soil return for Vertical co-polarization

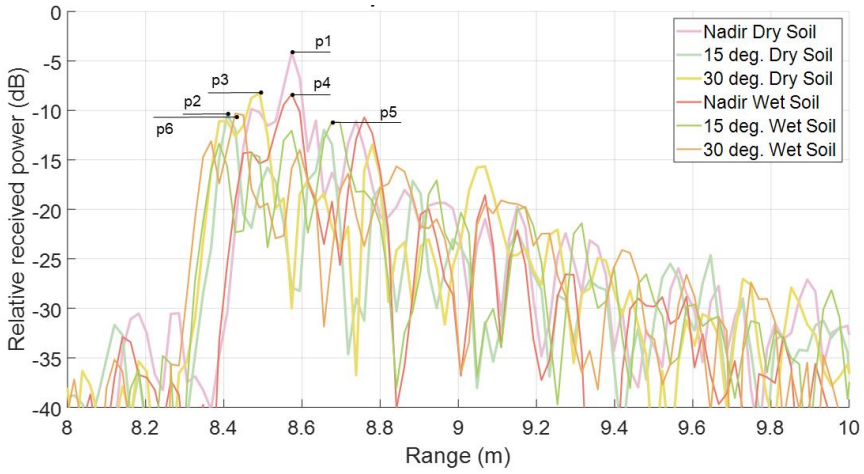

Label	Range (m)	Relative Received Power (dB)
p1	8.5736	-4.17
p2	8.4087	-10.4
p3	8.4911	-8.26
p4	8.5736	-8.35
p5	8.6767	-11.13
p6	8.4293	-10.3

Figure 5-17: Close-up of the Radar soil return for Horizontal co-polarization

An increase in relative received power is observed for the vertical co-polarization at nadir, but at the 20 dB cut-off from the peak. The cut-off reference must be extended by 10 dB relative to the VNA results to accurately discern the radar measurements. On the other hand, in spite of the horizontal polarization showing increased power levels, the relative measurement between dry and wet soil is similar for all three look angles. Figure 5-18 (a) to (c) show the highlighted sections that indicate the differences between dry and wet soil. There are areas with difference in relative power by more than 6 dB, yet the range of variations are similar for both measurements.

Although the watering method is uncalibrated and it is possible that the soil composition during the radar measurements is not exactly same as the VNA measurements, the lack of difference between dry and wet soil is likely due to a change in system parameters. The effect of negative amplitude slope in the pulse caused due to the RF section, change in window functions, and an increase in pulse length increase the corresponding range side-lobe levels [17]. These effects are compounded when the pulse is radiated by the antenna front-end and the drop in nadir gain at 5.5 GHz, 8.5 GHz, and 13 GHz degrade the amplitude of the main range lobe and further increase the side-lobe levels. Furthermore, it is observed that the noise floor of the radar increases by 10 dB relative to the VNA. The consequence of these undesirable effects is the target

characteristics from the main lobe are obscured by range side-lobes and clutter. Hence, the differences between dry and wet soil are not conspicuous.

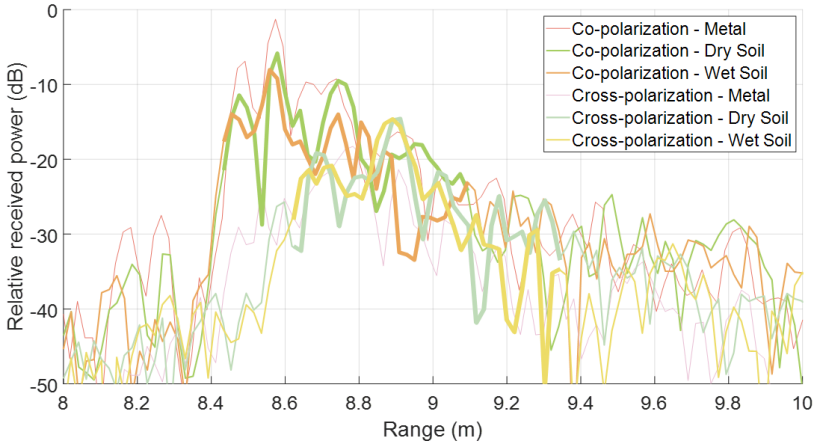

(a)

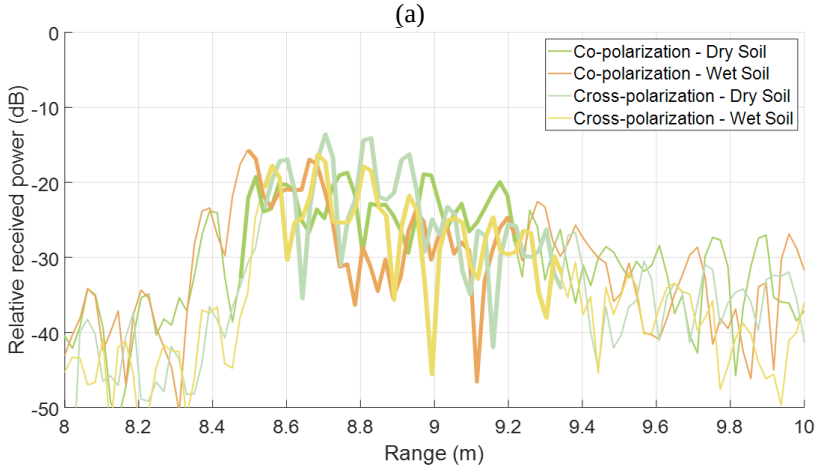

(b)

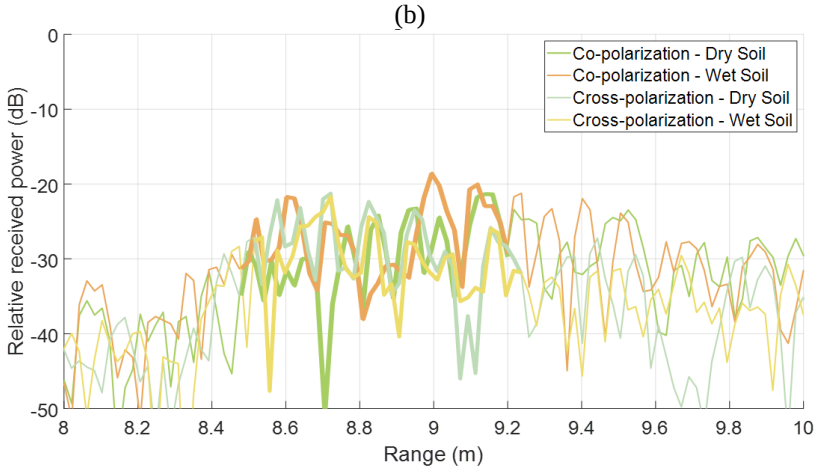

(c)

Figure 5-18: Close-up of the Radar soil return for vertical polarization at (a) Nadir, (b) 15 degrees, and (c) 30 degrees and the highlighted sections indicate the difference between dry and wet soil

One of the solutions to this problem is sub-band processing. As mentioned in the previous chapter, the entire 16 GHz bandwidth is divided into four separate sub-bands. Table 5-6 shows the starting and ending frequency points, sub-bandwidth, and the corresponding theoretical range resolution when a Hanning window is applied. The received waveform is divided into the corresponding bands and the Fourier Transform is performed over each sub-band separately. Additionally, the four sub-bands are stitched together and the transform is performed over the equivalent 13.3 GHz band. This results in a 2.7 GHz loss of bandwidth and causes the range resolution to be coarser by 16.85%. This is not a cause for concern when doing scatterometer measurements. The vertical resolution is crucial for sounding applications where sub-surface features like internal layers need to be interpreted. For this application, the backscatter received over a surface area is integrated and aggregate features of the target are interpreted [17]. The advantage of sub-banding is that it results in five more data products from each measurement. Each data product presents a slightly different characteristic of the target and hence new information can be interpreted from each one. The total information of the scene is deduced from an aggregate of all six data products, including the full-band without sub-banding.

Table 5-6: Frequency and range resolution values for all six data products considered in sub-band processing

	Start Frequency (GHz)	End Frequency (GHz)	Bandwidth (GHz)	Theoretical Resolution with Hanning Window (cm)
Full-band	2	18	16	1.53
Sub-band 1	2	4.8	2.8	8.73
Sub-band 2	5.8	8.2	2.4	10.19
Sub-band 3	9.2	12.6	3.4	7.19
Sub-band 4	13.3	18	4.7	5.2
Equivalent full-band	2	18	13.3	1.84

Figure 5-19 shows the frequency domain response for the large metal sheet at nadir for all four sub-bands. It also shows the nadir gain of the vertically polarized array in the final configuration with the rotorcraft. Each sub-band plot shows the backscatter response for vertical and horizontal co-polarization and vertical cross-polarization.

The coarse resolution of the backscatter response for all three polarizations is easily distinguishable. The peak for cross-polarization is again displaced to the right of the co-polarization responses similar to the full bandwidth response in Figure 5-13. The consistency observed across the bandwidth indicates that this effect is inherent to the cross-polarization type. However, this must be cross-verified with horizontal cross-polarization but a similar effect is likely to be observed.

The peaks for both co-polarization in sub-band 1 show a distinct main lobe with a long, gradual leading edge and an immediate null on the trailing edge. In particular, the horizontal polarization has a deep null at nearly -55 dB. In other words, the shape is similar to that of the delay line response. It indicates that the signal did not experience significant losses and since a calibration target is used, this is attributed to the effect of the antenna gain in sub-band 1. This is corroborated by the low variation in nadir gain of 2.2 dB from 2 – 4.6 GHz, which is 92.86% of the sub-bandwidth. Moreover, the response for sub-band 4 shows a diminished main-lobe with increased side-lobe levels for all three polarization types. In particular, the increased trailing edge side-lobes over a large range can obscure target information, as previously discussed. The total variation in nadir gain for sub-band 4 is 9.89 dB and this is greater than the 6 dB limit considered for dividing into sub-bands. Hence, this shows the importance of nadir gain flatness for resolving target information in scatterometer mode and a solution to overcome the undesirable effects by processing over 6 dB sub-bands.

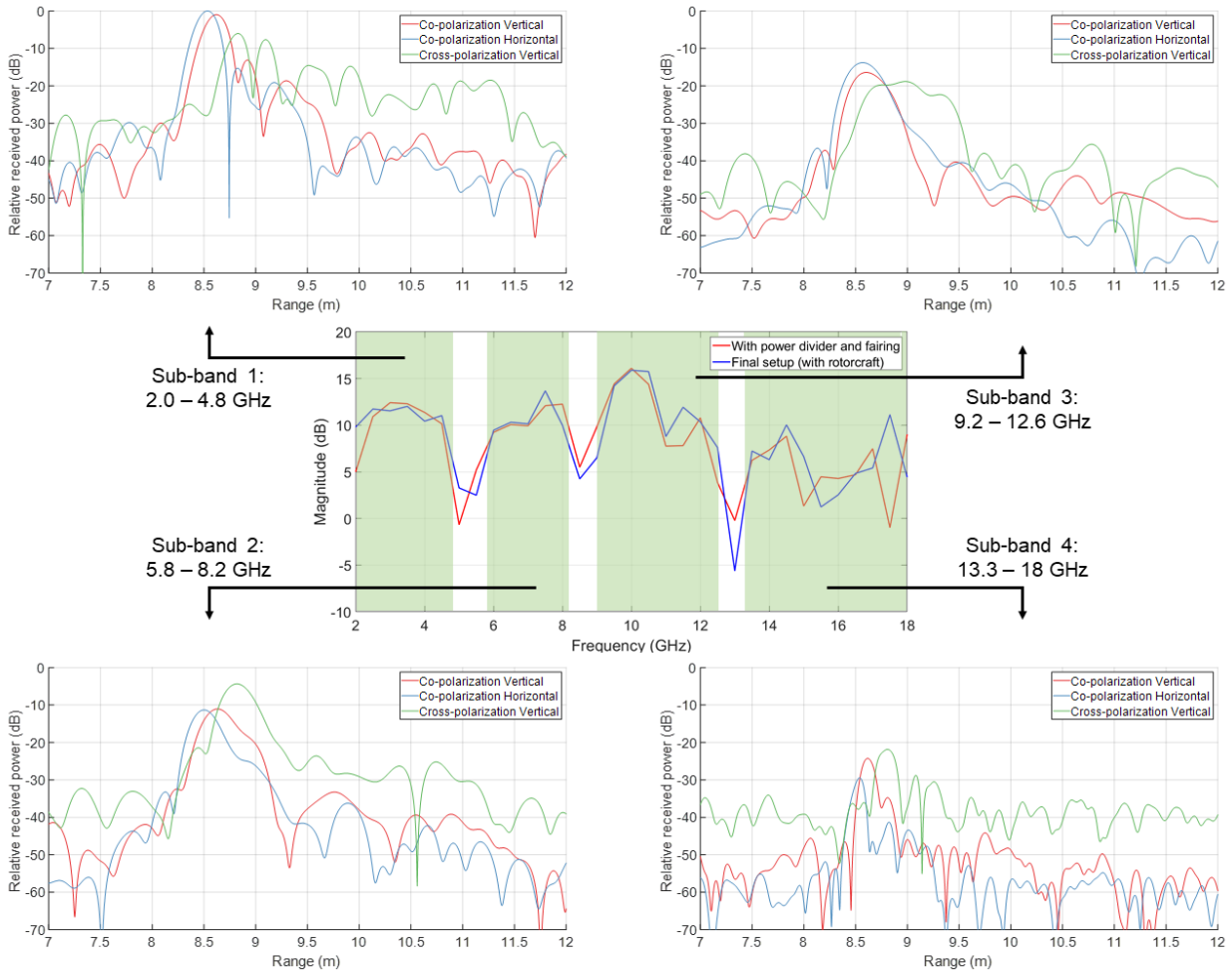

Figure 5-19: Close-up of the frequency domain response of the radar for large metal sheet calibration at nadir over all four sub-bands (top and bottom rows). The nadir gain of the vertically polarized array with rotorcraft is also shown for reference (center)

The top plot in Figure 5-20 shows the frequency domain response for the metal sheet at nadir and for vertical co-polarization. The traces show the differences between the responses when integrated over the entire 16 GHz bandwidth and the stitched 13.3 GHz bandwidth. The range and relative power values for the peak, leading-edge side-lobe, and trailing-edge side-lobe (in that order) are shown in Table 5-7.

The magnitude of the peak for the stitched sub-bands decreases to -4.6 dB due to a reduction in signal power from the null-bands removal process. The leading-edge SLL, which is the first received backscatter from the direct transmission, decreases by 8.63 dB and the trailing-

edge SLL is 0.42 dB. The sub-banding process results in an effect similar to a window function and this causes a reduction in the side-lobe levels. Nonetheless, the second received backscatter is the primary signal and therefore this effect is favorable to discern target returns.

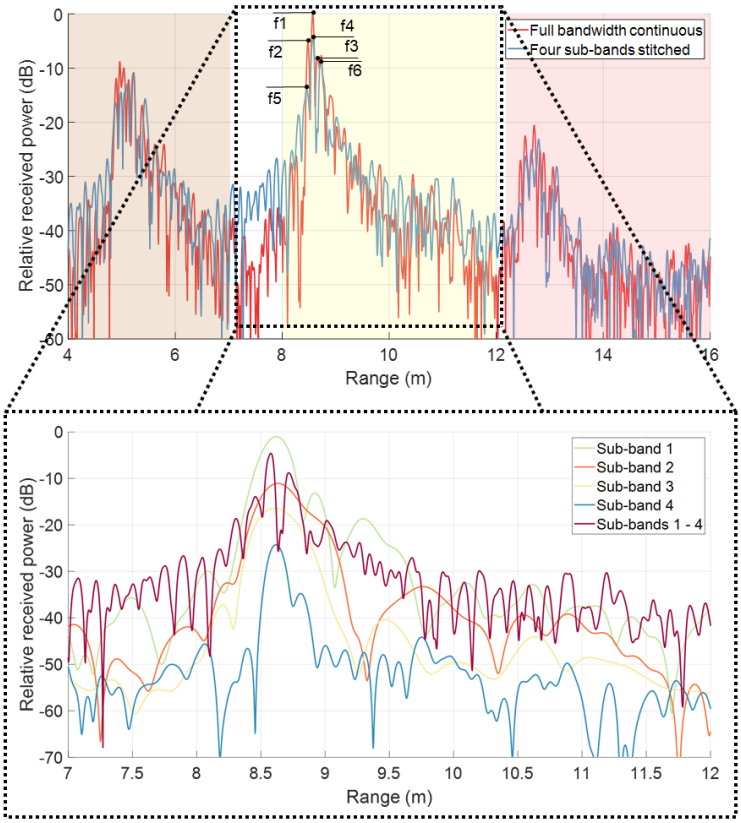

Figure 5-20: Frequency domain response of the radar for large metal sheet calibration at nadir. The plot on the top shows the vertical co-polarization response when integrated over the entire 16 GHz bandwidth (red) and over the stitched 13.3 GHz bandwidth (blue). The plot on the bottom shows the response when integrated over each sub-band and the trace 'Sub-bands 1 – 4' shows the stitched 13.3 GHz bandwidth response.

Table 5-7: Range and relative power values for the data points marked in Figure 5-20

Signal Type	Label	Range (m)	Relative Received Power (dB)
Full bandwidth continuous	f1	8.5713	0
	f2	8.4804	-5.27
	f3	8.6566	-8.35
Four sub-bands stitched	f4	8.5774	-4.6
	f5	8.4568	-13.9
	f6	8.7165	-8.77

The bottom plot in Figure 5-20 shows the frequency domain response for all four individual sub-bands. The traces for sub-band 1 and the stitched sub-bands 1 – 4 are similar and overlap significantly over the entire range for the backscatter. This indicates that the lowest part of frequency band, that is, 2 – 4.8 GHz contributes towards most of the backscatter power. However, the higher frequency bands contribute by resolving features of the target as indicated by a trend of increasing sinusoids in the response when observed sequentially from sub-bands 1 to 4.

Figure 5-21 shows the results of sub-band processing for dry and wet soil. The time-domain response is divided, stitched, and then integrated over the 13.3 GHz bandwidth. The frequency domain response is shown for vertical co-polarization at nadir, 15 degrees, and 30 degrees. A picture on the left in Figure 5-21 shows the test setup during the radar measurements. The test area is highlighted in yellow and a representation of the illuminated antenna footprint on the soil is shown in red. The dimensions of the represented footprint are not to scale. The backscatter profile corresponding to the range covered by the representative footprint is highlighted in the plots. The values of these highlighted ranges in the plots is a rough estimation from the test setup and is intended for easy visualization.

In the nadir plot for dry and wet soil, the magnitude of the response for wet soil (blue) is distinctly larger than dry soil (red) from 8.74 m to 10.79 m. This indicates an aggregate increase in relative received power for wet soil over dry soil for an extended range from the nadir point. The continuous and uniform increase in backscatter power is attributed to the addition of moisture content in soil. Similar increases in magnitude are observed in the 15 degree and 30 degree plots, with the latter having four easily distinguishable peaks. The overall spreading of the energy in increasing range is indicative of angular observation as the pulse-limited illumination interacts with the soil at an oblique angle.

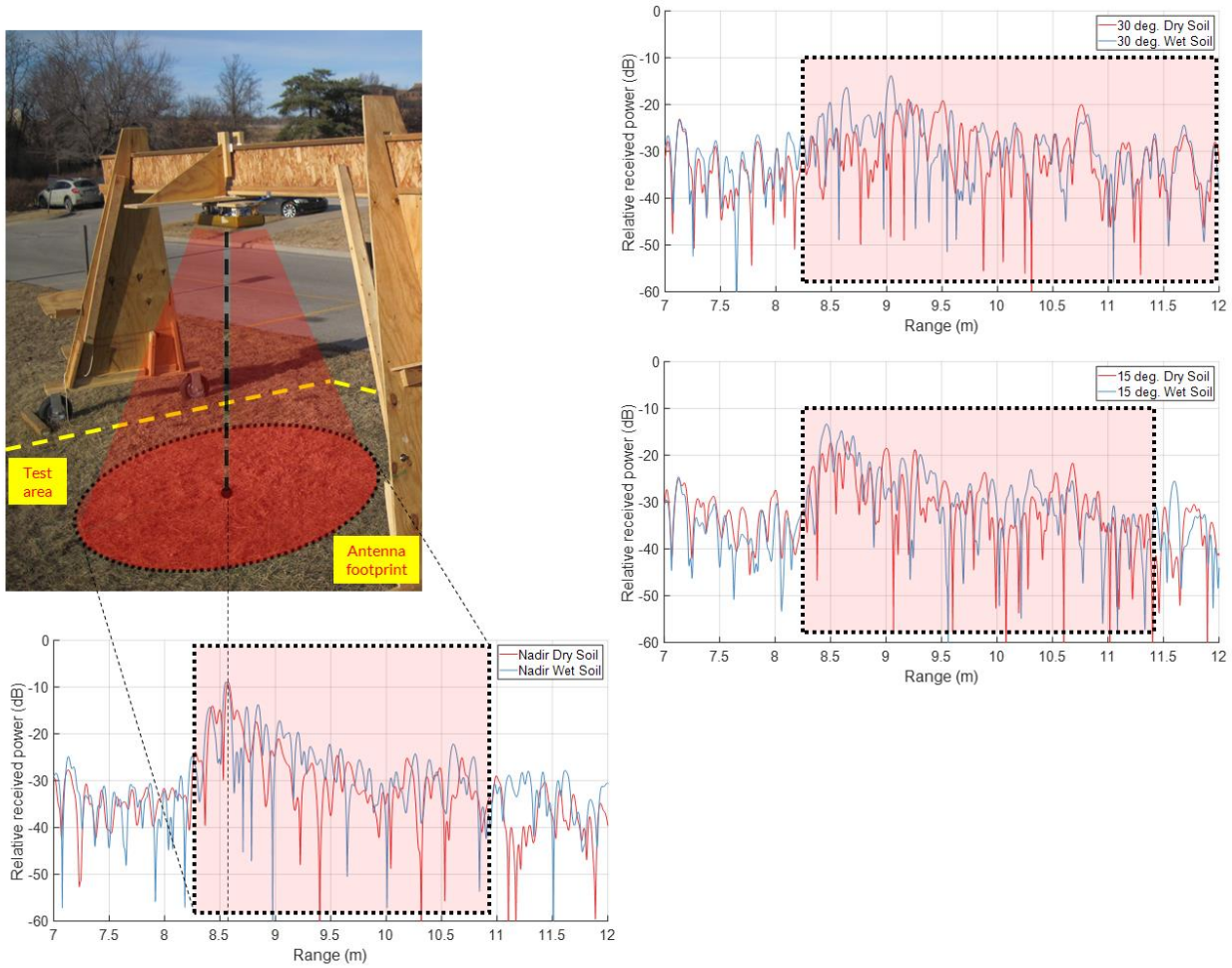

Figure 5-21: Picture of the test setup and a representation of the illuminated test area. The plots show the equivalent stitched frequency domain response of dry and wet soil at nadir, 15 degrees, and 30 degrees for vertical co-polarization. The highlighted section

Figure 5-22 shows a close-up of the frequency domain response at nadir, 15 degrees, and 30 degrees and compares the full 16 GHz integrated bandwidth and two individual sub-bands that show differences between dry and wet soil. While Figure 5-21 clearly shows a different response for wet soil, analyzing the individual sub-bands also provides additional information. As previously discussed, each data product indicates a slightly different characteristic due to a change in frequency of observation.

The widening of the main backscatter signal for wet soil is observed in the VNA measurements but is not apparent in the initial radar measurements. After sub-band processing, the

widening is observed for wet soil (yellow) at nadir in sub-band 1 as shown in Figure 5-22 (a). The peak widens and the roll-off of the trailing edge increases at the 10 dB level by 6.5 cm. Increased soil returns are also observed at 9.5 and 9.79 m. On the other hand, for sub-band 4, a distinct peak is observed at 8.71 m for wet soil with an increase in magnitude of 11.43 dB. The higher part of the frequency bandwidth is observed to be sensitive to moisture at nadir for co-polarization but the poor SNR suggests high losses.

Contrastingly, in Figure 5-22 (b), the widening of the backscatter peak is not observed for wet soil at 15 degrees. In fact, the width for dry soil at 10 dB is greater by 10.76 cm than wet soil. At a non-zero observation angle, the increase in reflectivity due to an increase in moisture content causes the forward scattering to be dominant over back scattering. Moreover, the presence of moisture can be attributed to the increased soil returns at 9.3 and 9.76 m, similar to the nadir response. On the other hand, for sub-band 2, a distributed response with a maximum at 8.99 m for dry soil turns into two distinct peaks at 8.59 m and 9.27 m for wet soil. An increase in relative power of 7.8 dB and 1.32 dB is observed respectively. The maximum peak for wet soil moves to the left of dry soil and closer to the nadir peak. This indicates an increase in nadir return due to the moisture, in spite of the 15 degree look angle.

Similar change in backscatter is also observed for the 30 degree response, as shown in Figure 5-22 (c). The equal width of the primary backscatter peak between dry and wet soil indicates that at this angle, the forward scattering is dominant over change in moisture state. However, the magnitude of the backscatter peak increases by 3.82 dB and there is an increase in soil returns at 9.3 m, 9.59 m, 10.04 m, and 11.07 m. For sub-band 2, a distributed response is again observed due to illumination over a large swath at the 30 degree look angle. The magnitude of the peak increases by 4 dB and occurs at 8.97 m for wet soil.

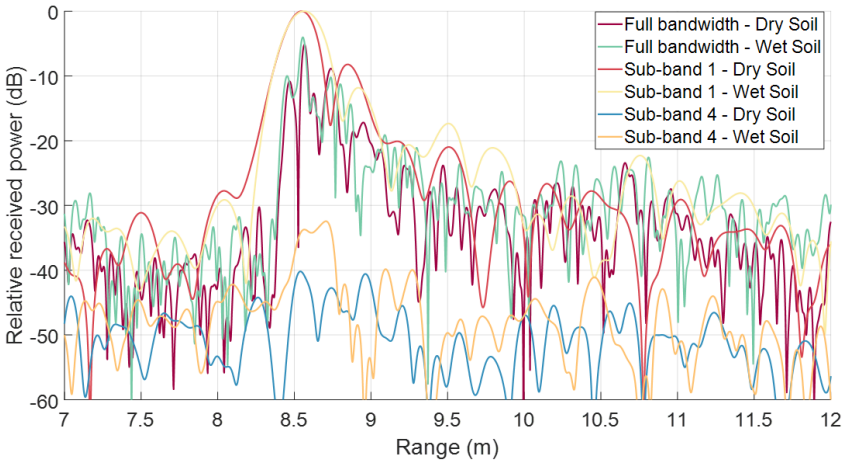

(a)

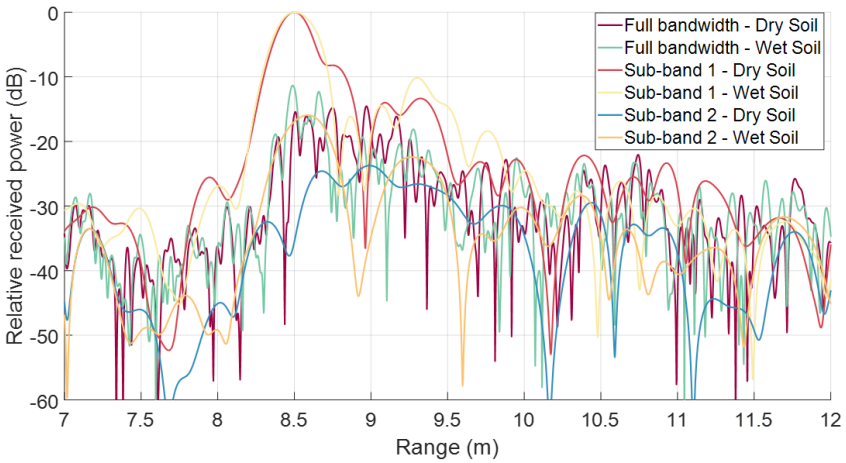

(b)

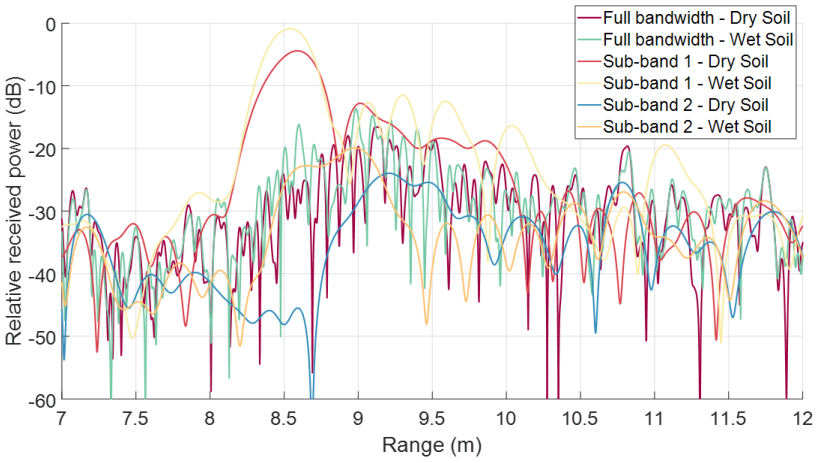

(c)

Figure 5-22: Close-up of the frequency domain response of the radar for dry and wet soil for vertical co-polarization at (a) nadir, (b) 15 degrees, and (c) 30 degrees. The response integrated over the full 16 GHz bandwidth is compared with the responses integrated

The sub-band processing results clearly show that the radar and antenna front-end are capable of detecting differences between two moisture states. However, since the backscattering coefficient is inter-dependent on multiple factors, more measurements must be done to generate statistical models. The precise correlation between change in backscatter power over an extended range and change in only moisture content is difficult to ascertain.

Furthermore, the surface roughness is also a significant contributor to the backscatter. The effects observed on the received signal are caused due to a combination of both the moisture and roughness and hence must be analyzed as an aggregate over numerous data products. Repeated measurements performed over a large area of land, for all four polarizations, at different look angles, and for different types of soil are required to accurately develop models that describe soil moisture and roughness.

6 Conclusions and Future Work

The development of a miniaturized 2 – 18 GHz FMCW radar system is presented. The DC bias circuitry, Phase-Locked Loop (PLL), transmitter, and receiver are designed on a compact two-board solution. The RF board is a two-layer PCB, while the Mixed-signal board is four-layers and both measure 15 cm in length and 11.21 cm in width. These two sections along with the DC power module section, Arena module, Clock board, and GPS board are integrated together in an Aluminum chassis of dimensions 23.88 cm x 19.56 cm x 8.64 cm. The volume of the radar electronics is 4,035.68 cm^3 and it weighs less than 2.72 kg.

The current draw, power consumption, and heat dissipation levels are all within recommended operating limits. The LFM signal is generated using a PLL- based multiplier where an 11 – 19 GHz band swept by a Voltage Controlled Oscillator is translated in frequency to result in a 2 – 18 GHz chirp signal. The measured amplitude slope of the chirp signal is greater than the

simulated prediction by approximately 11 dB. This is caused due to the physical imperfections during the board merging process. External components like gain equalizers are used to condition the amplitude slope.

The measured range resolution from the delay-line test is 1.45 cm (with Hanning window) and this is within expectations. However, the trailing-edge side-lobe level is 16.88 dB relative to the peak. This is larger than typical values and delay-line tests commonly show side-lobes at least 20 – 25 dB below the peak. Large side-lobe levels are preferred as it improves target identification in post-processing. However, for scatterometer applications, this effect is not as significant as for sounding applications.

The antenna front-end consists of four four-element antenna arrays housed in a Delrin plastic fixture and are fed using custom-designed microstrip power dividers. The dimensions of the fixture are 13.7 cm x 5.9 cm x 5.5 cm and the uniform elemental distance is 2.5 cm. The arrays are fastened to a metal sheet and integrated under the payload tray of the rotorcraft. The measured return loss on the full setup with the rotorcraft covers 2 – 18 GHz and the highest value is -7.22 dB at 5.23 GHz. The radiation pattern shows a distinct nadir-pointing main lobe for nearly the entire bandwidth, however the effects due to the platform increases the average side-lobe levels for 10 – 18 GHz by nearly 10 dB. The increase in side-lobe levels do not negatively impact scatterometer measurements as the backscatter is received over an integrated surface area. The measured maximum nadir gain is 15.88 dB at 10 GHz and the average nadir gain across the 16 GHz bandwidth is 8.34 dB.

Two full system tests are performed as proof-of-concept measurements to record backscatter returns of soil for dry and wet-state. The antenna front-end is exclusively characterized with a large metal sheet as a calibration target using a VNA. Measurements are recorded for all

four polarization combinations and for thre look angles, namely, nadir, 15 degrees, and 30 degrees. Gravimetric measurements of collected soil samples indicate an average change of 9.5% between the two moisture states. Vertical co-polarization measurements indicate a widening of the primary backscatter peak at the 10 dB cut-off from the peak and is more sensitive to moisture content than the horizontal counterpart. The horizontal polarization results in a larger peak received power for the primary backscatter signal and is less affected at smaller rotation angles in cross-track direction.

The radar measurements are performed with a rack-mount (1U) test bed and antenna front-end on the same patch of land. Initial results do not clearly indicate a difference in backscatter response between dry and wet soil, as seen in the VNA results. The 16 GHz bandwidth is sub-divided in four separate bands and the signal integration is performed over a stitched bandwidth of 13.3 GHz Each frequency sub-band represents less than 6 dB variation in nadir gain and the frequency domain response over each band indicates slightly new information about the soil. After sub-band processing, the responses for each sub-band and the stitched band indicate differences between dry and wet soil. The target information obtained through this process is an aggregate of all the data products. Therefore, the radar system is capable of detecting differences in moisture state and indicate differences in the backscatter return for each polarization and look angle.

The recommended future work for this project is divided into: immediate work and future extension. Immediate work covers the next steps needed to further characterize the radar and eventually record measurements from the UAS. Future extension includes suggestions on how to expand the capabilities of the system further.

Immediate Work:

1. The full system tests described in Chapter 5 should be repeated for the assembled miniaturized radar. Measurements must be compared to characterize the effects of the system.
2. System tests with soil should be repeated with a standard horn antenna to further characterize the effects of the antenna front-end, particularly the change in nadir gain across the bandwidth.
3. Full system tests should be repeated over a larger test area to make accurate moisture correlation.
4. The surface roughness of the soil should also be characterized and processed together with the moisture data.
5. Finally, the full miniaturized radar system can be integrated on the UAS and surface measurements may be performed on numerous targets.

Future Extension:

1. A new antenna front-end that is more low-profile can be designed. Some antenna types that can be explored are phased arrays, frequency independent antennas, and cavity-backed slot antennas. More compact methods of integration can greatly improve the performance.
2. The radar electronics can be expanded to accommodate higher transmit power and a new chassis can be built for a different physical arrangement of subsystems to enable further miniaturization.
3. Re-fabricate the RF and Mixed-signal boards and re-merge for better connections and assembly. This is a pivotal step in the development process and ensuring exact mechanical integration results in high signal integrity. Specifically, this reduces the frequency roll-off

within the bandwidth. An increase in noise floor can also be prevented by having uniform ground continuity between the boards.

4. Only bare soil is considered in this work due to the proof-of-concept objective. However, the next step is to measure soil moisture with vegetation cover. The backscatter received is also dependent on the moisture and reflectivity of the vegetation. Hence, tests must be done to characterize the effect from both targets. Consequently, the radar can also be used to map vegetation canopy and perform crop phenotyping.
5. Snow measurements can be done to characterize the radar's maximum penetration into the surface and the vertical resolution required to discern top snow layers. In this case, a higher transmit power should be explored to ensure consistent target returns.

7 Bibliography

[1] A Comprehensive Review of Recent Progress on GaN High Electron Mobility Transistors: Devices, Fabrication and Reliability. Fanming Zeng, Judy Xilin An, Guangnan Zhou, Wenmao Li, Hui Wang, Tianli Duan, Lingli Jiang, and Hongyu Yu. 12, 2018, Electronics, Vol. 7.

[2] Evolutionary Trends in Transmit/Receive Module for Active Phased Array Radars. Somsing Rathod, K. Sreenivasulu, K.S. Beenamole, K.P. Ray. 6, November 2018, Vol. 68, pp. 553-559.

[3] Machine Learning driven Advanced Packaging and Miniaturization of IoT for Wireless Power Transfer Solutions. Hakki M. Torun∗, Colin Pardue, Mohamed L. F. Belladredj, Anto K. Davis and Madhavan Swaminathan. 2018. IEEE 68th Electronic Components and Technology Conference.

[4] Miniaturization of optical spectrometers. Zongyin Yang, Tom Albrow-Owen, Weiwei Cai. 6528, s.l. : Science, 2021, Vol. 371.

[5] Radar Technologies for Earth Remote Sensing From CubeSat Platforms. al., E. Peral et. 3, s.l. : IEEE, March 2018, Proceedings of the IEEE, Vol. 106, pp. 404-418.

[6] Laboratory, Jet Propulsion. Strategic Technologies 2019. NASA JPL. [Online] 2019. [Cited: November 30, 2021.] https://scienceandtechnology.jpl.nasa.gov/sites/default/files/documents/JPL_Strategic_Technologies_2019.pdf.

[7] Overview and Current Status of Remote Sensing Applications Based on Unmanned Aerial Vehicles (UAVs). Pajares, Gonzalo. 4, s.l. : Photogrammetric Engineering & Remote Sensing, April 2015, Vol. 81, pp. 281–329.

[8] UAS-Based Archaeological Remote Sensing: Review, Meta-Analysis and State-of-the-Art. Efstathios Adamopoulos, Fulvio Rinaudo. 3, s.l. : MDPI, August 2020, Drones, Vol. 4.

[9] Forestry applications of UAVs in Europe: A review. Torresan, Chiara, et al. 8–10, s.l. : Taylor & Francis Group, 2017, International Journal of Remote Sensing, Vol. 38, pp. 2427–2447.

[10] Water resource management at catchment scales using lightweight UAVs: Current capabilities and future perspectives. DeBell, L., et al. 7-30, s.l. : NRC Research Press, 2015, Journal of Unmanned Vehicle Systems, Vol. 4.

[11] Temporal and spatial variability in surface roughness and accumulation rate around 88° S from repeat airborne geophysical surveys. al., Michael Studinger et. 10, s.l. : Copernicus Publications, October 2020, Vol. 14, pp. 3287–3308.

[12] Satellite observations of Antarctic sea ice thickness and volume. Markus, N. T. Kurtz and T. C8, s.l. : American Geophysical Union, August 2012, JOURNAL OF GEOPHYSICAL RESEARCH, Vol. 117.

[13] The Scientific Legacy of NASA’s Operation IceBridge. MacGregor, JA, et. al. 2021, Reviews of Geophysics.

[14] Climate change and drought: the soil moisture perspective. Berg, Alexis, and Justin Sheffield. s.l. : Springer, April 2018, Current Climate Change Reports, pp. 180-191.

[15] Dara Entekhabi, et al. SMAP Handbook. Pasadena, California : NASA, 2014.

[16] Advanced Multifrequency Radar Instrumentationfor Polar Research. Rodríguez-Morales, Fernando, et al. 5, s.l. : IEEE, MAY 2014, TRANSACTIONS ON GEOSCIENCE AND REMOTE SENSING, Vol. 52, pp. 2824-2842.

[17] Ulaby, F. T., and D. Long. Microwave radar and radiometric remote sensing. s.l. : Norwood, MA: Artech House, 2014.

[18] Garcia-Alvestegui, Daniel Gomez. A LINEARIZATION METHOD FOR A UWB VCO-BASED CHIRP GENERATOR USING DUAL COMPENSATION. Lawrence : s.n., 2011.

[19] Carr, K., 2019. Development of a Multichannel Wideband Radar Demonstrator. Master's Thesis. University of Kansas.

[20] Vapor 55 Datasheet. AeroVironment. [Online] July 2021. https://www.avinc.com/images/uploads/product_docs/Vapor_55_Datasheet_07122021.pdf.

[21] Kornelsen, Kurt C., and Paulin Coulibaly. "Advances in soil moisture retrieval from synthetic aperture radar and hydrological applications." Journal of Hydrology 476 (2013): 460-489.

[22] Ulaby, F. "Radar measurement of soil moisture content." IEEE Transactions on Antennas and propagation 22.2 (1974): 257-265.

[23] Bartalis, Zoltan, et al. "Initial soil moisture retrievals from the METOP-A Advanced Scatterometer (ASCAT)." Geophysical Research Letters 34.20 (2007).

[24] Joseph, Alicia T., et al. "Soil moisture retrieval during a corn growth cycle using L-band (1.6 GHz) radar observations." IEEE Transactions on Geoscience and Remote Sensing 46.8 (2008): 2365-2374.

[25] Kim, Seung-Bum, et al. "Soil moisture retrieval using time-series radar observations over bare surfaces." IEEE Transactions on Geoscience and Remote Sensing 50.5 (2011): 1853-1863.

[26] Chapin, Elaine, et al. "AirMOSS: An airborne P-band SAR to measure root-zone soil moisture." 2012 IEEE Radar Conference. IEEE, 2012.

[27] Yueh, Simon H., et al. "Airborne Ku-band polarimetric radar remote sensing of terrestrial snow cover." IEEE Transactions on Geoscience and Remote Sensing 47.10 (2009): 3347-3364.

[28] Capozzi, Vincenzo, et al. "Retrieval of snow precipitation rate from polarimetric X-band radar measurements in Southern Italy Apennine mountains." Atmospheric Research 236 (2020): 104796.

[29] Panzer, Ben, et al. "An ultra-wideband, microwave radar for measuring snow thickness on sea ice and mapping near-surface internal layers in polar firn." Journal of Glaciology 59.214 (2013): 244-254.

[30] Yan, Jie-Bang, et al. "Ultrawideband FMCW radar for airborne measurements of snow over sea ice and land." IEEE Transactions on Geoscience and Remote Sensing 55.2 (2016): 834-843.

[31] F. Rodriguez-Morales, J. Li, D. Gomez-Garcia, J. Shang, E. Arnold, C. Leuschen, C. Larsen, A. Shepherd, S. Hvidegaard, and R. Forsberg, A Compact, Reconfigurable, Multi-UWB Radar for Snow Thickness Evaluation and Altimetry: Development and Field Trials,

IEEE J. Sel. Top. App. Earth Obs. Remote Sens. Vol. 14, 2021, pp. 6755–6765, 10.1109/JSTARS.2021.3092313

[32] D. Gomez-Garcia,Snow Thickness Measurements with Snow Radar Installed on Vanilla UAS, CReSIS Internal Report, Nov. 2021.

[33] A. Tan, K. Eccleston, I. Platt, I. Woodhead, W. Rack, and J. McCulloch, “The design of a UAV mounted snow depth radar: Results of measurements on Antarctic sea ice,” in Proc. IEEE Conf. Antenna Meas. Appl., Tsukuba, Japan, Feb. 2017, pp. 316–319.

[34] M. Oyan, S. Hamran, L. Damsgard, and T. Berger, “Compact airborne C-Band radar sounder,” IEEE Trans. Geosci. Remote Sens., vol. 52, no. 10, pp. 6323–6332, Oct. 2014.

[35] P. Pomerleau et al., “Low cost and compact FMCW 24 GHz radar applications for snowpack and ice thickness measurements,” Sensors, vol. 20, no. 14, Jul. 2020, Art. no. 3909, doi: 10.3390/s20143909.

[36] R. O. R. Jenssen, M. Eckerstorfer, and S. Jacobsen, “Drone-mounted ultrawideband radar for retrieval of snowpack properties,” IEEE Trans. Instrum. Meas., vol. 69, no. 1, pp. 221–230, Jan. 2020

[37] Steatite Antennas. Wideband Horn Antenna 2 to 18 GHz, www.steatite-antennas.co.uk/wp-content/uploads/2017/09/QWH-SL-2-18-S-SG-R.pdf

[38] Ulaby, Fawwaz T., Percy P. Batlivala, and Myron C. Dobson. "Microwave backscatter dependence on surface roughness, soil moisture, and soil texture: Part I-bare soil." IEEE Transactions on Geoscience Electronics 16.4 (1978): 286-295.

[39] Hallikainen, Martti T., et al. "Microwave dielectric behavior of wet soil-part 1: Empirical models and experimental observations." IEEE Transactions on Geoscience and Remote Sensing 1 (1985): 25-34.

[40] 2019. Arena Series 300 Product Overview. [ebook] Remote Sensing Solutions (now part of Tomorrow.io). Available at: <https://secureservercdn.net/198.71.233.51/c9q.cac.myftpupload.com/wp-content/uploads/2019/09/Series_300_ProductOverview.pdf> [Accessed 12 August 2021].

[41] Talasila, H., 2017. MODULAR FREQUENCY MULTIPLIER AND FILTERS FOR THE GLOBAL HAWK SNOW RADAR. Master's Thesis. University of Kansas.

[42] Gomez-Garcia, D., 2019. Scattering Analysis and Ultra-Wideband Radar for High-Throughput Phenotyping of Wheat Canopies. PhD Dissertation. University of Kansas.

[43] Gomez-Garcia, Daniel, et al. "High-Throughput Phenotyping of Wheat Canopy Height Using Ultrawideband Radar: First Results." IEEE Geoscience and Remote Sensing Letters (2020).

[44] Balanis, Constantine A. Antenna theory: analysis and design. John wiley & sons, 2015.

[45] Cicchetti, Renato, et al. "Wideband, multiband, tunable, and smart antenna systems for mobile and UWB wireless applications 2016." (2017).

[46] Liang, Jianxin, et al. "Study of a printed circular disc monopole antenna for UWB systems." IEEE transactions on antennas and propagation 53.11 (2005): 3500-3504.

[47] Ahmed, Osama, and Abdel-Razik Sebak. "A printed monopole antenna with two steps and a circular slot for UWB applications." IEEE Antennas and Wireless Propagation Letters 7 (2008): 411-413.

[48] Lin, Chi-Chang, and Huey-Ru Chuang. "A 3-12 GHz UWB planar triangular monopole antenna with ridged ground-plane." Progress In Electromagnetics Research 83 (2008): 307-321.

[49] Bao, X. L., and M. J. Ammann. "Investigation on UWB printed monopole antenna with rectangular slitted groundplane." microwave and optical technology letters 49.7 (2007): 1585-1587.

[50] Wu, Qi, et al. "Printed omni-directional UWB monopole antenna with very compact size." IEEE transactions on antennas and propagation 56.3 (2008): 896-899.

[51] Oraizi, Homayoon, and Shahram Hedayati. "Miniaturized UWB monopole microstrip antenna design by the combination of Giusepe Peano and Sierpinski carpet fractals." IEEE antennas and wireless propagation letters 10 (2011): 67-70.

[52] Verma, Sudhanshu, and Preetam Kumar. "Printed Newton's egg curved monopole antenna for ultrawideband applications." IET Microwaves, Antennas & Propagation 8.4 (2014): 278-286.

[53] T. Wang, J. M. Keller, P. D. Gader and O. Sjahputera, "Frequency Subband Processing and Feature Analysis of Forward-Looking Ground-Penetrating Radar Signals for Land-Mine Detection," in IEEE Transactions on Geoscience and Remote Sensing, vol. 45, no. 3, pp. 718-729, March 2007, doi: 10.1109/TGRS.2006.888142.

[54] Xu, Xiaojian, and Jia Li. "Ultrawide-band radar imagery from multiple incoherent frequency subband measurements." Journal of Systems Engineering and Electronics 22.3 (2011): 398-404.

[55] Yi, Jianxin, et al. "Robust clutter rejection in passive radar via generalized subband cancellation." IEEE Transactions on Aerospace and Electronic Systems 54.4 (2018): 1931-1946.

[56] Feng, Jin, et al. "Application of subband spectral cancellation for SAR narrow-band interference suppression." IEEE Geoscience and Remote Sensing Letters 9.2 (2011): 190-193.

[57] Cohn, Seymour B. "A class of broadband three-port TEM-mode hybrids." IEEE Transactions on Microwave Theory and Techniques 16.2 (1968): 110-116.

[58] McDaniel, J., 2015. Design, Integration, and Miniaturization of a Multichannel Ultra-Wideband Snow Radar Receiver and Passive Microwave Components. Master's Thesis. University of Kansas.

[59] 2021. H20E-PFC Silver Epoxy Datasheet. [ebook] Epoxy Technology, Inc. Available at: <https://www.epotek.com/docs/en/Datasheet/H20E-PFC.pdf> [Accessed 8 December 2021].

[60] Stutzman, Warren L., and Gary A. Thiele. Antenna theory and design. John Wiley & Sons, 2012.

[61] Ortiz, Javier Alejandro. "Impact of Edge Diffraction in Dual-Polarized Phased Array Antennas." (2020). PhD Dissertation. University of Oklahoma.

[62] Moore Jr, Charles L., and Gary A. Thiele. Satellite antenna pattern distortion due to ground plane edges. OHIO STATE UNIV COLUMBUS ELECTROSCIENCE LAB, 1975.

[63] Skolnik, Merrill I. "Introduction to radar." Radar handbook 2 (1962): 21.

[64] Kinzie, Nicola Jean. Ultra-wideband pulse Doppler radar for short-range targets. Diss. University of Colorado at Boulder, 2011. PhD Dissertation. University of Colorado.

8 Appendix

8.1 TGA2567 Amplifier Bias Sequence

	Bias-up procedure		Bias-down procedure
1	Set I_D limit to 160 mA, I_G limit to 24 mA	1	Turn off RF supply
2	Apply −1.5 V to V_{G1}	2	Reduce V_{G1} to −1.5 V; ensure I_{DQ} is approx. 0 mA
3	Apply +5 V to V_D; ensure I_{DQ} is approx. 0 mA	3	Set V_{G2} to 0 V
4	Apply +1.3 V to V_{G2}	4	Set V_D to 0 V
5	Adjust V_{G1} until I_{DQ} = 100 mA (V_{G1} ~ −0.7 V Typ.)	5	Turn off V_D supply
6	Adjust V_{G2} to obtain desired gain	6	Turn off V_{G1} and V_{G2} supplies
7	Turn on RF supply		

8.2 ADRF5020 Single Positive Supply Performance

Ilke, Selcuk. “ADRF5020 Single Positive Supply Performance.” Analog Devices, 4 Sept. 2019.https://ez.analog.com/rf/f/q-a/115384/need-info-regarding-adrf5020-negative-supply-connection-vss. Date Accessed. 17 November 2020.

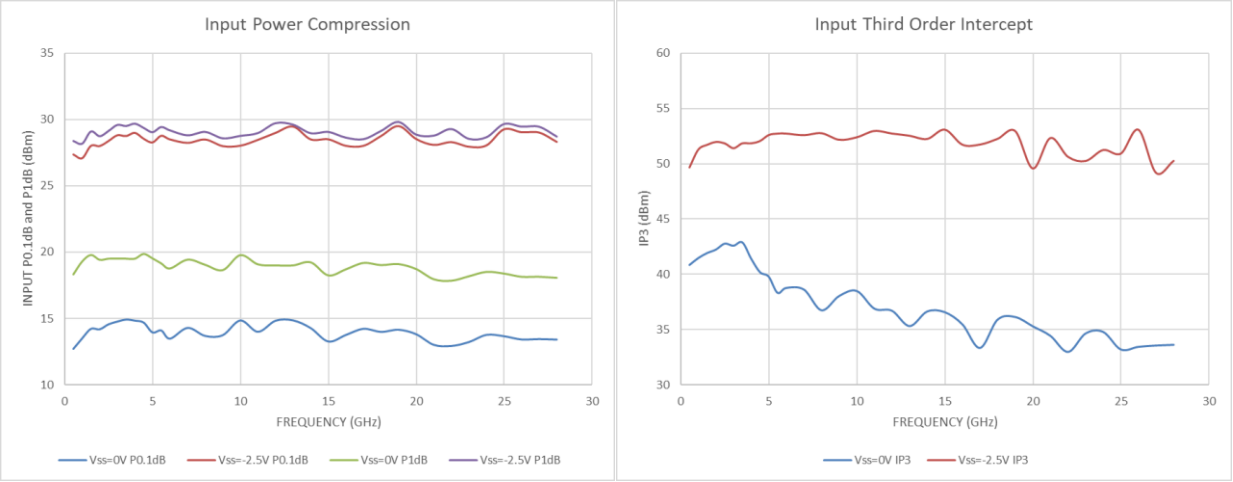

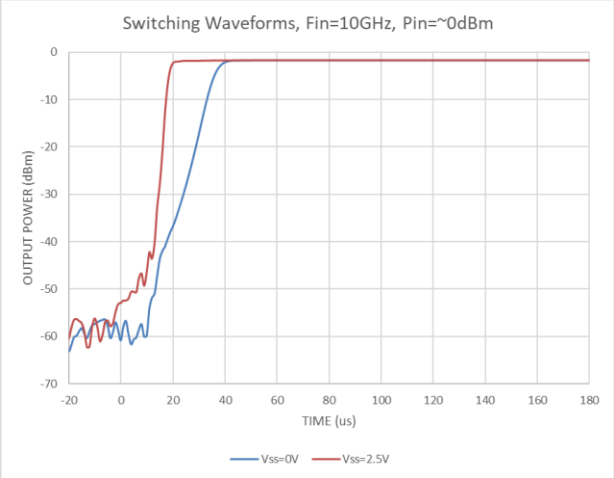

For V_{ss} = -2.5 V, 0.1 dB settling = 30 ns

For V_{ss} = 0 V, 0.1 dB settling = 45 ns

8.3 Thermal testing of power section

Figure: Picture of the FLIR Infrared Camera screen showing the temperature measurement of the three LDOs on one of the power boards

8.4 Fiberglass fairing fabrication process

Figure: Picture of the vacuum bagging process of the fiberglass fairing. A prototype fairing and metal sheet with antenna arrays can be seen at the back.

8.5 Fairing ground clearance

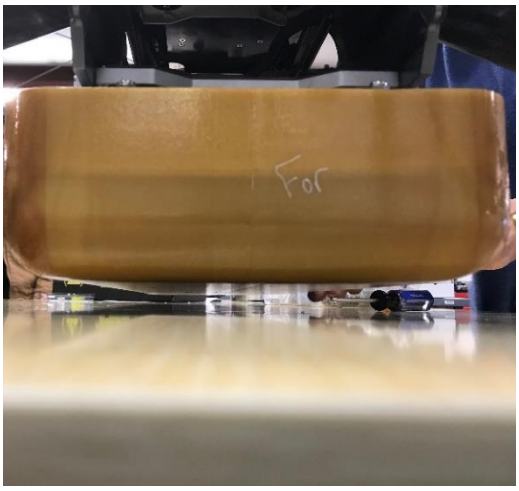

8.6 Integrated standard horn antenna for future work

8.7 Radar calibration data for 10 cm x 10 cm metal plates

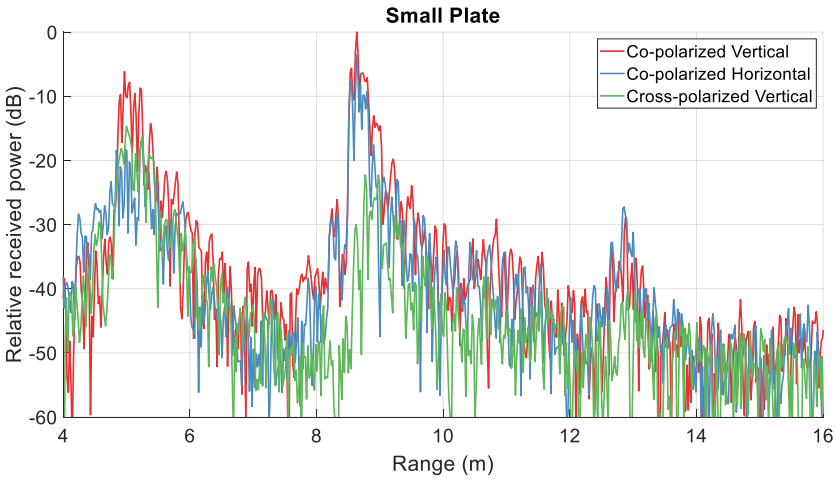

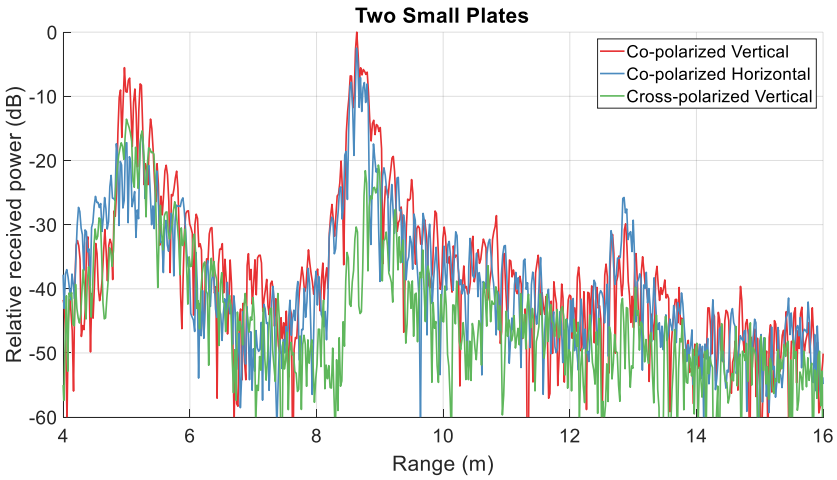

8.8 Comparison of VNA and Radar data

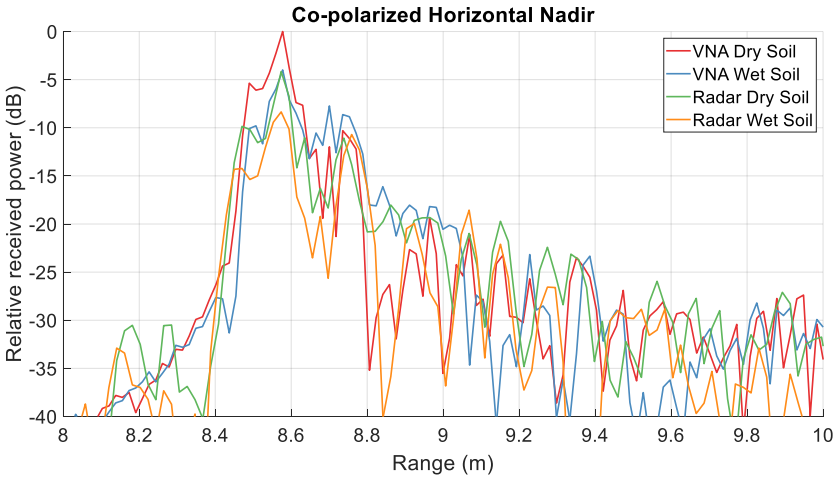

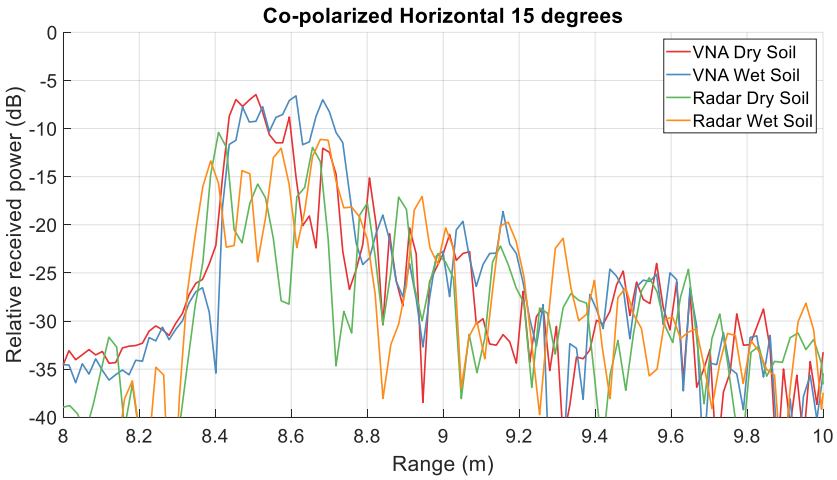

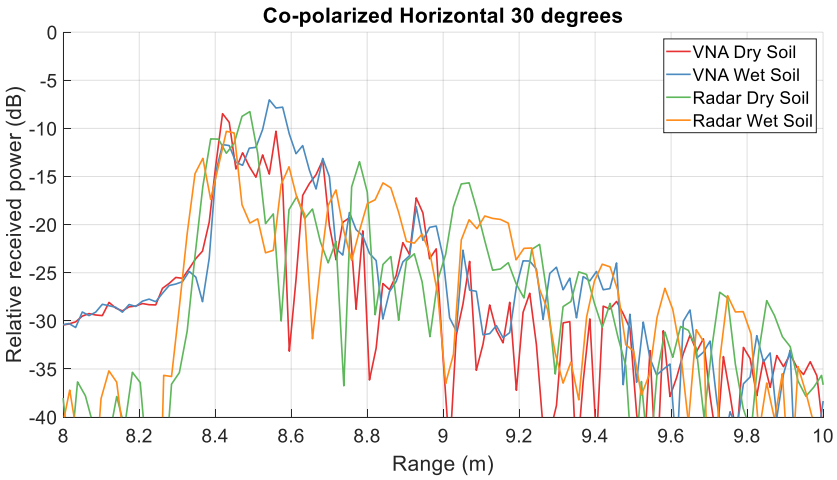

8.9 Sub-band radar results from other data products

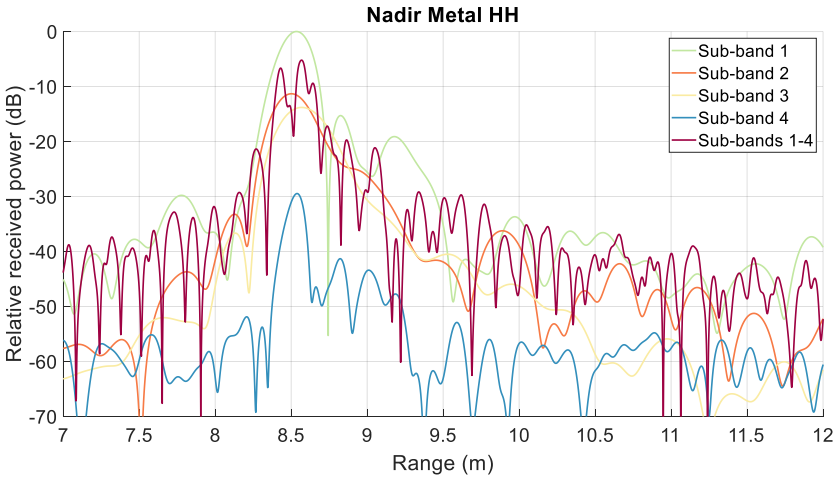

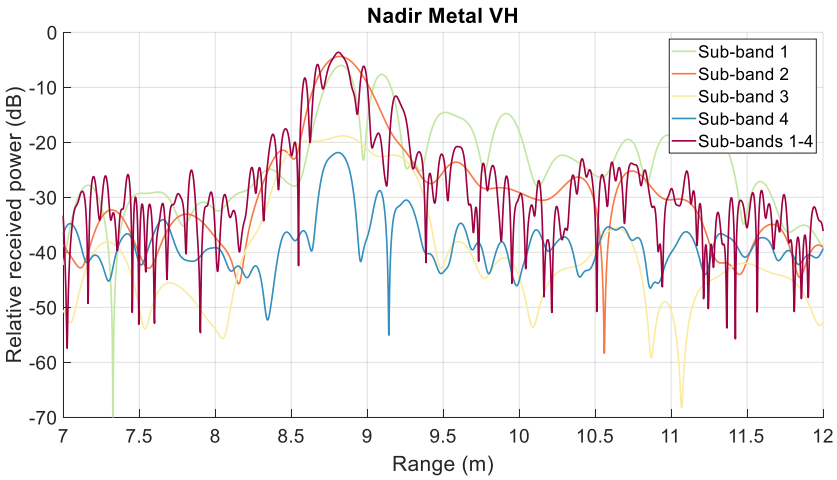

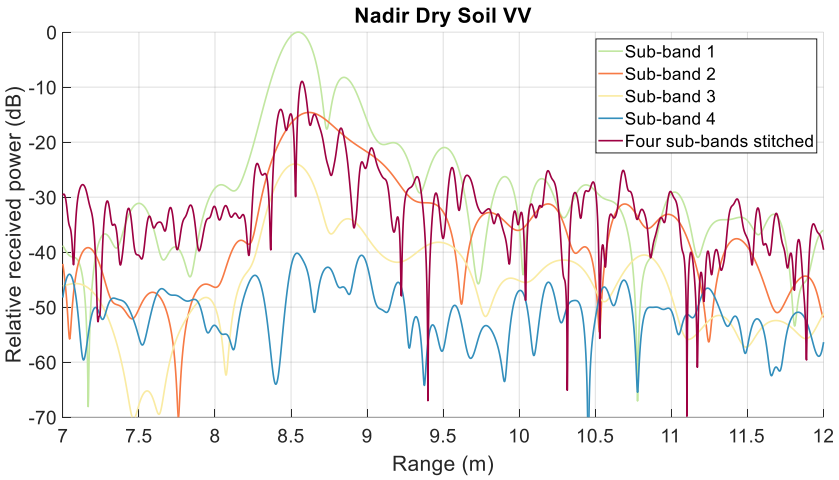
Nadir Dry Soil VV
Relative received power (dB)
Range (m)
Sub-band 1
Sub-band 2
Sub-band 3
Sub-band 4
Four sub-bands stitched

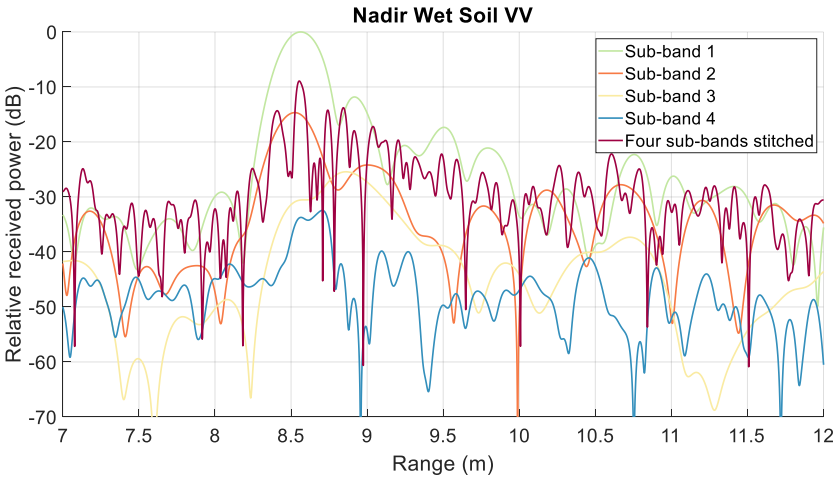
Nadir Wet Soil VV
Relative received power (dB)
Range (m)
Sub-band 1
Sub-band 2
Sub-band 3
Sub-band 4
Four sub-bands stitched

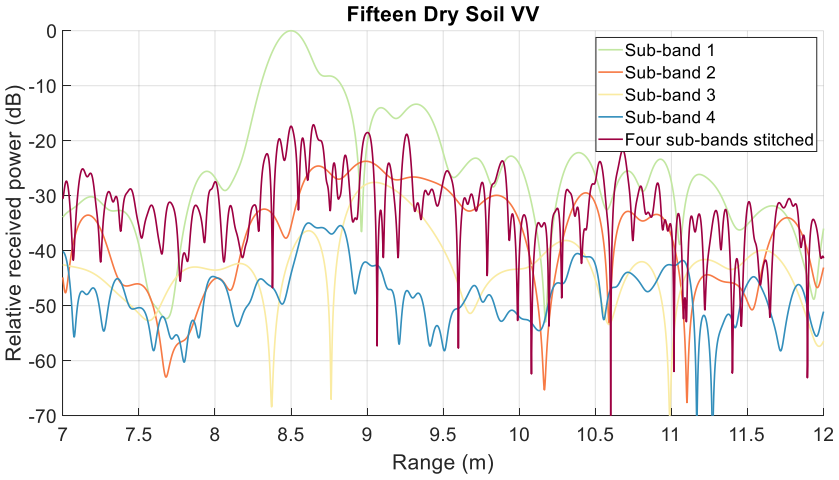
Fifteen Dry Soil VV
Relative received power (dB)
Range (m)
Sub-band 1
Sub-band 2
Sub-band 3
Sub-band 4
Four sub-bands stitched

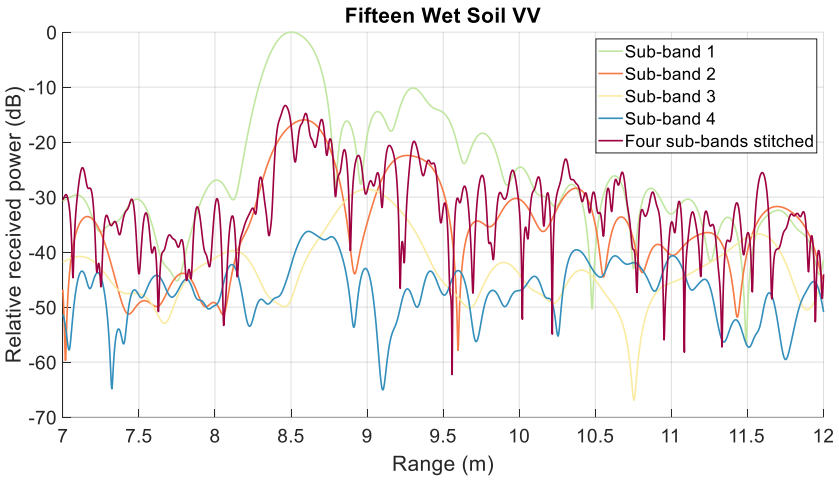
Fifteen Wet Soil VV
Relative received power (dB)
Range (m)
Sub-band 1
Sub-band 2
Sub-band 3
Sub-band 4
Four sub-bands stitched

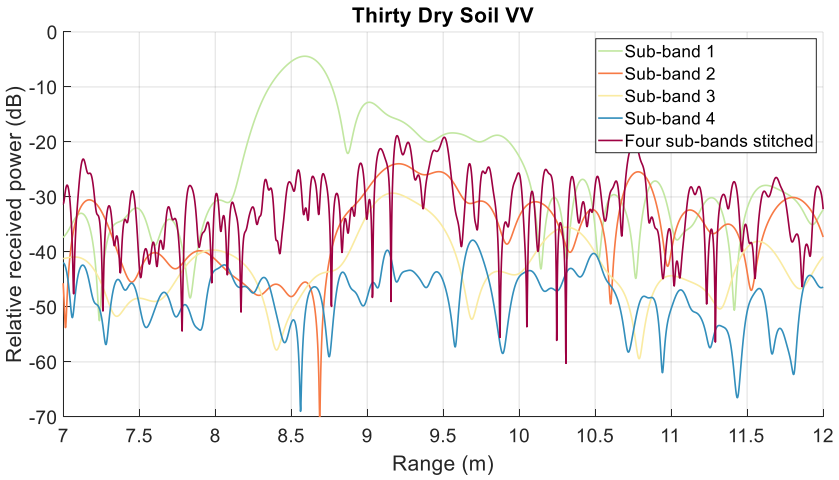
Thirty Dry Soil VV
Relative received power (dB)
Range (m)
Sub-band 1
Sub-band 2
Sub-band 3
Sub-band 4
Four sub-bands stitched

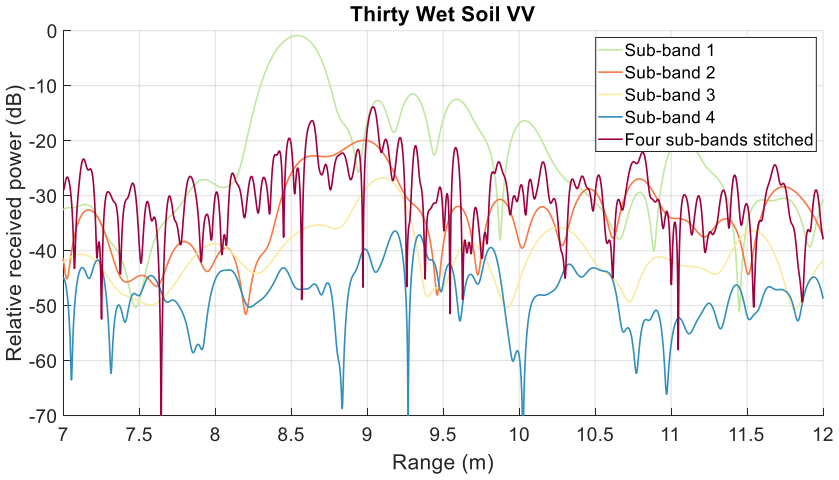
Thirty Wet Soil VV
Relative received power (dB)
Range (m)
Sub-band 1
Sub-band 2
Sub-band 3
Sub-band 4
Four sub-bands stitched